

Fall 2015

A MODEL STUDY OF ADLAYER PATTERN FORMATION OF RIGID DI- TRI- AND TETRATOPIC MOLECULES ON SQUARE AND TRIANGULAR LATTICES

Moh'd Ibrahim Alomari
University of New Hampshire, Durham

Follow this and additional works at: <https://scholars.unh.edu/dissertation>

Recommended Citation

Alomari, Moh'd Ibrahim, "A MODEL STUDY OF ADLAYER PATTERN FORMATION OF RIGID DI- TRI- AND TETRATOPIC MOLECULES ON SQUARE AND TRIANGULAR LATTICES" (2015). *Doctoral Dissertations*. 2230.
<https://scholars.unh.edu/dissertation/2230>

This Dissertation is brought to you for free and open access by the Student Scholarship at University of New Hampshire Scholars' Repository. It has been accepted for inclusion in Doctoral Dissertations by an authorized administrator of University of New Hampshire Scholars' Repository. For more information, please contact nicole.hentz@unh.edu.

**A MODEL STUDY OF ADLAYER PATTERN FORMATION OF RIGID DI-
TRI- AND TETRATOPIC MOLECULES ON SQUARE AND
TRIANGULAR LATTICES**

BY

Mohammed I. Alomari

B.S. Chemistry, Jordan University of Science and Technology, 1996

Master's Degree, Yarmouk University, 1999

DISSERTATION

**Submitted to the University of New Hampshire
in Partial Fulfillment of
the Requirements for the Degree of**

**Doctor of Philosophy
in**

Chemistry

December, 2015

This dissertation has been examined and approved in partial fulfillment of the requirements for the degree of PhD in chemistry

Dissertation Director, Howard R. Mayne
Professor of Chemistry

Sterling A. Tomellini
Professor of Chemistry

Karsten Pohl
Professor of Physics

Margaret E. Greenslade
Associate Professor of Chemistry

Gonghu Li
Associate Professor of Chemistry

On 08/26/2015

Original approval signatures are on file with the University of New Hampshire Graduate School.

ACKNOWLEDGMENTS

The author wishes to acknowledge the research support provided by the following university support:

The University of New Hampshire Graduate School

TA Fellowship for the Summer (2013)

The University of New Hampshire Chemistry Department

The Chemistry Department Award for the Summer 2011

Cindi Rohwer, Department Manager

Peg Torch, Administrator Assistant

Bob Constantine, Department Library Manager

I am heartily thankful to my supervisor Howard R. Mayne for his help and encouragement, guidance and support from the initial to the final level of this work.

Also I appreciated the work done by the committee members for their help and suggestions to complete this dissertation.

I would like to acknowledge and dedicate this work to my parents, my lovely wife Noor, my kids, my siblings and to all of my friends who encouraged and supported me during my PhD study.

TABLE OF CONTENTS

ACKNOWLEDGMENTS	iii
TABLE OF CONTENTS.....	iv
List of Figures	viii
List of Tables	xix
Abstract.....	xx
Chapter I Introduction.....	1
I.1 Motivation and Background	1
I.1.a Applications:.....	2
I.1.b Experimental Studies:	4
I.1.c Theoretical studies:.....	5
I.2 The Present Work	9
Chapter II Overview of Di-, Tri- and Tetratopic Molecules on Square and Triangular Lattices .	11
II.1 Introduction	11
II.2 Identification of Adlayer Patterns – Radial Distribution Functions and Orientational Order Parameters	14
II.3 Concepts	21
II.4 Procedure	24
II.5 Method.....	25
Potential energy function.....	27
II.6 Simplified unit cell notation and some definitions.....	33
II.7 Summary.....	36
Chapter III A Model Study of Adlayer Geometries of Rigid Ditopic Molecules on a Square Lattice	37
III.1 Introduction	37
III.2 Method	39
III.2.a Energy Landscape.....	39
III.2.b Orientational Order Parameters	39
III.2.c Key Geometries	40
III.2.d Distortion Pathways.....	44
III.3 Results and Discussion for Square Lattice	48

III.3.a Parameter “Phase Diagram” for the Lennard-Jones Potential	48
III.3.b Local Minima for the Lennard-Jones Potential	55
III.3.c Parameter Phase Diagrams for Other Potentials.....	58
III.4 Ditopic Molecule on Square Lattice (All Lattice Sites are Occupied) Conclusions and Comments.....	63
Chapter IV A Model Study of Adlayer Geometries of Rigid Ditopic Molecules on a Triangular Lattice	65
IV.1 Introduction.....	65
IV.2 Method	66
IV.2.a Energy Landscape.....	66
IV.2.b Orientational Order Parameters.....	67
IV.2.c Key Geometries	67
IV.3 Results and Discussion for a Triangular Lattice	72
IV.3.a Parameter “Phase Diagram” for the Lennard-Jones Potential.....	72
IV.3.b Special case $\rho=0.5$, $r_e=0.4$ (4X4 unit cell).....	76
IV.4 Conclusions and comments on the Adlayers of the Ditopic Molecule on a Triangular Lattice.....	77
Chapter V A Model Study of Adlayer Geometries of Rigid Tritopic Molecules on Triangular and Square Substrates	80
V.1 Introduction	80
V.2 Result and discussion (Tritopic on a Triangular Lattice).....	81
V.2.a Distortion Pathways.....	82
V.2.b Order parameters	83
V.2.c Results of full potential energy search on a triangular lattice.....	86
V.3 Conclusion for a Tritopic Molecule on a Triangular Lattice.....	98
V.4 Results and discussion (Tritopic on a Square Lattice)	99
Results at constant values of r_e of tritopic molecule on a square lattice.....	104
V.5 Conclusion for a Tritopic Molecule on a Square Lattice	114
Chapter VI A Model Study of Adlayer Geometries of Rigid Tetratopic Molecules on Square and Triangular Lattices	115
VI.1 Introduction.....	115

VI.2 Method	116
VI.3 Results and Discussion of a Tetratopic Molecule on Square Lattice:.....	117
VI.3.a Order parameters	120
VI.3.b Results of a Full Space Minimization	122
VI.3.c Local Minima	129
VI.4 Results and Discussion of a Tetratopic Molecule on a Triangular Lattice:	134
VI.4.a Orientational order parameters	134
VI.4.b Result of full search at constant values of r_e	135
VI.5 Tetratopic Adlayer Conclusion and Comparison with Previous Studies	144
Chapter VII Monte Carlo Model Study of Adlayer Geometries of Rigid Ditopic Molecules on Square and Triangular lattices	145
VII.1 Introduction.....	145
VII.2 Model.....	145
VII.2.a. Model molecule 1	145
VII.2.b. Model molecule 2.....	147
VII.3 Method.....	148
VII.3.a NVT canonical Monte Carlo ensemble	148
VII.3.b Grand canonical ensemble:	149
VII.3.c Order Parameters.....	151
VII.4 Result and Discussion.....	152
VII.4.a Molecule 1, $\rho=0.29$, $r_e=0.4$ on square lattice, lattice constant =1:.....	152
VII.4.b Molecule 1, $\rho=0.42$, $r_e=0.4$ on square lattice, lattice constant =1:.....	153
VII.4.c Molecule 1, $\rho=0.5$, $r_e=0.4$ on a square lattice, lattice constant =1:	154
VII.4.d Molecule 1, $\rho=0.34$, $r_e=0.4$ on a triangular lattice, lattice constant =1:.....	155
VII.4.h Molecule 2, $\rho=0.50$, $r_e=0.2$ on a square lattice, lattice constant =0.18.....	160
Appendix A : Method	164
A.I Method for Finding Stationary Points.....	164
A.I.a Method for finding global minima:	164
A.I.b Method for finding local minima:	164
A.II Quasi-Newton Broyden–Fletcher–Goldfarb–Shanno (BFGS) minimization method.....	166

A.III Method for Finding Radial Distribution Function of a ditopic molecule a square lattice:	167
Appendix B : The potential function and its gradient and hessian	168
Appendix C : Wallpaper Symmetry Groups	169
Appendix D : Calvo's approach of Temperature Replica Exchange Monte Carlo (T-REMC)..	178
Supporting Material: Chemical structures mentioned in the dissertation	179
List of References	181

List of Figures

- Figure II-1: The model molecules, di-, tri- and tetratopic on square lattice (n-topic: n refers to number of arms of the molecule). (a) Shows porphyrin derivative with four hydrogen bonds can be model by using coarse-graining tetratopic molecule. (b) A tritopic model on the lattice site, θ is the angle of the rotor with the universal x axis, ρ the length of the rotor arm from its center of mass to the tip. (c) The unit cell of the system with angles $(\theta_1, \theta_2, \theta_3, \theta_4)$. (d) Interactions between two tritopic rotors showing one of the interactions at the equilibrium distance of the potential. 12
- Figure II-2: Energy, heat capacity, and two order parameters as a function of temperature from Monte Carlo trajectories for ditopic molecule with Lennard-Jones potential, $r_e=0.40$ $\rho = 0.5$. (For explanation of parameters, see Section II-1 and II-5.) Shown on the left of the figure is a snapshot of a typical structure at low ($T=0.1$) temperature; shown on the right is a snapshot of a typical structure at high temperature ($T=0.4$). (note: for clarity the snapshot on the right is zoomed in) 13
- Figure II-3: Starting from upper most left and proceeding left to right in two rows. The 2×2 unit cell $[\theta_1, \theta_2, \theta_3, \theta_4]$ on square lattice is highlighted; Model ditopic molecule (ρ is the distance between the molecule center of mass and a site); The 2×2 unit cell $[\theta_1, \theta_2, \theta_3, \theta_4]$ on triangular lattice is highlighted; Schematic representation of the tessellation of the unit cell to an infinite square lattice; and Schematic representation of the tessellation of the unit cell to an infinite triangular lattice. The angles are taken with reference to the lattice x-axis..... 14
- Figure II-4: Schematic representation of simple geometries of a ditopic molecule on square lattice. 19
- Figure II-5: Tetratopic molecule on a square lattice. (Upper) The nearest-neighbor (NN) nearest-neighbor site-to-site separation s , as a function of molecular size, ρ . The functional forms are from **Table II-1**. (Lower) The total potential energy (in LJ energy units) as a function of molecular size, ρ , for the three geometries denoted as square (SQ), cross (CR) and compact (CO). The Lennard-Jones length parameter $r_e = 0.44$. The adlayer geometries are shown as cartoons. 22
- Figure II-6: Illustration of the site-to-site (r) distances between two adjacent rotors i and j used in the intermolecular potential energy interactions. 26
- Figure II-7: Schematic representation of Lennard-Jones and Morse potential with two different stiffness parameters $\beta = 10$ and 20 . Note that minimum at $r = r_e$ and that $V=0$ at $r = \infty$ 28
- Figure II-8: Space-filling “footprint” diagram for a ditopic molecule on a square lattice, showing pore size, shape, and orientation. 29
- Figure II-9: The model ditopic molecule (upper panel). To illustrate the effect of changing the molecular parameters, the potential energy is shown for a single atom-like site interacting with the molecule. This site has plane polar coordinates (R, γ) , or Cartesian coordinate $(R \cos \gamma, R \sin \gamma)$. Contour energy plots $V(\rho=0.3, 0.5, 0.6, r_e=0.2, 0.4, 0.5, \gamma)$ of the molecule with single site. $\gamma \in [0, 2\pi]$ is the angle of a single site moved around the molecule with the universal x-axis. Note: ρ is length of the each arm of the molecule from center of mass; r_e is the site-to-site equilibrium distance of Lennard-Jones potential. 30

- Figure II-10: The model tritopic molecule (upper panel). To illustrate the effect of changing the molecular parameters, the potential energy is shown for a single atom-like site interacting with the molecule. This site has plane polar coordinates (R, γ) , or Cartesian coordinate $(R \cos \gamma, R \sin \gamma)$. Contour energy plots $V(\rho=0.3, 0.4, 0.5, r_e=0.2, 0.4, 0.5, \gamma)$ of the molecule with a single site. $\gamma \in [0, 2\pi]$ is the angle of a single site moved around the molecule from the universal x-axis..... 31
- Figure II-11: The model tetratopic molecule (upper panel). To illustrate the effect of changing the molecular parameters, the potential energy is shown for a single atom-like site interacting with the molecule. This site has plane polar coordinates (R, γ) , or Cartesian coordinate $(R \cos \gamma, R \sin \gamma)$. Contour energy plots $V(\rho=0.3, 0.4, 0.5, r_e=0.2, 0.4, 0.5, \gamma)$ of the molecule with a single site. $\gamma \in [0, 2\pi]$ is the angle of a single site moved around the molecule from the universal x-axis..... 32
- Figure II-12: Space-filling representations of two forms of herringbone. (Left) ABBA on a square lattice; (Right) AABB on a triangular lattice. For the two adlayers shown above, the unit cell would have crystallographic notation $|\mathbf{a}| = |\mathbf{b}| = 2, \gamma = \pi/2$ (square lattice); $|\mathbf{a}| = 1, |\mathbf{b}| = 2, \gamma = \pi/3$ (triangular lattice). 35
- Figure II-13: “Butterfly” adlayer geometry (c2mm). Left, square lattice. Angle notation $[3\pi/8, 3\pi/4, \pi/4, \pi/8]$. Crystallographic notation $|\mathbf{a}|=|\mathbf{b}|=2, \gamma = \pi/2$. Right, triangular lattice. $[3\pi/12, 5\pi/6, \pi/6, \pi/12]$. Crystallographic notation $|\mathbf{a}| = |\mathbf{b}| = 2, \gamma = \pi/3$ 36
- Figure III-1: Schematic representation of the seven key geometries used for the ditopic molecule on a square lattice. (a) Short Stripe (SS); (b) Symmetric Windmill (WM1); (c) Chiral Windmill (WM2) $\{\pi/8, 5\pi/8\}$; (d) Long Stripe (LS); (e) Perfect Herringbone (PHB); (f) Herringbone (HB) $\{7\pi/18, 5\pi/9\}$; (g) Butterfly (BF) $[7\pi/18, 3\pi/4, \pi/4, \pi/9]$. Shown on the figure are the NN site-to-site distances in each case. A range of angles is possible for the chiral windmill. .41
- Figure III-2: Nearest-neighbor site-to-site distance, $s(\rho)$, as a function of molecule arm length, ρ , for chosen geometries. The geometry labels PHB, HB, LS, WM2, WM1, BF and SS are defined in **Figure III-2**..... 43
- Figure III-3: Two pathways from the SS to the PHB geometries. Path I begins (Step 1) with a disrotatory rotation through ϕ (via p2mg geometries) to the symmetric windmill (WM1). This is followed (Step 2) by a conrotatory rotation through ϕ' . Path II begins (Step 1) with a conrotatory rotation through ϕ (via p2 geometries) to the long stripe (LS). This is followed (Step 2) by a disrotatory rotation through ϕ' (via HB geometries). 45
- Figure III-4: the order parameters as a function of rotation angle ϕ or ϕ' for the paths shown in **Figure III-3**. (a) Ψ_4^c , (b) $|\Psi_4^s|$, (c) Ψ_2^{cl} (d) Ψ_{HB} . The legends describe the path (I or II). 47
- Figure III-5: Contour plots of various properties of the most stable geometry as a function of Lennard-Jones parameters (ρ, r_e) . Panels (b) potential energy, V ; (c), (d), (e), (f) orientation order parameters $\Psi_4^c, |\Psi_4^s|, \Psi_2^{cl}, \Psi_{HB}$ respectively. Panel (a) summarizes this in the “phase diagram”, in which geometries are assigned using the criteria given in the text. The “phase boundaries” established in panel (a) are reproduced in the other panels. (Abbreviations used: SS = short stripe; WM1 = symmetric windmill; WM2= chiral windmill; HB = herringbone; PHB = perfect herringbone; BF = butterfly.) 49

Figure III-6: Representative adlayer geometries for ditopic molecule on a square lattice with the Lennard-Jones potential. (See Figure III-5 .) The geometries are drawn using the space-filling representation (see Chapter II). All are actual GM's, with the exception of the LS (f), which is a global minimum for a Morse potential. The (σ , ρ) parameters for each structure are: (a) SS (0.36, 0.29); (b) Distorted SS* (0.46, 0.34); (c) WM1 (0.36, 0.39); (d) WM2 (0.36, 0.53); (e) PHB (0.62, 0.36); (f) LS (0.67, 0.35); (g) HB (0.62, 0.40); (h) BF (0.45, 0.45). *Note that this geometry could be "binned" as either SS or WM1 depending on the orientational order parameter criteria.	50
Figure III-7: Plots of $V(s(\rho))$ for the Lennard-Jones potential for the geometries observed in Figure III-6 . Upper panel $r_e = 0.7$; Middle panel, $r_e = 0.52$; Lower panel, $r_e = 0.4$	52
Figure III-8: Potential energy, V , as a function of rotation angle along the two paths shown in Figure III-3 . At the lefthand side (path I) of each panel ($\phi=0$) the geometry is the SS. At the right (path II) of each panel ($\phi'=\pi/2$), the geometry is the PHB. In the center of the panel, the geometry is WM1. The potential is the Lennard-Jones, with $r_e=0.4$. Each panel has a different value of ρ . In each case, the global minimum (GM) geometry is indicated by a cartoon.....	54
Figure III-9: Probability of reaching local minima for LJ potential with $r_e=0.40$, and various values of ρ	56
Figure III-10: Probability of reaching local minima for LJ potential with $r_e=0.52$, and various values of ρ	57
Figure III-11: Parameter "phase diagrams" for: (top) Morse, $\beta=20$; (middle) Morse, $\beta=10$; (bottom) LJ. 59	
Figure III-12: The potential energy function $V(\rho)$ for the key geometries described in Figure III-1 , for $r_e = 0.7$ for (upper panel) Morse ($\beta=20$); (middle panel) Morse ($\beta=10$); (bottom panel) LJ pair potentials. The solid gray line is the potential of the GM obtained through the unbiased search.....	60
Figure III-13: $V(\phi)$ at $r_e = 0.70$ with two different values of ρ for different pair potentials. The pair potentials are: (upper panel) Morse ($\beta=20$) (middle panel) Morse ($\beta=10$) and (lower panel) Lennard-Jones. The global minimum is indicated by a cartoon.....	61
Figure III-14: Probability of reaching local minima for $r_e=0.7$, at ρ values of 0.35 and 0.40. The pair potentials are: (upper panel) Morse ($\beta=20$) (middle panel) Morse ($\beta=10$) and (lower panel) Lennard-Jones.	62
Figure IV-1: Structure of the ground state key patterns for different ρ and r_e . The abbreviation are described in Table IV-2 . In parenthesis are the symmetry wall paper group (explained in details Appendix C).	69
Figure IV-2: The nearest-neighbor site-site distance, $s(\rho)$, as a function of molecule length, ρ , for chosen fixed geometries. Upper panel are the pinwheel 2 "PW2", pinwheel 1 "PW1", butterfly "BF", honeycomb "HC", and the short stripe "SS". The lower panel are the herringbone family: herringbone 2 "HB2", herringbone 1 "HB1", distorted short stripe "DSS" and perfect herringbone "PHB". The geometry labels are described in Table IV- 2 and shown in Figures IV-3, 4, 5 . Note: the PW2 orientational angles= [2, 65, 50, 123] $^\circ$, the PW1 angles = [8, 126, 69, 33] $^\circ$, the BF angles = [$\pi/2$, 0, $4\pi/9$, $5\pi/9$], The HB2 angles= $\{\pi/5, 4\pi/5\}$, the HB1 angles= {20, 91} $^\circ$, the DSS angles= {170, 15} $^\circ$	70

- Figure IV-3: a) The adlayer GM geometries “ phase diagram” as a function of ρ , and r_e , b) The contour plots potential energy $V(\rho, r_e)$, c) Order parameter Ψ_3^{cl} , d) Order parameter Ψ_3^{sl} , e) Order parameter $|\Psi_6^c|$, f) Order parameter $|\Psi_6^s|$. The labeling of the geometries PHB, SS, DSS, HC, HB, BF and PW are shown in **Table IV-2**. The geometries are shown in **Figures IV-1**. In each plots the color bars show the values of the contours..... 74
- Figure IV-4: Plots of $V(s(\rho))$ for the Lennard-Jones potential for the geometries observed in **Figure IV-1**. (A) Upper panel $r_e = 0.6$; (B) Middle panel, $r_e = 0.4$; (C) Lower panel, $r_e=0.3$. Note: The DSS angles= $\{170\ 15\}^\circ$ 75
- Figure IV-5: The radial distribution function of perfect herringbone “PHB” and short stripe “SS” for two different rotor length $\rho=0.1$ and 0.35 at constant $r_e=0.3$. The black line is the Lennard-Jones potential at $r_e=0.3$ 76
- Figure IV-6: A) The global minimum “BF” upper panel, and (B) local minimum “PW” of a 4X4 unit cell at $r_e=0.4$, and $\rho=0.5$ 77
- Figure V-1: Schematic representation of the three key geometries on a triangular lattice with the value of their order parameters $|\Psi_3^s|$, $|\Psi_3^c|$ and Ψ_3^{cl} , a) Honeycomb “HC”, b) Perfect Chevron “PCh”, c) Reverse Chevron “RCh”. Note: The dashed red lines are the nearest neighbor NN, site-to-site distances s (Values and the relationships, as a function of ρ , are shown in **Figure V-2** and **Table V-1**). In parenthesis are the wallpaper symmetry. 81
- Figure V-2: the nearest-neighbor site-to-site distance, $s(\rho)$, as a function of molecule length, ρ , for the key geometries. The geometry labels HC, RCh and PCh stand for “Honeycomb”, “Reverse Chevron”, “Perfect Chevron”, **Figure V-2**. Note: The relationships are shown in **Table V-1**. 82
- Figure V-3: Schemes of the suggested paths (see the text), Path I conrotatory $\{\phi\}$ starting with Honeycomb “HC” $\{\pi/2\}$ geometry and ends with HC $\{\pi/6\}$, Path II, disrotatory $\{\phi, -\phi\}$ starts with HC $\{\pi/2\}$ and ends with HC $\{\pi/6\}$. Note: rotatory paths $\{\phi\}$, $\{\phi, -\phi\}$ are different from geometry abbreviation $\{\theta\}$, under each geometry. Note: the paths are of geometries on a triangular lattice..... 83
- Figure V-4: The order parameter as a function of paths shown in **Figure V-3** A) $|\Psi_3^s|$, B) $|\Psi_3^c|$, and C) Ψ_3^{cl} . The legends describe each path (I and II) inside each graph. The cartoons in A) show the patterns of path II while in B) show patterns of path I. Note: Path I and II are degenerate in both $|\Psi_3^s|$ and $|\Psi_3^c|$. Note: $\{\phi\} \in [0, \pi/2]$; is the rotatory angle and it is different from geometry abbreviation $\{\theta\}$ 85
- Figure V-5: The parameter phase diagram of a tritopic molecule on a triangular lattice as a function of (ρ , r_e) (Left). The contour plots of potential as a function of ρ and r_e (Right). The labels “HC”, “Ch”, “HB”, “RCh” and “PCh” stand for honeycomb, chevron, herringbone, reverse chevron, and perfect chevron, respectively. All geometries are shown in **Figure V- 8, 12 and 15**. The broken black lines show the borders between the patterns. The color bar is the color codes of the value of the energy 87
- Figure V-6: the contour plots of the order parameters of tritopic molecule on triangular lattice; (a) Order parameter, $|\Psi_3^s|$, (b) Order parameter $|\Psi_3^c|$; (c) Order parameter Ψ_3^{cl} . The borders are

described in Figure V-5 . The color bars beside each diagram represent the color-code values of the order parameters.....	87
Figure V-7: The potential energy function $V(\rho)$ for the key geometries described in Figure V-1 , for $r_e = 0.3$. The solid black line is the potential of the GM obtained through the unbiased search. The legends shown inside the graph represent the labeling of the key geometries shown in Figure V-1	88
Figure V-8: The geometries of tritopic molecule on triangular lattice of the unbiased search for different ρ 's (horizontal cut at constant $r_e=0.3$ of Lennard-Jones potential $V(\rho)$, Figure V-5 and Figure V-7). In the parentheses is the symbol for the wallpaper symmetry (for details see Appendix C). The labels below each geometry are abbreviations that stand for "HC" honeycomb, "RCh" reverse chevron, "HB" herringbone, "Ch" chevron. Chevron structure is chiral, because it has no symmetry mirror plane. Chevron family has the same orientational angle, $\{\theta\}$	89
Figure V-9: Potential energy as a function of the rotatory paths $V(\phi, r_e=0.3)$ at constant values of ρ (see Figure V-3). Each graph shows path I conrotatory (Solid black line) and path II disrotatory (cut green line). Shown in each panel is a cartoon of the global minimum "GM" of the paths. Note: for clarity graph 1 ($\rho=0.2$), V-scale is different from the other scales. For $\rho=0.49$ path II is repulsive.	90
Figure V-10: The probability histogram energy potentials at constant $r_e=0.3$ for rotor lengths $\rho=0.2, 0.34, 0.36, 0.40,$ and 0.49 . In each plot shown the cartoons of the minima found by the unbiased search of many starting points. Note: at $\rho=0.2$ the energies of the minima are very close (for clarity the inner panel shows a different energy scale).....	91
Figure V-11: The potential energy function $V(\rho)$ for the key geometries (on triangular lattice) described in Figure V-1 , for $r_e = 0.4$. The solid black line is the potential of the GM obtained through the unbiased search. The legends shown inside each graph represent the labeling of the key geometries shown in Figure V-1	93
Figure V-12: The geometries (on a triangular lattice) of the unbiased search for different values of ρ (horizontal cut at constant $r_e=0.4$ of Lennard-Jones potential $V(\rho)$, Figure V-5 and Figure V-11). In the parentheses is the symbol for the wallpaper symmetry (for details see Appendix C). The labels below each geometry are abbreviations that stand for "HC" honeycomb, "Ch" chevron. Note: Chevron structure is chiral as it possess no mirror plane.	93
Figure V-13: Potential energy as a function of the rotatory paths $V(\phi, r_e=0.4)$ (on a triangular lattice) at a constant value of ρ (see Figure V-3). Each graph shows path I conrotatory (Solid black line) and path II disrotatory (cut green line). Shown in each panel is a cartoon of the global minimum "GM" of the paths. Note: for clarity graph 1 ($\rho=0.24$), the inner panel's V-scale is different from the other scales. For $\rho=0.39$ and 0.49 path II is repulsive.....	94
Figure V-14: The probability histogram energy potentials at constant $r_e=0.4$ for rotor lengths $\rho= 0.24 , \rho=0.34, 0.39,$ and 0.49 . In each plot shown are the cartoons of the minima found by the unbiased search of many starting points. (The lattice is triangular)	94

Figure V-15: The potential energy function $V(\rho)$ for the key geometries described in **Figure V-1**, for $r_e = 0.5$. The solid black line is the potential of the GM obtained through the unbiased search. The legends located inside each graph represent the labeling of the key geometries shown in **Figure V-1**. 96

Figure V-16: The geometries of the unbiased search for different ρ 's (at constant $r_e=0.5$ of Lennard-Jones potential $V(\rho)$, **Figure V-5** and **Figure V-11**). In the parentheses is the symbol for the wallpaper symmetry (for details see Appendix C). The labels below each geometry are abbreviations that stand for "HC" honeycomb, "Ch" chevron and "PCh" perfect chevron. 96

Figure V-17: Potential energy as a function of the rotatory paths $V(\phi, r_e=0.5)$ at constant ρ 's (see **Figure V-3**). Each graph shows path I conrotatory (Solid black line) and path II disrotatory (cut green line). Shown in each panel is a cartoon of the global minimum "GM" of the paths. Note: for clarity graph 1 ($\rho=0.20$), the inner panel's V-scale is different from the other scales. For $\rho=0.41$ the path II is repulsive. 97

Figure V-18: The probability histogram energy potentials at constant $r_e=0.5$ for rotor lengths $\rho= 0.20$, $\rho=0.28$ 0.31 , and 0.41 . In each plot are shown the cartoons of the minima found by the unbiased search of many starting points. 97

Figure V-19: Geometry distribution "phase diagram" (Left) as a function of (ρ, r_e) of the ground states of the tritopic system on a square lattice. Contour energy plot (Right) $V(\rho, r_e)$. The black cut lines indicate the borders between different patterns explained in **Figure V-21, 22 and 23**. The key of the plots colorations represent the potential energy per rotor. For clarity the abbreviations for all geometries labeling are in **Table V-3**. 100

Figure V-20: The nearest-neighbor site-to-site distance, $s(\rho)$, as a function of molecule length, ρ , for chosen fixed geometries on a square lattice. The geometry labels RCH, CH, DCH, OCT, and RB stand for "Reversed Chevron", "Chevron", "Distorted Chevron", "Octagon" and "Ribbon", respectively are shown in **Figure V-21, 22 and 23**. 100

Figure V-21: The geometries of the unbiased search (on a square lattice) for different values of ρ (at constant $r_e=0.2$ of Lennard-Jones potential $V(\rho)$). In the parentheses is the symbol for the wallpaper symmetry (for details see Appendix C). The labels below each geometry are the abbreviations described in **Table V-3**. DOCT and DRCH1 structures are chiral, because they have no symmetry mirror plane. 101

Figure V-22: The geometries of the unbiased search (on a square lattice) for different values of ρ (at constant $r_e=0.4$ of Lennard-Jones potential $V(\rho)$). In the parentheses is the symbol for the wallpaper symmetry (for details see Appendix C). The labels below each geometry are abbreviations described in **Table V-3**. DOCT and DRCH structures are chiral, because they have no symmetry mirror plane. 102

Figure V-23: The geometries of the unbiased search (on a square lattice) for different values of ρ (at constant $r_e=0.5$ of Lennard-Jones potential $V(\rho)$). In the parentheses is the symbol for the wallpaper symmetry (for details see Appendix C). The labels below each geometry are abbreviations described in **Table V-3**. DOCT and DRCH structures are chiral, because they have no symmetry mirror plane. 103

Figure V-24: The potential energy function $V(\rho)$ for the geometries described in Figures V-21, 22, 23 (Table V-3) at $r_e = 0.2$. The solid black line is the potential of the GM obtained through the unbiased search.....	105
Figure V-25: Radial distribution function, showing the number of neighbor counts, N_1 as a function of site-to-site distance $s(\rho)$, for RB and OCT geometries for the case $r_e=0.2$. The labels RB, and OCT are described in Table V-3 and Figure V-21 . The black line is the Lennard-Jones potential at $r_e=0.2$	105
Figure V-26: Probability histograms of the minima of Lennard-Jones at constant $r_e=0.2$ for several rotor lengths ρ . In each plot are shown the cartoons of the minima found by the unbiased search of many starting points.	107
Figure V-27: The potential energy function $V(\rho)$ for the geometries (on a square lattice) described in Figure V-22 for $r_e = 0.4$. The solid black line is the potential of the GM obtained through the unbiased search.....	109
Figure V-28: Radial distribution function, showing the number of neighbor counts, N_1 as a function of site-to-site distance $s(\rho)$, for RB, OCT and CH geometries (on a square lattice) for the case $r_e=0.4$. The labels RB, OCT and CH are described in Table V-3 and Figure V-22	109
Figure V-29: Probability histograms of minima (on a square lattice) of Lennard-Jones at constant $r_e=0.4$ for several rotor lengths ρ . In each plot shown the cartoons of the minima found by the unbiased search of many starting points.	110
Figure V-30: The potential energy function $V(\rho)$ for the geometries (on a square lattice) described in Figure V-25 at $r_e = 0.5$. The solid black line is the potential of the GM obtained through the unbiased search. The abbreviations are shown in Table V-3	112
Figure V-31: Probability histograms of minima (on a square lattice) of Lennard-Jones at constant $r_e=0.5$ for several rotor lengths ρ . In each plot the cartoons of the minima, found by the unbiased search of many starting points, are shown. Note: For $\rho=0.40$ the chevron structure are highly positive (repulsive).	112
Figure V-32: Radial distribution function, showing the number of neighbor counts, N_1 as a function of site-to-site distance s , for CH, DCH and RCH geometries (on a square lattice) for the case $r_e=0.5$. The labels CH, DCH and RCH are described in Figure V-23 and Table V-3	113
Figure VI-1: The main ground state pattern for the tetratopic system of rotors on a square lattice. a) Square (SQ), b) Checkerboard (CB), c) Cross (CR), d) Compact (CO), e) Tilt (TI). The symmetry plane groups are given in parenthesis (described Appendix C).	118
Figure VI-2: The nearest-neighbor site-to-site distance, $s(\rho)$, as a function of molecular length, ρ , for key geometries. The geometry labels square “SQ”, checkerboard “CB” cross “CR”, compact “CO” and tilt “TI” are shown in Figure VI-1 . The number of nearest-neighbors NN (N_1) are shown in Table VI-1	119
Figure VI-3: The description of rotating the square pattern. Path I conrotatory, Path II disrotatory (both lead to cross pattern), Path III and IV lead to checkerboard pattern. The patterns are described in Figure VI-1	121

- Figure VI-4: The order parameters as a function of paths that are shown in **Figure VI-1**, A) Ψ_4^c , B) Ψ_4^{cl} and C) $|\Psi_4^s|$. The legends describe each path (I, II, III and IV). Note in A path I and II coincide, path III and IV coincide. In B path II and IV are coincided. In C path I and II are coincided, path III and IV are coincided. 123
- Figure VI-5: The contour plots of a full energy search. a) Geometry (ρ , r_e), b) Potential energy $V(\rho, r_e)$, c) Order parameter Ψ_4^c , d) Order parameter Ψ_4^{cl} and e) Order parameter $|\Psi_4^s|$. In each plots the color bars show the values of the contours. The labeling of the geometries SQ, CR, CB, CO and TI represent square, cross, checkerboard, compact, and tilt, respectively. The geometries are shown in **Figure VI-1**. 124
- Figure VI-6: The potential energy function $V(\rho)$ for the geometries described in, **Figures VI-1**, at $r_e = 0.2$. The solid brown line is the potential of the GM obtained through the unbiased search. The abbreviations are described in **Table VI-1**. 126
- Figure VI-7: The geometries of the unbiased search for different ρ 's (at constant $r_e=0.2$). In the parenthesis are the wallpaper symmetry group symbols (for details see Appendix C). 126
- Figure VI-8: The potential energy $V(\phi)$ as a function of the rotation angle ϕ for different molecule size (ρ) at fixed $r_e=0.2$, the cartoons on the figures show the global minimum pattern among all the other geometries of paths. Note: for $\rho= 0.41, 0.59$ and 0.63 the global minimum patterns are chiral. Path IV coincide with path III because they are almost degenerate. For $\rho=0.45$ the global minimum goes through path IV. 127
- Figure VI-9: The potential energy function $V(\rho)$ for the key geometries at $r_e = 0.4$. The solid brown line is the potential of the GM obtained through the unbiased search. The abbreviations are described in **Table V-1**. 129
- Figure VI-10: The geometries found from the unbiased search for different values of ρ (at constant $r_e=0.4$). In the parentheses are the wallpaper symmetry group symbols (for details see Appendix C). 131
- Figure VI-11: The potential energy $V(\phi)$ as a function of the rotation angle ϕ for different molecule size (ρ) at fixed $r_e=0.4$. The cartoons on the figures show the global minimum pattern among all the other geometries of paths. Note: for $\rho=0.32, 0.33$, and 0.45 the global minimum patterns are chiral. Path IV is align with path III because they are almost degenerate. For $\rho=0.55$ path II, III, IV are repulsive and for clarity has a different scale. 132
- Figure VI-12: Probability histograms of minima of Lennard-Jones at constant $r_e=0.4$ for several rotor lengths, $\rho=0.29, 0.32, 0.37, 0.41$ and 0.55 . In each plot are shown the cartoons of the minima found by an unbiased search of many starting points. 133
- Figure VI-13: Contour plots of various properties of the most stable geometry of tetratopic molecule on a triangular lattice as a function of Lennard-Jones parameters (ρ , r_e). Panels (b) potential energy, V ; (c)-(f) orientation order parameters $\Psi_4^c(\Delta\theta)$, $P_2(\Delta\theta)$, Ψ_6^{cl} , and $|\Psi_6^s|$, respectively. Panel (a) summarizes this in the “phase diagram”, in which geometries are assigned using the criteria given in the text. The “phase boundaries” established in panel (a) are reproduced in the other panels. (Abbreviations used: CB = checkerboard; rectangle = RC; HB= herringbone; PW = pinwheel; CR = cross; TCB = Twisted checkerboard.) 136

- Figure VI-14: The geometries of the unbiased search for different values of ρ (at constant $r_e=0.2$). The abbreviations are described in **Figure VI-13**. In the parenthesis are the wallpaper symmetry group symbols (for details see Appendix C). Note: Two equivalent patterns of CB and three equivalent patterns of the RC pattern are shown. 137
- Figure VI-15: The geometries of the unbiased search for different values of ρ (at constant $r_e=0.28$). The abbreviations are described in **Figure VI-13**. In the parenthesis are the wallpaper symmetry group symbols (for details see Appendix C). 138
- Figure VI-16: The geometries of the unbiased search for different values of ρ (at constant $r_e=0.40$). The abbreviations are described in **Figure VI-13**. In the parenthesis are the wallpaper symmetry group symbols (for details see Appendix C). 139
- Figure VI-17: (Upper panel) the nearest neighbor NN s_1 ; (Lower panel) the next nearest neighbor NNN s_2 of the tetratopic model on a triangular lattice system. The legend inside each plot is the abbreviation of the adlayer described in **Figure VI-13**. 140
- Figure VI-18: The potential energy function $V(\rho)$ for the geometries described in, **Figures VI-14**, at $r_e = 0.2$. The solid black line is the potential of the GM obtained through the unbiased search. The abbreviations in the legend are described in **Figure VI-13**. 141
- Figure VI-19: The potential energy function $V(\rho)$ for the geometries described in, **Figures VI-15**, at $r_e = 0.28$. The solid black line is the potential of the GM obtained through the unbiased search. The abbreviations in the legend are described in **Figure VI-13**. 142
- Figure VI-20: The potential energy function $V(\rho)$ for the geometries described in, **Figures VI-16**, at $r_e = 0.4$. The solid black line is the potential of the GM obtained through the unbiased search. The abbreviations in the legend are described in **Figure VI-13**. 143
- Figure VII-1: A) Dicarbonitrile-triphenyl molecule. B) Model of Molecule, L is the length of the molecule which is equal to 2ρ as described in **Chapter II, Figure II-1**. C) Scheme represents the interactions between two adjacent model molecules. σ is the van der Waals radius of the Lennard-Jones potential. 147
- Figure VII-2: A) Oligo-phenylene-ethynylene with two main carboxylic groups. B) The force field coarse graining, the angle $\gamma=2\pi/3$, $L=1$, $l=0.2$, C) Scheme represents the interactions between two adjacent model molecules. σ is the van der Waals radius of the Lennard-Jones potential. Note: γ is selected to resemble the angle of the carboxylic group in oligo-phenylene-ethynylene with the stem of the molecule. 148
- Figure VII-3: Energy, the heat capacity, and two order parameters as a function of temperature from NVT the Monte Carlo trajectories for a ditopic molecule with the Lennard-Jones potential, $r_e=0.40$, $\rho = 0.29$. (For an explanation of the parameters, see text.) Shown on the left of the figure are snapshots of typical structures at low temperature ($T=0.01, 0.10$); shown in the middle is a snapshot of a typical structure at the phase transition temperature ($T=0.15$); shown on the right are snapshots of typical structures at high temperature ($T=0.2, 0.3$). 153
- Figure VII-4: Energy, heat capacity, and two order parameters as a function of temperature from NVT Monte Carlo trajectories for a ditopic molecule with the Lennard-Jones potential, $r_e=0.40$ $\rho = 0.42$. (For an explanation of the parameters, see text.) Shown on the left of the figure are snapshots of typical structures at low temperature ($T=0.10, 0.20$); shown in the middle is a

	snapshot of a typical structure at the phase transition temperature ($T=0.30$); shown on the right are snapshots of typical structures at high temperature ($T=0.35, 0.4$).	154
Figure VII-5:	Energy, the heat capacity, and two order parameters as a function of temperature from NVT Monte Carlo trajectories for a ditopic molecule with the Lennard-Jones potential, $r_e=0.40$ $\rho = 0.5$. (For an explanation of the parameters, see text.) Shown on the left of the figure are snapshots of typical structures at low temperature ($T=0.10, 0.20$); shown in the middle is a snapshot of a typical structure at the phase transition temperature ($T=0.27$); shown on the right are snapshot of typical structures at high temperature ($T=0.35, 0.4$).	155
Figure VII-6:	Energy, the heat capacity, and two order parameters as a function of temperature from NVT Monte Carlo trajectories for a ditopic molecule with the Lennard-Jones potential, $r_e=0.40$ $\rho = 0.34$. (For an explanation of the parameters, see text.) Shown on the left of the figure are snapshots of typical structures at low temperature ($T=0.01, 0.15$); shown on the middle is a snapshot of a typical structure at the phase transition temperature ($T=0.30$); shown on the right are snapshots of typical structures at high temperature ($T=0.35, 0.5$).	156
Figure VII-7:	Energy, the heat capacity, and two order parameters as a function of temperature from NVT Monte Carlo trajectories for a ditopic molecule with the Lennard-Jones potential, $r_e=0.40$ $\rho = 0.45$. (For an explanation of the parameters, see text.) Shown on the left of the figure are snapshot of typical structures at low temperature ($T=0.01, 0.10$); shown in the middle is a snapshot of a typical structure at the phase transition temperature ($T=0.26$); shown on the right are napshtos of typical structures at high temperature ($T=0.35, 0.5$).	157
Figure VII-8:	Energy, the heat capacity, and two order parameters as a function of temperature from NVT Monte Carlo trajectories for a ditopic molecule with the Lennard-Jones potential, $r_e=0.40$ $\rho = 0.5$. (For an explanation of the parameters, see text.) Shown on the left of the figure is a snapshot of a typical structure at low temperature ($T=0.01$); shown in the middle is a snapshot of a typical structure at the phase transition temperature ($T=0.15$); shown on the right is a snapshot of a typical structure at high temperature ($T=0.25$).	158
Figure VII-9:	Energy, the heat capacity, the molecular density per lattice sites N/N_s , and two order parameters as a function of temperature from the grand canonical Monte Carlo trajectories for molecule 2 with the Lennard-Jones potential, $r_e=0.20$ $\rho = 0.5$. Note: low density square lattice is used. (For a explanation of the parameters, see text.)	159
Figure VII-10:	Snapshots of Monte Carlo simulation of molecule 2, $r_e=0.20$ $\rho = 0.5$; A) high $T=0.5$, B) medium $T=0.20$ and C) low $T=0.01$	160
Figure VII-11:	Energy, the heat capacity, the molecular density and two order parameters as a function of temperature from grand canonical Monte Carlo trajectories for a ditopic molecule with Lennard-Jones potential, $r_e=0.40$ $\rho = 0.5$. (For an explanation of the parameters, see text.). Shown on the left of the figure is a snapshot of a typical structure at low temperature ($T=0.20$); shown on the middle is a snapshot of a typical structure at the phase transition temperature ($T=0.35$); shown on the right is a snapshot of a typical structure at high temperature ($T=0.45$).	161
Figure A-1:	A schematic representation of an energy funnel and the global minimizing method. (a) Global minimum. (b) Allowed local minimizing. (c) Minimizing path to global minimum not allowed. V is the potential energy calculated by using the equations method shown in Chapter II (see the text).	165

Figure A-2: (A) The radial distribution function RDF, the frequency peaks are the number of nearest neighbors within 0.01 threshold distance unit. (B) A schematic representation of the herringbone structure (LJ , $\rho = 0.84$ and $r_e = 0.7$) showing θ_i , the center rotor and the counted nearest neighbor rotors, located inside the oval structure..... 167

Figure C-1: The main symmetry elements and the wallpaper symmetry groups of the main patterns of a ditopic molecule on the square lattice surface. The abbreviations are described in the text (**Chapter III**) except for DSS which stand for distorted short stripe..... 171

Figure C-2: The main symmetry elements and the wallpaper symmetry groups of the main patterns of a ditopic molecule on the triangular lattice surface. The abbreviations are described in the text (**Chapter III**). 172

Figure C-3: The main symmetry elements and the wallpaper symmetry groups of the main patterns of a tritopic molecule on the square lattice surface. The abbreviations are described in the text (**Chapter IV**)..... 173

Figure C-4: The main symmetry elements and the wallpaper symmetry groups of the main patterns of a tritopic molecule on the triangular lattice surface. The abbreviations are described in the text (**Chapter IV**)..... 174

Figure C-5: The main symmetry elements and the wallpaper symmetry groups of the main patterns of a tetratopic molecule on the square lattice surface. The abbreviations are described in the text (**Chapter V**). 175

Figure C-6: The main symmetry elements and the wallpaper symmetry groups of the main patterns of a tetratopic molecule on the triangular lattice surface. The abbreviations are described in the text (**Chapter V**). Cont'd see next page for g and h. 176

List of Tables

Table II-1: Tetratopic molecule on a square lattice. For three sample adlayer geometries, the nearest-neighbor site-to-site separation s , is shown as a function of molecular size, ρ . The geometries are shown in Figure II-4	23
Table III-1: Closest nearest-neighbor (NN) site-to-site distance, s , for specified geometry as a function of ρ . Also included is the number of nearest-neighbor interactions. Note that there are two possible NN distances for the LS geometry, with differing NN coordination. The geometries are defined in Figure III-1	42
Table III-2: Values of order parameters of the seven key geometries described in Figure III-1	43
Table IV-1: Closest nearest-neighbor (NN) site-site distance, s , for specified geometry as a function of ρ . Including the number of nearest-neighbor. HB2 angles = $\{\pi/5, 4\pi/5\}$. BF angles = $[\pi/2, 0, 4\pi/9, 5\pi/9]$. The abbreviations are described in Table IV-2	71
Table IV-2: Geometry name, abbreviation and symmetry plane group of the adlayers on a triangular lattice. See Figures IV-2 , for geometries, and Appendix C for symmetry plane groups.	71
Table V-1: Closest nearest-neighbor (NN) site-to-site distance, s , for specified geometry on a triangular lattice as a function of ρ . Including the number of nearest-neighbor sites N_1	82
Table V-2: Closest nearest-neighbor (NN) site-to-site distance, s , for specified geometry (on a square lattice) as a function of ρ . Including the number of nearest-neighbor. Note that there are two possible NN distances for the Reversed Chevron and Distorted Chevron geometry.	100
Table V-3: Geometry name, abbreviation and symmetry plane group of the adlayers on a square lattice (see Figure V-21, 22 and 23 , and Appendix C).	101
Table VI-1: Closest nearest-neighbor (NN) site-to-site distance, s , for specified geometries as a function of ρ . In the last column the number of the nearest-neighbors (N_1) are included.	119
Table VI-2: Closest nearest-neighbor (NN) site-to-site distance, s_1 , for specified geometry as a function of ρ . Including the number of nearest-neighbor. Note: There are two possible NN distances for the PW1 and HB geometry. Note: $\vartheta = 3\pi/10, \theta_1 = 5\pi/18, \theta_2 = \pi/18$	139
Table VI-3: Closest nearest-neighbor (NN) site-to-site distance, s_2 , for specified geometry as a function of ρ . We include the number of nearest-neighbor. Note: There are two possible NN distances for the SQ, PW1 and HB geometry. Note: $\vartheta = 3\pi/10, \theta_1 = 5\pi/18, \theta_2 = \pi/18$	141
Table C-1: Schematic representation of the symmetry elements of the wallpaper plane groups.....	169

Abstract

A MODEL STUDY OF ADLAYER PATTERN FORMATION OF RIGID DI- TRI- AND TETRATOPIC MOLECULES ON SQUARE AND TRIANGULAR LATTICES

BY

Mohammed I. Alomari

University of New Hampshire, December 2015

In this work we considered the adlayer self-assembly of three model molecules di-, tri- and tetratopic with different sizes and potential energy parameters on square and hexagonal (triangular) lattices. For each case, we carry out minimization using an analytical gradient to find the most stable minima. In all cases we use “coarse-grained” site-to-site pairwise additive potential. We have explored how the change in the size of the molecule affects the pattern formation in the molecular adlayer. A primary focus of this work restricts the exploration of the landscape to a “unit cell” of 2×2 angles, labeled $[\theta_1, \theta_2, \theta_3, \theta_4]$ and extrapolate this to an infinite lattice by the application of tessellation. The model we study represents a 2-dimensional surface with fully occupied lattice sites and with boundary conditions to resemble the infinitely occupied surface.

To investigate the patterns we have used several order parameters that can distinguish between the adlayers. We have found several adlayers varied as the shape and the size of the molecules' change. We also have reported the chirality of the adlayer by using the order parameters. We note that homochiral patterns can be formed by using achiral molecules, and comment on the areas of parameter space where this occurs.

The molecular pattern hierarchy of the ditopic molecule on a square lattice distributed from highly ordered motifs such as a linear sheet “short stripe” geometry to fourfold achiral windmill structure and chiral windmill pattern. On the other hand we have reported a pinwheel chiral structure of ditopic molecule on a triangular lattice. On both square and triangular lattices we also found several herringbone structures.

Depending on the shape of the molecule and the surface lattice, the porous shape and size of the adlayer change wildly. We note several porous shapes such as square, rectangle, hexagon and octagon with their sizes depend on the molecular distance parameters. For instance we note a honeycomb structure of tritopic molecule on a triangular lattice distorts to a semi-hexagonal pattern as the size of the molecule increases.

We have also conducted Monte Carlo simulation for a range of molecular sizes of ditopic molecule on both square and triangular lattices. We note that the adlayer patterns of the simple minimization method and the Monte Carlo simulation are quite consistent.

Chapter I

Introduction

I.1 Motivation and Background

Since surface microscopies such as scanning tunneling microscopy (STM) and atomic force microscopy (AFM) have become available, there has been considerable effort in researching the structure of adsorbed thin layers on a variety of surfaces (1-4). One area that has received considerable attention is the investigation of the possibility of forming self-assembled adlayers, utilizing the nonbonding interactions between adsorbed molecules. Self-assembly is a term used to describe a processes, in which a number of molecules that are spatially in a disordered pattern at some particular time will order themselves overtime via intermolecular interactions. In several cases, interesting patterns have been observed, particularly when the pattern formation has been driven by hydrogen bonding (5-11). Also many other adlayer geometries can be built due to other nonbonding van der Waals interactions (12-27).

The monolayer self-assembly adlayers of compounds such as ditopic (19, 24, 28-45), tritopic (20-24, 46) and tetratopic (20, 25) have been studied theoretically widely in the literature. The n-topic term has been used in literature to represent the molecules where n functional groups play the main role in directing the self-assembly (5). This term (ditopic) was used first to describe the diamine poly organic ligand that can chelate metal atoms (47).

I.1.a Applications:

Self-assembled adlayers of organic molecules on a metal surface have a wide range of potential applications in the fields of molecular and organic electronics (48-51), organic solar cells (52), and solid state quantum computation (53). Other applications are related to the chirality of the adsorbate and the adlayer such as, heterogeneous asymmetric catalysis (54-57), enantiomeric separation and chiral sensors (57-60).

A typical solar cell needs: light-absorbing material, together with an electron-transport agent. The guiding idea of choosing organic molecules of high π -electron density is to enhance the electrical properties of semiconductors. This leads to promising applications in photovoltaic cells (52, 61, 62). Compared with nature's energy-conversion molecular devices, the efficiencies of man-made photovoltaic (PV) devices are still very poor. The most promising candidates of synthetic compounds in this field are porphyrins and phthalocyanine derivatives, which absorb visible light with high efficiency. Porphyrins and phthalocyanines are heterocyclic molecules that have 18 π electrons in the inner membered ring; that obey Hückel's rule of aromaticity (aromatic systems contain $4n + 2 \pi$ electrons). As a consequence, they usually have very intense absorption bands in the visible region (61). In addition they can coordinate with metals in their central cavity, and it is possible to add a great variety of functional groups around the central part.

In conjunction with porphyrins and phthalocyanines (acting as a light absorber), the fullerene C_{60} is a good choice to play a role as an electron acceptor (electron transport agent) using its LUMO molecular orbital (61). After being discovered 30 years ago (63, 64), fullerene has been a particular focus of interest of many research groups (50-52). The molecule resembles the shape of a soccer ball, and has high π -electron density which gives it a dual property as electron donor

(through the HOMO molecular orbital) and electron acceptor (through the LUMO molecular orbital) (52).

Molecular sieves are materials with small cavities that allow certain molecules to pass while blocking others. Zeolites are 3D materials used to separate gas molecules such as CO₂, N₂, CH₄, and CO (65). As the molecules get larger it is not easy to discriminate between them because of their size and shape. One way to do this is to use the cavities constructed by a monolayer self-assembled on surfaces. For instance, Schull et al investigated the size selectivity of the honeycomb pattern of (1,3,5-tris[(*E*)-2-(3,5-didecyloxyphenyl)-ethenyl]-benzene (TSB35) on a graphite surface (66). The honeycomb cavities (size of ~1.3 nm in diameter) can accommodate molecules such as coronene (1 nm) and hexabenzocoronene (1.3 nm).

When adsorbed on graphite 1,3,5-tris(10-carboxydecyloxy) benzene (TCDB) forms nearly tetragonal cavities (67). The host nanoporous cavities have been explored using three guest molecules triphenylene, 1-phenyloctane and copper(II) phthalocyanine. Studies considering the competitive adsorption and dynamic processes concluded that the flexible network can adjust itself according to the shape and the size of the guest molecule.

Discrimination between enantiomers of chiral molecules using a self-assembled adlayer leads to potential applications such as chiral molecular separation and chiral sensors. Kühnle et al reported, using STM studies of cysteine on a gold surface Au(110), that adsorbed molecular pairs of cysteine are exclusively homochiral and formed from a racemic mixture of this amino acid (68). Pan et al observed chiral molecular cavities when enantiomer mixtures of chiral calix[4]arene (crown molecule) were adsorbed on Au(111). This is of interest in chemical sensors and chiral

recognition (69). Lopinski et al investigated the recognition of (R or S) chiral center when (cis or trans) simple alkenes were adsorbed on Si(100) using STM technique (70).

I.1.b Experimental Studies:

Experimental studies have focused on the self-assembly of organic species, influenced by the classic carboxyl group dimer building unit (71) on metal surfaces (5). Carboxyphenyl-substituted porphyrins are examples that form an assembly of two- or four- membered clusters on a gold surface Au(111) (72). A linear-chain motif of ditopic molecules, such as terephthalic acid, was observed (5). By contrast an open network honeycomb structure is created with the threefold symmetric, tritopic, trimesic-acid molecule both on triangular and square substrates (73-75). Flower and heptamer structures of cyanuric acid (a tritopic molecule) occur on a graphite surface (76). These patterns are driven by the hydrogen bonding of the hydroxyl group of the acid. These examples illustrate how the structure and the functional group influence the geometry of the self-assembled adlayer on the solid surface.

A honeycomb network can be formed by a heterogeneous mixture of tritopic melamine and ditopic perylenetetracarboxylic di-imide (PTCDI) molecules, driven by hydrogen bond self-assembly (77). The porous network can serve as a template for heptamers of fullerene and tetradecamers of dodecanethiol guest molecules. Chiral networks have also been observed from achiral molecules such as anthraquinone on Cu(111), dicyanoquinquiphenyl on Ag(111), and co-adsorbed pentacene and PTCDI molecules on Ag(111) (77).

Self-assembly of organic molecules can be directed by van der Waals forces other than a hydrogen bond, see for instance reference (78). Organometallic molecules with very high electron density around a metal center, such as metal-phthalocyanines, are among the most interesting

examples (13, 14, 79-84). Long carbon chain supramolecules, such as a Fréchet dendron (85, 86), also have been shown to build self-assembled monolayers. Another example is the formation of the honeycomb pattern of trioctylamine on the Au(111) surface (87).

Linderoth et al have studied the chiral ordering of a class of oligo-phenylene-ethynylenes (ditopic molecules) on an Au(111) surface (6, 7, 88-90). With a high dense layer of triphenyl-dicarbonitrile molecule, on an Ag(111) surface a windmill structure has been observed (91). Another chiral adlayer related to “crankshaft” C_{2h} -symmetric molecule bisisophthalic acids, also have been observed on a graphite surface (9). Chiral ordering of tetratopic molecules such as metal-phthalocyanine derivatives has been investigated by Toader et al (79) and Calmettes et al (13).

I.1.c Theoretical studies:

As experimental techniques such as STM and AFM can image and characterize the self-assembled adlayer, they provide a partial insight to predict the way the physical phenomenon play a role in the assembly. There is a need for theoretical modeling to achieve this goal and complement the experimental studies.

Pioneering studies in this field (92, 93) which led to much of the fundamental understanding of adlayer geometries were carried out using realistic intermolecular potentials – typically the quadrupole-quadrupole interaction to model the interaction of small molecules such as H_2 and N_2 on graphite. More recently, Dawoud et al studied the role played by quantum effects of H_2 , D_2 and N_2 intermolecular interactions, in organizing adlayers on metal oxide and metal halides surfaces at low temperature (94-99).

Several studies using a lattice model with linear molecular adsorbates interacting through a pairwise additive potential have been carried out (28-36). Most of these studies have focused on the phase behavior of the adlayers as a function of temperature and density.

However, relatively little work has been done on understanding the effect of systematic variations in the intermolecular potential on the adlayer structure. This is in marked contrast to such areas as gas phase atomic and molecular clusters, where a large body of systematic analysis exists investigating the role of the potential in the structure and in growth sequences (100-104).

After finding the geometry of the adlayer experimentally, electronic structure calculations, using density functional theory (DFT), for a single point energy calculation can characterize the adsorbate-adsorbate or adsorbate-adsorbent molecular structure and bonding characteristics. For instance Besenbacher et al used a DFT calculation to interpret the quartet network geometry of guanine on an Au(111) surface (105). They used a single point energy calculation for clusters up to tetramers to determine the hydrogen bond binding energy and its electron density in the absence of the substrate. This calculation becomes highly expensive for large clusters and in the presence of the substrate.

Coarse-Grained Force Field

One choice to reduce the computing cost for large clusters is using a coarse graining model of intermolecular forces. Generally, the molecule functional groups are reduced to a smaller set of interaction sites (pseudoatoms or united-atoms), which are then used to calculate the potential energy of the system (11, 106-109). For instance, Bubnis and Mayne (11, 108) used Girifalco's potential (110) to study the self-assembly of fullerene derivatives on an Au(111) surface. The potential integrated all the carbon-carbon interactions between two fullerene molecules into one united-atoms pair interaction, rather than utilize the full atom-atom potential.

This same idea, coarse graining, has been used by Franosch et al (26, 86) and Pint et al (17) to simulate the self-assembly of hydrocarbon molecules. Both used the Martini force field model to represent the interactions between carbon chains (111). The former studied the self-assembly of Fréchet dendrons on isotropic 2D surfaces using Monte Carlo simulation. They have found several patterns such as saw-tooth, honeycomb, jigsaw, and tiretrack. Pint et al used molecular-dynamics to study the temperature effect on the adlayer including herringbone molecular pattern of hexane on graphite surface. They represented interactions between molecules as beads of certain potential for each functional group in the chain. For instance, CH₂ units, exhibiting short-range van der Waals attractions were described by the Lennard-Jones potential.

A series of articles by Szabelski et al (19-25) simulated the self-assembly of different structures of ditopic, tritopic, and tetratopic molecules on a solid surface using Metropolis Monte Carlo. With a drastic simplification of the model using short range site-to-site interactions, each arm of the molecule contains beads representing the active sites where molecules interact with each other, the authors have found a variety of rhombic and rectangular chiral nanoporous networks pattern.

Another site-to-site coarse-grained simulation was carried out by Balbas Gamba et al (26). These authors built rigid model molecules (dendrons, with roughly C_{2v} symmetry) using several sites along the “arms”. Their site-to-site interaction was a Lennard-Jones potential. Molecules were placed on all sites of a triangular lattice, and the potential energy was explored using Monte Carlo as the axis of the molecules was rotated. Several adlayer patterns were identified (often having large unit cells). The energy of each of these structures was plotted as the lattice size was varied. Some of the patterns were chiral, but this was due to the presence of a 3-fold lattice symmetry.

Glotzer et al used the term “patchy particles” to represent a model of nanoparticles with certain shapes, such as a sphere, that have patches form the basis of the intermolecular interaction potential (112). In these particles they used the coarse graining model with a Lennard-Jones potential to represent the site-to-site interaction. The patchy particles resemble the Janus particles (a term used in late eighties to describe nanoparticles composed of two different parts one being hydrophilic and the other being hydrophobic) (113).

The patchy model of different symmetry has been used, by Doye’s group, such as tetratopic “ D_{4h} ”, pentatopic “ D_{5h} ”, and hexatopic “ D_{6h} ” (114). They have used a Lennard-Jones potential arranged regularly on a surface of a two dimensional disk to represent the site-to-site interactions.

One of the research interests of the Mayne group in recent years has been to model pattern formation of model molecules on a variety of substrates-particularly metals (10, 11). A particular focus has been on adsorbate molecules containing fullerene, since these have been possible applications in molecular electronics. Cleary et al investigated how fullerene derivatives formed layers through a thiolate linkage on gold, and illustrated the role played by fullerene-metal interaction in disrupting pattern formation (10). Bubnis and Mayne looked at pattern formation of fullerene derivatives on gold with a variety of nonbonding interactions, including hydrogen bonding (11). It was shown in this work how important is the role played by fullerene-fullerene intermolecular forces in deriving the adlayer formation. In this work, a small number of molecules was simulated adsorbing on the surface, and their behavior studied as a function of time using Molecular Dynamics (MD) and as a function of temperature using Metropolis Monte Carlo (MMC). A variety of adlayer patterns was observed, and varied with the form of the nonbonding interactions.

Berezutskiy also looked at adlayer formation using a model (115). He reduced each molecule to a small ditopic with two atom-like sites. He placed the molecules on all sites of a surface lattice. Using a pairwise-additive site-to-site model nonbonding potential, he was able to generate a potential energy landscape for the system as a function of the parameters for nonbonding interactions as they systematically varied. The main focus in Berezutskiy's work was to locate the most stable global minimum (GM) configuration.

In the study of gas phase clusters, there has been extensive work carried out to determine the ground state geometry of atomic clusters using a wide variety of potential energy function (100-103). The most frequently employed have been the Lennard-Jones and Morse atom-atom potentials. A large literature exists in this area, and several concepts in this field are now well established: Cluster geometry can be predicted from these principles for a large range of cluster size.

I.2 The Present Work

As far as the self-assembly on surfaces is concerned, this motivated by thermodynamic properties of the model system (78), we need to build a model starting from a disordered state to the spontaneity of the system to self-assembled itself via intermolecular interactions. In other words finding all the minima, including the metastable local minima that the system could be kinetically trapped in and the most stable minima, leads to a full understanding of the energy landscape of the self-assembled molecules on solid surfaces.

We built a model of rigid rotors on two different lattices, square and triangular lattices, to study the self-assembly of three types of molecules, ditopic, tritopic and tetratopic, on solid surfaces. To study the effect of the size of the molecule on the self-assembly, the length of the model rotor and the site-to-site equilibrium distance of the potential has been varied gradually. The

model represented is a 2D surface with fully occupied lattices and with boundary conditions to resemble the infinitely occupied surface. We have used Lennard-Jones and Morse potentials to represent the site-to-site interactions between molecules. First we utilize the potential energy and search for the entire minima including the global minimum and the local minima. Also we have introduced order parameters to distinguish between the hierarchies of the structures.

Our method and analysis elements are described in detail in **Chapter II**. Then in **Chapter III** and **IV** we show the main adlayer geometries found on a square and hexagonal (triangular) lattices as the length of the rotor and the site-to-site equilibrium distance (r_e) increase. After that, for some cases, the local minima have been located needed to build the full landscape of those systems.

Chapter V describes the global minima of tritopic molecules on square and triangular lattices. Also full energy minima are shown for illustrative systems. **Chapter VI** describes the minima of tetratopic on both lattices. In the last chapter we show Monte Carlo results of some ditopic systems on both square and triangular lattices to compare the geometries found by using high lattice sites with the model used in previous chapters.

Note: Some of the chemical structures that have mentioned in the **Chapter I** are shown in the supporting materials at the end of this dissertation.

Chapter II

Overview of Di-, Tri- and Tetratopic Molecules on Square and Triangular Lattices

II.1 Introduction

As mentioned in Chapter I, this dissertation considers the behavior of molecules forming adsorbed layers on a solid surface. The intermolecular interactions will be modeled by a coarse-grained site-to-site pairwise-additive potential. We will consider here symmetric molecules with two, three and four sites, and refer to these as ditopic, tritopic, and tetratopic, respectively. These sites are located on “arms” at a distance ρ from the molecule’s center of mass (**Figure II-1** shows the model molecule on a square lattice as an example). Experimental studies have been carried out on adsorbate molecules where the number of “spokes” has been changed, but the molecular structure and functionality remain similar throughout (6).

One of our primary interests will be to explore how the change in the size of the molecule, ρ , affects the pattern formation in the molecular adlayer (23, 46, 91, 116, 117). Several authors have explicitly investigated how changes in the size of molecules affect their behavior in a monolayer. Our primary strategy will place molecules at all sites on a lattice of fixed size, as we change the molecule size. This is similar in spirit to work as the surface concentration is varied (8) or in which the adlayer is subject to strain. In addition, we will systematically vary the parameters of the potential energy acting between the molecules. We note that several groups have carried out model calculations in a similar spirit (19, 37).

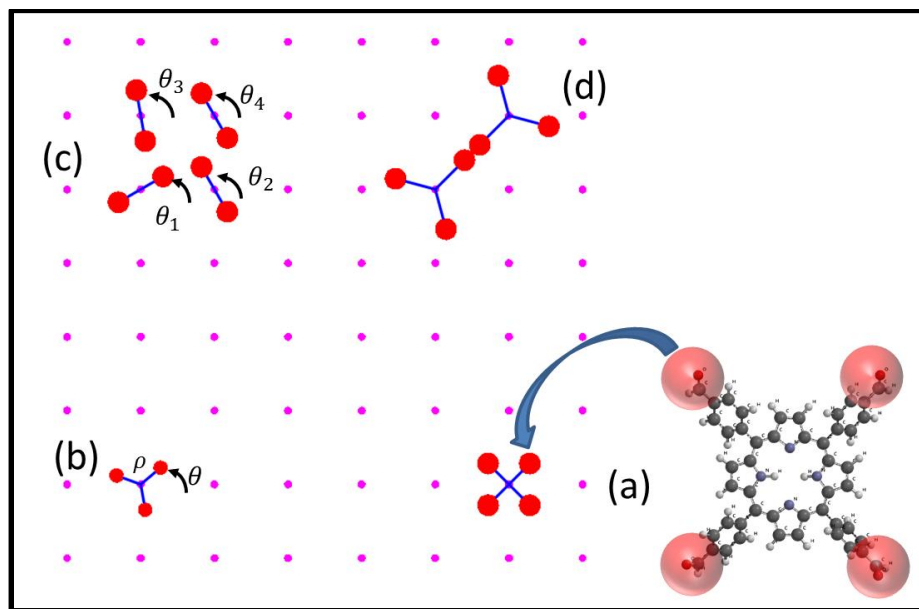


Figure II-1: The model molecules, di-, tri- and tetratopic on square lattice (n-topic: n refers to number of arms of the molecule). (a) Shows porphyrin derivative with four hydrogen bonds can be model by using coarse-graining tetratopic molecule. (b) A tritopic model on the lattice site, θ is the angle of the rotor with the universal x axis, ρ the length of the rotor arm from its center of mass to the tip. (c) The unit cell of the system with angles $(\theta_1, \theta_2, \theta_3, \theta_4)$. (d) Interactions between two tritopic rotors showing one of the interactions at the equilibrium distance of the potential.

The potential energy landscape can be explored by traditional methods such as molecular dynamics or Monte Carlo calculations. In **Figure II-2**, we illustrate a high temperature and a low temperature “snapshot” from a Monte Carlo simulation (whose details are given in a later chapter) of a ditopic molecule (Lennard-Jones dimer) on an isotropic (flat) surface. (The potential energy parameters are given in the Figure’s caption.) As can be seen, at low temperature, the preferred geometry is a windmill (which is chiral, with p4 wallpaper symmetry). This is presumably the ground state of the system. Similar calculations could be carried out for a range of parameters, such as interaction strength and molecular size. However, the calculation for the results shown here was extremely resource-intensive. In order to explore a range of parameters, the cost would be prohibitive.

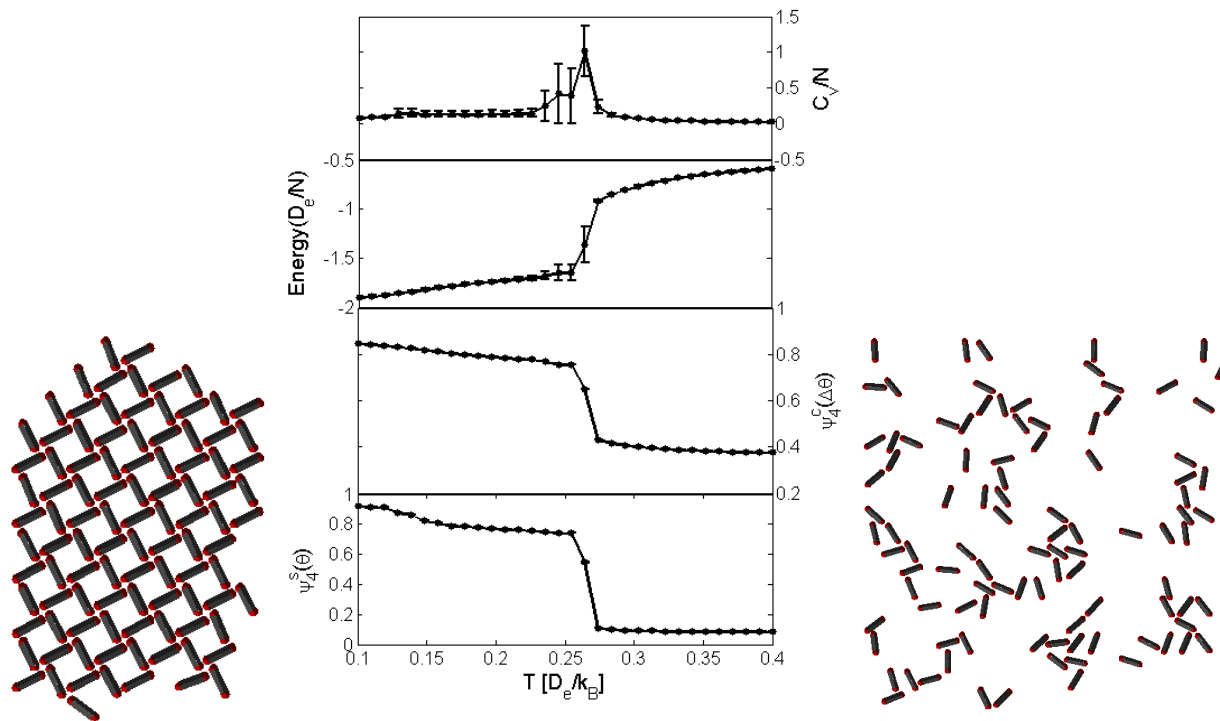


Figure II-2: Energy, heat capacity, and two order parameters as a function of temperature from Monte Carlo trajectories for ditopic molecule with Lennard-Jones potential, $r_e=0.40$ $\rho = 0.5$. (For explanation of parameters, see Section II-1 and II-5.) Shown on the left of the figure is a snapshot of a typical structure at low ($T=0.1$) temperature; shown on the right is a snapshot of a typical structure at high temperature ($T=0.4$). (note: for clarity the snapshot on the right is zoomed in)

Therefore, in order to further limit the scope of the problem, in the following chapters, we fix the molecules on a periodic lattice, and attempt to identify the significant (low potential energy) geometries for several combinations of parameters. Here we use a square lattice and a triangular lattice. Since we wish to determine the ground state (the global minimum of the potential energy) for a large number of points in the parameter space, we further restrict the exploration of the landscape to a “unit cell” of 2×2 angles, labeled $[\theta_1, \theta_2, \theta_3, \theta_4]$ and extrapolate this to an infinite lattice by the application of tessellation. See **Figure II-3**.

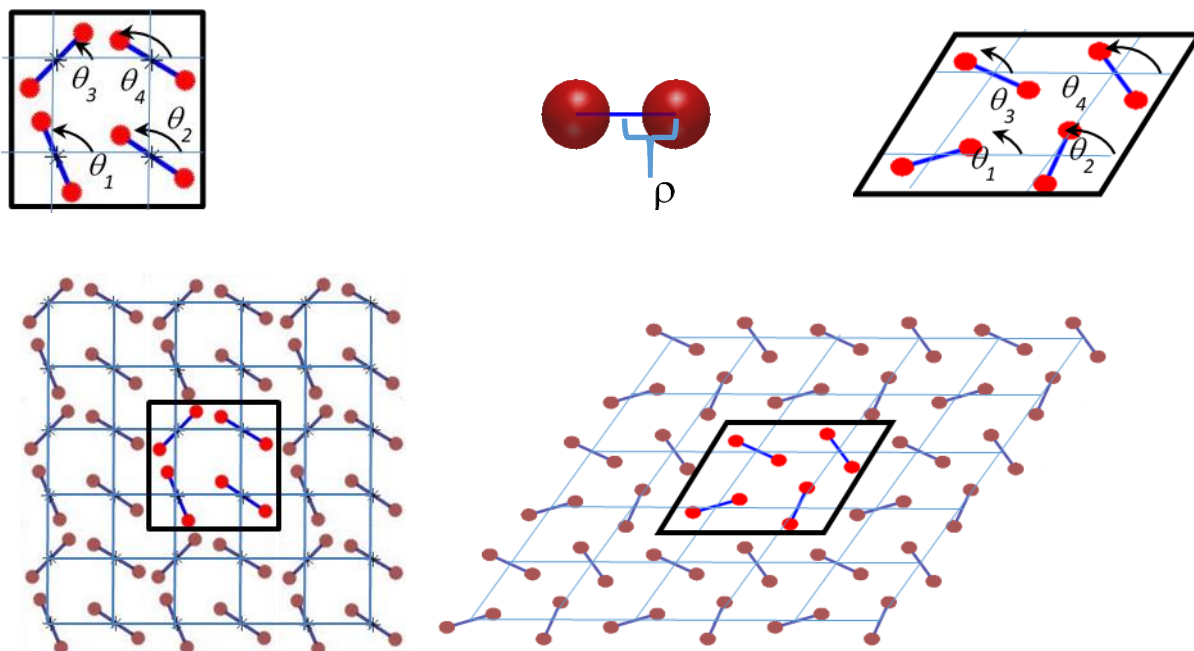


Figure II-3: Starting from upper most left and proceeding left to right in two rows. The 2x2 unit cell [$\theta_1, \theta_2, \theta_3, \theta_4$] on square lattice is highlighted; Model ditopic molecule (ρ is the distance between the molecule center of mass and a site); The 2x2 unit cell [$\theta_1, \theta_2, \theta_3, \theta_4$] on triangular lattice is highlighted; Schematic representation of the tessellation of the unit cell to an infinite square lattice; and Schematic representation of the tessellation of the unit cell to an infinite triangular lattice. The angles are taken with reference to the lattice x-axis.

II.2 Identification of Adlayer Patterns – Radial Distribution Functions and Orientational Order Parameters

In a simulation of N rigid molecules in a plane, each molecule is characterized by its center-of-mass displacement \mathbf{R} , and its orientation angle, θ . For any pair of molecules i and j , joint pair distributions of the form $(|\mathbf{R}_i - \mathbf{R}_j|, \theta_i, \theta_j)$ are, in principle, available from the simulation, but represent vast amounts of data. It is more usual to break the information into pair (or radial) distribution functions, which depend only on the distances between sites on molecules, and angular distributions, which depend only on the angles of the molecules.

The radial distribution functions are treated in great detail in **Appendix A.III**. (See, for instance ref. (118)). Essentially, this is carried out by performing a frequency analysis (histogram) of the site-to-site distances in an adlayer geometry, with all of the angular information averaged

out. Each geometry will, in principle, have a characteristic frequency pattern. This construction will be discussed in more detail in the next Chapters.

The angle distribution (with the distance dependence averaged out) gives information on the “pattern” adopted by the molecules. We shall focus on that in this section. For a system containing N molecules in a plane, the angular distribution is given by the (normalized) angular distribution function $I(\theta)$, where $0 \leq \theta \leq 2\pi$, and $I(\theta) = \frac{1}{N} \sum_{i=1}^N \delta(\theta - \theta_i)$. Typically, for a large simulation run, $I(\theta)$ will be displayed as a histogram with angular “bins” replacing the delta functions. However, the above form will be useful for the “fixed lattice” model calculations considered in chapter III and IV, in which only a small number of molecules is considered. We note that for an n -topic symmetric molecule (for n -topic term see **Figure II-1**), we can relabel θ with $n\theta$ such that $0 \leq \theta \leq 2\pi/n$. (That is, for a ditopic molecule, for instance, we need only consider angles between 0 and π ; angles between π and 2π merely repeat this information.)

The angular distribution function can be expanded in a Fourier series:

$$I(\theta) = I_o + \sum_{l=1}^{\infty} (c_l \cos(nl\theta) + d_l \sin(nl\theta)) \quad 0 \leq \theta \leq 2\pi/n \quad \text{II-1}$$

I_o is simply the average value of I over the interval, and contains no new information. The coefficients c_l and d_l give information on the deviation of $I(\theta)$ from being isotropic (equal at all angles). Using the orthogonality of the trigonometric functions, we have:

$$\begin{aligned} c_l &= \frac{1}{\pi} \int_0^{2\pi} I(\theta) \cos(nl\theta) d(n\theta) = \frac{n}{\pi} \int_0^{2\pi/n} I(\theta) \cos(nl\theta) d\theta \\ d_l &= \frac{1}{\pi} \int_0^{2\pi} I(\theta) \sin(nl\theta) d(n\theta) = \frac{n}{\pi} \int_0^{2\pi/n} I(\theta) \sin(nl\theta) d\theta \end{aligned} \quad \text{II-2}$$

We note immediately that some of these coefficients will be zero by symmetry. In particular, since the sine is an odd function $d_l = 0$ for all values of l for any distribution that obeys $I(\theta) = I(\theta - \pi/n)$. Therefore, nonzero values of the d_l coefficient can serve as a measure of chirality, as we discuss below.

In order to touch base with one of the best-known order parameters in the literature, consider the case of linear (ditopic, $n=2$) molecules. We have:

$$I(\theta) \approx I_o + c_1 \cos 2\theta \quad \text{II-3}$$

The coefficient c_1 is given by:

$$c_1 = \frac{2}{\pi} \frac{1}{N} \sum_{i=1}^N \cos 2\theta_i = \frac{2}{\pi} \langle \cos 2\theta \rangle \quad \text{II-4}$$

where the $\langle \dots \rangle$ denotes the ensemble average from the simulation.

If all the molecules lie at angles close to some average angle, this angle can be used to define the reference axis. For a “tight” distribution about this average, $\langle \cos 2\theta \rangle$ will be close to unity.

This is closely related to the nematic order parameter used in work on polymers and liquid crystals, where the reference axis is usually referred to as the “director”. The nematic order parameter in this case is given by:

$$OP = \langle P_2(\cos \theta) \rangle = \frac{3}{2} \langle \cos^2 \theta \rangle - \frac{1}{2} \quad \text{II-5}$$

(where the $\langle \dots \rangle$ denotes the ensemble average.) We note that $\cos^2 \theta = (1 + \cos 2\theta)/2$. Therefore,

$OP = \frac{1}{4}(1 + 3 \langle \cos 2\theta \rangle)$. Thus, a value of $\langle \cos 2\theta \rangle$ which is close to unity (often referred to later

in **Chapter III** and **IV** as a “striped” adlayer geometry) corresponds to a nematic order parameter of unity.

In Monte Carlo and molecular dynamics calculations of particles, order parameters based on the ideas developed above have been used to detect local ordering of the particles – particularly for spherical particles (119-121) and diatomic molecules (122). Therefore, one of the goals of this dissertation is to develop order parameters which can help identify local pattern formation for the model molecules investigated here, which can be carried out “on the fly” during large simulations.

Examples

From the definitions of the Fourier components given above, we note they are related to the ensemble averages of the appropriate functions of the angles. We define the order parameters Ψ in the following way, typically normalizing them so that the maximum value they can have is unity. For any “geometry” defined by four angles, $[\theta_1, \theta_2, \theta_3, \theta_4]$ we have $I(\theta) = \frac{1}{4} \sum_{i=1}^4 \delta(\theta - \theta_i)$, where the sum is over the four rotors of the (2x2) unit cell for the model calculations.

We define the integrals that occur in the Fourier expansion with the following new notation, which will be used throughout the dissertation:

$$\begin{aligned} \Psi_{nl}^c &= \int_0^{2\pi/n} I(\theta) \cos(nl\theta) d\theta = \frac{1}{4} \sum_{i=1}^4 \cos(nl\theta_i) \\ \Psi_{nl}^s &= \int_0^{2\pi/n} I(\theta) \sin(nl\theta) d\theta = \frac{1}{4} \sum_{i=1}^4 \sin(nl\theta_i) \end{aligned} \quad \text{II-6}$$

In the case of the ditopic rotor ($n=2$) the leading term in the Fourier expansion has $l=1$, and so we consider:

$$\Psi_2^c = \frac{1}{4} \sum_{i=1}^4 \cos(2\theta_i) \quad \text{II-7}$$

$$\Psi_2^s = \frac{1}{4} \sum_{i=1}^4 \sin(2\theta_i) \quad \text{II-8}$$

Another pair of useful order parameters for a ditopic molecule ($n=2$, $l=2$) are:

$$\Psi_4^c = \frac{1}{4} \sum_{i=1}^4 \cos(4\theta_i) \quad \text{II-9}$$

$$\Psi_4^s = \frac{1}{4} \sum_{i=1}^4 \sin(4\theta_i) \quad \text{II-10}$$

These order parameters are similar to ones used previously to detect local fourfold symmetry (11, 123). We used the labels shown in **Figure II-4**, to describe some of the most important geometries.

We now consider some simple cases for the ditopic molecule, paying particular attention to the arbitrariness of our choice of angle (shown in **Figure II-4**). The molecules are parallel (nematic order parameter = 1) if all their angles are the same. If, for instance, they all lie along the x-axis (y-axis), the set of angles is $[0,0,0,0]$ ($[\pi/2, \pi/2, \pi/2, \pi/2]$). (We refer to this as a “short stripe”.) Alternatively, they are also parallel if the set of angles is $[\pi/4, \pi/4, \pi/4, \pi/4]$ (which we refer to as a “long stripe”). In both cases, $(|\Psi_2^c|^2 + |\Psi_2^s|^2) = 1$. However, $|\Psi_2^c| = 1$ for the short stripe, but $|\Psi_2^c| = 0$ for the long stripe. For an isotropic ensemble, $(|\Psi_2^c|^2 + |\Psi_2^s|^2) = 0$. Thus, the Ψ_2 order parameters are useful in the form $(|\Psi_2^c|^2 + |\Psi_2^s|^2)$ to detect nematic behavior in a simulation, but will not be useful individually.

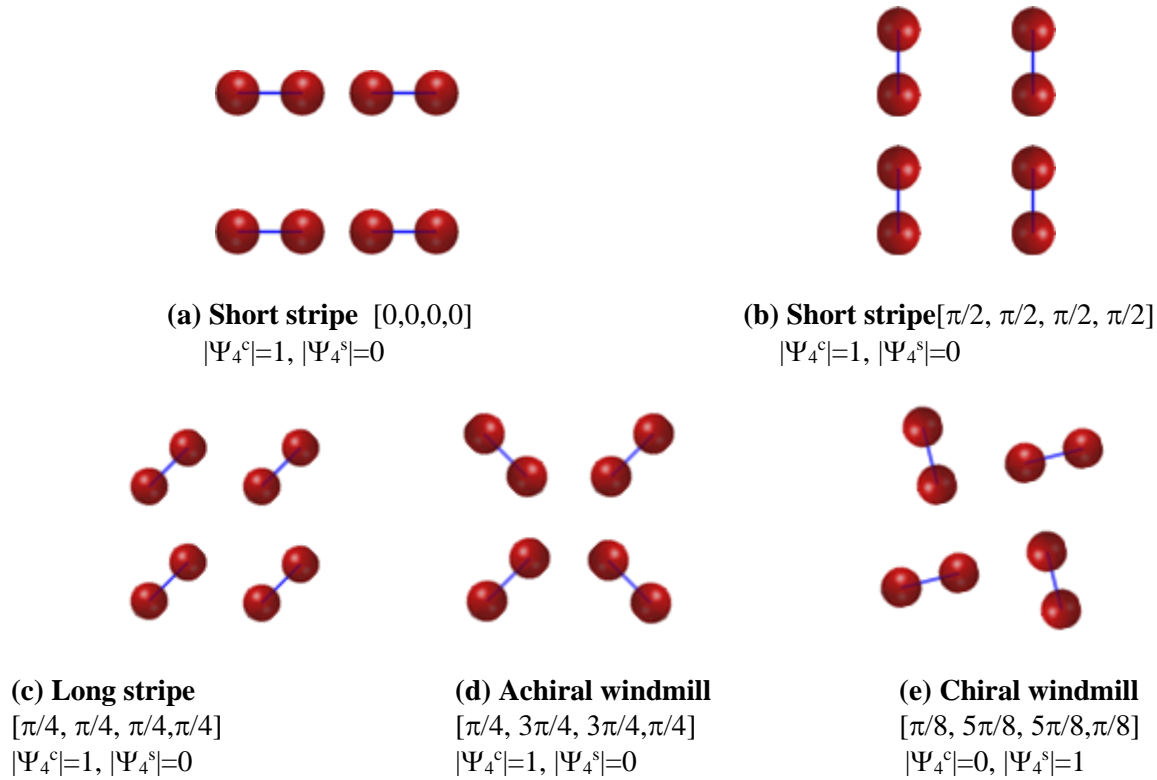


Figure II-4: Schematic representation of simple geometries of a ditopic molecule on square lattice.

By contrast, $|\Psi_4^c|=1$ for both forms of stripe, with $|\Psi_4^s|=0$ in both cases. Thus, Ψ_4 is a more promising candidate for detecting order. In this spirit, consider the case $[\pi/4+\delta, 3\pi/4+\delta, 5\pi/4+\delta, 7\pi/4+\delta]$. When $\delta=0$, the geometry is achiral, and the molecules define a square “pore”. (We describe this as a “symmetric windmill”). In this case $|\Psi_4^c| = 1$ and $\Psi_4^s = 0$. If δ is 5 degrees, say, (“chiral windmill”) then $|\Psi_4^c| = 0.94$ and $|\Psi_4^s| = 0.34$ in both cases, and $(|\Psi_4^c|^2 + |\Psi_4^s|^2) = 1$. An isotropic ensemble would have $(|\Psi_4^c|^2 + |\Psi_4^s|^2) = 0$. Thus, the Ψ_4 order parameters (i) detect local fourfold symmetry, since $(|\Psi_4^c|^2 + |\Psi_4^s|^2) = 1$, whatever the value of δ , and whatever the orientation of the geometry; (ii) detect chirality through a nonzero value of Ψ_4^s .

As will be discussed later, when we expect to observe three-fold order for a ditopic molecule, we will find that the Ψ_3 order parameters depend on the choice of axes, whereas the Ψ_6 order parameters do not.

In order to demonstrate the utility of these order parameters we show in **Figure II-2** the values of two of the Ψ_4 order parameters at high and low temperature, respectively, for a full Monte Carlo simulation. At high temperature, the adlayer is disordered, and therefore the angles are random on the interval 0 to π , yielding a value $\Psi_2^s = \Psi_4^s = 0$. However, for the ordered chiral “windmill” adlayer shown in **Figure II-2**, $|\Psi_4^s|$ is close to unity. (The absolute value is taken since the sense of rotation is arbitrary.) As can be seen from the figure, the angles making up a unit cell are (approximately) $\pi/8$ and $5\pi/8$. This large nonzero value of Ψ_4^s is a strong indicator of chirality. As was the case for the (2x2) model calculations, these particular parameters detect the local 4-fold symmetry of the adlayer at low temperature.

Another type of adlayer geometry that is frequently observed is the so-called “herringbone”. This consists of two “sub-lattices”, one characterized by an orientation angle θ_A , the other by orientation angle θ_B . The pattern is most extreme if the two sublattices are perpendicular to each other; that is, if $|\theta_A - \theta_B| = \pi/2$. This suggests a herringbone order parameter (17, 124, 125) given by:

$$\Psi_{HB} = \frac{1}{4} \sum_{i=1}^4 \sum_{j \neq i}^4 \sin(|\theta_i - \theta_j|) = \frac{1}{4} \sum_{i=1}^4 \frac{1}{2} \sum_{j>i}^4 \sin(|\theta_i - \theta_j|) \quad \text{II-11}$$

and we shall sometimes use $\Delta\theta_{ij} = |\theta_i - \theta_j|$. The formulation given above can be used for more complicated unit cells. However, it should be noted that it will reach its maximum value for the case described above: namely, when there are two mutually perpendicular sublattices. (We note that using this definition, both the symmetric and chiral windmill geometries will yield a herringbone order parameter of 1; stripes will yield a value of zero.)

For each of the six cases considered in detail in the next chapter, we will search for order parameters that will help identify the various families of adlayer geometry.

II.3 Concepts

Some of the concepts and tools used in determining the most stable geometry for a given molecule, lattice, and parameter set are illustrated in **Figure II-5** and **Table II-1**. The example given is that of a tetratopic molecule on a square lattice. First “candidate” adlayer structures must be identified. In **Figure II-5**, we consider three such structures. One is a square (SQ) in which the arms of the molecule lie parallel to the lattice axes. The second structure is the cross (CR) in which the arms of all molecules are oriented at an angle of 45° to the lattice axes. Finally, we look at what we have labeled the “compact” structure (CO). (The name derives from the geometry of the adlayer observed for a model tetratopic molecule at high density by the Szabelski group (20)). In this case, the molecules are all oriented at $\pi/8$ to the lattice x-axis.

The geometries are illustrated by the cartoons in **Figure II-5**. The space group symmetries of the three adlayer structures shown are p4mm, p4mm, and p4 respectively. It can be seen that the first two possess mirror planes, and are therefore achiral. However, the third adlayer is chiral. This is despite the fact that the molecule itself is achiral (D_{4h}). The expression of chiral monolayers using achiral molecules as “building blocks” has been the subject of considerable interest recently (8, 126-129). In our analysis, we pay particular attention to chirality, and shall attempt to identify which regions of the parameter space give rise to chiral adlayers.

As has been described in **Appendix A**, the total potential energy is the pairwise sum of all the intermolecular site-to-site interactions. This sum is dominated by the contributions from the nearest-neighbor (NN) pair interactions. This NN distance is denoted by s .

Clearly, as the length of the molecule's arm ρ changes, so too does the nearest-neighbor distance. The dependence of s on ρ for the three geometries shown is given in **Table II-1**, and is plotted in **Figure II-5**. As is clear from the figure, the shortest NN distance is obtained from the square geometry, for all molecular sizes.

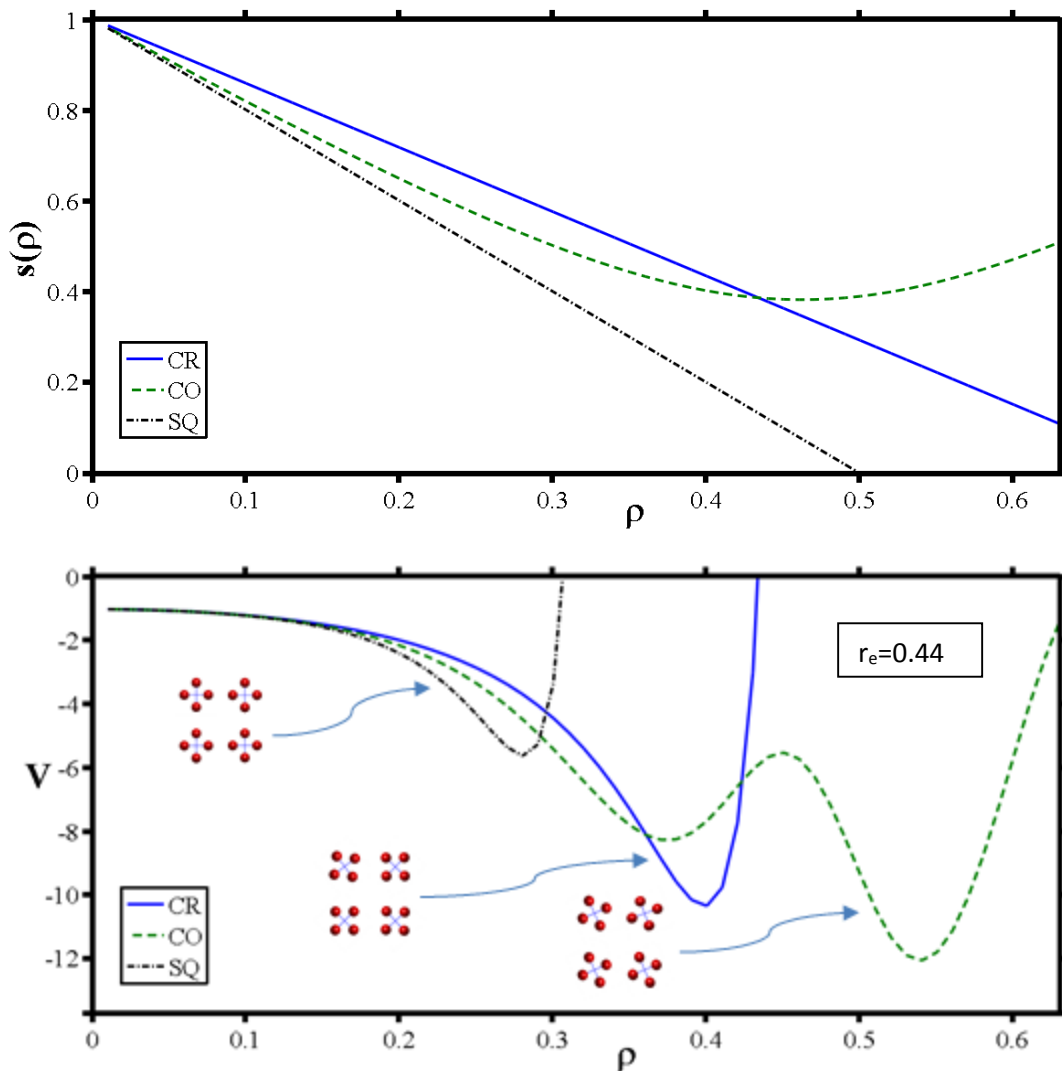


Figure II-5: Tetratopic molecule on a square lattice. (Upper) The nearest-neighbor (NN) nearest-neighbor site-to-site separation s , as a function of molecular size, ρ . The functional forms are from **Table II-1**. (Lower) The total potential energy (in LJ energy units) as a function of molecular size, ρ , for the three geometries denoted as square (SQ), cross (CR) and compact (CO). The Lennard-Jones length parameter $r_e = 0.44$. The adlayer geometries are shown as cartoons.

Table II-1: Tetratopic molecule on a square lattice. For three sample adlayer geometries, the nearest-neighbor site-to-site separation s , is shown as a function of molecular size, ρ . The geometries are shown in **Figure II-4**.

Geometry	Site-to-site distance	NN count
Square, SQ	$s(\rho) = 1 - 2\rho$	4
Cross, CR	$s(\rho) = 1 - \sqrt{2}\rho$	8
Compact, CO ($\pi/8$)	$s(\rho) = \sqrt{1 - 4\rho \cos\left(\frac{\pi}{8}\right) + 4\rho^2}$	4

We can now use this information to predict which is the most stable geometry for each value of the molecular size, ρ . To help visualize this, consider **Figure II-5**, where we plot the pair potential as a function of molecular size, $V(s(\rho))$ for the three geometries. (The figure is for the LJ pair potential with an r_e value of 0.44.)

Using the SQ geometry as an example, we see that for $\rho=0$, the molecule has shrunk to a point, the NN separation is equal to the lattice size (unity), and the pair potential is small, since $s \gg r_e$. As the molecule increases in size, the $s(\rho)$ decreases. Therefore the potential becomes increasingly attractive until $s=r_e$. (Recall that r_e is the separation of maximum attraction.) From **Table II-1**, we see that this occurs at $\rho_e=(1- r_e)/2$. Since there are four NN interactions, the potential at ρ_e is approximately -4 (in Lennard-Jones energy units). (It is actually a little more attractive, because of next-NN (NNN) attractions.) As the molecule increases in size beyond ρ_e , however, the potential becomes rapidly repulsive. This means that the SQ geometry is no longer viable. A similar argument can be made for the cross (CR) geometry, which we predict to be the most stable (of the three candidate geometries considered here) when ρ is approximately equal to 0.4. For ρ values much greater than about 0.45, however, the CR geometry has also become repulsive. Of the three geometries we consider here, then, at large molecular size, only the chiral “compact” geometry is viable. Referring to the cartoons it can be seen that this makes intuitive

sense: the sites can avoid crowding best in the compact geometry. We comment that this tendency for the largest molecules to adopt a chiral pattern is one of our findings in this dissertation.

We note at this point that several candidate adlayer geometries are intuitively obvious and predictable. For instance, in the previous discussion, both the square and cross patterns would have been obvious candidate structures, with unambiguous values of the angles – either all 0 for the square or all $\pi/4$ for the cross. However, the compact (chiral, p4) geometry has a range of angles values that are possible. (In fact, any rotational angle on the open interval $(0, \pi/4)$ is possible. The rotation angle appears in the formula for $s(\rho)$. As can be seen in **Table II-1**, we arbitrarily used the value $\pi/8$ for the analysis.) This will be addressed in detail in each of the discussions of the results that follow.

II.4 Procedure

In the Results chapter(s) (**Chapter III, Chapter IV, Chapter V, Chapter VI, and Chapter VII**), we adopt the following procedure. The adsorbate geometry is explored for di-, tri-, and tetratopic molecules fixed on square and triangular lattices. In particular, we consider how the preferred geometry varies as a function of the molecular size, ρ . We also vary the distance parameter, r_e , of the Lennard-Jones potential to explore what impact this has.

The four-angle “unit cell” is searched by the method detailed in **Appendix A**, and the most stable geometries are identified. We classify the geometries into a limited number of families using inspection and order parameters developed for each case. We present our results in the form of the most stable geometry as a function of the (ρ, r_e) “parameter space”. We will refer to this construction (loosely) as the “parameter phase diagram.” By using the $s(\rho)$ data for each family of geometries we can rationalize a parameter “phase diagram”. In selected cases, we also undertake

a more detailed study of the potential energy landscape, seeking local minima, in addition to the global minimum. This information is useful in predicting thermodynamic and kinetic data for the system. The global minimum of the potential is the free energy minimum at $T=0$. However, for nonzero temperatures, local minima need to be included in the calculation of the free energy. In addition, rate behavior is governed by transitions between these minima. Hence, a knowledge of transition states yields insight into the kinetics and dynamics of a system.

II.5 Method

The study considers di-, tri- and tetra-topic molecules on both a square and a triangular (hexagonal) lattice. The lattice is infinitely large but we use a small portion with periodicity to represent the full lattice. A primary 2x2 “unit cell” is defined by four independent angles, $[\theta_1, \theta_2, \theta_3, \theta_4]$. (The angles are taken with reference to the lattice x-axis.) The remainder of the lattice is then populated by translating the 2x2 cell in the x and y directions for the square lattice. The Cartesian coordinates of each of the $P=2, 3,$ or 4 sites on each molecule can then be obtained by simple trigonometry. For the triangular lattice, the new Cartesian coordinates for each site are obtained by counter-clockwise rotation through $\pi/6$ (rotation matrix = $\begin{pmatrix} 1 & -\tan \pi/6 \\ 0 & \frac{1}{\cos \pi/6} \end{pmatrix}$). For any pair of molecules, i and j , say, the potential energy is the pairwise sum of all P sites on molecule i with those on j . That is, (see **Figure II-6**)

$$V^{ij}(\theta_i, \theta_j) = \sum_{p=1}^p \sum_{q=1}^q v(r_{pq}^{ij}) \quad \text{II-12}$$

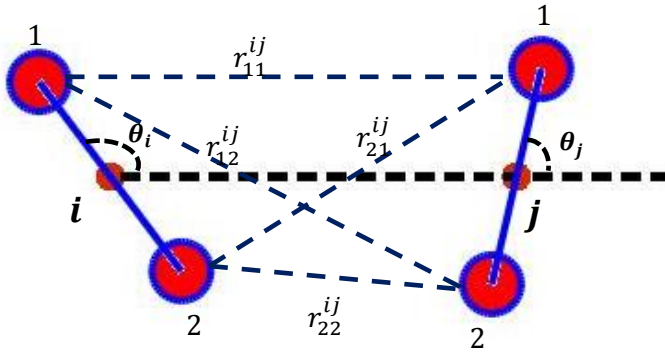


Figure II-6: Illustration of the site-to-site (r) distances between two adjacent rotors i and j used in the intermolecular potential energy interactions.

where $v(r)$ is the pairwise site-to-site potential energy (typically Lennard-Jones, but occasionally Morse). The total potential felt by the i th molecule is given by the sum over all the intermolecular pair potentials:

$$V^i = \sum_{j \neq i} V^{ij} \quad \text{II-13}$$

The sum is, in principle, infinite, but in practice can be truncated after the second nearest-neighbor molecule. The mean potential felt by a molecule in the adlayer is then given by

$$\bar{V} = \frac{1}{d} \sum_{i=1}^4 V^i \quad \text{II-14}$$

where d is the number of nearest-neighbor and next-nearest-neighbor sites (8 for the square lattice; 12 for the triangular lattice). In what follows, we will refer to this as the potential energy (and remind the reader it is a function of $(\theta_1, \theta_2, \theta_3, \theta_4)$). This will be the term that is minimized in the potential energy optimization. **Figure II-3** illustrates the four angles of the unit cell and the tessellated images of that cell for both the square and the triangular lattices. The specific case shown is for the ditopic molecule.

Potential energy function

The molecule-molecule pairwise potential energy between two adjacent rotors is given by a sum over pairwise site-to-site pair potentials. The sites are separated by a distance, r . Typically, the pair potential used will be the Lennard-Jones potential. This potential has two parameters: the well depth, D_e , which measures the strength of the interaction; and r_e , which measures the interaction length of the potential. However, on occasion, we will also use the Morse potential, which has an additional “stiffness” parameter, β , which modulates how gradually the potential attains the maximum attraction. Both potentials have the maximum attraction at $r=r_e$, where $V = -D_e$. It is convenient to scale the potential by quoting it in units of D_e .

$$\frac{V_{LJ}(r)}{D_e} = \left(\frac{r_e}{r}\right)^{12} - 2\left(\frac{r_e}{r}\right)^6 \quad \text{II-15}$$

$$\frac{V_{morse}(r)}{D_e} = e^{-\beta(r-r_e)}[e^{-\beta(r-r_e)} - 2] \quad \text{II-16}$$

The Lennard-Jones potential and the Morse potential for two different values of β are shown in **Figure II-7**. (In fact, the two potentials are similar in the vicinity of r_e when $\beta = 6$ when $r_e = 1$.) Thus varying the parameter β is a useful way to smoothly deform the potential away from a Lennard-Jones, without altering minimum energy lengths or energies.

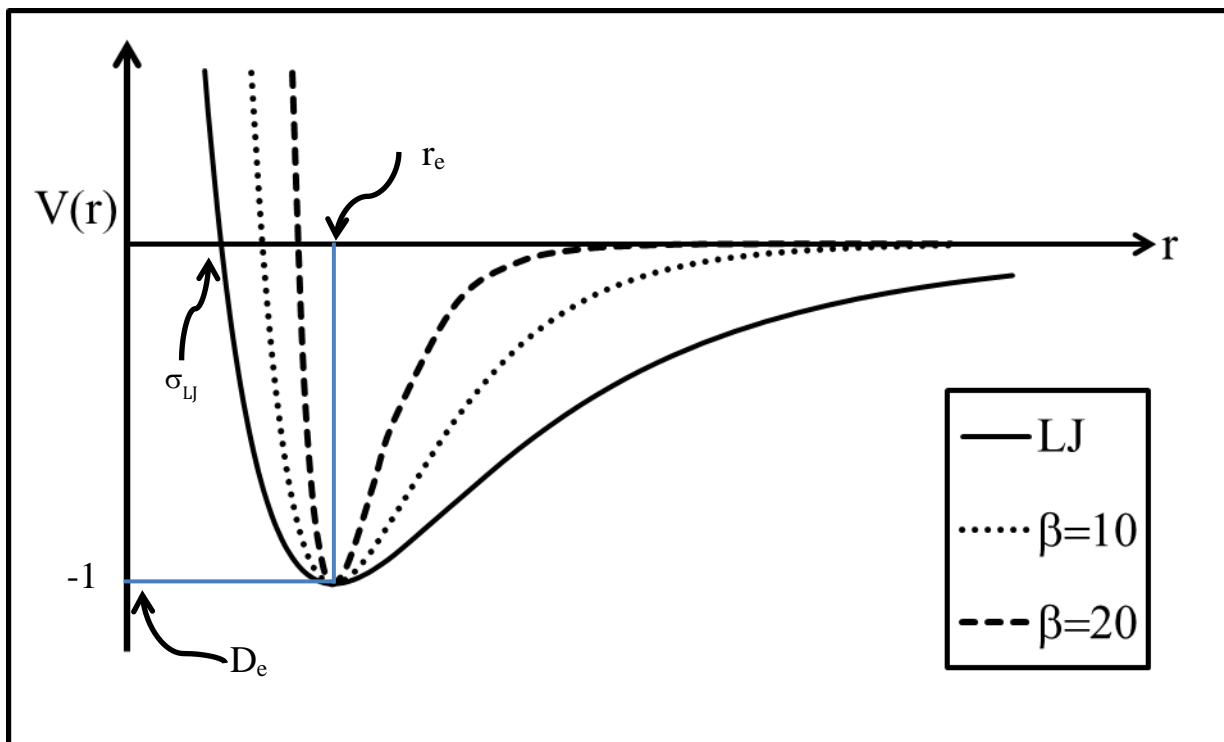


Figure II-7: Schematic representation of Lennard-Jones and Morse potential with two different stiffness parameters $\beta = 10$ and 20 . Note that minimum at $r = r_e$ and that $V=0$ at $r = \infty$.

A useful parameter of LJ and Morse potential which is shown in **Figure II-7** is the hard sphere radius, σ . This is essentially the van der Waals radius, the distance below which the potentials become repulsive.

$$\sigma_{LJ} = \frac{r_e}{2^{1/6}} \quad \text{II-17}$$

$$\sigma_{Morse} = r_e - \frac{\ln(2)}{\beta} \quad \text{II-18}$$

The van der Waals radius will sometimes be used to show the space-filling “footprint” of the molecule (**Figure II-8**). This will be particularly important when the primary focus is on the “pore” sizes of the adlayer. An example is shown below for p4 adlayer formed by a ditopic molecule on a square lattice. The radius of the (red) end-cap of the molecule is $\sigma/2$, making the width of the “shaft” of the molecule σ . (The division by two guarantees that two sites repel each

other at a separation of σ .) The two sites on the same molecule are separated by a length 2ρ . As can be seen, the adlayer creates a square “pore” tilted about 30 degrees from the lattice x-axis. In each of the chapters that follows, we shall look at how the pore size(s) and shape(s) change as the parameters change.

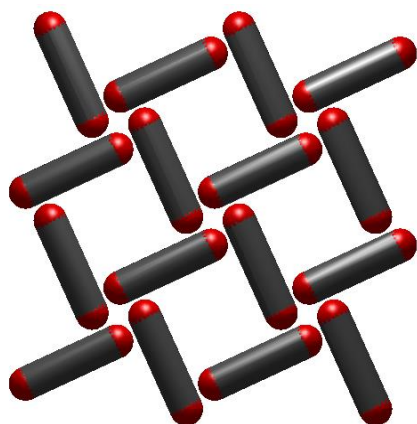


Figure II-8: Space-filling “footprint” diagram for a ditopic molecule on a square lattice, showing pore size, shape, and orientation.

In **Figures II-9, II-10** and **II-11** (for di-, tri, and tetratopic, respectively) we illustrate the effect of varying of the parameters (ρ , r_e) by showing the contour energy plots of a single atomic site moving around the molecule with angle $\gamma \in [0, 2\pi]$.

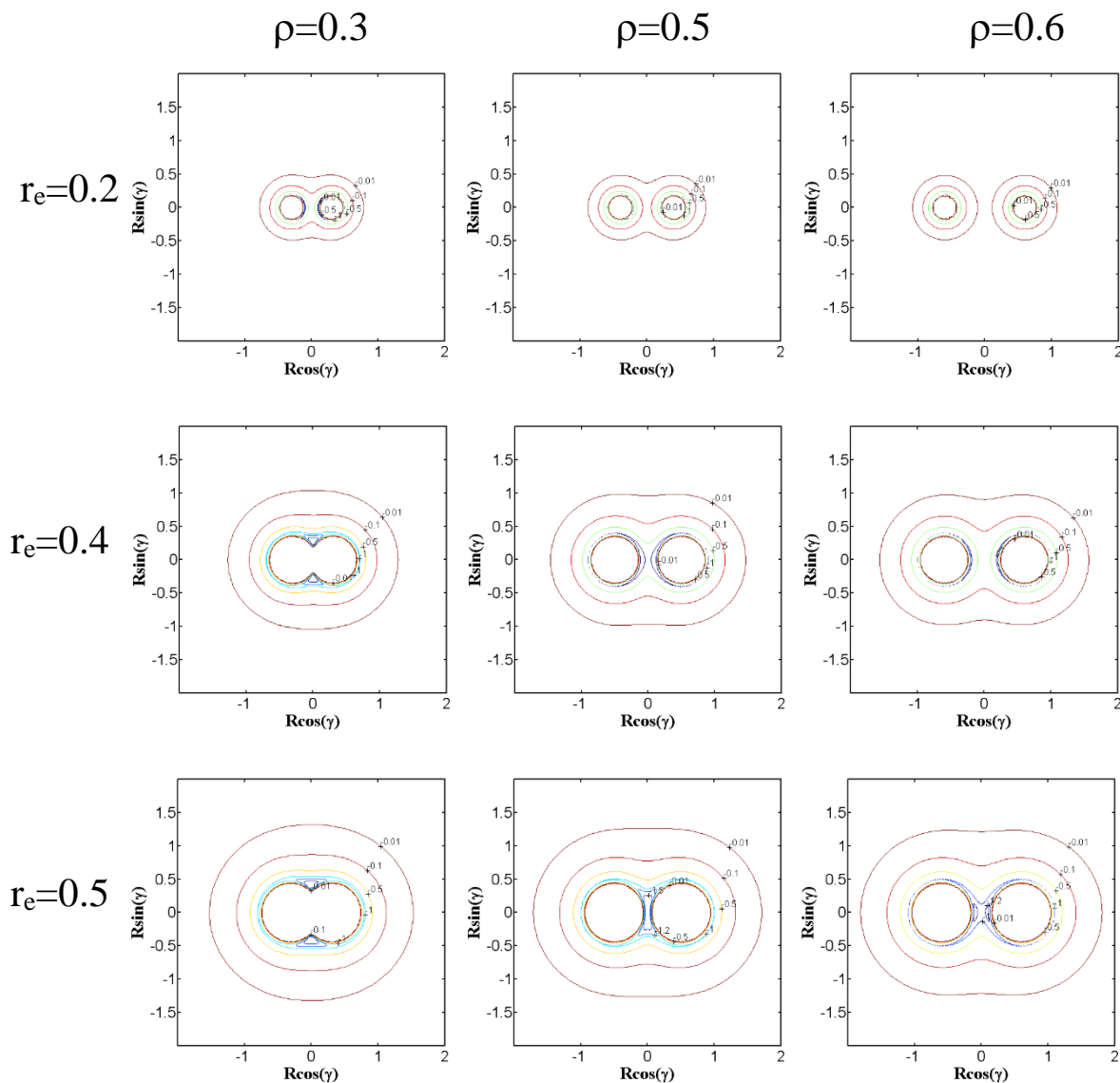
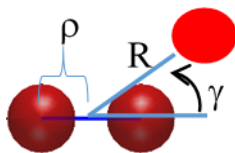


Figure II-9: The model ditopic molecule (upper panel). To illustrate the effect of changing the molecular parameters, the potential energy is shown for a single atom-like site interacting with the molecule. This site has plane polar coordinates (R, γ) , or Cartesian coordinate $(R \cos \gamma, R \sin \gamma)$. Contour energy plots $V(\rho=0.3, 0.5, 0.6, r_e=0.2, 0.4, 0.5, \gamma)$ of the molecule with single site. $\gamma \in [0, 2\pi]$ is the angle of a single site moved around the molecule with the universal x-axis. Note: ρ is length of the each arm of the molecule from center of mass; r_e is the site-to-site equilibrium distance of Lennard-Jones potential.

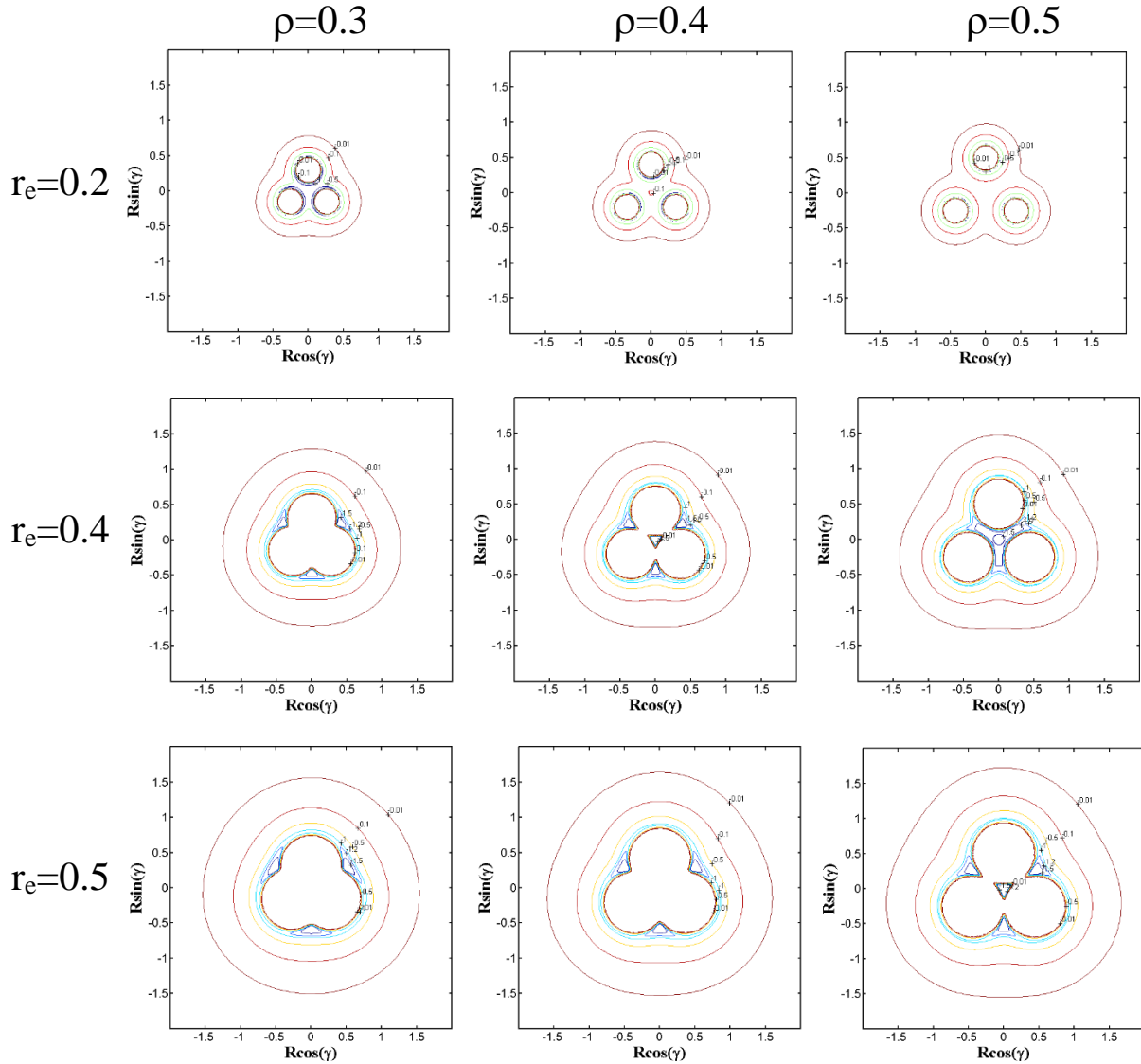
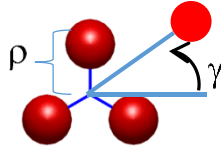


Figure II-10: The model tritopic molecule (upper panel). To illustrate the effect of changing the molecular parameters, the potential energy is shown for a single atom-like site interacting with the molecule. This site has plane polar coordinates (R, γ) , or Cartesian coordinate $(R \cos \gamma, R \sin \gamma)$. Contour energy plots $V(\rho=0.3, 0.4, 0.5, r_e=0.2, 0.4, 0.5, \gamma)$ of the molecule with a single site. $\gamma \in [0, 2\pi]$ is the angle of a single site moved around the molecule from the universal x-axis.

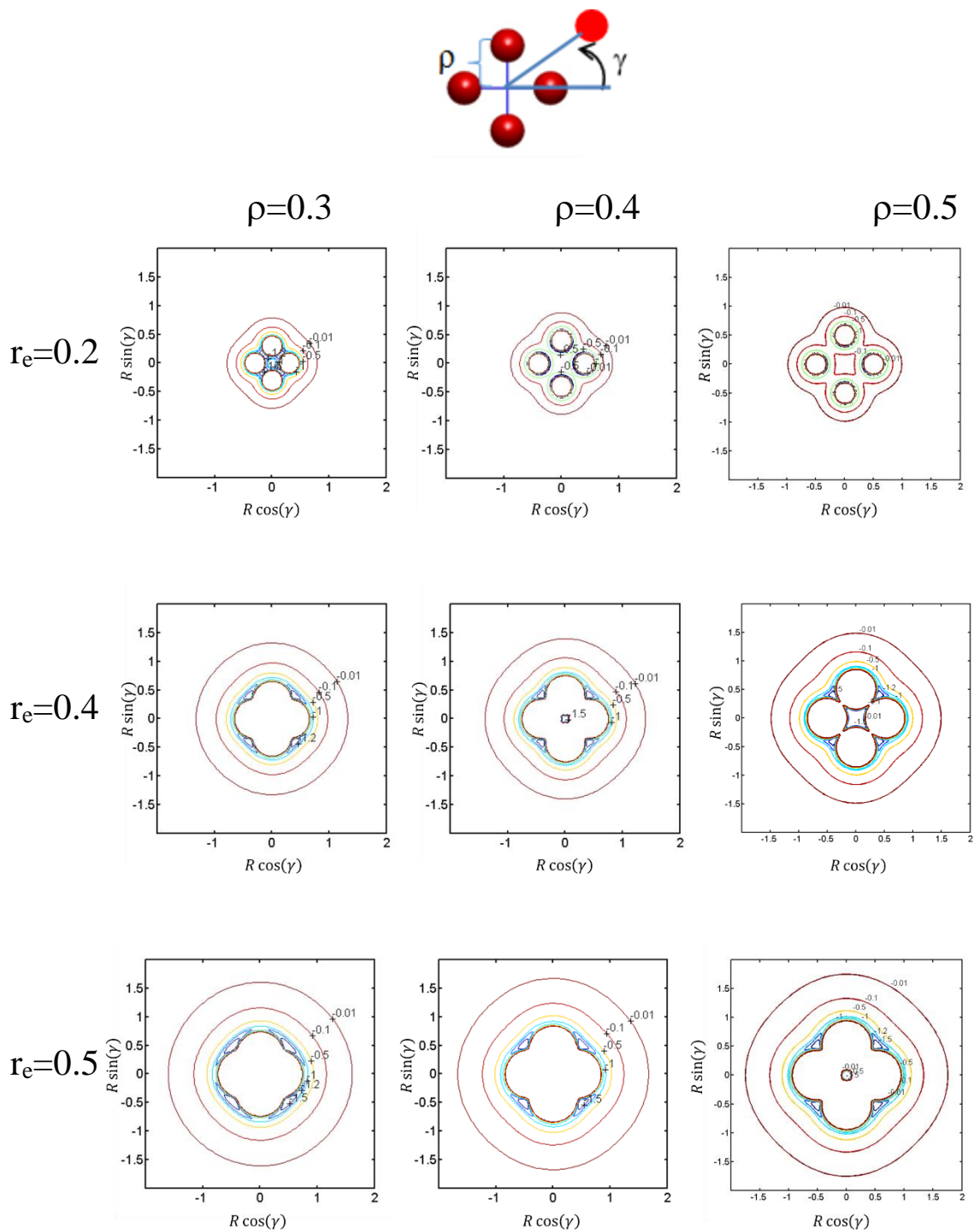


Figure II-11: The model tetraatomic molecule (upper panel). To illustrate the effect of changing the molecular parameters, the potential energy is shown for a single atom-like site interacting with the molecule. This site has plane polar coordinates (R, γ) , or Cartesian coordinate $(R \cos \gamma, R \sin \gamma)$. Contour energy plots $V(\rho=0.3, 0.4, 0.5, r_e=0.2, 0.4, 0.5, \gamma)$ of the molecule with a single site. $\gamma \in [0, 2\pi]$ is the angle of a single site moved around the molecule from the universal x-axis.

II.6 Simplified unit cell notation and some definitions

The full notation of the unit cell $\theta = [\theta_1, \theta_2, \theta_3, \theta_4]$ (see **Figure II-3.**) is occasionally too cumbersome to write when not all the angles are independent of each other. Therefore we will use a short notation to describe some special geometries. This notation will be described here briefly. We will also mention some adlayer notation that may be used in the discussions. This notation is also known as superlattice notation (130), since the adlayer is a periodic structure with periodicity related to the underlying surface lattice.

If all the rotor angles are the same, then the adlayer periodicity is the same as that of the surface lattice. That is, the adlayer repeats every 1 unit in the x and 1 unit in the y direction (for a square lattice). This is accordingly labeled a (1x1) superlattice. The single angle which repeats is θ , say, and we denote this as $\{\theta\}$. Depending on the molecule and the angle, this can have different appearances. For instance, for a ditopic molecule, $\{0\}$ (or equivalently $\{\pi/2\}$) on a square lattice the geometry can be described as a “short stripe”. For a ditopic molecule $\{\pi/4\}$ on the square lattice, this can be described as a “long stripe”. Alternatively, for a tetratopic molecule on a square lattice, $\{0\}$ would denote the square (SQ) adlayer already shown in **Figure II-5** of this chapter, whereas $\{\pi/4\}$ would be the cross (CR) adlayer. The chiral compact (CO) also described in **Figure II-5** could be described by $\{\pi/8\}$.

A pattern that occurs frequently is one in which the same angle occurs along a “diagonal” of the unit cell. This is referred to as a “herringbone” adlayer. It would have the full notation $[\theta_1, \theta_2, \theta_2, \theta_1]$. Clearly, this means that the periodicity in both the x and the y directions is now 2, and this would be written in superlattice notation as (2x2). One extreme form of this adlayer has

already been mentioned, in which the angles alternate between zero and $\pi/2$. We will refer to this geometry $\{0, \pi/2\}$ as a “perfect” herringbone.

Another type of adlayer geometry that is frequently observed is the so-called “herringbone” (HB). This consists of two “sub-lattices”, one characterized by an orientation angle θ_A , the other by orientation angle θ_B . The herringbone pattern is ubiquitous in the packing of hard ellipsoids (131). This can occur in one of two morphologies. (See **Figure II-12.**) In the more typical form, the same angle occurs along a “diagonal” of the unit cell. It would have the full notation $[\theta_A, \theta_B, \theta_B, \theta_A]$, which will sometimes be abbreviated to HB(ABBA). Clearly, this means that the periodicity in both the x and the y directions is now 2, and this would be written in superlattice notation as (2x2). One extreme form of this type of herringbone adlayer has already been mentioned, in which the angles alternate between zero and $\pi/2$. We will refer to this geometry $\{0, \pi/2\}$ as a “perfect” herringbone. The other herringbone morphology has $[\theta_A, \theta_A, \theta_B, \theta_B]$ (or AABB) form. These two geometries are illustrated in **Figure II-12.** Both structures would have the abbreviated form $\{\theta_A, \theta_B\}$. When necessary, we will distinguish between the ABBA and the AABB variants.

The notation will be particularly useful when we attempt to investigate the stability of a given adlayer. In such cases, we will plot the potential energy as we systematically vary the rotor angles. We will motivate this by considering the family of adlayers described by the ditopic molecule on the square lattice described by a single rotor angle $\{\theta\}$. When $\theta=0$, we have the (p2mm) adlayer already described as a short stripe. When $\theta=\pi/4$, we have the (p2mm) adlayer already described as a long stripe. As has been noted above, between those extremes, the adlayer has only p2 symmetry, and is chiral. Since all the angles are the same, we can describe the rotation

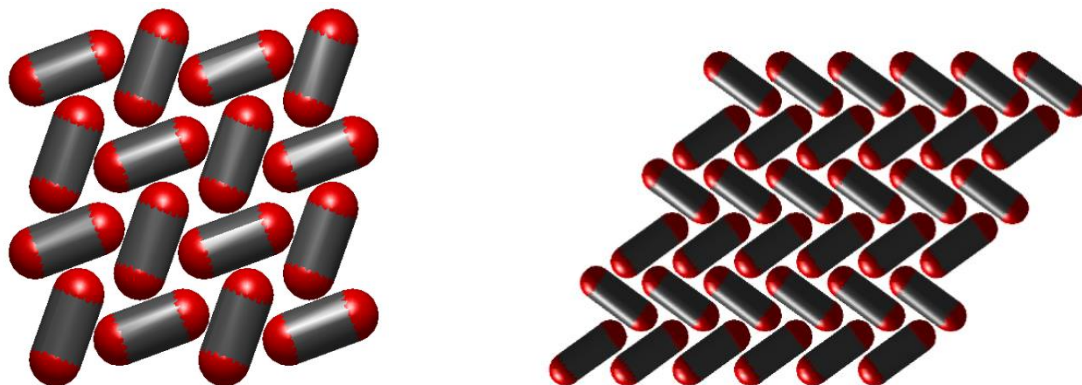


Figure II-12: Space-filling representations of two forms of herringbone. (Left) ABBA on a square lattice; (Right) AABB on a triangular lattice. For the two adlayers shown above, the unit cell would have crystallographic notation $|\mathbf{a}| = |\mathbf{b}| = 2$, $\gamma = \pi/2$ (square lattice); $|\mathbf{a}| = 1$, $|\mathbf{b}| = 2$, $\gamma = \pi/3$ (triangular lattice).

as conrotatory, in analogy with the rotation of molecules in electrocyclic reactions. Remaining with ditopic molecules on the square lattice, the mapping from $\{0\}$ (short stripe) with a disrotatory mapping through $\{\theta, -\theta\}$ retains $p2mm$ symmetry at all times, until it reaches the important structure $\{\pi/4, -\pi/4\}$, which has $p4mm$ symmetry, and we refer to it as a symmetric “windmill” (WM1). Conrotatory distortion of this symmetric windmill through $\{\theta + \pi/4, \theta - \pi/4\}$ produces chiral windmill adlayers with $p4$ symmetry. These will be labeled as WM2.

A rather unexpected adlayer structure that was detected in the searches is referred to as the “butterfly” geometry. The (2×2) structure is shown in **Figure II-13**.

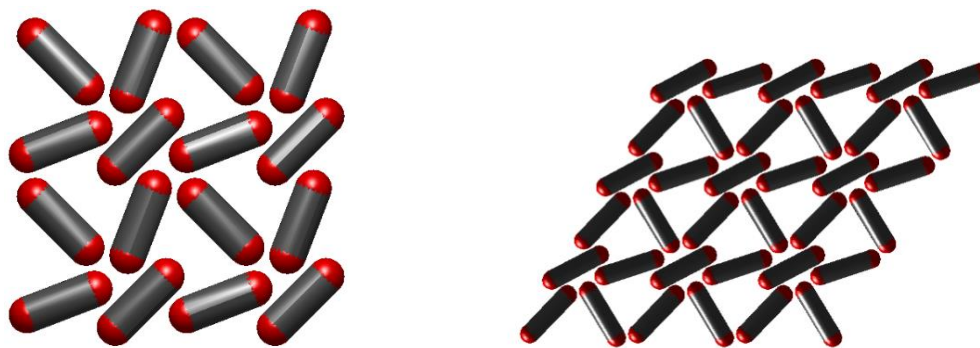


Figure II-13: “Butterfly” adlayer geometry (c2mm). Left, square lattice. Angle notation $[3\pi/8, 3\pi/4, \pi/4, \pi/8]$. Crystallographic notation $|\mathbf{a}|=|\mathbf{b}|=2, \gamma= \pi/2$. Right, triangular lattice. $[3\pi/12, 5\pi/6, \pi/6, \pi/12]$. Crystallographic notation $|\mathbf{a}| = |\mathbf{b}| =2, \gamma= \pi/3$.

II.7 Summary

In this chapter, we have introduced some concepts and notations of the method and the model that will be used in the following chapters. In these subsequent chapters we shall consider the six possible combinations of di-, tri-, tetratopic molecules fixed on, respectively, a square and a hexagonal (triangular) lattice.

Chapter III

A Model Study of Adlayer Geometries of Rigid Ditopic Molecules on a Square Lattice

III.1 Introduction

As has been described in the previous chapter we carry out here a model study designed to elucidate some of the effects that details of the adsorbate-adsorbate interaction potential can have on adlayer patterning. To do this we choose ditopic molecules (explained in chapter I), and consider a substrate lattice of square symmetry. The adsorbate pattern depends on both the adsorbate-adsorbate interaction potential and the adsorbate-substrate interaction. In order to simplify the problem, we have chosen the limit in which all adsorbate molecules are bound to a surface site, and all sites are occupied. Furthermore, each molecule is constrained to move only in the plane of the surface, making the molecule a plane rotor. The theoretical approach to obtaining adlayer geometry, that is adopted here, is very similar to that of the Anisotropic Plane Rotor model of several previous authors (34, 36).

The goal of this chapter (and the next) is to examine the potential energy landscape of a rigid ditopic molecular “rotor” adsorbed on a square lattice using the Lennard-Jones and Morse functions to model the site-to-site potential energy. Primarily we search for the ground state structure of the adlayer, that is, the geometry that yields the global minimum (GM) of the potential energy. In addition, we have investigated the most stable local minima of the system by considering a large number of minimization starting points. We systematically investigate the role played by: (i) the size of the rotor and (ii) the site-to-site interaction length.

The size of the molecular rotor is defined using ρ , distance (“arm length”) from the rotor center of mass to the tip of the rotor, shown in **Chapter II (Figure II-3)**. This means that the length of the ditopic rotor is given by 2ρ . The length r_e is the site-to-site equilibrium distance of the potential. This was illustrated in the previous chapter, and is shown in **Figure II-9**, the contour plot of several illustrative examples.

As both r_e and ρ increase in size, the space-filling “footprint” of the molecule will increase. Therefore, this can be envisaged as an increase in monolayer density, experimentally realizable by increasing the surface pressure. In principle, with a full knowledge of all the local minima of a potential energy landscape, statistical mechanics can be applied to obtain the temperature dependence of the system. We have not done this here, but we do identify several of the local minima at various points of the parameter space for the Lennard-Jones pair potential.

Our methods are presented in **Section III.2**, in which we introduce the orientational order parameters and the “key” geometries we shall focus on. Results and Discussion for the global minimum of Lennard-Jones potential are in **Section III.3.A**. The results are summarized in a parameter “phase diagram”, with the geometries shown in a contour plot as a function of (ρ, r_e) . These are central findings for this chapter. Local minima are explored in **Section III.3.B**, and the effect of changing the pair potential is considered in **Section III.3.C**. Conclusions, and comparisons with available experimental data appear in **Section III.4**.

III.2 Method

III.2.a Energy Landscape

As discussed in the previous chapter, the search is restricted to the (2x2) “unit cell” space, $[\theta_1, \theta_2, \theta_3, \theta_4]$ with the full adlayer generated by tessellation. The potential energy $V(\theta_1, \theta_2, \theta_3, \theta_4)$ is explored for each point in parameter space by methods described more fully in the **Appendix A**. The principal results reported are the global minima (GM) of the potential energy. In certain cases, local minima (LM) are explored and reported.

III.2.b Orientational Order Parameters

In order to classify the adlayer geometries, several order parameters were employed. The ideas behind the order parameters were presented in the previous chapter. Here, we use the following four order parameters to differentiate between the geometries.

$$\Psi_4^c = \frac{1}{4} \sum_i \cos(4\theta_i) \quad (\text{III-1})$$

$$|\Psi_4^s| = \left| \frac{1}{4} \sum_i \sin(4\theta_i) \right| \quad (\text{III-2})$$

$$\Psi_2^{|cl|} = \frac{1}{4} \sum_i |\cos(2\theta_i)| \quad (\text{III-3})$$

where the sum is over the unit cell.

$$\Psi_{HB} = \frac{1}{8} \left| \sum_{i=1}^4 \sum_{i \neq j}^4 \sin(\Delta\theta_{ij}) \right| \quad (\text{III-4})$$

where $\Delta\theta_{ij} = |\theta_i - \theta_j|$, and the sum is over the 4 unit cell rotors.

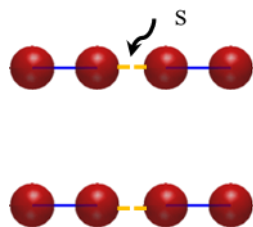
As mentioned in the previous chapter, $|\Psi_4^s|$ proves to be an indicator of chirality. $\Psi_4^c, \Psi_2^{|c|}$ and Ψ_{HB} provides information on the geometry that is a useful complement to visual inspection.

III.2.c Key Geometries

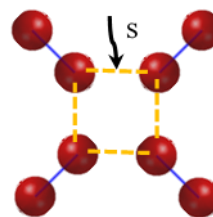
As discussed in the previous chapter, we need to identify the key adlayer geometries which will be used to construct the “parameter phase diagram.” These are obtained using preliminary investigations. We have chosen to focus on **seven** key adlayer geometries in this chapter. These are shown in **Figure III-1**. All the other geometries we identified could be “binned” into one of the following categories.

We discuss each of these adlayer geometries briefly below.

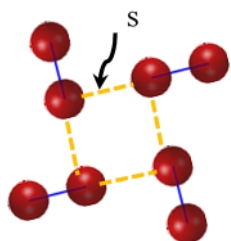
- (a) The short stripe (SS) has p2mm wallpaper symmetry. In our notation, it is written $\{0\}$. (We note that this is equivalent to $\{\pi/2\}$).
- (b) The symmetric windmill (WM1) has p4mm symmetry, with angles $\{\pi/4, 3\pi/4\}$. This geometry is achiral.
- (c) The chiral (or “distorted”) windmill (WM2), with p4 symmetry, has geometry $\{\phi, \pi/2+\phi\}$. As noted before, a range of $0 < \phi < \pi/4$ is possible. Shown is $\phi = \pi/8$.
- (d) The long stripe (LS) geometry $\{\pi/4\}$ has p2mg symmetry. (This is equivalent to $\{3\pi/4\}$).
- (e) The “perfect” herringbone (PHB) $\{0, \pi/2\}$ (of ABBA type) has p4gm symmetry.
- (f) The herringbone (HB) shown is the example $\{7\pi/18, \pi/9\}$ has (of ABBA type) p2gg symmetry.
- (g) The butterfly (BF) shown is the example $[7\pi/18, 3\pi/4, \pi/4, \pi/9]$ has symmetry c2mm.



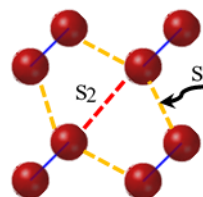
(a) SS



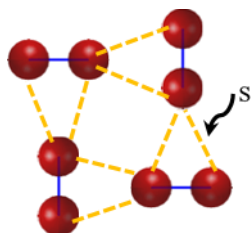
(b) WM1



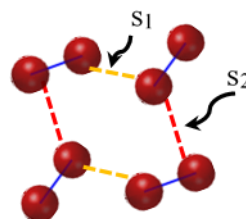
(c) WM2



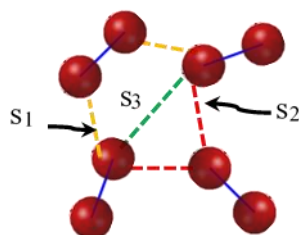
(d) LS



(e) PHB



(f) HB



(g) BF

Figure III-1: Schematic representation of the seven key geometries used for the ditopic molecule on a square lattice. (a) Short Stripe (SS); (b) Symmetric Windmill (WM1); (c) Chiral Windmill (WM2) $\{\pi/8, 5\pi/8\}$; (d) Long Stripe (LS); (e) Perfect Herringbone (PHB); (f) Herringbone (HB) $\{7\pi/18, 5\pi/9\}$; (g) Butterfly (BF) $[7\pi/18, 3\pi/4, \pi/4, \pi/9]$. Shown on the figure are the NN site-to-site distances in each case. A range of angles is possible for the chiral windmill.

These particular geometries were chosen since they illustrate the major intermolecular “bonding” motifs that are possible. The “stripes” show 2-center bonds. The “windmills” illustrate 4-center bonds. The herringbone is the dominant motif for hard ellipsoids (131). Other geometries were identified by our exploration, and will be discussed more fully in the Results and Discussion section.

Table III-1: Closest nearest-neighbor (NN) site-to-site distance, s , for specified geometry as a function of ρ . Also included is the number of nearest-neighbor interactions. Note that there are two possible NN distances for the LS geometry, with differing NN coordination. The geometries are defined in **Figure III-1**.

Geometry	Site-to-site distances	Number of NN
SS	$s(\rho) = 1 - 2\rho$	2
WM1	$s(\rho) = 1 - \sqrt{2}\rho$	4
WM2	$s(\rho) = \sqrt{1 - 2\sqrt{2}\rho \cos\left(\frac{\pi}{8}\right) + 2\rho^2}$	4
LS	$s(\rho) = \min\left(\sqrt{2} - 2\rho, \sqrt{1 - 2\sqrt{2}\rho + 4\rho^2}\right)$	4, 2
PHB	$s(\rho) = \sqrt{1 - 2\rho + 2\rho^2}$	8
HB	$s(\rho) = \min\left(\sqrt{1 + 2\rho^2 + 2\rho^2 \cos\frac{5\pi}{18} - 2\sqrt{2}\rho \cos\frac{5\pi}{36}}, \sqrt{1 + 2\rho^2 - 4\sqrt{2}\rho \cos\frac{5\pi}{36}}\right)$	4, 2
BF	$s(\rho) = \min\left(\sqrt{1 + 2\rho^2 + 2\rho^2 \cos\frac{5\pi}{36} - 2\rho \sin\frac{7\pi}{18} - \sqrt{2}\rho}, \sqrt{1 + 2\rho^2 - 2\rho^2 \sin\frac{5\pi}{36} - 2\rho \sin\frac{7\pi}{18} - \sqrt{2}\rho}, \sqrt{2} - 2\rho \cos\frac{5\pi}{36}\right)$	2, 1, 1

This functional dependence of $s(\rho)$ is shown graphically in **Figure III-2**.

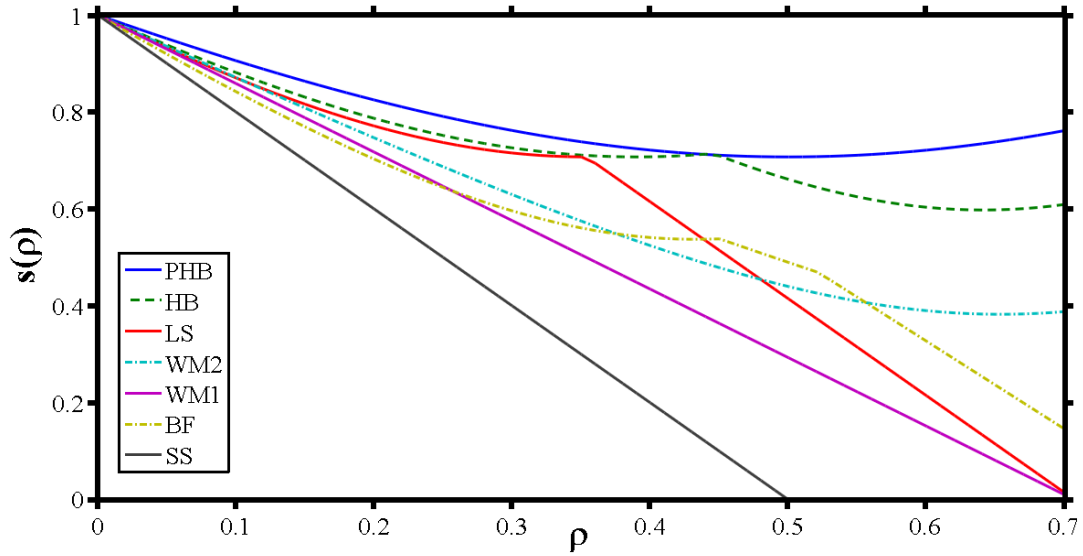


Figure III-2: Nearest-neighbor site-to-site distance, $s(\rho)$, as a function of molecule arm length, ρ , for chosen geometries. The geometry labels PHB, HB, LS, WM2, WM1, BF and SS are defined in **Figure III-2**.

Table III-2: Values of order parameters of the seven key geometries described in **Figure III-1**.

Geometry	Ψ_4^c	$ \Psi_4^s $	$\Psi_2^{ c }$	Ψ_{HB}
SS	1	0	1	0
WM1	-1	0	0	1
WM2	0	1	$1/\sqrt{2}$	1
LS	-1	0	0	0
PHB	1	0	1	1
HB	0.2	0	0.8	0.8
BF	-0.4	0	0.4	1

One of the ways to distinguish geometries is the combination of the values of the orientational order parameters. The values for the seven geometries listed above are given in **Table III-2**.

Also shown in **Figure III-1** in each case (as a dotted line) are the nearest neighbor NN site-to-site interaction distances. In **Table III-1**, we give the explicit dependence of this distance on the molecular rotor arm length, $s(\rho)$. In **Figure III-2**, we plot the $s(\rho)$ functions identified in **Table III-1** for the seven key geometries.

III.2.d Distortion Pathways

The potential energy minimization is carried out in a four-dimensional angle space. This is difficult to visualize. Certain “cuts” through that space, though, enable one to gain insight into the variables as the angle space is traversed, and may yield insight into the findings. Particularly simple are one-dimensional plots of variables (particularly the energy) as a function of a single angle variable. While they do not represent an exploration of the full angle space, they can assist in understanding the role played by the geometry in determining the potential energy.

We note that all “stripes” can be represented by a single distortion angle $\{\phi\}$, with the points $\phi = 0$ and $\phi = \pi/4$ being the SS and LS, respectively. The intermediate geometries would all be of (chiral) p2 symmetry. We can also deform the short stripe (SS) into the “perfect” herringbone (PHB) using the path $\{0,\phi\}$, with $\phi = 0$ giving the SS, and $\phi = \pi/2$ giving the PHB, with all the intermediate points being of the HB(ABBA) type. Rather than follow this path, we consider two different distortion paths which traverse several of the key geometries. Path I begins with a disrotatory rotation through ϕ (via p2mg geometries) to the symmetric windmill (WM1), followed by a conrotatory rotation through ϕ' to the chiral windmill (WM2) and PHB. Path II begins with a conrotatory rotation through ϕ (via p2 geometries) to the long stripe (LS), followed by a disrotatory rotation through ϕ' (via HB (ABBA) geometries) to the HB and PHB.

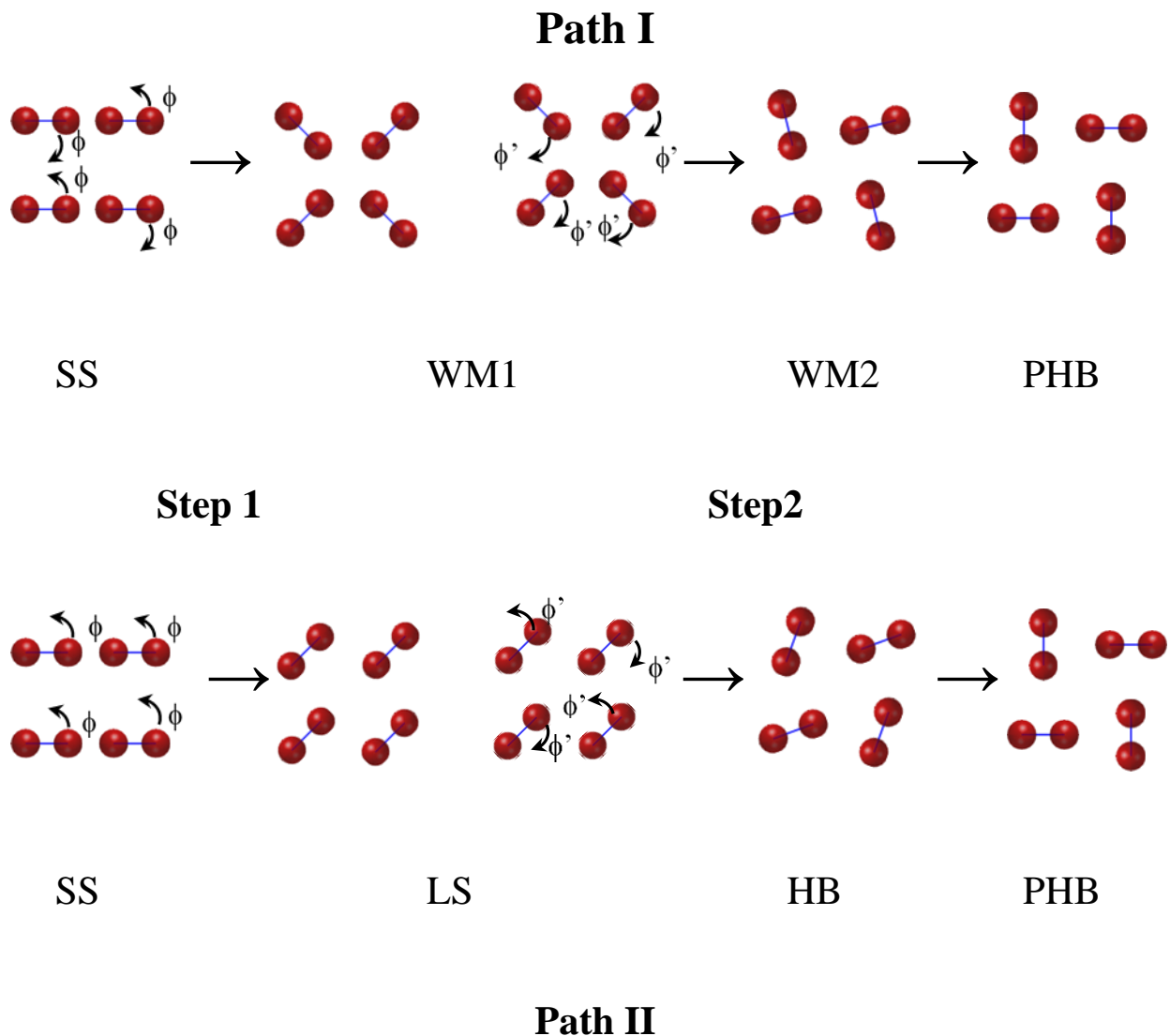


Figure III-3: Two pathways from the SS to the PHB geometries. Path I begins (Step 1) with a disrotatory rotation through ϕ (via p2mg geometries) to the symmetric windmill (WM1). This is followed (Step 2) by a conrotatory rotation through ϕ' . Path II begins (Step 1) with a conrotatory rotation through ϕ (via p2 geometries) to the long stripe (LS). This is followed (Step 2) by a disrotatory rotation through ϕ' (via HB geometries).

We can utilize these pathways to help visualize some of the criteria needed to use the orientational order parameters to distinguish geometries. The four order parameters are shown as a function of the deformation angles along the two paths in **Figure III-4**. Of particular interest is the $|\Psi_4^s|$ parameter. This is zero when the adlayer is achiral, nonzero when the adlayer is chiral. Enantiomers with the same angle would have $\Psi^s \rightarrow -\Psi^s$ when the angles are reflected about either

the x or the y axis. Therefore we take the absolute value of this order parameter, since the actual sense of rotation of the degenerate chiral structures depends arbitrarily on the details of the minimization to get both homochiral structures. The only geometry of the seven key structures, shown in **Figure III-1**, that is chiral is the chiral windmill, WM2, which has $|\Psi_4^s|=1$; the other six geometries considered here have $|\Psi_4^s|=0$ (that is, they are achiral), since they all possess a plane of symmetry. We note that the mirror planes are maintained in Step 1 of Path I; hence the adlayers along that path are achiral.

However, the conrotatory Step 1 of Path II passes through chiral p2 geometries, with the “maximum chirality” evidenced at $\phi=\pi/8$. By contrast, Step 2 of Path I takes us through p4 geometries, with the order parameter recording its maximum value at $\phi=\pi/8$.

The cosine order parameter Ψ_4^c moves through a wider range of values, being unity for the starting and final points on the paths, and -1 for both the LS and the symmetric windmill.

Using the order parameters in combination with a visual inspection allows us to “bin” intermediate adlayer geometries into the appropriate family. We bin the geometries using the $\Psi_2^{|c|}$ order parameter.

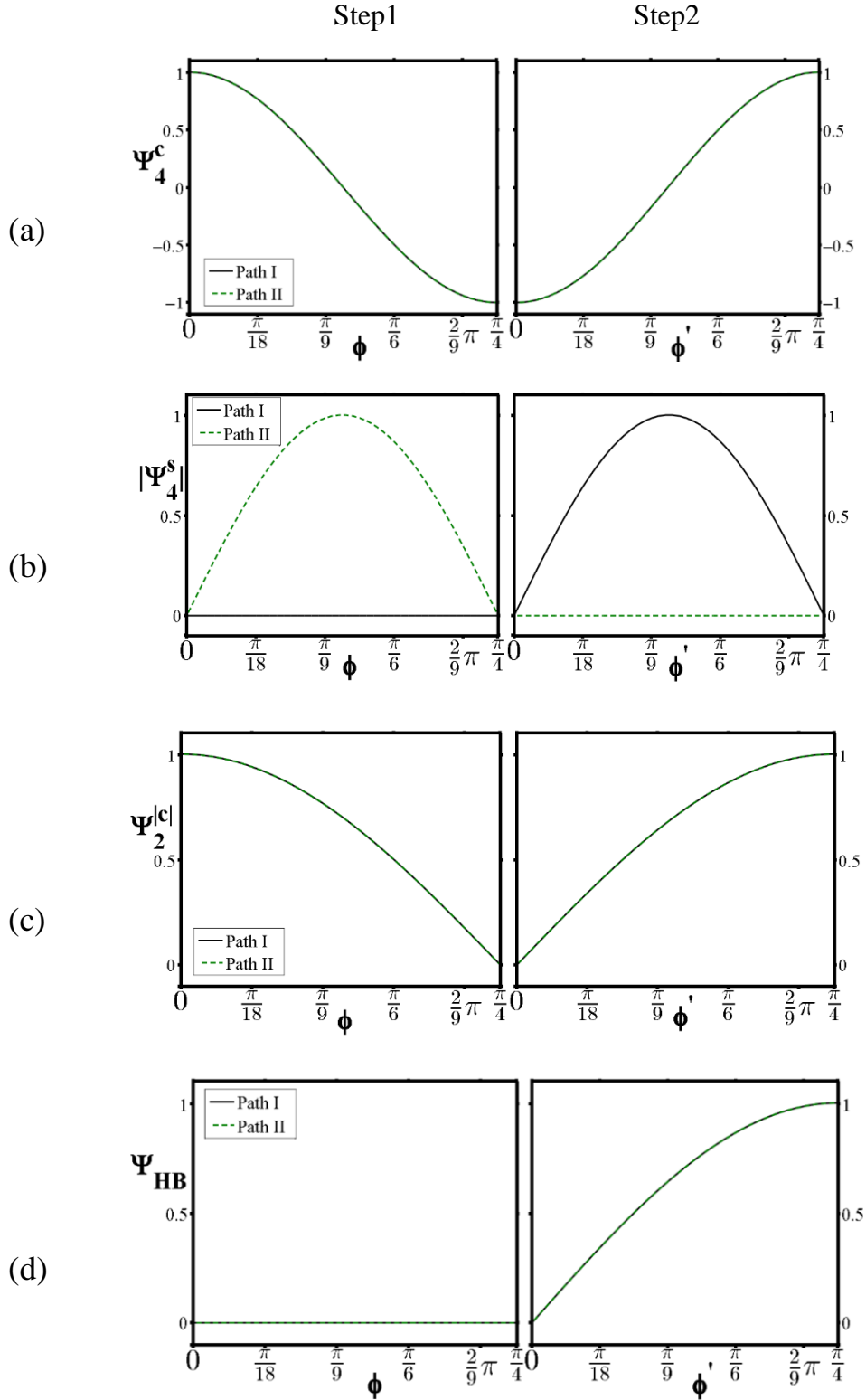


Figure III-4: the order parameters as a function of rotation angle ϕ or ϕ' for the paths shown in **Figure III-3**. (a) Ψ_4^c , (b) $|\Psi_4^s|$, (c) $\Psi_2^{|c|}$ (d) Ψ_{HB} . The legends describe the path (I or II).

III.3 Results and Discussion for Square Lattice

III.3.a Parameter “Phase Diagram” for the Lennard-Jones Potential

The Lennard-Jones potential energy was minimized for all points in the (ρ, r_e) parameter space. Once the minimum energy geometry is obtained, we can obtain the orientational order parameters from the values of the angles. The potential energy, Ψ_4^c , $|\Psi_4^s|$, Ψ_2^{cl} , Ψ_{HB} are shown as contour plots in **Figure III-5 (b), (c), (d), (e), (f)** respectively. In order to assign geometries, a visual inspection was carried out and NN counts taken (SS and BF have two NN; WM1 and WM2 have three). Geometries that were “transitional” between the seven key geometries were “binned” to one of these geometries using the Ψ_2^{cl} orientation parameter sort criteria. A non-zero value of $|\Psi_4^s|$ unambiguously identified chiral windmills. In the border between SS and WM1, if $\Psi_2^{cl} > 0.5$, the distorted geometries are added to the SS region, else to the WM1 region. Using these criteria, all the geometries could be assigned to one of the seven key geometries.

The results are summarized as the “parameter phase diagram” in **Figure III-5 (a)**. The dashed lines on the other contour plots show the boundaries that were established for the phase diagram. (These are not true phase changes – or even phase transformations—since the energy changes smoothly as the parameters are changed. However, uniquely demarking the dominant geometry in each region of the parameter space allows us to understand the role played by the parameters.) This “phase diagram” is the principal finding for this chapter.

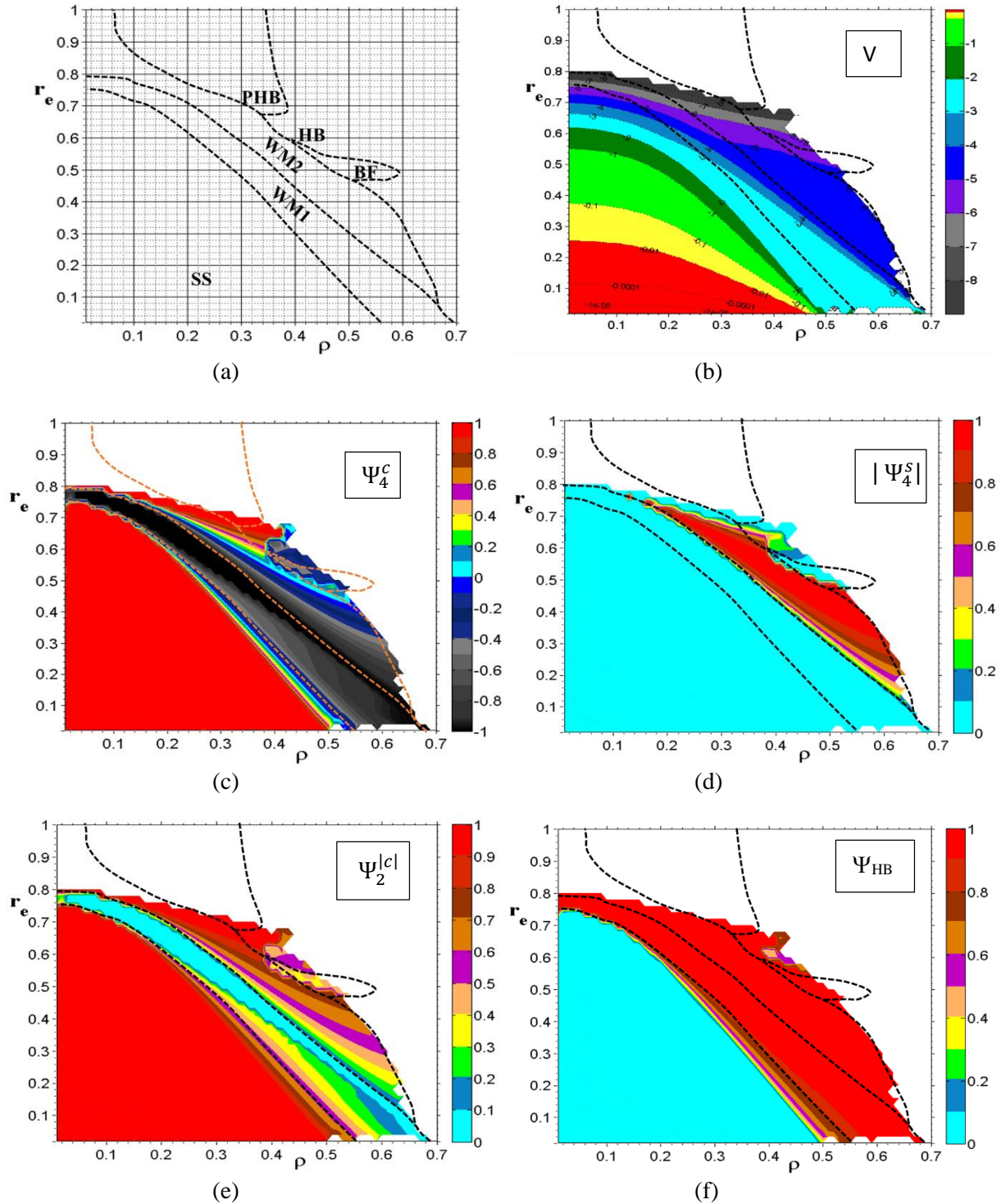


Figure III-5: Contour plots of various properties of the most stable geometry as a function of Lennard-Jones parameters (ρ , r_e). Panels (b) potential energy, V ; (c), (d), (e), (f) orientation order parameters Ψ_4^c , $|\Psi_4^s|$, $\Psi_2^{|c|}$, Ψ_{HB} respectively. Panel (a) summarizes this in the “phase diagram”, in which geometries are assigned using the criteria given in the text. The “phase boundaries” established in panel (a) are reproduced in the other panels. (Abbreviations used: SS = short stripe; WM1 = symmetric windmill; WM2= chiral windmill; HB = herringbone; PHB = perfect herringbone; BF = butterfly.)

In order to better visualize the findings, we show examples in **Figure III-6** of the space-filling versions of the adlayer geometries identified in **Figure III-5**. In most cases, these correspond to the parameters at which the geometry is the true GM. The single exception is for the long stripe (LS) geometry, which is not a GM for the Lennard-Jones potential. Shown is the geometry obtained using a Morse potential (see later discussion).

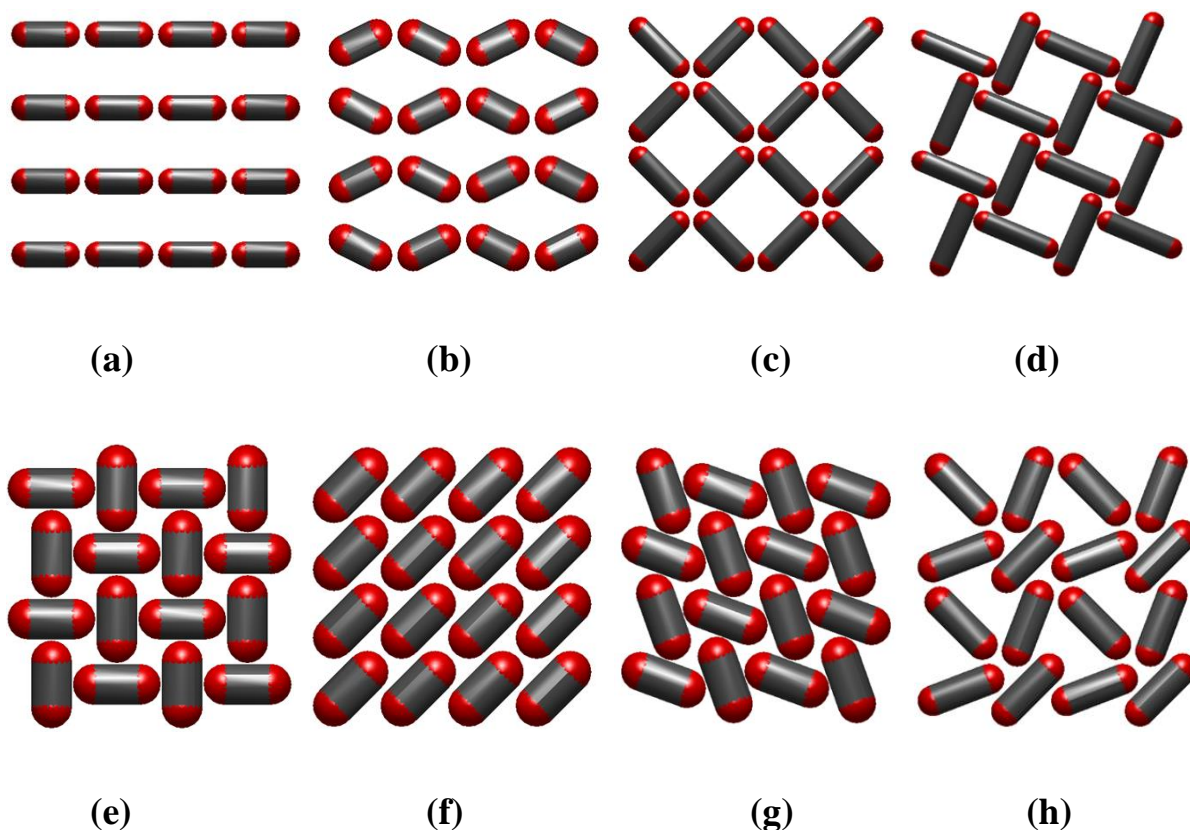


Figure III-6: Representative adlayer geometries for ditopic molecule on a square lattice with the Lennard-Jones potential. (See **Figure III-5**.) The geometries are drawn using the space-filling representation (see Chapter II). All are actual GM's, with the exception of the LS (f), which is a global minimum for a Morse potential. The (σ, ρ) parameters for each structure are:

(a) SS (0.36, 0.29); (b) Distorted SS* (0.46, 0.34); (c) WM1 (0.36, 0.39); (d) WM2 (0.36, 0.53); (e) PHB (0.62, 0.36); (f) LS (0.67, 0.35); (g) HB (0.62, 0.40); (h) BF (0.45, 0.45).

*Note that this geometry could be “binned” as either SS or WM1 depending on the orientational order parameter criteria.

In order to understand the phase diagram, we consider the following plots of $V(s(\rho))$ for three different values of r_e , (**Figure III-7**). In these figures, the parameter r_e is fixed, the geometry is fixed by holding the appropriate angles constant, and the potential energy as a function of ρ is plotted. Also shown on the figure is the potential energy found in the full (unbiased) search of the angle space described above at a given set of parameter values. This is labeled V_{unbiased} .

These values have been chosen since they represent three distinctive areas of the “phase diagram”. The value of $r_e=0.4$ represents the upper limit of the “low r_e ” region. In this region, the ratio ρ/r_e is the most typical of realistic molecular systems. For values of r_e less than 0.4, we see that the SS (short stripe) is favored at low values of ρ , since this achieves the closest NN interaction. (See **Figure III-2**.) This geometry, however, becomes strained and untenable as ρ increases. The symmetric windmill (WM1) is favored for intermediate values of ρ , since this geometry achieves 4-center intermolecular “bonds”, while avoiding the short 2-center “bonds” typical of the short stripe. As ρ further increases, this geometry too becomes strained, and the pattern distorts away from the $p4mm$ symmetry. However, as can be seen, it retains its fourfold symmetry, maintaining the $p4$ symmetry up to very large values of ρ . Although the LS is attractive up to $\rho = 0.55$ (see bottom panel of **Figure III-7**), the range of angles available to the chiral windmill (WM2) allow it to remain the GM. Indeed, for this value of r_e , the geometry manages to minimize the strain for all physically reasonable values of ρ .

At a somewhat larger value of r_e (here arbitrarily chosen to be 0.52) the chiral windmill (WM2) becomes repulsive near $\rho = 0.45$. This is about the same value as that at which the LS becomes repulsive, and hence this geometry is also infeasible. But the butterfly geometry, which manages to access 3-center bonding is here a feasible alternative, and avoids repulsion.

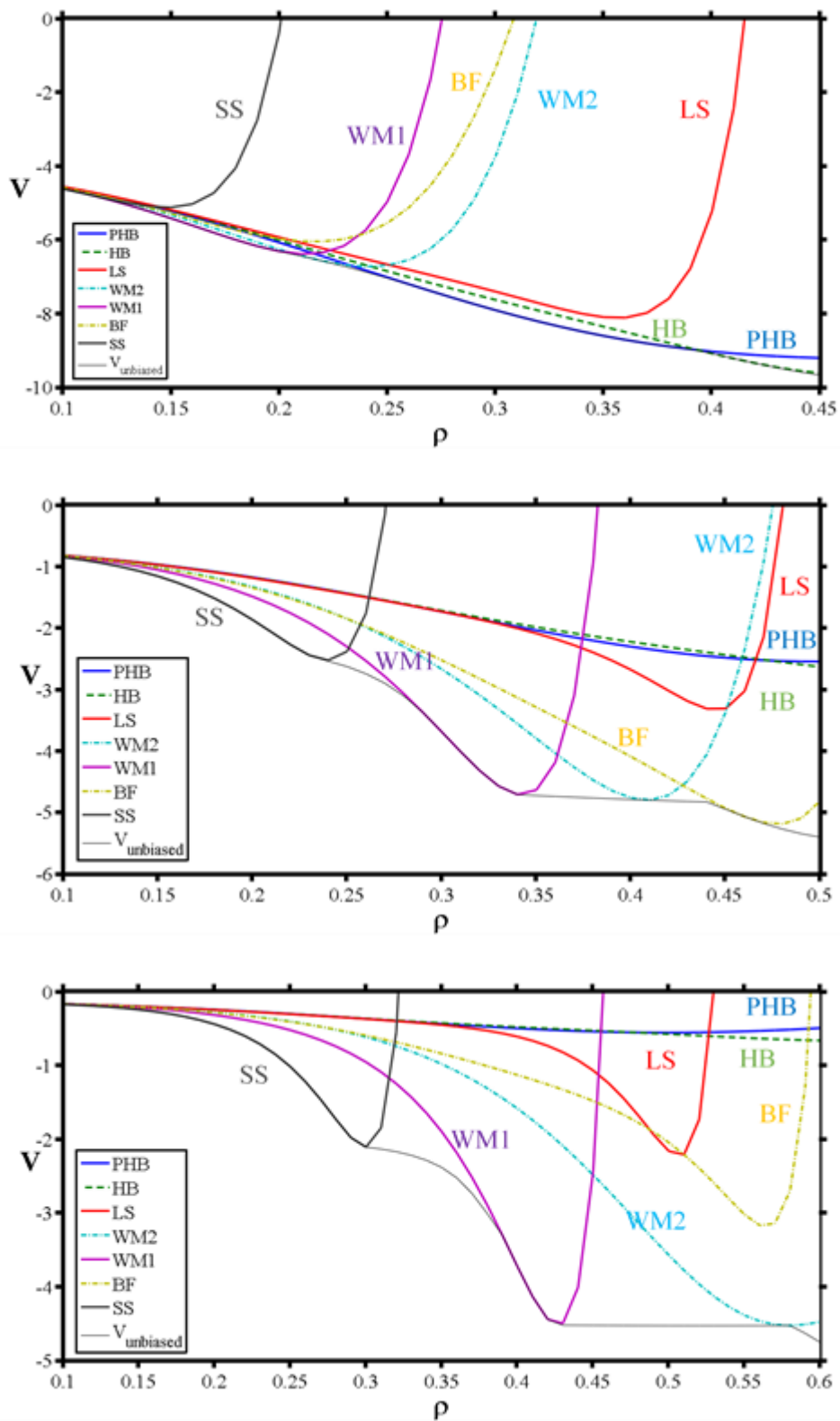


Figure III-7: Plots of $V(s(\rho))$ for the Lennard-Jones potential for the geometries observed in **Figure III-6**. Upper panel $r_e = 0.7$; Middle panel, $r_e = 0.52$; Lower panel, $r_e = 0.4$.

When r_e is unrealistically large for the model, and ρ is small, all the geometries “smear” into an isotropic sum over the site-to-site interactions for large molecule-molecule separations. Each geometry becomes strained in roughly the same order as for the lower values of r_e , but there is little difference in the attractive parts of the potential. The model results for these parameters almost certainly do not resemble those for any realistic molecular system.

We consider next a much more detailed analysis of the potential energy for $r_e = 0.4$ in **Figure III-8**. This figure shows the potential energy along the distortion paths shown in **Figure III-3** for selected values of the molecular arm length, ρ . For the smallest value of ρ (0.29) the SS is preferred: any distortion of the angle from linearity increases the potential energy. However, as the molecule’s size increases, the SS becomes increasingly strained, leaving the (achiral) “distorted” SS ($\rho = 0.34$), then ($\rho = 0.39-0.42$) the (achiral) windmill with its 4-center interaction becomes the most stable geometry. Further increase in the molecule’s size ($\rho > 0.53$) introduces strain in the 4-center interaction that twists the geometry to the chiral windmill structure.

At large molecular sizes ($\rho > 0.53$) we note that the path that would lead to HB-like structures (path II) is not favored: The fourfold attraction (evidenced by a potential energy of about -4) always leads to more stable geometries than the HB family, with its 2-center attraction (evidenced by a potential energy of about -2). This information will be used in the next section.

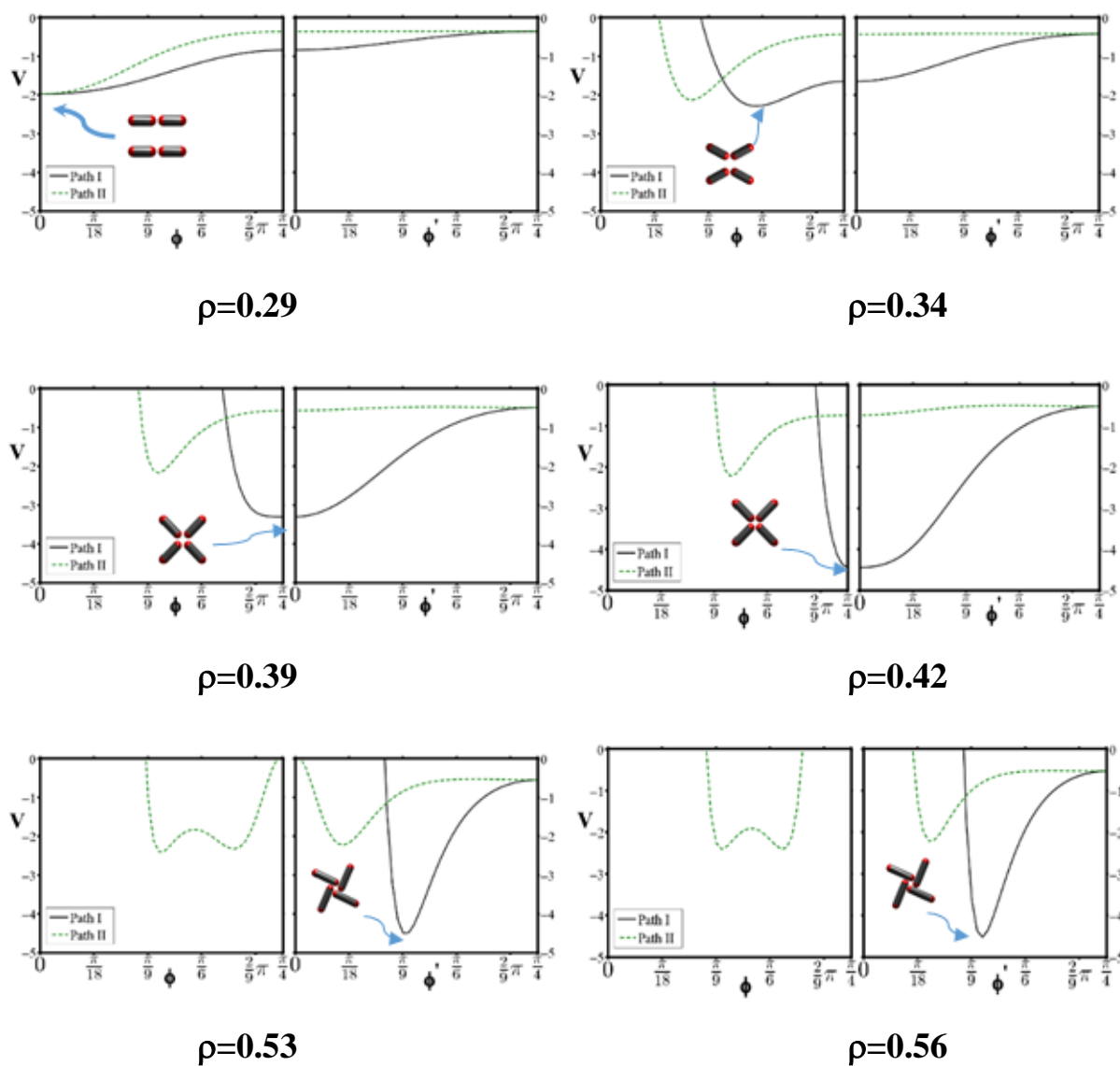


Figure III-8: Potential energy, V , as a function of rotation angle along the two paths shown in **Figure III-3**. At the lefthand side (path I) of each panel ($\phi=0$) the geometry is the SS. At the right (path II) of each panel ($\phi'=\pi/2$), the geometry is the PHB. In the center of the panel, the geometry is WM1. The potential is the Lennard-Jones, with $r_e=0.4$. Each panel has a different value of ρ . In each case, the global minimum (GM) geometry is indicated by a cartoon.

III.3.b Local Minima for the Lennard-Jones Potential

The GM is the geometry reported in the “phase diagram” (**Figure III-5**). This is the geometry the system would adopt at $T = 0$. However, for nonzero temperatures, energetically excited states (that is, local minima) have to be included in the partition function. We therefore also report the local minima (LM) found in the searches by randomly (in the angle space) initiating a large number of “quenches” to the nearest local minimum. Each local minimum can be associated with a probability depending on the number of “quenches” that lead to that minimum.

The histograms of the potential energies of the local minima for several values of ρ at $r_e=0.40$ and $r_e=0.52$ are shown in **Figure III-9**, and **Figure III-10**.

For $r_e=0.4$, $\rho = 0.29$ **Figure III-9** shows the system has a sole minimum, the GM. By $\rho = 0.34$, the stripe has distorted, with incipient 4-center “bonding” beginning to appear. Both the GM and the LM are on the achiral path. As ρ is further increased (say from 0.34 to 0.53) we see a herringbone-like local minima appear, but the dominant minimum is the windmill. For $\rho > 0.5$ something weird is going on since the GM should be $p4$. What is interesting is that its catchment area seems small, and the irregular geometries are easier to access. This might suggest that, as we increase the temperature at $r_e=0.4$, herringbone-like structures might be the thermodynamically stable adlayer geometry.

For the larger value of r_e , we see that various herringbone structures appear as local minima. In addition, the 3-center “bond” which underlies the butterfly (BF) geometry makes its appearance as a local minimum. (As explained above, these geometries are rather unphysical for molecular systems.)

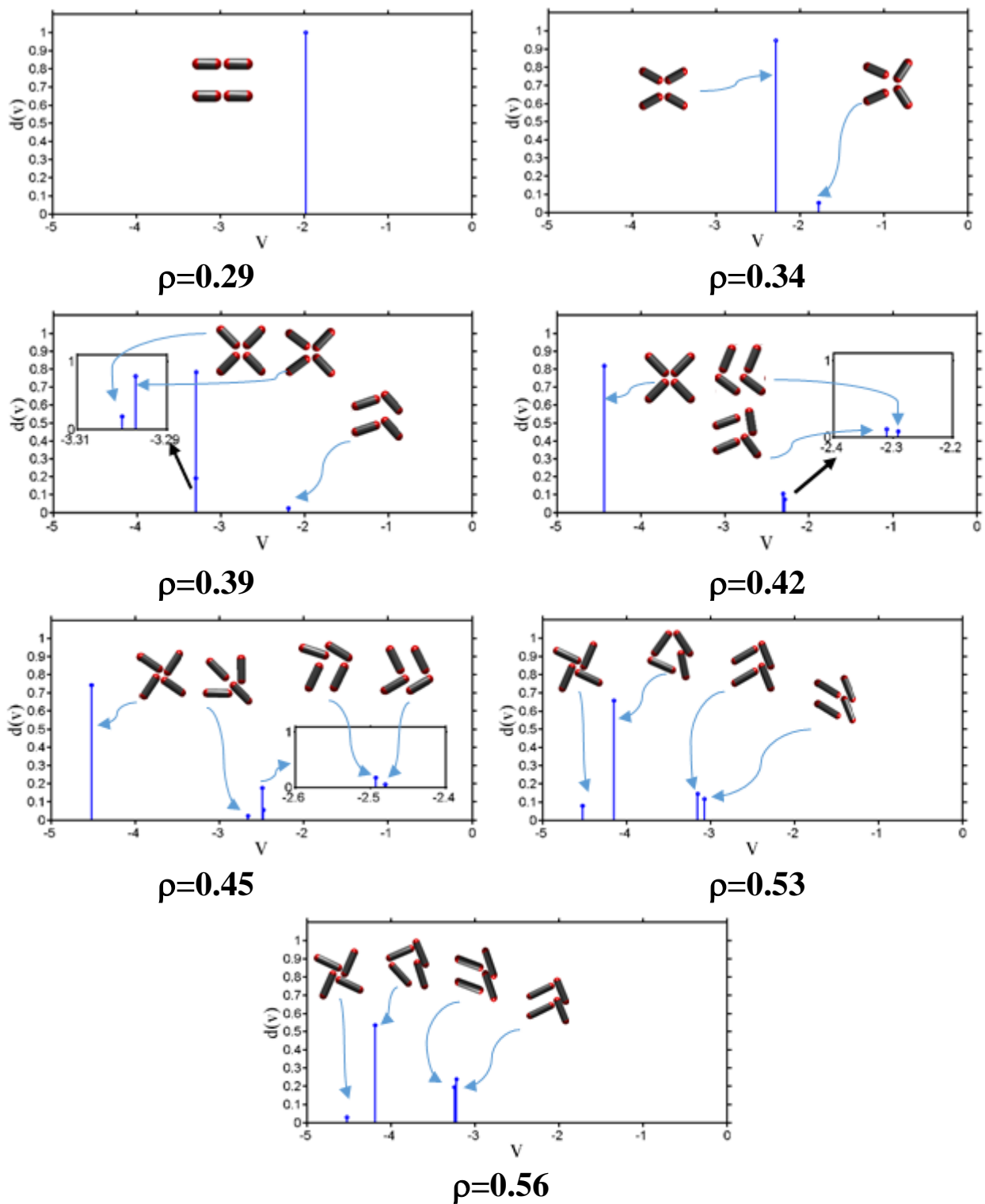


Figure III-9: Probability of reaching local minima for LJ potential with $r_e=0.40$, and various values of ρ .

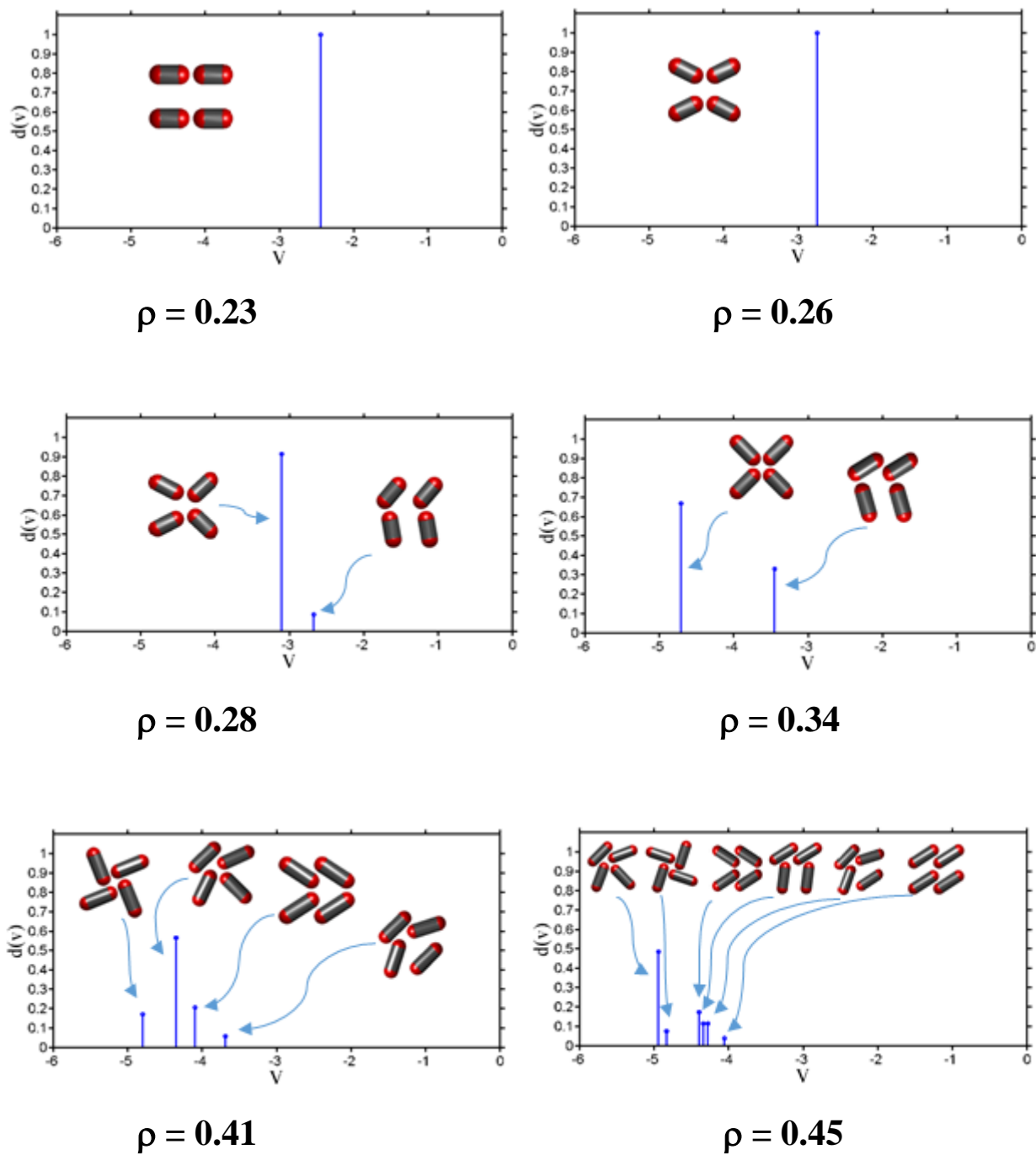


Figure III-10: Probability of reaching local minima for LJ potential with $r_e = 0.52$, and various values of ρ .

III.3.c Parameter Phase Diagrams for Other Potentials.

While the Lennard-Jones potential is the most commonly employed site-to-site potential, the Morse potential has also been used effectively in gas-phase cluster calculations. The Morse potential has the advantage that it has an additional parameter (β , the “range” parameter) which can adjust how gradually the potential changes away from its minimum. As is discussed elsewhere, the primary effect of changing this parameter is to change the van der Waals radius, σ : σ increases with β , reaching a limit of $\sigma = r_e$ for very large values of β .

With this in mind, we have repeated several of the calculations carried out for the LJ potential with two different values of β . These are shown, together with the LJ parameter “phase diagram” in **Figure III-11**.

As can be seen from **Figure III-11**, the “phase diagram” is very similar in all three cases. The one region where we see the appearance of a geometry that is not a GM for the LJ potential is in the (unphysical) $r_e=0.7$ region of parameter space. The long stripe (LS) geometry is the GM for a small area of the parameter space here. To explain this, we show the $V(\rho)$, $V(\phi)$ diagrams for the three different potentials in **Figure III-12** and **Figure III-13** together with the “density of states” quenches at these parameter values **Figure III-14**.

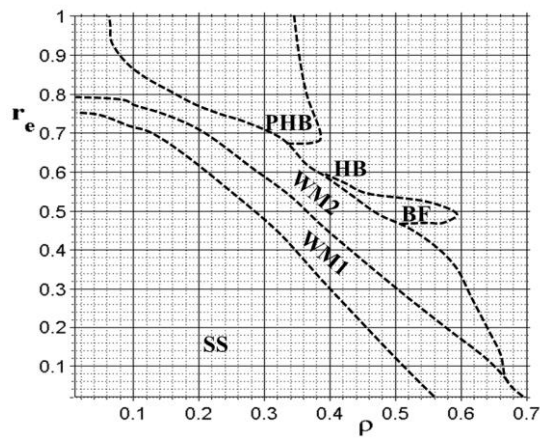
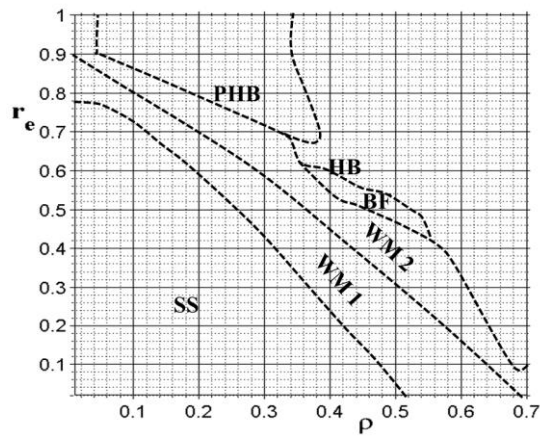
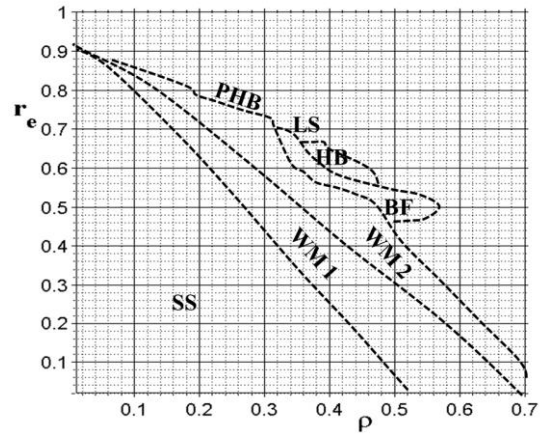


Figure III-11: Parameter “phase diagrams” for: (top) Morse, $\beta=20$; (middle) Morse, $\beta=10$; (bottom) LJ.

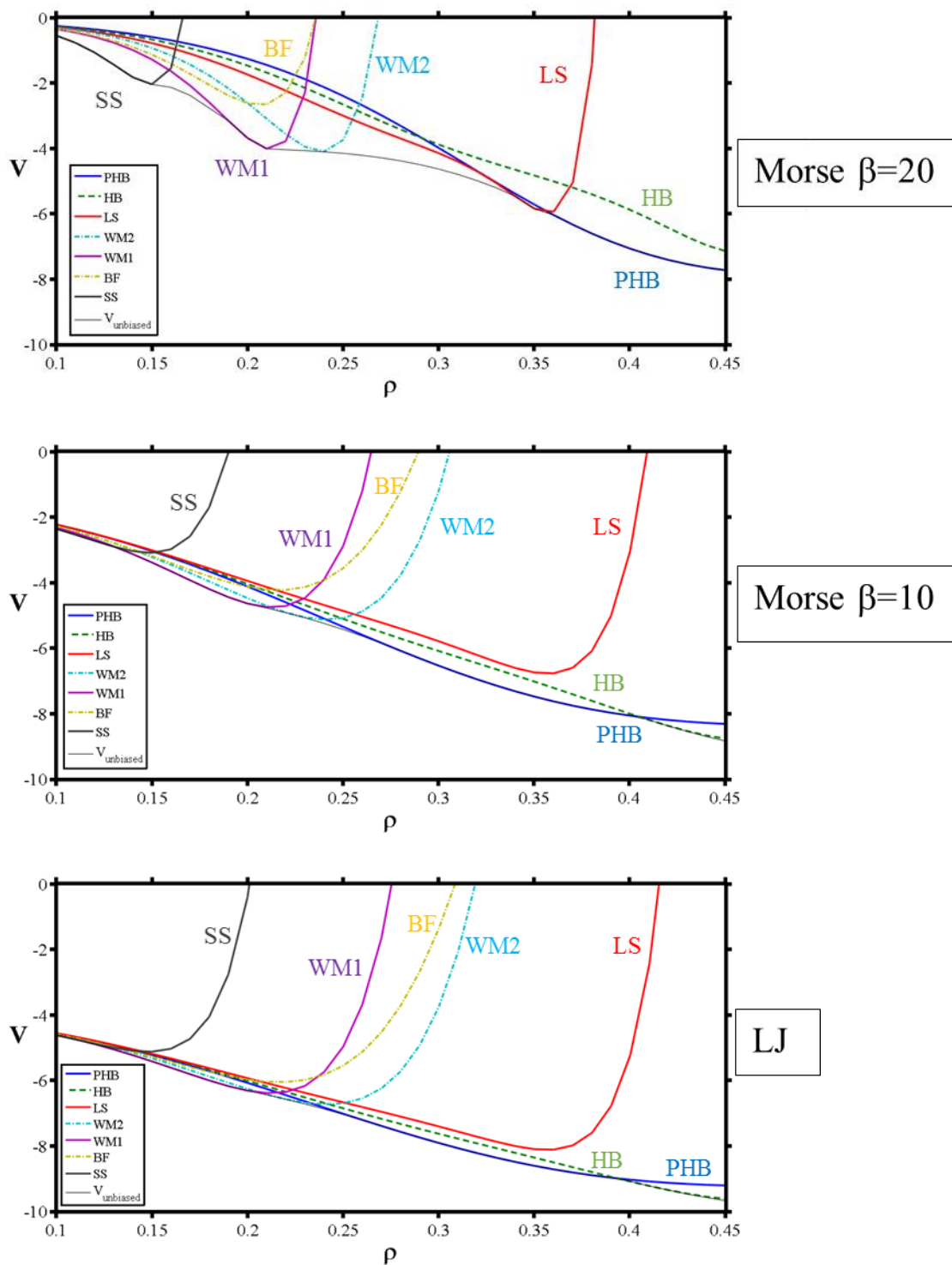


Figure III-12: The potential energy function $V(\rho)$ for the key geometries described in **Figure III-1**, for $r_e = 0.7$ for (upper panel) Morse ($\beta=20$); (middle panel) Morse ($\beta=10$); (bottom panel) LJ pair potentials. The solid gray line is the potential of the GM obtained through the unbiased search.

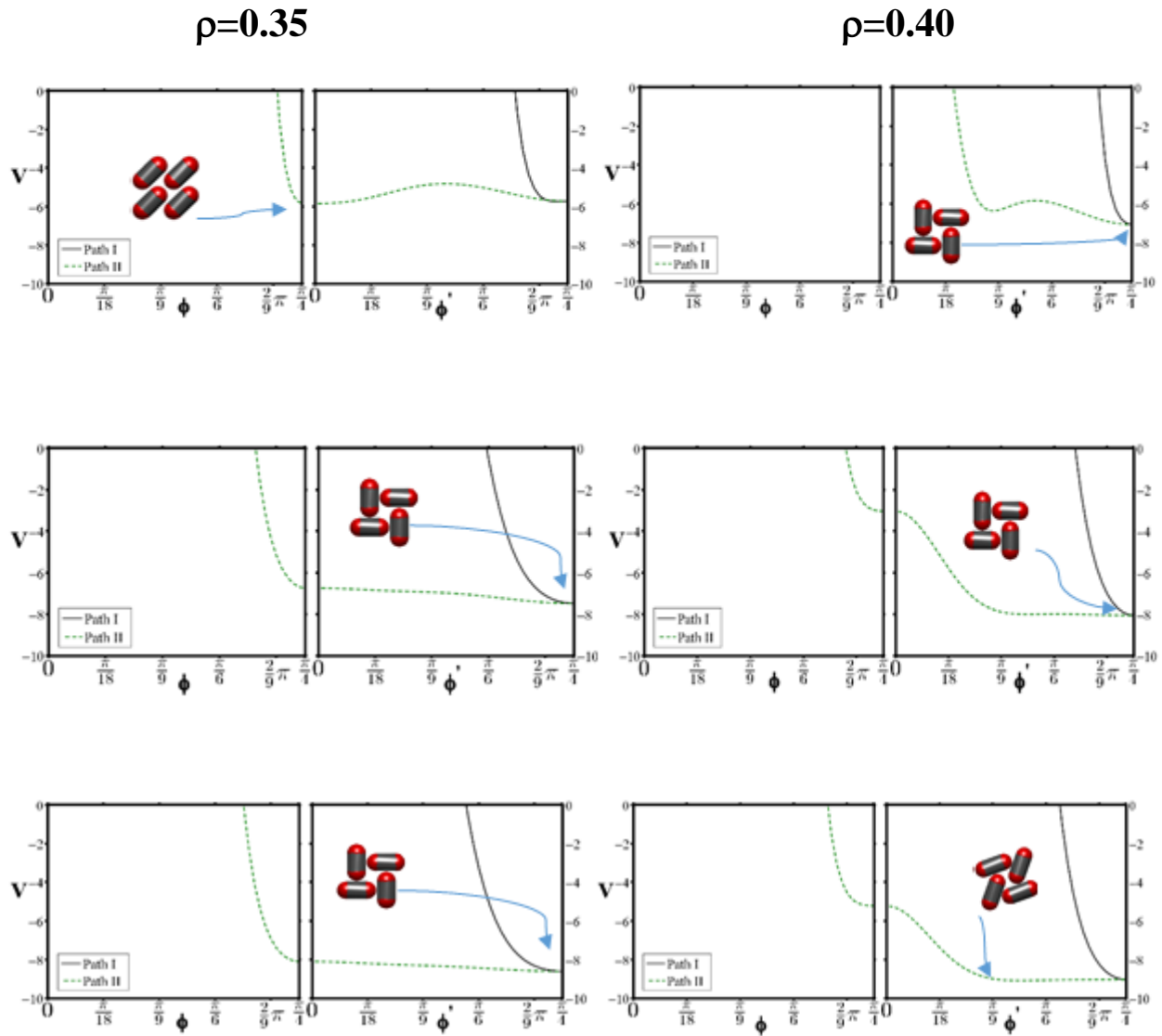


Figure III-13: $V(\phi)$ at $r_e = 0.70$ with two different values of ρ for different pair potentials. The pair potentials are: (upper panel) Morse ($\beta=20$) (middle panel) Morse ($\beta=10$) and (lower panel) Lennard-Jones. The global minimum is indicated by a cartoon.

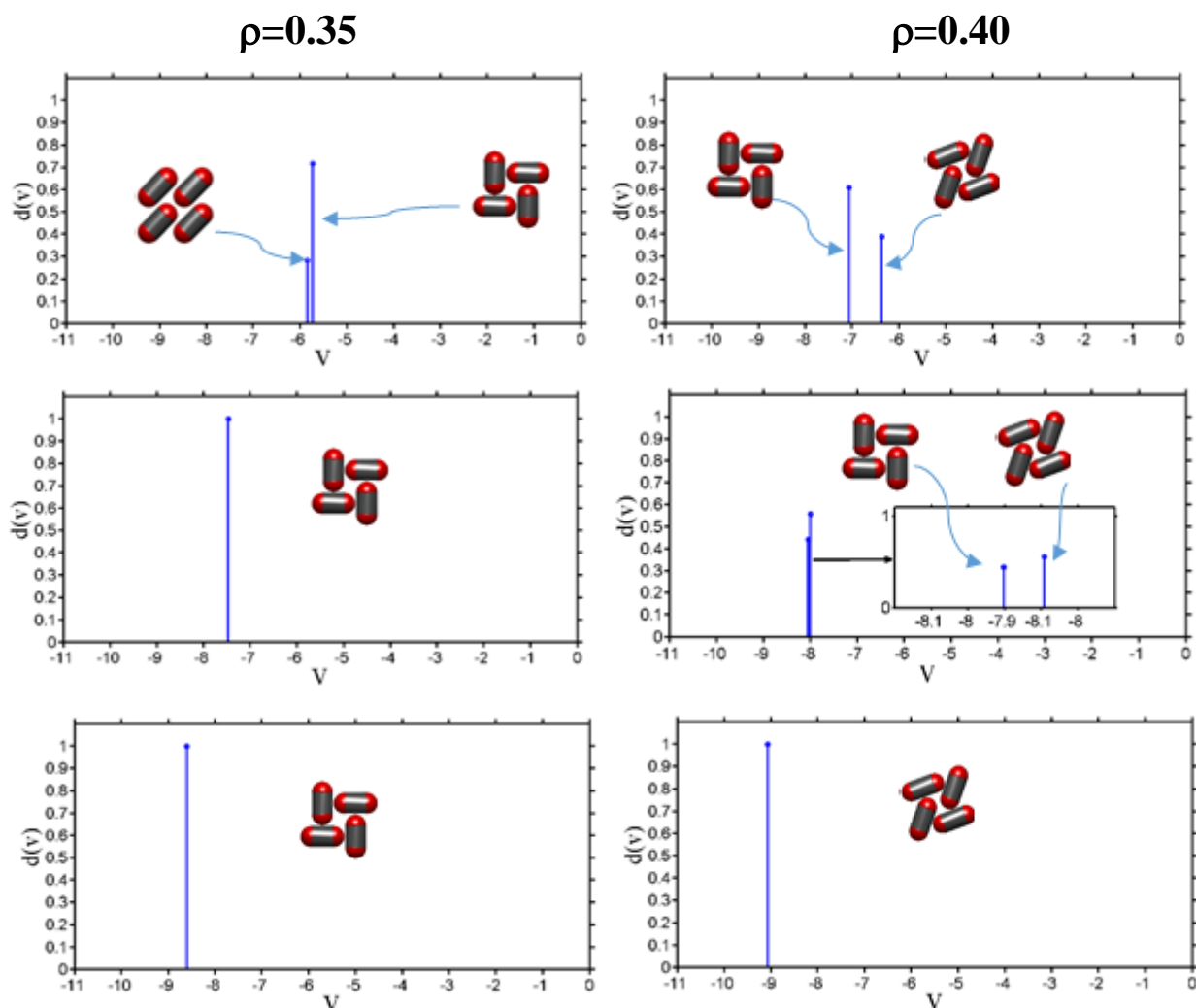


Figure III-14: Probability of reaching local minima for $r_e=0.7$, at ρ values of 0.35 and 0.40. The pair potentials are: (upper panel) Morse ($\beta=20$) (middle panel) Morse ($\beta=10$) and (lower panel) Lennard-Jones.

In **Figure III-12**, $V(\rho)$, that of a representative herringbone (HB) key geometry is presented, since this is an important motif in this region of parameter space. As can be seen from **Figure III-12**, decreasing σ has the effect of straining any given geometry at a smaller value of ρ . It can be seen that, although the differences in energy are very slight, the long stripe (LS) is marginally more attractive than the herringbone family of geometries for the Morse ($\beta=20$) potential. Thus, in principle, slight massaging of the pair potential can lead to dramatic changes in

the preferred geometry. This point is also made clear in **Figures III-13** and **Figure III-14**, where it is shown that for the Morse ($\beta=20$) potential alone, and in a limited region of parameter space, the LS competes with the herringbone geometries.

III.4 Ditopic Molecule on Square Lattice (All Lattice Sites are Occupied) Conclusions and Comments

We have systematically investigated a system of rigid ditopic rotor model molecules forming a monolayer on a square lattice as a function of both the interaction distance (r_e) and molecular size (ρ). Most of the work involved the use of a pairwise Lennard-Jones potential. The effect of a different pair potential (the Morse potential) was also investigated. For physically realistic systems ($\rho/r_e > 1$) we find that 2-center intermolecular “bonds” dominate for low ρ/r_e ratios, and this pattern is designated as the (short) stripe. The short stripe (or “ribbon”) is the dominant motif for linear ditopic molecules interact via hydrogen-bonding groups at the tips of the molecule (for instance, terephthalic acid by Clair et al (132)).

For larger values of the ρ/r_e ratio, the most common motif involves 4-center intermolecular interactions, with the pattern buckling to become chiral at the highest values. These we label “windmill” (WM) geometries, and they have been observed experimentally. (We use WM1 to denote the achiral version; WM2 the chiral version.) This motif has been observed experimentally by Lindroth et al (6, 7, 88-90). They studied the geometries of an adlayer of oligo-phenylene-ethynylene derivatives (which we could classify as linear ditopic molecules) on Au(111). Similar structures have been reported using dicyanobenzene (91) and oligo(p-phenylenevinylene) (133) molecules as adsorbate.

For large r_e (0.5-0.7) values, ($\rho/r_e < 1$, and the model’s relationship with molecular systems is tenuous) the main geometries are the herringbone adlayers. The dominant structures here are the

herringbone (HB and PHB). The former has been observed experimentally in a packed layer of triphenyl-dinitrile adsorbate on Ag(111) surface (91, 134). While the latter has been located for symmetric linear BDA (4,4'-biphenyldicarboxylic) on a square surface Cu(100) (135). For an extremely “rugged” potential (Morse, with $\beta=20$) we located the long stripe (LS) as a global minimum in a small area of parameter space. Similar geometries have been observed in the experimental literature; in particular the brick wall geometry of a highly dense adlayer of para-oligo-phenylene-ethynylene on Au(111) surface (6, 7).

In conclusion we have located the most stable geometries for linear molecules on a square lattice interacting with anisotropic potential energy. We have noticed that the geometries of the adlayer depend on the property of the potential, (such as the softness parameter β). The richest variety of adlayer patterns are obtained for $r_e=0.4-0.7$, and with small differences between the Morse ($\beta=10$) and Lennard-Jones potentials. Highly symmetric long stripe “LS” geometries can be attained for low ρ/r_e ratios in the case of the most rugged Morse potential ($\beta=20$). By contrast, we find that chiral adlayers (such as windmill “WM2”) will be ubiquitous for high ρ/r_e ratios.

Chapter IV

A Model Study of Adlayer Geometries of Rigid Ditopic Molecules on a Triangular Lattice

IV.1 Introduction

Several studies have reported ground states of self-assembled layers of rigid linear molecules on a triangular lattice (29, 92, 93, 136, 137). For instance, Mederos et al used Monte Carlo simulation to study the self-assembly of rigid ditopic molecules on a triangular lattice (137). The study has been done with the molecules fixed at the sites of the triangular lattice allowing the molecules to rotate around the axis normal to the surface plane. They have reported two ordered GM adlayer patterns. These include structures of a herringbone with two different orientational angles (it has the AABB form, see **Chapter II** for details), and a pinwheel phase with vacancies in one fourth of the lattice sites. Although the authors did not mention it, the pinwheel structure is chiral.

Berezutskiy and Lawrence-Hurt also studied the self-assembly of rigid linear molecules on a triangular lattice (115, 138). Both have reported the effect of the variations in the intermolecular distance parameters of the adsorbate itself on the adlayer geometry. For instance, Berezutskiy (115) studied a 2X2 unit cell angle space and applied tessellation by translation (see **Chapter II** for more details) to represent an infinite lattice space. While Lawrence-Hurt (138) studied a large angular space and applied the same tessellation method as described in **Chapter II**. In general both have reported the same geometries except for small regions of the intermolecular parameters. So one of our goals was to study the effect of the lattice size on the adlayer structure. Also we add more orientational order parameters than were used by Berezutskiy (115).

As mentioned in the previous chapters the goal of this chapter is to study the self-assembly adlayer of a ditopic molecule on a hexagonal (triangular) lattice. We expect to find several new geometries other than the geometries on a square lattice, due to the strain of the lattice site geometry, that is, the ability to occupy the most favorable geometry. The method and model substrate are described in **Chapter II** and **Appendix A**. In our work we have been able to identify previously observed geometries such as the herringbone and the pinwheel geometries and several new ground state geometries (which will be explained in detail).

The method is presented in **Section IV-2** including the energy landscape, the orientational order parameters and the key geometries found. Our results and discussions are presented in **Section IV-3.a** in which we present the full energy landscape “parameter phase diagram” results, with the geometries shown in a contour plot as a function of (ρ, r_e) . In **Section IV-3.b** we show results for a larger unit 4X4 cell. Conclusions and comparison with previous theoretical and experimental data appear in **Section IV-4**.

IV.2 Method

IV.2.a Energy Landscape

As discussed in Chapter II, the search is restricted to the (2x2) “unit cell” space, $[\theta_1, \theta_2, \theta_3, \theta_4]$ with the full adlayer generated by tessellation. The potential energy $V(\theta_1, \theta_2, \theta_3, \theta_4)$ is explored for each point in parameter space by methods described more fully in **Appendix A**. The principal results reported are the global minima (GM) of the potential energy.

IV.2.b Orientational Order Parameters

In order to classify the adlayer geometries, several order parameters were employed. The ideas behind the order parameters were presented in Chapter II. Here, we use the following four order parameters to differentiate between the geometries.

$$\Psi_3^{|c|} = \frac{1}{4} \sum_i |\cos(3\theta_i)| \quad \text{IV-1}$$

$$\Psi_3^{|s|} = \frac{1}{4} \sum_i |\sin(3\theta_i)| \quad \text{IV-2}$$

$$|\Psi_6^c| = \frac{1}{4} \left| \sum_i \cos(6\theta_i) \right| \quad \text{IV-3}$$

$$|\Psi_6^s| = \frac{1}{4} \left| \sum_i \sin(6\theta_i) \right| \quad \text{IV-4}$$

where θ_i are the angles of the unit cell.

IV.2.c Key Geometries

We need to identify the key adlayer geometries which will be used to construct the “parameter phase diagram.” These are obtained using preliminary investigations. We have chosen to focus on **nine** key adlayer geometries in this chapter. These are shown in **Figure IV-1**. In most cases, these correspond to the parameters at which the geometry is the true GM.

We discuss each of these adlayer geometries briefly below.

- (a) The perfect herringbone “PHB” structure with p2mm symmetry.

- (b) The short stripe “SS” structure with c2mm symmetry and orientational angles all the same $\{0\} \equiv \left\{\frac{\pi}{3}\right\}$.
- (c) The distorted short stripe “DSS” with p2gg symmetry.
- (d) The honeycomb “HC” geometry as it has a hexagonal porous shape and has c2mm symmetry.
- (e) The pinwheel “PW” pattern has p2 symmetry group.
- (f) The butterfly “BF” pattern has c2mm symmetry.
- (g) The herringbone 1 “HB1” pattern has p2 symmetry.
- (h) The herringbone 2 “HB2” pattern has p2gg symmetry.

The geometries that possess no mirror plane such as PW and HB1 are homochiral. These geometries will be discussed in detail in the next sections.

These particular geometries were chosen since they illustrate the major intermolecular “bonding” motifs that are possible. The “stripes” show 2-center bonds. The “honeycomb” demonstrates 3-center bonds. Other geometries were identified in our exploration, and are discussed more fully in the Results and Discussion section.

The nearest neighbor “NN” site-to-site distances as a function of ρ , $s(\rho)$, for the selected main geometries are shown in **Figure IV-2** and **Table IV-1**. The symmetry and abbreviation keys are described in **Table-IV-2** as well.

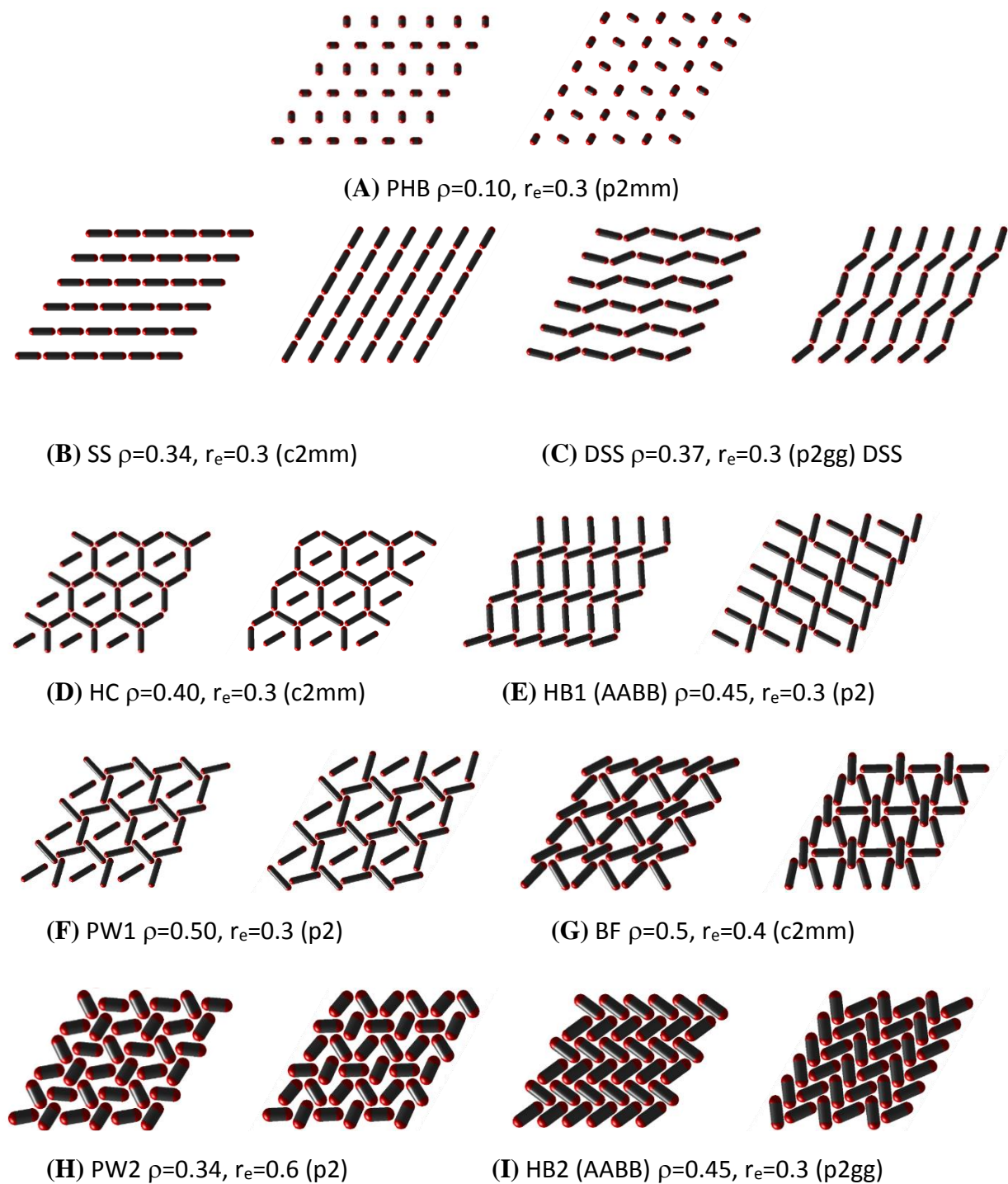


Figure IV-1: Structure of the ground state key patterns for different ρ and r_e . The abbreviations are described in **Table IV-2**. In parenthesis are the symmetry wall paper group (explained in details Appendix C).

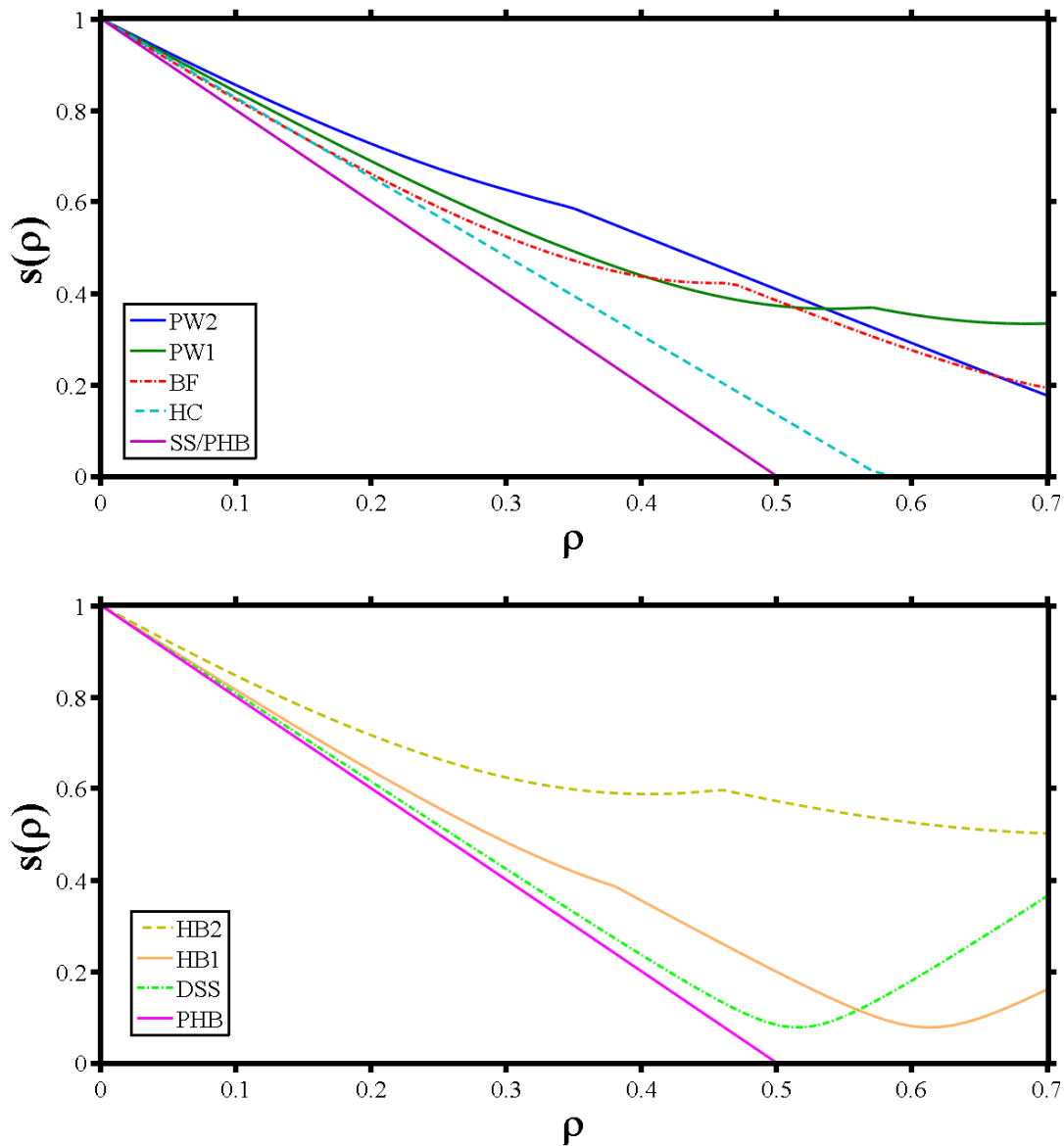


Figure IV-2: The nearest-neighbor site-site distance, $s(\rho)$, as a function of molecule length, ρ , for chosen fixed geometries. Upper panel are the pinwheel 2 “PW2”, pinwheel 1 “PW1”, butterfly “BF”, honeycomb “HC”, and the short stripe “SS”. The lower panel are the herringbone family: herringbone 2 “HB2”, herringbone 1 “HB1”, distorted short stripe “DSS” and perfect herringbone “PHB”. The geometry labels are described in **Table IV- 2** and shown in **Figures IV-3, 4, 5**. Note: the PW2 orientational angles = $[2, 65, 50, 123]^\circ$, the PW1 angles = $[8, 126, 69, 33]^\circ$, the BF angles = $[\pi/2, 0, 4\pi/9, 5\pi/9]$, The HB2 angles = $\{\pi/5, 4\pi/5\}$, the HB1 angles = $\{20, 91\}^\circ$, the DSS angles = $\{170, 15\}^\circ$.

Table IV-1: Closest nearest-neighbor (NN) site-site distance, s , for specified geometry as a function of ρ . Including the number of nearest-neighbor. HB2 angles = $\{\pi/5, 4\pi/5\}$. BF angles = $[\pi/2, 0, 4\pi/9, 5\pi/9]$. The abbreviations are described in **Table IV-2**.

Geometry	site-site distances	Number of nearest-neighbors NN (N_i)
SS	$s(\rho) = 1 - 2\rho$	2
PHB	$s(\rho) = 1 - 2\rho$	1
BF	$s(\rho)$ $= \min \left(\sqrt{1 - \rho \left(\sqrt{3} + \cos \frac{4\pi}{9} + \sqrt{3} \sin \frac{4\pi}{9} \right) + 2\rho^2 \left(\sin \frac{4\pi}{9} + 1 \right)}, \sqrt{1 - \rho \left(1 - \cos \frac{4\pi}{9} + \sqrt{3} \sin \frac{4\pi}{9} \right) + 2\rho^2 \left(1 - \cos \frac{4\pi}{9} \right)} \right)$	2,2
HC	$s(\rho) = 1 - \sqrt{3}\rho$	3
HB2	$s(\rho)$ $= \min \left(\sqrt{1 - 4\rho \cos \frac{\pi}{5} + 4\rho^2}, \sqrt{1 - 2\sqrt{3}\rho \sin \frac{\pi}{5} + 4\rho^2 (\sin \frac{\pi}{5})^2} \right)$	2,4
DSS		2
HB1		1, 2
PW1		3
PW2		3

Table IV-2: Geometry name, abbreviation and symmetry plane group of the adlayers on a triangular lattice. See **Figures IV-2**, for geometries, and Appendix C for symmetry plane groups.

Geometry name	Abbreviation	Symmetry plane group
Perfect herringbone	PHB	p2mm
Short stripe	SS	c2mm
Distorted short stripe	DSS	p2gg
Honeycomb	HC	c2mm
Herringbone 1	HB1	p2
Pinwheel 1	PW1	p2
Butterfly	BF	c2mm
Pinwheel 2	PW2	p2
Herringbone 2	HB2	p2gg

IV.3 Results and Discussion for a Triangular Lattice

IV.3.a Parameter “Phase Diagram” for the Lennard-Jones Potential

The Lennard-Jones potential energy was minimized for all points in the (ρ, r_e) parameter space. Once the minimum energy geometry is obtained, we can obtain the orientational order parameters from the values of the angles. The potential energy, Ψ_3^{cl} , Ψ_3^{sl} , $|\Psi_6^c|$, and $|\Psi_6^s|$ are shown as contour plots in **Figure IV-3 (b), (c), (d), (e), and (f)** respectively. In order to assign geometries, a visual inspection was carried out and NN counts taken (SS, DSS, BF, and HB2 have two NN; PHB, and HB1 have one; HC, PW1 and PW2 have three), (see **Table IV-1**).

Also we used the order parameters to distinguish between patterns. We notice from **Figure IV-3 (c), (d), (e), and (f)**, the following areas. The PHB pattern has $\Psi_3^{cl} = \Psi_3^{sl} = 1/2$ and $|\Psi_6^c| = |\Psi_6^s| = 0$; the SS has $\Psi_3^{cl} = |\Psi_6^c| = 1$ and $\Psi_3^{sl} = |\Psi_6^s| = 0$; the HC has $\Psi_3^{cl} = |\Psi_6^s| = 0$ and $\Psi_3^{sl} = |\Psi_6^c| = 1$. The other geometries have order parameter values which fluctuate between zero and unity. For instance, the HB2 pattern (AABB; see Chapter II), with orientational angles $\{42, 138\}^\circ$, has $\Psi_3^{cl} \approx 0.7$ and $|\Psi_6^c| \approx 0.3$, while HB2 $\{146, 34\}^\circ$ has $\Psi_3^{cl} \approx 0.2$ and $|\Psi_6^c| \approx 0.9$.

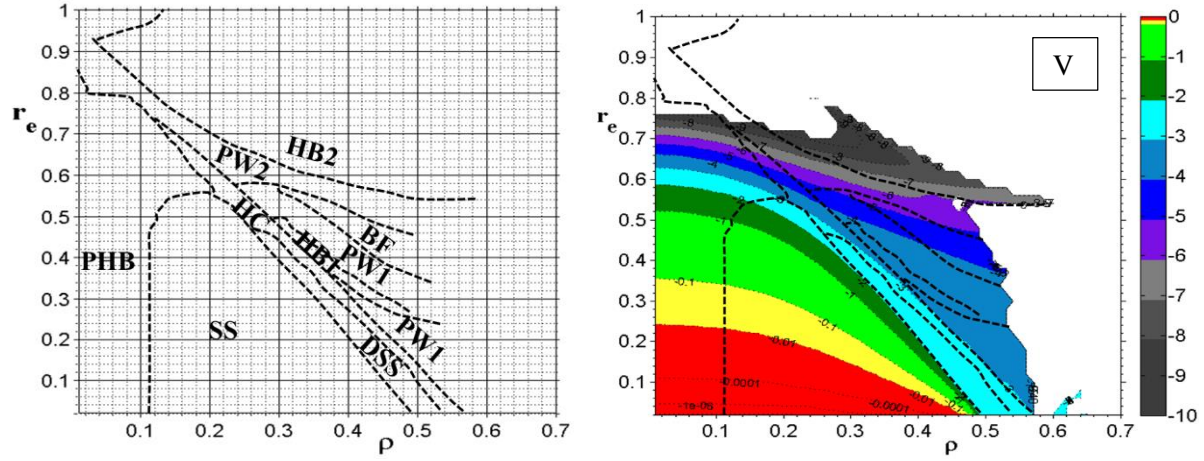
The chirality of the adlayer can be detected by the $|\Psi_6^s|$ order parameter, see **Figure IV-3(f)**. All the patterns such as PW, and HB1 that have a non-zero value of $|\Psi_6^s|$ are chiral because they possess no mirror plane as mentioned earlier. All the patterns such as PHB, HC, HB2, BF and DSS with zero value of $|\Psi_6^s|$ are achiral; they all possess at least one mirror plane of symmetry.

The results are summarized as the “parameter phase diagram” in **Figure IV-3 (a)**. The dashed lines on the other contour plots show the boundaries that were established for the phase diagram. (These are not true phase changes – or even phase transformations—since the energy changes smoothly as the parameters are changed. However, uniquely demarking the dominant

geometry in each region of the parameter space allows us to understand the role played by the parameters.) This “phase diagram” is the principal finding for this chapter.

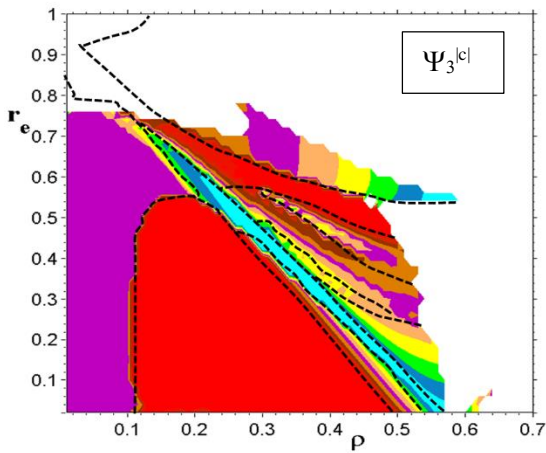
In order to understand the phase diagram, we consider the following plots of $V(s(\rho))$ for three different values of r_e , (**Figure IV-4**). In these figures, the parameter r_e is fixed, the geometry is fixed by holding the appropriate angles constant, and the potential energy as a function of ρ is plotted. Also shown on the figure is the potential energy found in the full (unbiased) search of the angle space described above at a given set of parameter values. This is labeled V_{unbiased} .

For short rotors the global minimum is the PHB. Looking back to the $s(\rho)$ graph, **Figure IV-2**, the s for both SS and PHB are degenerate. However by a small energetic difference the PHB is the global minimum because of its s_2 (which the second nearest neighbor) is closer to the potential well than the one for the SS, see the radial distribution function “RDF” of ($\rho=0.1$, $r_e=0.3$) **Figure IV-5** (for details on how to construct the RDF see **Chapter II** and Appendix A.III). By $0.25 < \rho < 0.35$ (see **Figure IV-4(C)**) the global minimum is clearly the SS as the $s(\rho)$ becomes closer to the value of $r_e=0.3$. An example at $\rho=0.35$ of the RDF is shown in **Figure IV-5** which show that the number of nearest neighbor, $N_1=2$, of the SS pattern is located in the potential well, while the $N_1=1$ of the case of PHB. The SS geometry, however, becomes strained and untenable as ρ increases and the geometry buckles to a DSS pattern. The honeycomb (HC) is favored for intermediate values of ρ , since this geometry achieves 3-center intermolecular “bonds”, while avoiding the short 2-center “bonds” typical of the short stripe and distorted short stripe. As ρ further increases, this geometry too becomes strained, and the pattern distorts away from the $c2mm$ symmetry to the pinwheel structure. However, as can be seen, it retains its threefold symmetry, maintaining the $p2$ symmetry up to very large values of ρ .

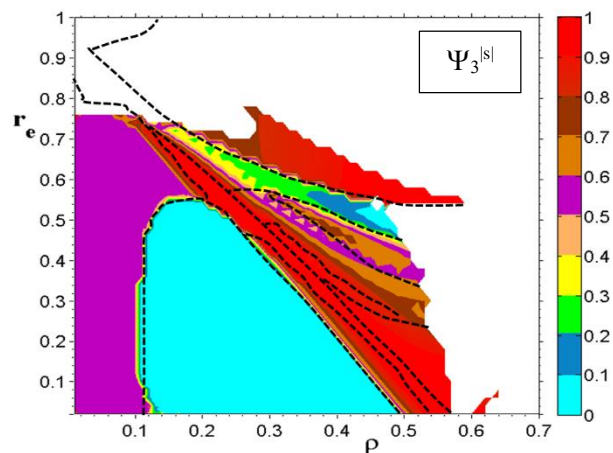


(a)

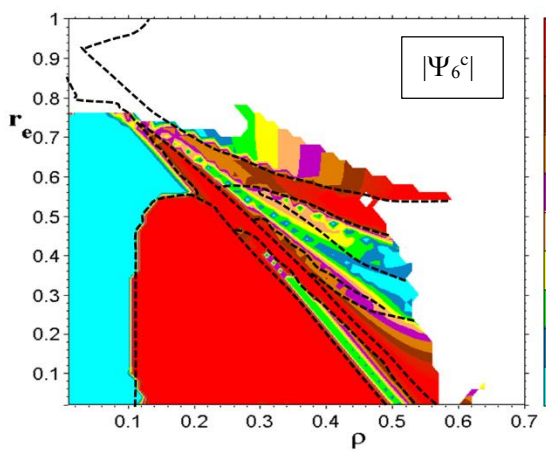
(b)



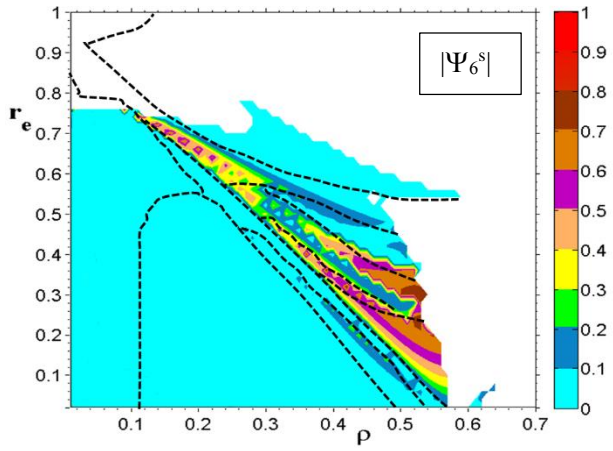
(c)



(d)



(e)



(f)

Figure IV-3: a) The adlayer GM geometries “ phase diagram” as a function of ρ , and r_e , b) The contour plots potential energy $V(\rho, r_e)$, c) Order parameter $\Psi_3^{|c|}$, d) Order parameter $\Psi_3^{|s|}$, e) Order parameter $|\Psi_6^c|$, f) Order parameter $|\Psi_6^s|$. The labeling of the geometries PHB, SS, DSS, HC, HB, BF and PW are shown in **Table IV-2**. The geometries are shown in **Figures IV-1**. In each plots the color bars show the values of the contours.

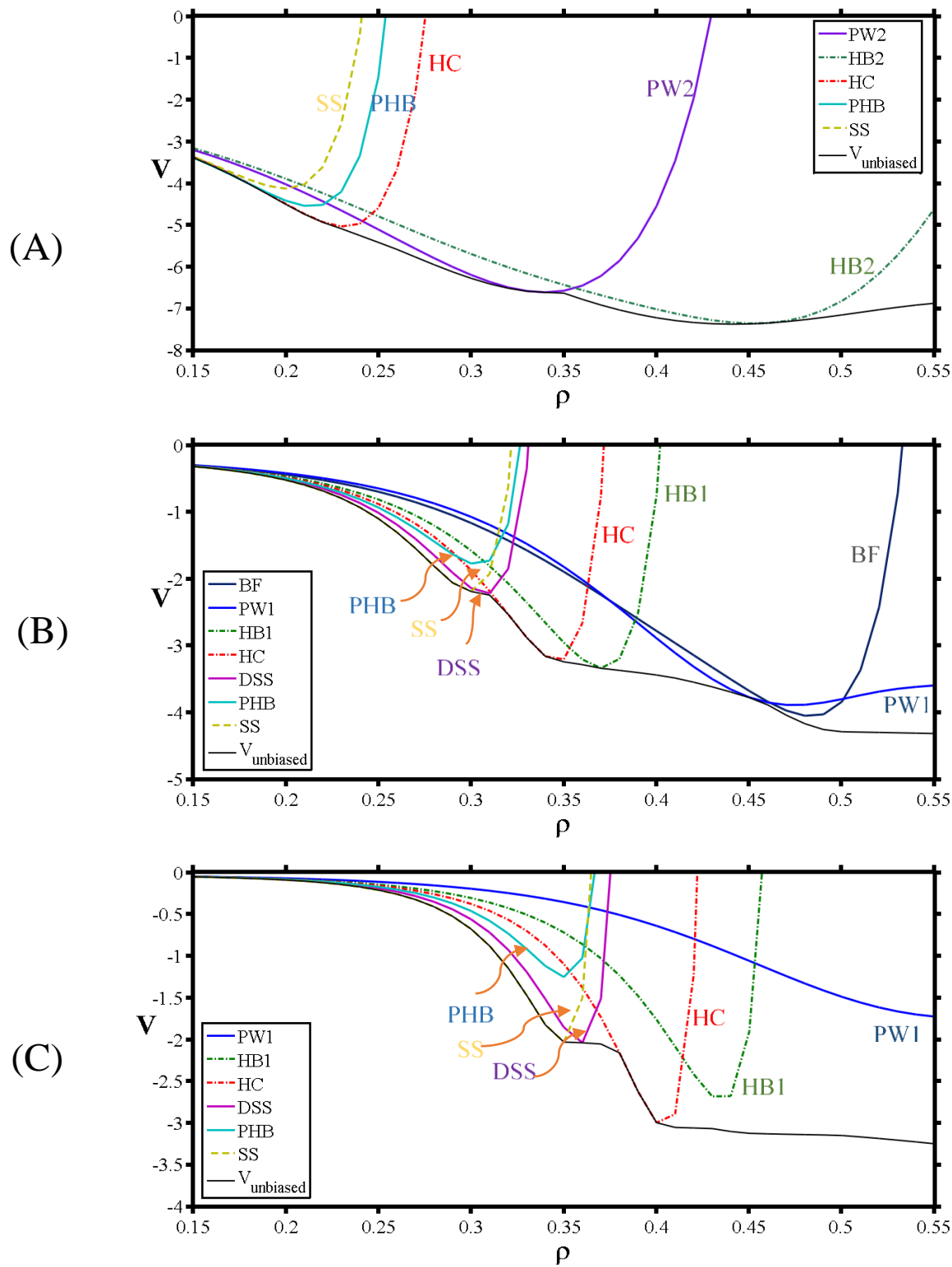


Figure IV-4: Plots of $V(s(\rho))$ for the Lennard-Jones potential for the geometries observed in **Figure IV-1**. (A) Upper panel $r_e = 0.6$; (B) Middle panel, $r_e = 0.4$; (C) Lower panel, $r_e = 0.3$. Note: The DSS angles = $\{170\ 15\}^\circ$

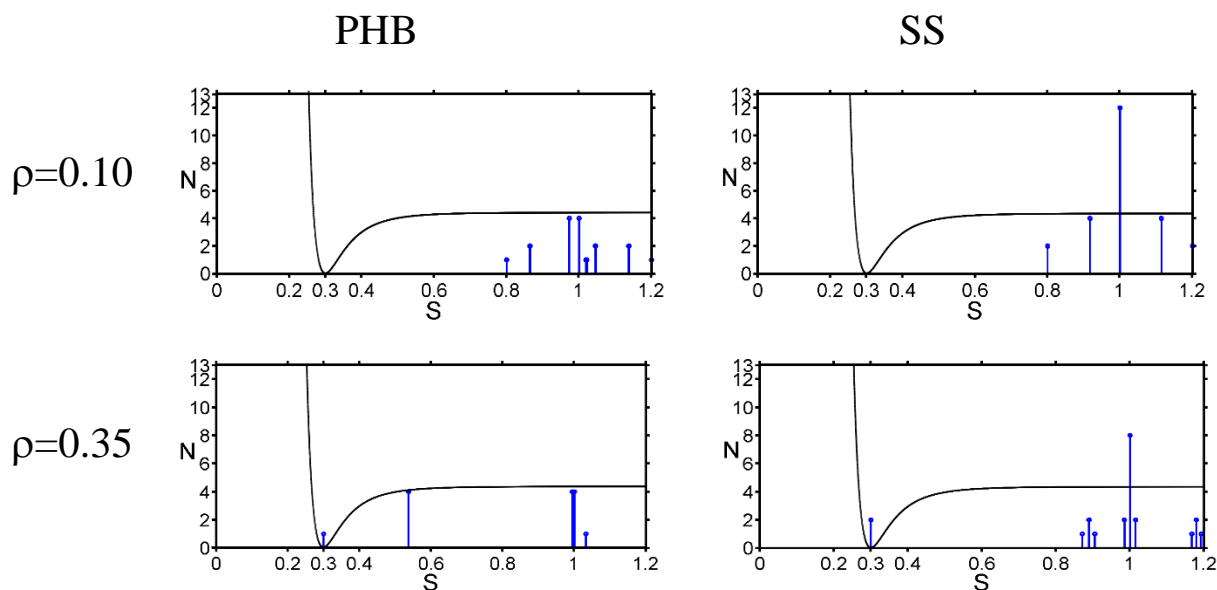


Figure IV-5: The radial distribution function of perfect herringbone “PHB” and short stripe “SS” for two different rotor length $\rho=0.1$ and 0.35 at constant $r_e=0.3$. The black line is the Lennard-Jones potential at $r_e=0.3$.

By increasing the $r_e=0.4$, **Figure IV-4(B)**, two new geometries become accessible as GM which are the chiral herringbone “HB1” and the butterfly “BF”. Upon further increasing $r_e=0.6$, **Figure IV-4(A)**, we notice the pinwheel “PW2” and the achiral herringbone “HB2” patterns as global minima.

IV.3.b Special case $\rho=0.5$, $r_e=0.4$ (4X4 unit cell)

Lawrence-Hurt has studied a larger cluster with a 3X3 unit cell on triangular lattice sites using the Morse potential (138). He reported a GM geometry at around $\rho=0.5$, $r_e=0.4$ other than what we found in this study. He called it a triangle geometry because it has triangular porous shape. Accordingly, to investigate whether the 2X2 unit cell represents a large space lattice we conducted the same method of minimization using a larger (4X4) lattice with an example system $V(r_e=0.4$, $\rho=0.5$).

Two geometries which have been located are the global minimum butterfly “BF”, and pinwheel “PW” local minimum. The geometries are shown in **Figure VI-12**. These same GM was found by using the smaller 2X2 unit cell.

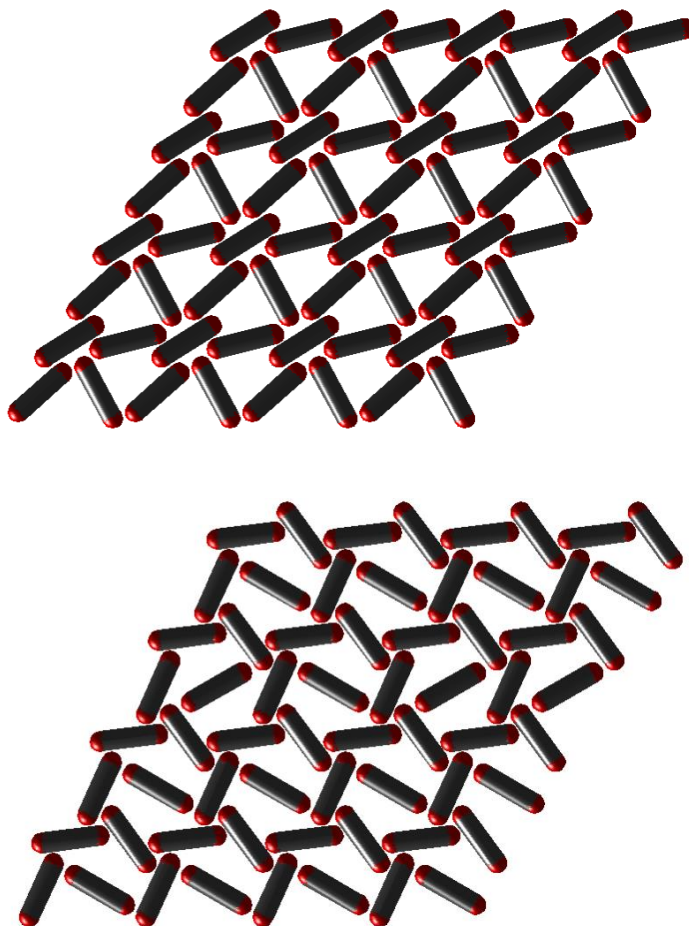


Figure IV-6: A) The global minimum “BF” upper panel, and (B) local minimum “PW” of a 4X4 unit cell at $r_e=0.4$, and $\rho=0.5$.

IV.4 Conclusions and comments on the Adlayers of the Ditopic Molecule on a Triangular Lattice

We have investigated the ground state energy and the structure of a rigid ditopic model molecule “rotor” on a triangular lattice as a function of both the interaction distance r_e and the molecular size ρ . All of the work involved the use of a pairwise Lennard-Jones potential. We have noticed that for low ρ and r_e the most stable structures are the ones which have 2-center

intermolecular interactions, with these patterns designated as the short stripe “SS” and perfect herringbone “PHB”. The short stripe “SS” structure can be related to the brick wall structure of 1,4 bis(phenyl(ethynyl))benzene on a Au(111) surface (90). The same structure has been reported by Fortuna et al (139), in which they have simulated the self-assembly of terephthalic acid, driven by hydrogen bonding, on a graphite surface (140).

For larger values of the ρ/r_e ratio, the most common motif involves 3-center intermolecular interactions, with the pattern buckling to become chiral at the highest values. These are labeled honeycomb “HC” and pinwheel “PW”. The pinwheel structure which is a homochiral pattern has been reported by Marx et al, Hammonds et al and Mederos et al (93, 136, 137).

For the highest r_e values the main geometry we found is the herringbone 2 “HB2 AABB” (see **Chapter II** for details). Such a structure is reported in the theoretical studies of diatomic molecule on triangular lattice (29, 93, 137). The structure also has been reported by Pint et al (17), although they have studied linear hexane on a graphite surface using the coarse graining model.

The adlayer structures that we have reported mostly resemble the ones reported by Lawrence-Hurt and Berezutskiy (115, 138). With one exception Lawrence-Hurt reported a triangular “TR” GM pattern which we could not locate in this work. This could be due to, the fact that he used a Morse potential while we used a Lennard-Jones potential. Also we have additional order parameters, more than the one has been used by Berezutskiy, that can distinguish between the adlayer geometries.

In conclusion theoretical minimization can be used as a simple method to investigate the self-assembly of a linear molecule with an anisotropic potential energy on a solid surface. We have located structures that resemble previous studies. We have noticed that the pattern geometries

depend mainly on lattice properties (compared with the square lattice discussed in previous chapter) as well as the distance parameters such as the size (ρ) of the rotor and the site-to-site equilibrium distance (r_e) of the potential function.

Chapter V

A Model Study of Adlayer Geometries of Rigid Tritopic Molecules on Triangular and Square Substrates

V.1 Introduction

Several theoretical studies by Szabelski and his coworkers have considered tritopic molecule monolayer self-assembly on a solid surface (20, 22-24, 46). In these studies the effect of intermolecular and intramolecular distances on the morphology of the adlayer has been reported. With a drastic simplification of the coarse-graining potential that represents the interaction between the molecules, they have found a variety of patterns, some of which possess chiral nanoporous networks. All of their calculations were carried out with an intermolecular site-to-site interaction potential that was relatively short-ranged.

In our study we have used the same method described in **Chapter II** to study the effect of varying the length parameters of the Lennard-Jones potential on the pattern of the self-assembled adlayer of tritopic model molecules on square and triangular lattices.

The chapter is organized as follows. In **Section V.2** we present the results and discussion of the adlayer geometries found on triangular lattice. In **Section V.3** we address the conclusions and comments of the adlayer structures on triangular lattice. In **Section V.4** we present the results and discussion of the model molecule on square lattice. Finally, in **Section V.5** we show the conclusions and comments.

V.2 Result and discussion (Tritopic on a Triangular Lattice)

In order to interpret our results we suggest three key geometries, shown in **Figure V-1**. These were obtained using preliminary investigations. The figure shows, a) the honeycomb “HC” (because it has a hexagonal pore site) has wallpaper symmetry $p3m1$ and orientational angle $\left\{\frac{\pi}{2}\right\} \equiv \left\{\frac{\pi}{6}\right\}$, b) the perfect chevron “PCh” has symmetry $p3m1$ and orientational angle $\{0\} \equiv \left\{\frac{\pi}{3}\right\}$, c) the reverse chevron “RCh” has symmetry $p2mg$ and orientational angle $\left\{0, \frac{\pi}{3}\right\}$. Note, the chevron family have the same orientational angle $\{\theta\}$ and $p3$ symmetry, one of which is the PCh has $\{0\} \equiv \left\{\frac{\pi}{3}\right\}$ geometry and $p3m1$ symmetry. Shown in the figure are the nearest neighbor NN site-to-site distances s as dashed red lines.

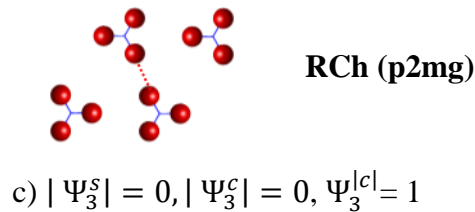
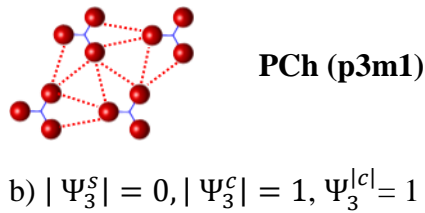
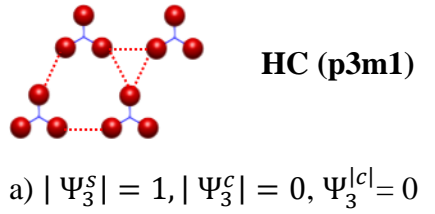


Figure V-1: Schematic representation of the three key geometries on a triangular lattice with the value of their order parameters $|\Psi_3^s|$, $|\Psi_3^c|$ and Ψ_3^{cl} , a) Honeycomb “HC”, b) Perfect Chevron “PCh”, c) Reverse Chevron “RCh”. Note: The dashed red lines are the nearest neighbor NN, site-to-site distances s (Values and the relationships, as a function of ρ , are shown in **Figure V-2** and **Table V-1**). In parenthesis are the wallpaper symmetry.

The NN distances $s(\rho)$ as a function of ρ for the key geometries are shown in **Figure V-2** and the relationships are identified in **Table V-1**.

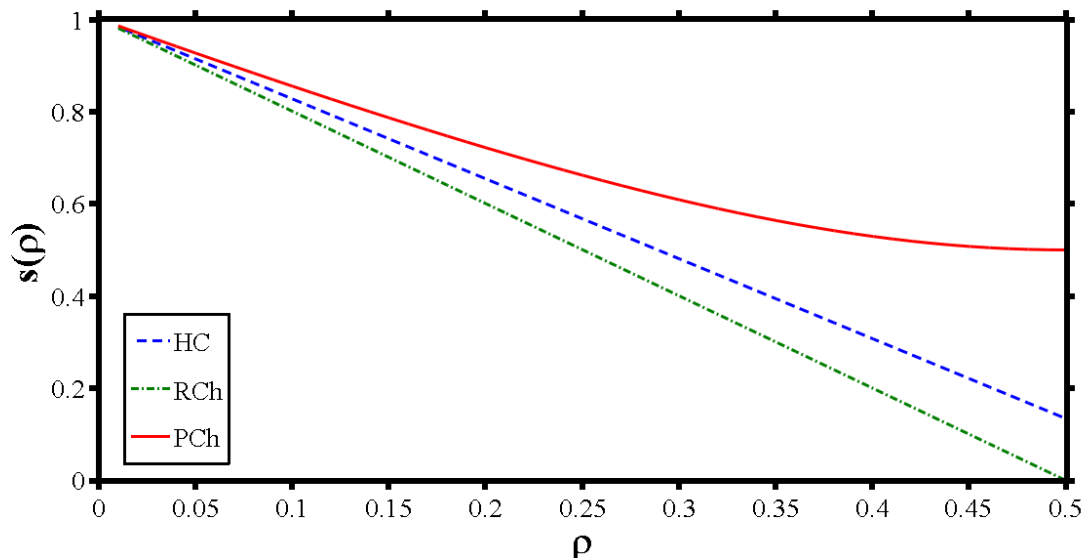


Figure V-2: the nearest-neighbor site-to-site distance, $s(\rho)$, as a function of molecule length, ρ , for the key geometries. The geometry labels HC, RCh and PCh stand for “Honeycomb”, “Reverse Chevron”, “Perfect Chevron”, **Figure V-2**. Note: The relationships are shown in **Table V-1**.

Table V-1: Closest nearest-neighbor (NN) site-to-site distance, s , for specified geometry on a triangular lattice as a function of ρ . Including the number of nearest-neighbor sites N_1 .

Geometry	site-to-site distances	Number of nearest-neighbors NN (N_1)
HC	$s(\rho) = 1 - \sqrt{3}\rho$	6
RCh	$s(\rho) = 1 - 2\rho$	2
PCh	$s(\rho) = \sqrt{1 - 3\rho + 3\rho^2}$	12

V.2.a Distortion Pathways

We also note that the geometries can be generated by a single distortion path starting from a certain geometry. Accordingly we suggest two arbitrary paths starting from the key honeycomb geometry in which all the orientational angles are $\frac{\pi}{2}$. These paths are shown in **Figure V-3**. In the figure, Path I, conrotatory of all rotors clockwise with angle $\{\phi\} \in [0, \frac{\pi}{3}]$; Path II disrotatory with angles $\{\phi, -\phi\} \in [0, \frac{\pi}{3}]$. (Note $\{\phi\} \in [0, \frac{\pi}{3}]$; is the rotatory angle and it is different from the

geometry abbreviation $\{\theta\}$). These paths will be used to explain the geometries that have been found in the unbiased minimizing of the potential $V(\rho, r_e)$ as a function of rotor length ρ and the equilibrium distance of the Lennard-Jones potential r_e .

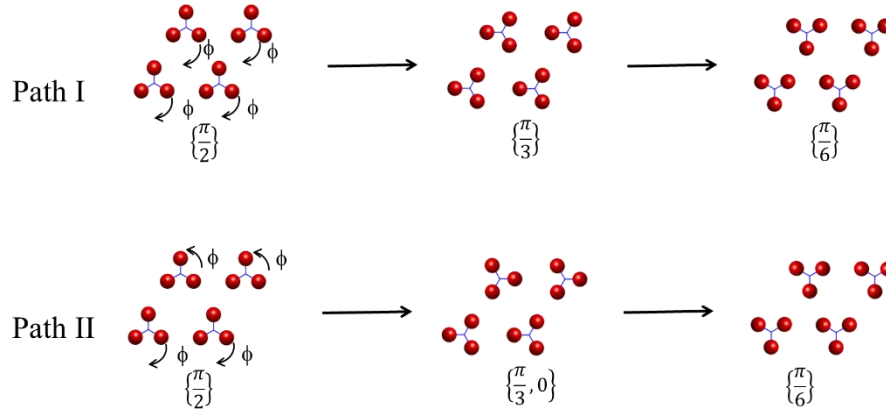


Figure V-3: Schemes of the suggested paths (see the text), Path I conrotatory $\{\phi\}$ starting with Honeycomb “HC” $\{\pi/2\}$ geometry and ends with HC $\{\pi/6\}$, Path II, disrotatory $\{\phi, -\phi\}$ starts with HC $\{\pi/2\}$ and ends with HC $\{\pi/6\}$. Note: rotatory paths $\{\phi\}$, $\{\phi, -\phi\}$ are different from geometry abbreviation $\{\theta\}$, under each geometry. Note: the paths are of geometries on a triangular lattice.

V.2.b Order parameters

To distinguish between the patterns we have used three order parameters. These order parameters have been used in the spirit of the idea discussed in chapter II.

$$|\Psi_3^s| = \left| \frac{1}{4} \sum_i \sin(3\theta_i) \right| \quad \text{V-1}$$

$$|\Psi_3^c| = \left| \frac{1}{4} \sum_i \cos(3\theta_i) \right| \quad \text{V-2}$$

$$\Psi_3^{|c|} = \frac{1}{4} \sum_i |\cos(3\theta_i)| \quad \text{V-3}$$

Where, $\theta_i \in \left[0, \frac{2\pi}{3}\right]$, are the angles of the unit cell rotors. We take the absolute value for the parameters because the angle is arbitrary. For instance the honeycomb “HC” geometry has two equivalent orientational angles, $\left\{\frac{\pi}{2}\right\} \equiv \left\{\frac{\pi}{6}\right\}$. The $\Psi_3^s = -1$ for the first “HC $_{\pi/2}$ ”, while $\Psi_3^s = 1$ for the second “HC $_{\pi/6}$ ”. On the other hand the perfect chevron “PCh” has also two equivalent orientational angles $\{0\} \equiv \left\{\frac{\pi}{3}\right\}$. The $\Psi_3^c = 1$ for the first “PCh $_0$ ”, while $\Psi_3^c = -1$ for the second “PCh $_{\pi/3}$ ”. The values of each order parameter are shown below the key geometries in **Figure V-1**. In **Figure V-4** we show the order parameters along the two arbitrary paths that has been described in **Figure V-3**.

In **Figure V-4**, we notice that the order parameters can distinguish between all of the key geometries and the patterns in between. For instance, see path I (**Figure V-4.A**) for honeycomb (HC) $\left\{\frac{\pi}{2}\right\} \equiv \left\{\frac{\pi}{6}\right\}$ the value of $|\Psi_3^s| = 1$ and decreases gradually to $|\Psi_3^s| = 0$ for the perfect chevron (PCh) $\left\{\frac{\pi}{3}\right\} \equiv \{0\}$. While $|\Psi_3^c|$ and $\Psi_3^{|c|}$, shown in **Figure V-4.B and C** both start with 0 for HC and develop to 1 for PCh. On the other hand path II $|\Psi_3^c|$ has a constant of value 0 along the path, while for path I both $|\Psi_3^c|$ and $\Psi_3^{|c|}$ have the same values.

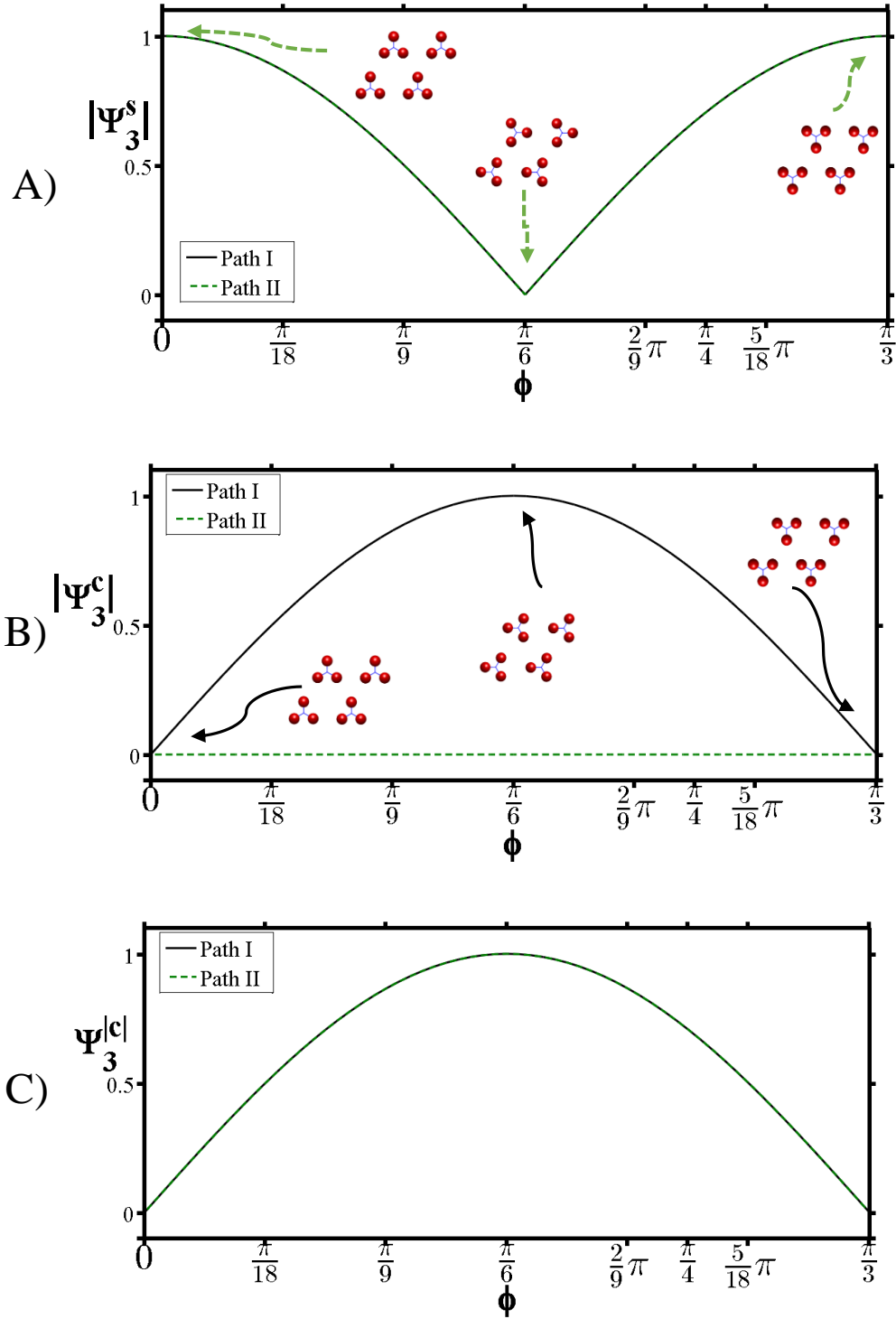


Figure V-4: The order parameter as a function of paths shown in **Figure V-3** A) $|\Psi_3^s|$, B) $|\Psi_3^c|$, and C) $\Psi_3^{|c|}$. The legends describe each path (I and II) inside each graph. The cartoons in A) show the patterns of path II while in B) show patterns of path I. Note: Path I and II are degenerate in both $|\Psi_3^s|$ and $|\Psi_3^c|$. Note: $\{\phi\} \in [0, \pi/2]$; is the rotatory angle and it is different from geometry abbreviation $\{\theta\}$.

V.2.c Results of full potential energy search on a triangular lattice.

The results of a full unbiased search of potential energy $V(\rho, r_e)$ as a function of ρ and r_e is shown in **Figure V-5**. In **Figure V-6** we show the order parameters contour diagram of the full unbiased search as a function of ρ and r_e . The large ρ and r_e are physically meaningless and not color coded.

We notice from **Figure V-5 and V-6** that the dominant GM geometry at low ρ and r_e is the honeycomb “HC” geometry. And at low r_e and large ρ the dominant pattern is the reverse chevron pattern. For a large ρ/r_e ratio the dominant geometries are the chevron structures (“Ch” and “PCh”). To explain the geometries in detail we will study horizontal cuts of the contour diagrams at constant r_e by using a biased calculation (the paths suggested earlier **Figure V-3**) and an unbiased calculation using the full space minimization. We will show low $r_e=0.3$, medium $r_e=0.4$ and high $r_e=0.5$. Those choices contain most the illustrative geometries of the full space potential energy minimization.

Case 1: Horizontal cut at $r_e=0.3$ for tritopic molecule on a triangular lattice

Figure V-7 shows the biased potential energy calculation of the three key geometries in addition to the unbiased full space potential energy minimization. Several geometries along this horizontal line ($r_e=0.3$) are shown in **Figure V-8**. Looking back to **Figure V-2** the reverse chevron “RCh” is expected to be the lowest energy state. However we noticed from **Figure V-7** that at low $\rho \in [0, 0.21]$, the HC and RCh geometries are energetically very close, with the HC being the global minimum as can be seen in **Figure V-5**. This can be explained by looking at **Table V-1** where we can see the number of the nearest neighbor site-to-site “ N_1 ” for HC and RCh are 6 and 2, respectively, which gives HC the chance to be the global minimum. In the region $0.21 < \rho < 0.34$,

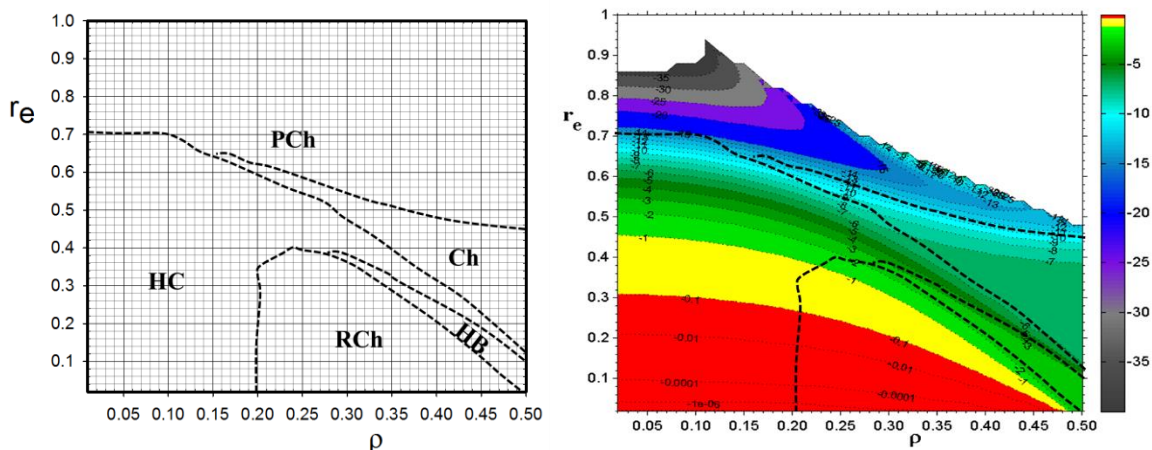


Figure V-5: The parameter phase diagram of a tritopic molecule on a triangular lattice as a function of (ρ , r_e) (Left). The contour plots of potential as a function of ρ and r_e (Right). The labels “HC”, “Ch”, “HB”, “RCh” and “PCh” stand for honeycomb, chevron, herringbone, reverse chevron, and perfect chevron, respectively. All geometries are shown in **Figure V- 8, 12 and 15**. The broken black lines show the borders between the patterns. The color bar is the color codes of the value of the energy.

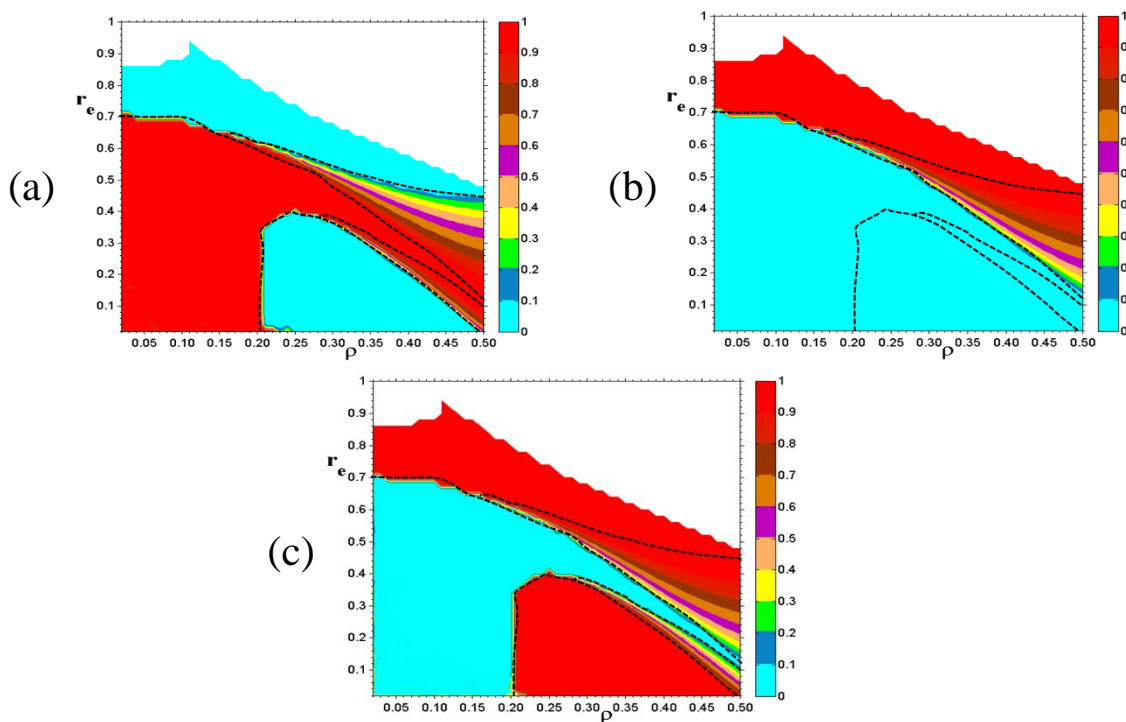


Figure V-6: the contour plots of the order parameters of tritopic molecule on triangular lattice; (a) Order parameter, $|\Psi_3^s|$, (b) Order parameter $|\Psi_3^c|$; (c) Order parameter Ψ_3^c . The borders are described in **Figure V-5**. The color bars beside each diagram represent the color-code values of the order parameters.

as the optimum NN distance s (s becomes closer to $r_e=0.3$) overcomes the number of the nearest neighbor N_1 , the global minimum is the RCh pattern. As ρ increases, the s of the RCh pattern hits the repulsive distance σ of the potential, the geometry buckles to herringbone structure. The herringbone structure has two different orientational angles $\{\theta, \pi-\theta\}$. By $\rho \in [0.37, 0.40]$ the global minimum is the HC geometry. After that the HC reaches the repulsive region (see **Figure V-2**) and buckles to Chevron “Ch” geometry. The Ch structure has $p3$ symmetry group and is chiral because it possess no mirror plane.

The same story can be seen using the biased potential energy calculation, as shown in **Figure V-9**, for path I and path II (which are described in **Figure V-3**). For $\rho=0.20$ the global minimum is the HC pattern $\{0\}$, where all the orientational angles are equal. By $\rho=0.34$ the global minimum is the RCh $\{\frac{\pi}{3}, 0\}$. The herringbone structure is the ground state for $\rho=0.36$. By $\rho=0.40$ the HC is the global minimum. Finally by $\rho=0.49$ the chevron “Ch” is the global minimum.

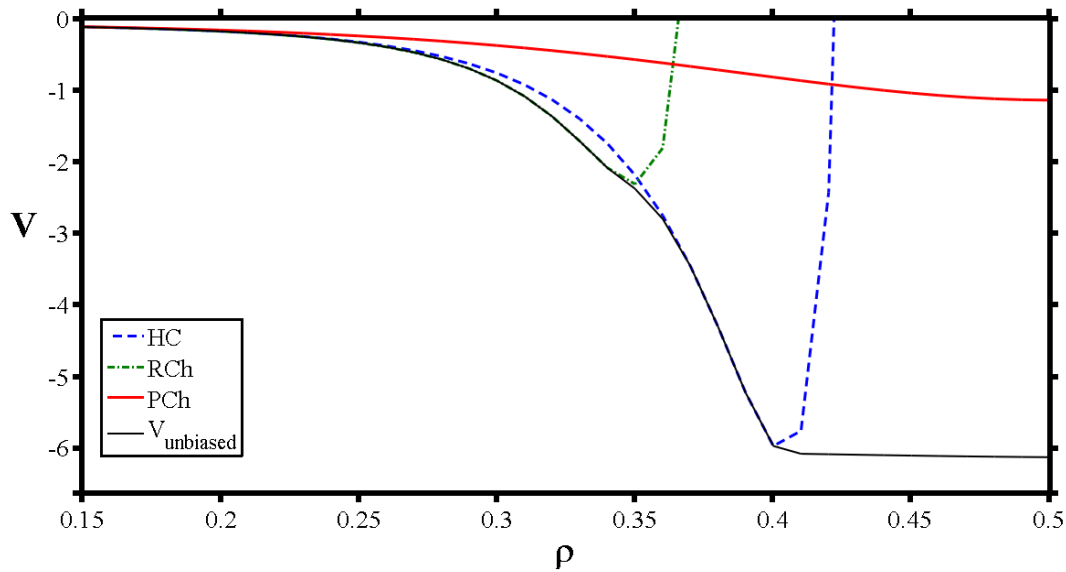


Figure V-7: The potential energy function $V(\rho)$ for the key geometries described in **Figure V-1**, for $r_e = 0.3$. The solid black line is the potential of the GM obtained through the unbiased search. The legends shown inside the graph represent the labeling of the key geometries shown in **Figure V-1**.

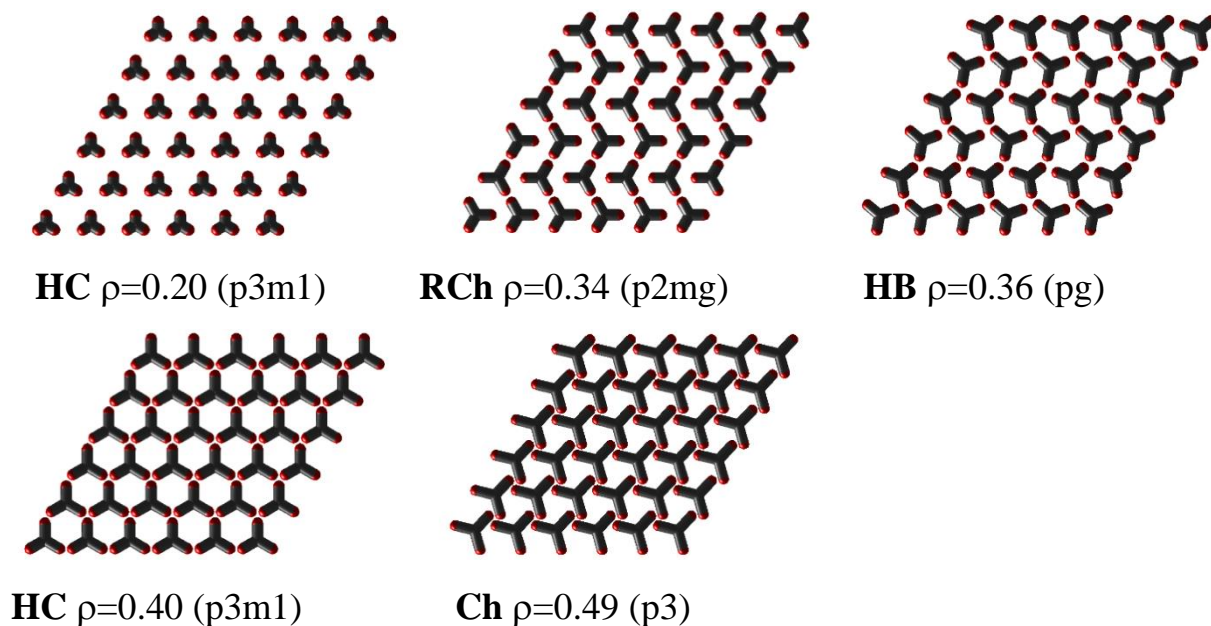


Figure V-8: The geometries of tritopic molecule on triangular lattice of the unbiased search for different ρ 's (horizontal cut at constant $r_e=0.3$ of Lennard-Jones potential $V(\rho)$, **Figure V-5** and **Figure V-7**). In the parentheses is the symbol for the wallpaper symmetry (for details see Appendix C). The labels below each geometry are abbreviations that stand for "HC" honeycomb, "RCh" reverse chevron, "HB" herringbone, "Ch" chevron. Chevron structure is chiral, because it has no symmetry mirror plane. Chevron family has the same orientational angle, $\{\theta\}$.

Local minima, $r_e=0.3$, of tritopic molecule on a triangular lattice

Figure V-10, shows some examples of the potential energy histogram of all the minima found by considering a large number of minimization for the system with $(\rho, r_e=0.3)$. As expected at $\rho=0.20$ the next higher energetic local minimum to the HC global minimum is the RCh pattern due to the fact that the two are energetically very close. By $\rho=0.34$ we have one minima which is the RCh pattern global minimum. By $\rho=0.36$ the only pattern found is the GM herringbone structure. At $\rho=0.40$ all the starting points descend to the HC structure where all the orientational angles $= \pi/2$. For a larger molecule with $\rho=0.49$ three minima are found with the chevron "Ch" geometry being the global minimum. The second minimum, an irregular shape, has the highest probability among the minima. The third one has orientational angles $\{76,16\}^\circ$.

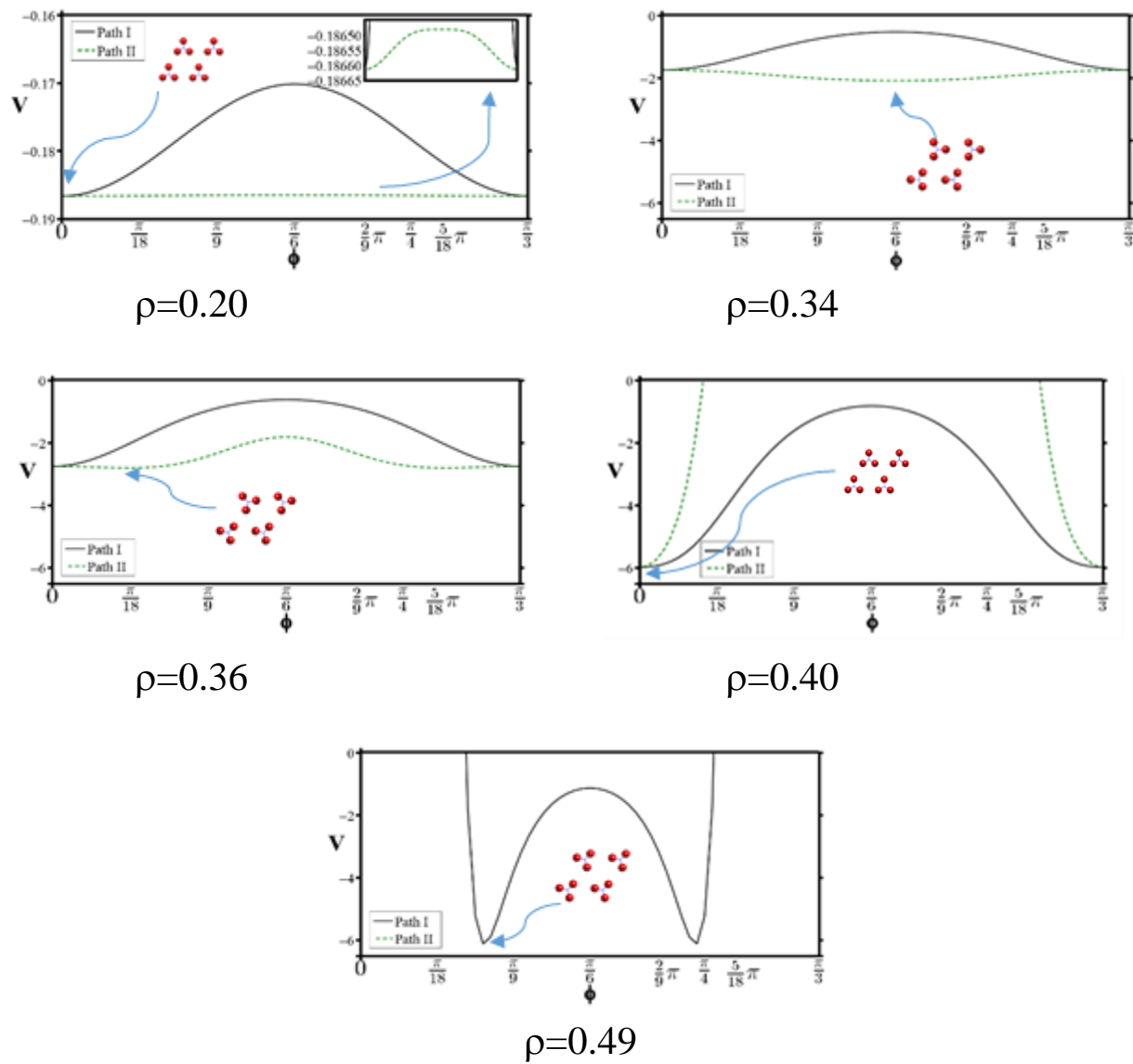


Figure V-9: Potential energy as a function of the rotatory paths $V(\phi, r_e=0.3)$ at constant values of ρ (see **Figure V-3**). Each graph shows path I conrotatory (Solid black line) and path II disrotatory (cut green line). Shown in each panel is a cartoon of the global minimum “GM” of the paths. Note: for clarity graph 1 ($\rho=0.2$), V-scale is different from the other scales. For $\rho=0.49$ path II is repulsive.

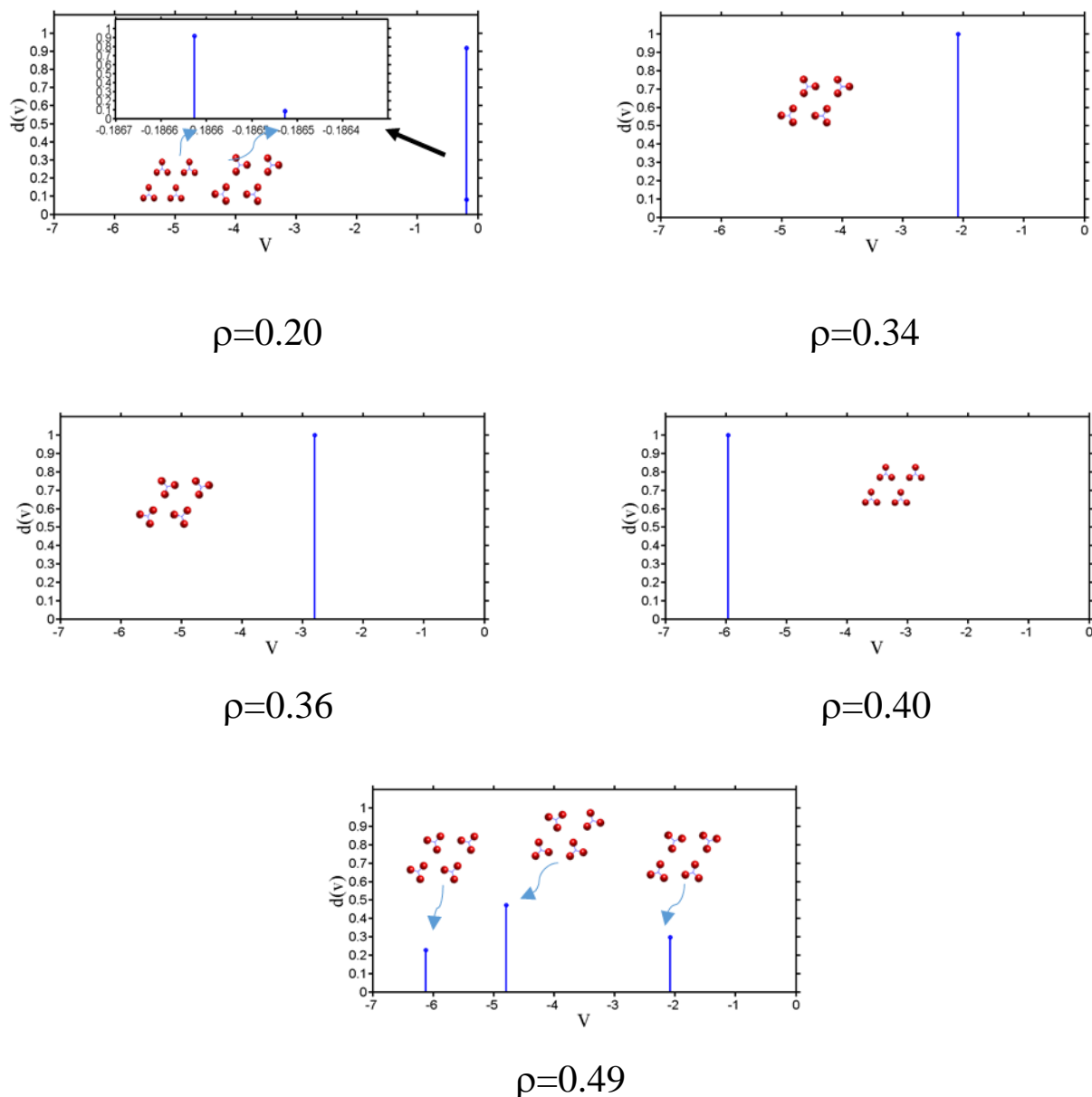


Figure V-10: The probability histogram energy potentials at constant $r_e=0.3$ for rotor lengths $\rho=0.2, 0.34, 0.36, 0.40,$ and 0.49 . In each plot shown the cartoons of the minima found by the unbiased search of many starting points. Note: at $\rho=0.2$ the energies of the minima are very close (for clarity the inner panel shows a different energy scale).

Case 2: Horizontal cut at $r_e=0.4$ for a tritopic molecule on a triangular lattice

The potential energy plot for the key geometries with the unbiased potential energy curve $V(\rho, r_e=0.4)$ are shown in **Figure V-11**. The global minima geometries along this potential energy curve, $V(\rho, r_e=0.4)$, are shown in **Figure V-12**. **Figure V-13** shows the potential energy $V(\phi)$, for

the rotor length shown in **Figure V-12**, as a function of the rotatory paths described above (see **Figure V-3**). As expected (look back to **Figure V-2 and Table V-1**) for a short rotor $\rho < 0.35$ the global minimum is the honeycomb structure, although for $\rho < 0.27$ the HC and RCh geometries energetically compete, the HC pattern being the global minimum. This also noticed in **Figure V-13**, panels, $\rho = 0.24$ and 0.34 , where the global minimum is HC in both panels. By $\rho > 0.35$ the global minimum is the chevron structure with all orientational angles being the same (see $\rho = 0.39$ and $\rho = 0.49$ as examples **Figure V-11 and 13**).

Local minima, $r_e = 0.4$, of a tritopic molecule on a triangular lattice

In **Figure V-14**, we show the potential energy histograms of several rotor lengths at a constant $r_e = 0.4$. For a small rotor, $\rho = 0.24$, the only minimum we found is the HC GM pattern. By increasing the rotor length, $\rho = 0.34$, we see a second local minimum where the HC GM pattern is the most probable geometry. By $\rho = 0.39$, two other local minima can be seen with the lowest energy LM has the highest probability. For larger $\rho = 0.49$ the irregular pattern LM which has the highest probability, and is found along with the chevron GM geometry.

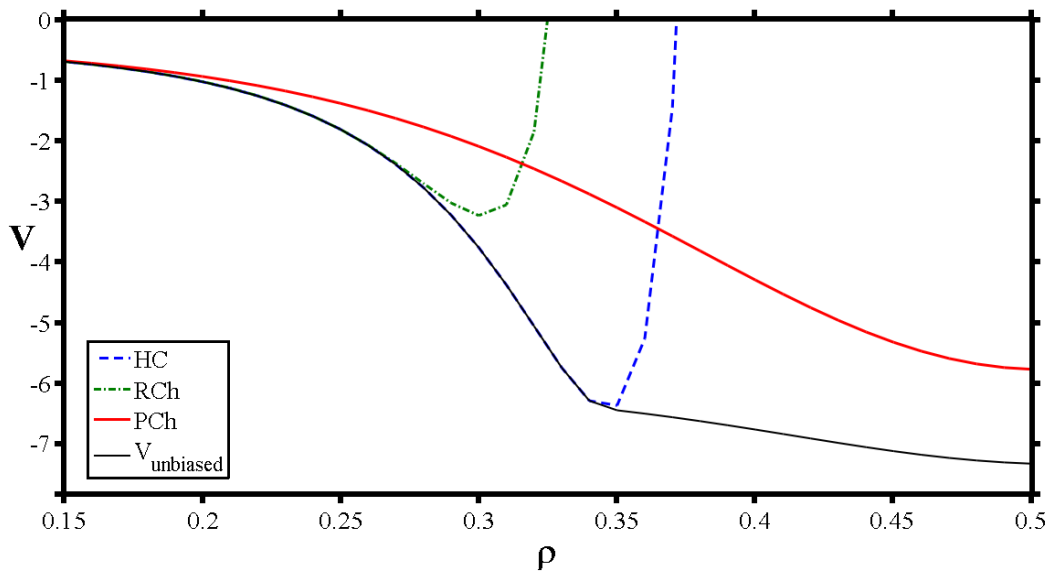


Figure V-11: The potential energy function $V(\rho)$ for the key geometries (on triangular lattice) described in **Figure V-1**, for $r_e = 0.4$. The solid black line is the potential of the GM obtained through the unbiased search. The legends shown inside each graph represent the labeling of the key geometries shown in **Figure V-1**.

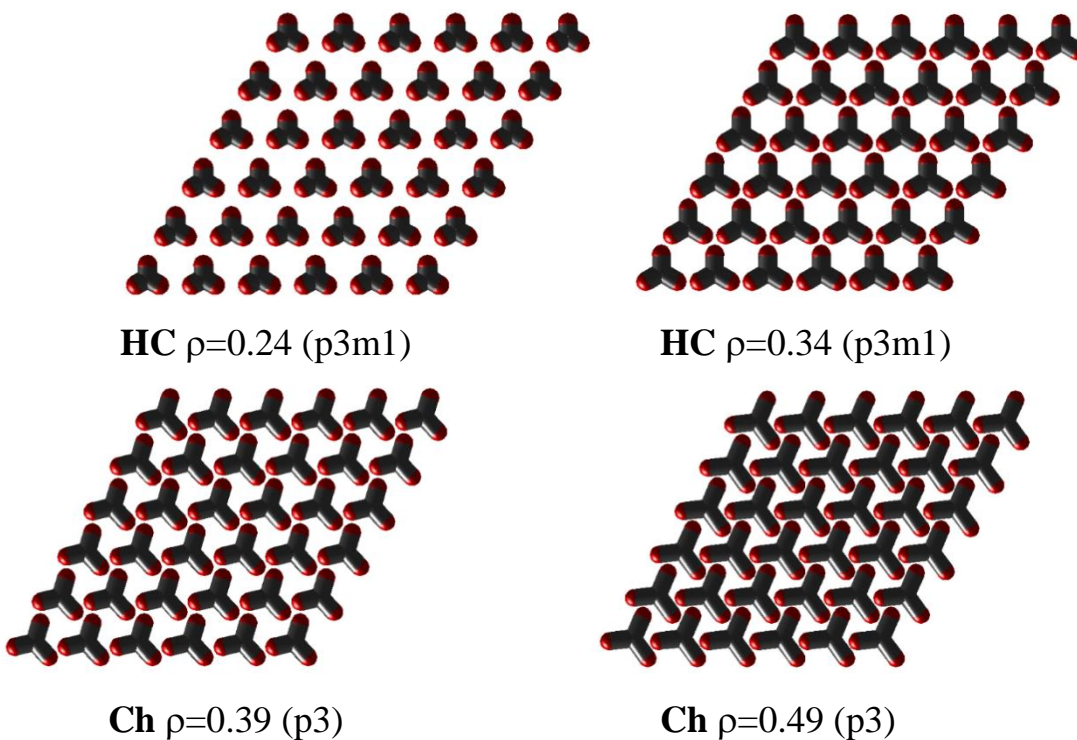


Figure V-12: The geometries (on a triangular lattice) of the unbiased search for different values of ρ (horizontal cut at constant $r_e=0.4$ of Lennard-Jones potential $V(\rho)$, **Figure V-5** and **Figure V-11**). In the parentheses is the symbol for the wallpaper symmetry (for details see Appendix C). The labels below each geometry are abbreviations that stand for “HC” honeycomb, “Ch” chevron. Note: Chevron structure is chiral as it possess no mirror plane.

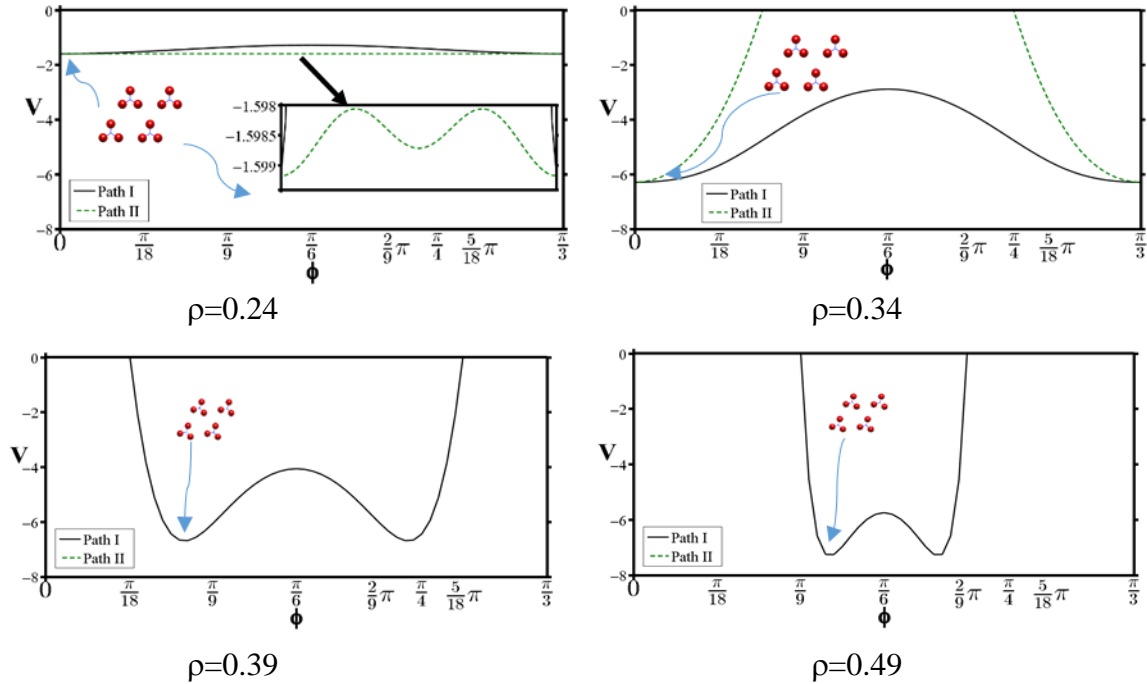


Figure V-13: Potential energy as a function of the rotatory paths $V(\phi, r_e=0.4)$ (on a triangular lattice) at a constant value of ρ (see **Figure V-3**). Each graph shows path I conrotatory (Solid black line) and path II disrotatory (cut green line). Shown in each panel is a cartoon of the global minimum “GM” of the paths. Note: for clarity graph 1 ($\rho=0.24$), the inner panel’s V-scale is different from the other scales. For $\rho=0.39$ and 0.49 path II is repulsive.

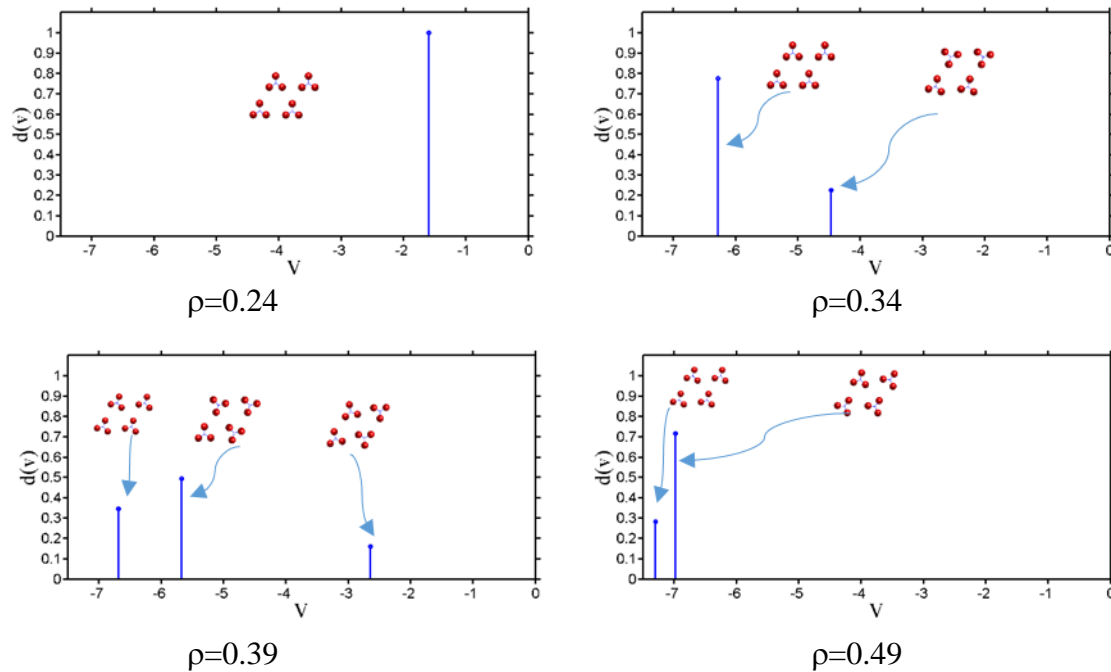


Figure V-14: The probability histogram energy potentials at constant $r_e=0.4$ for rotor lengths $\rho = 0.24$, $\rho=0.34$, 0.39, and 0.49. In each plot shown are the cartoons of the minima found by the unbiased search of many starting points. (The lattice is triangular)

Case 3: Horizontal cut at $r_e=0.5$ for tritopic molecule on a triangular lattice

Looking back to the $s(\rho)$ plot (**Figure V-2**) and the number of nearest neighbors $N1$ (**Table V-1**) the RCh structure has lower $s(\rho)$ distance but HC geometry possess larger $N1$. We predict that both the HC and the RCh patterns compete on the position of the GM. Also we predict from the figure that perfect chevron “PCh” geometry is accessible for large ρ . This is also can be seen in **Figure V-15**, which shows the potential energy of the key geometries (**Figure V-1**) with the unbiased potential energy search $V(\rho, r_e=0.5)$. In the figure we noticed that at low ρ the HC and RCh geometries are energetically very close. By $\rho > \sim 0.35$, the PCh structure, $\{0\} \equiv \left\{ \frac{\pi}{3} \right\}$, is the global minimum. Examples of the structure along this constant $r_e=0.5$ line are shown in **Figure V-16**.

In **Figure V-17** we show the potential energy $V(\phi, r_e=0.5)$ for the paths (described in **Figure V-2**). By looking at the figure the short rotors ($\rho=0.20$ as example) we see that the HC pattern is the global minimum. By $\rho=0.31$ the global minimum is the chevron structure with all the orientational angles being the same. As the ρ increases (example $\rho=0.41$) the GM is the perfect chevron $\{0\} \equiv \left\{ \frac{\pi}{3} \right\}$.

Local minima, $r_e=0.5$, for a tritopic molecule on a triangular lattice

Figure V-18 shows the potential energy histogram of the minima found at a constant $r_e=0.5$. The region that possess more than one minima is the region that has the chevron as the GM (example $\rho=0.28$). For the other regions, all the starting points descend to the global minima.

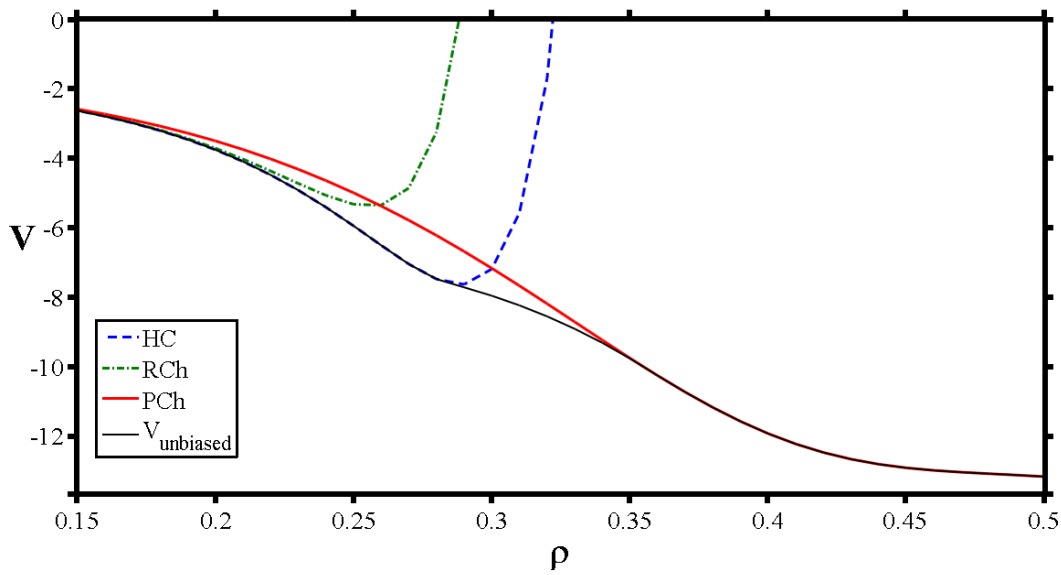


Figure V-15: The potential energy function $V(\rho)$ for the key geometries described in **Figure V-1**, for $r_e = 0.5$. The solid black line is the potential of the GM obtained through the unbiased search. The legends located inside each graph represent the labeling of the key geometries shown in **Figure V-1**.

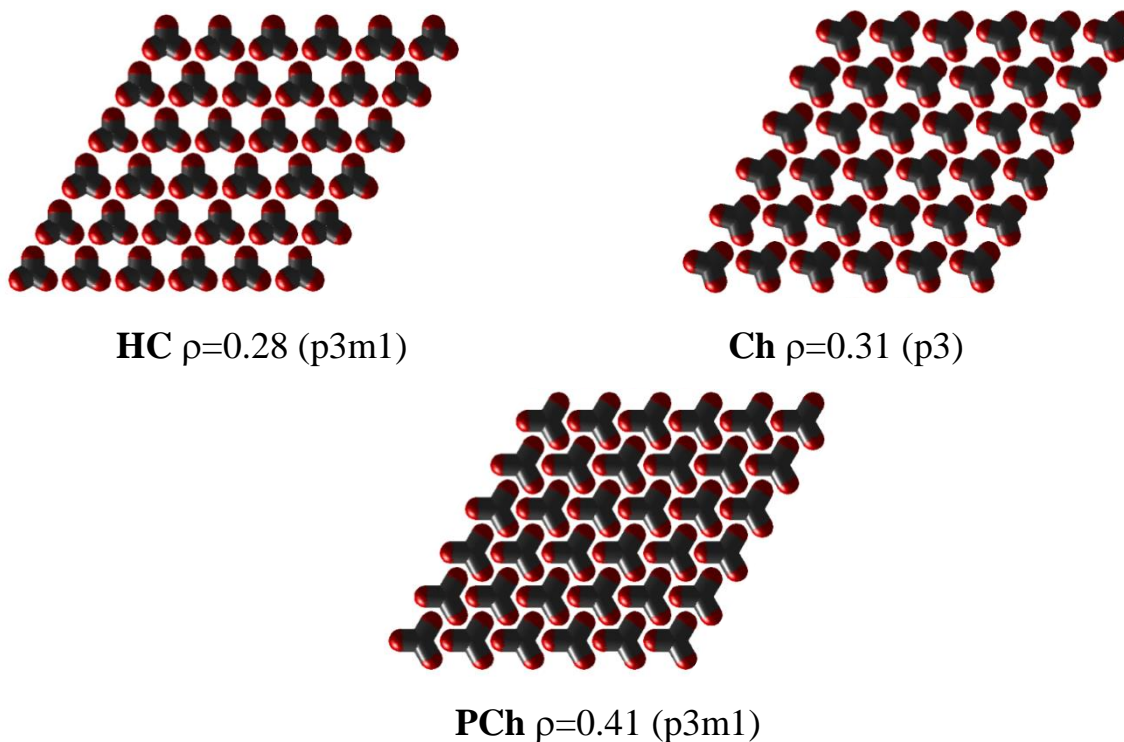


Figure V-16: The geometries of the unbiased search for different ρ 's (at constant $r_e=0.5$ of Lennard-Jones potential $V(\rho)$, **Figure V-5** and **Figure V-11**). In the parentheses is the symbol for the wallpaper symmetry (for details see Appendix C). The labels below each geometry are abbreviations that stand for “HC” honeycomb, “Ch” chevron and “PCh” perfect chevron.

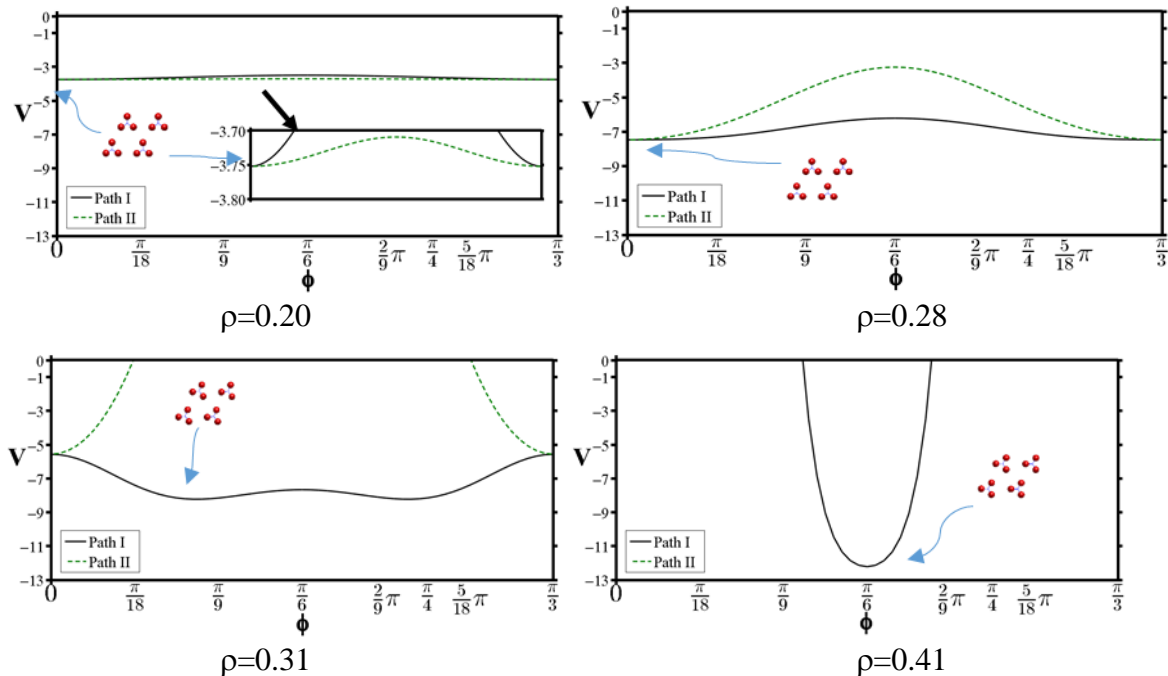


Figure V-17: Potential energy as a function of the rotatory paths $V(\phi, r_e=0.5)$ at constant ρ 's (see **Figure V-3**). Each graph shows path I conrotatory (Solid black line) and path II disrotatory (cut green line). Shown in each panel is a cartoon of the global minimum "GM" of the paths. Note: for clarity graph 1 ($\rho=0.20$), the inner panel's V -scale is different from the other scales. For $\rho=0.41$ the path II is repulsive.

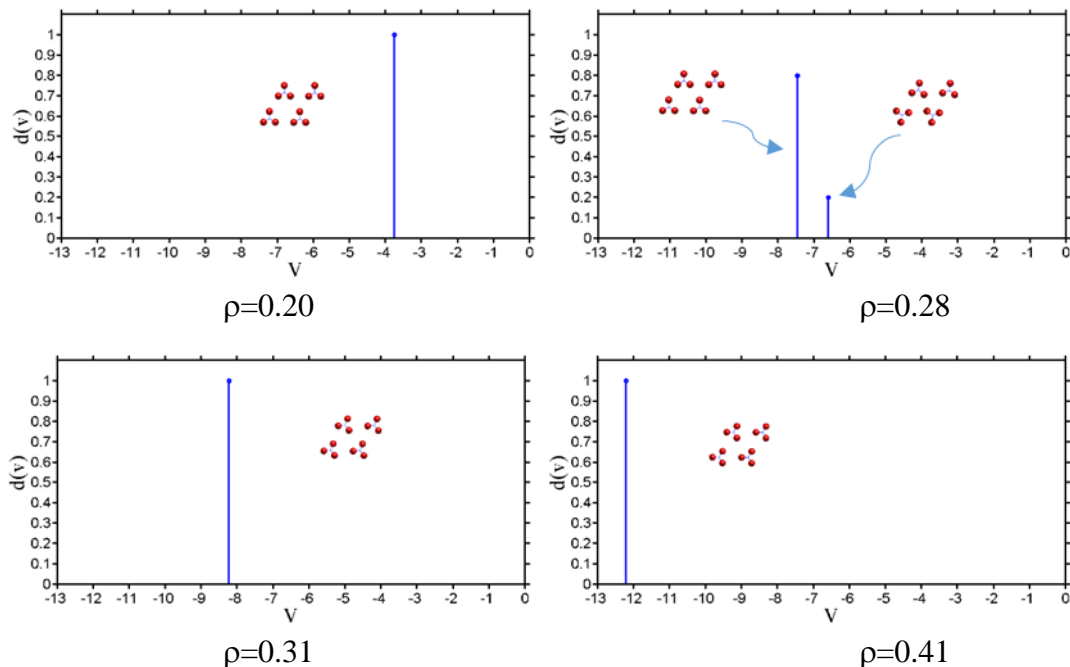


Figure V-18: The probability histogram energy potentials at constant $r_e=0.5$ for rotor lengths $\rho=0.20$, $\rho=0.28$, $\rho=0.31$, and $\rho=0.41$. In each plot are shown the cartoons of the minima found by the unbiased search of many starting points.

V.3 Conclusion for a Tritopic Molecule on a Triangular Lattice

We have investigated the adlayer self-assembly of a tritopic model molecule on a triangular lattice using a simple coarse-graining Lennard-Jones potential. We have found a variety of adlayer patterns that have different porous shapes such as a hexagon. We have located a chiral pattern such as chevron “Ch” on triangular lattice, although the adsorbate molecules are achiral and possess a D_{2h} symmetry point group.

At low ρ the honeycomb “HC” is the dominant GM while the reverse chevron “RCh” is the dominant global minimum for low r_e . The HC with 3-center of intermolecular interaction appears again as the GM for high ρ/r_e ratio. As the ρ/r_e ratio increases the honeycomb buckles to the chiral chevron “Ch” structure. Szabelski et al (23) have reported the reverse chevron “RCh” and the chevron “Ch” structure on a triangular lattice using theoretical simulation and an experimental study of 1,3,5-tris(pyridine-4-ylethynyl)benzene on graphite surface (46).

At the highest r_e values, the dominant GM is the perfect chevron “PCh” pattern which is achiral, compared with the other chevron structures, because the structure possess a mirror plane of symmetry. The perfect chevron “PCH” on a triangular lattice has been reported theoretically by Szabelski et al (23, 46) and experimentally by Kahn et al (141).

In the conclusion, we located some adlayers of a tritopic molecule on a triangular lattice which have been reported in previous studies as well as some newly observed geometries.

V.4 Results and discussion (Tritopic on a Square Lattice)

The contour plot of the ground state potential energy for the global minimum geometries is shown in **Figure V-19**. The nearest neighbor site-to-site distances $s(\rho)$ as a function of ρ for the selected high symmetry geometries are described in **Figure V-20** and **Table V-2**. The symmetry and abbreviation keys are shown in **Table V-3**. The geometries of the ground states and the symmetry plane groups at different values of r_e are depicted in **Figure V-21, 22 and 23**.

The main geometries are the followings:

1. The ribbon “RB” structure with p2mm symmetry and a hexagonal porous sites,
2. The octagon “OCT” as it has an octagon porous shape and has p4mm symmetry.
3. The distorted octagon “DOCT” has a distorted octagon shape and p4 symmetry.
4. The distorted ribbon “DRB” has cm symmetry group;
5. The chevron “CH” structure with all the orientational angle are the same $\left\{\frac{\pi}{4}\right\}$ with pm symmetry;
6. The reverse chevron “RCH” with p2mg symmetry; distorted chevron ‘DCH’ with p4gm symmetry.

In addition several distorted structures are found in the transition borders between the main geometries. These geometries will be discussed in detail in the next sections.

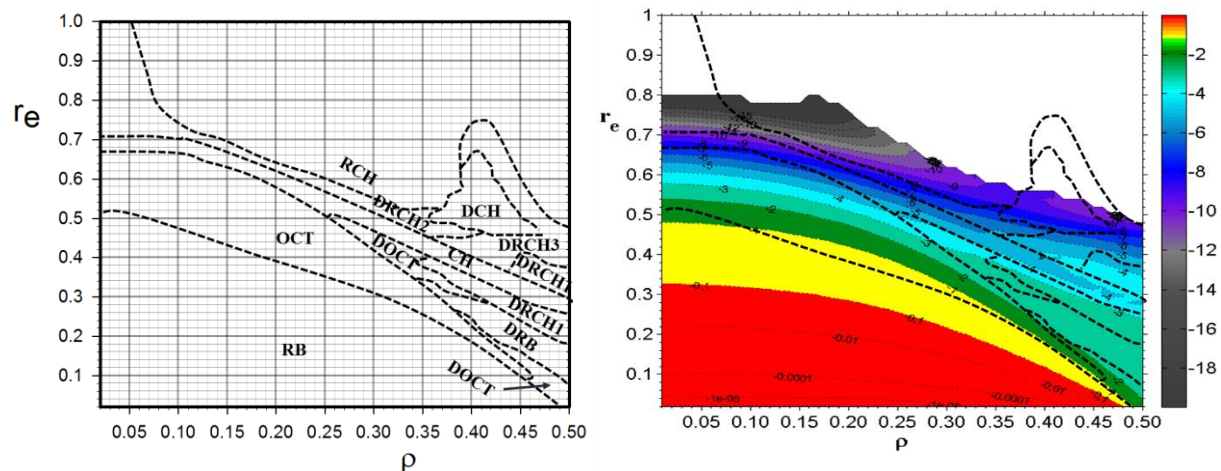


Figure V-19: Geometry distribution “phase diagram” (Left) as a function of (ρ, r_e) of the ground states of the tritopic system on a square lattice. Contour energy plot (Right) $V(\rho, r_e)$. The black cut lines indicate the borders between different patterns explained in **Figure V-21, 22 and 23**. The key of the plots colorations represent the potential energy per rotor. For clarity the abbreviations for all geometries labeling are in **Table V-3**.

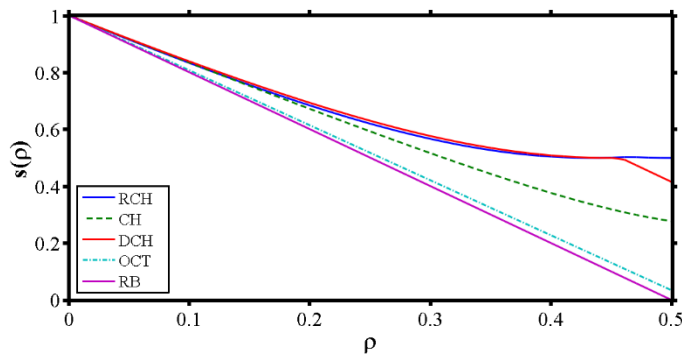


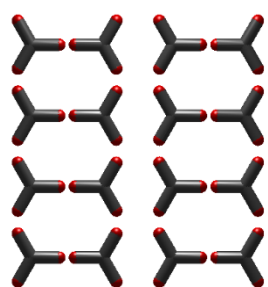
Figure V-20: The nearest-neighbor site-to-site distance, $s(\rho)$, as a function of molecule length, ρ , for chosen fixed geometries on a square lattice. The geometry labels RCH, CH, DCH, OCT, and RB stand for “Reversed Chevron”, “Chevron”, “Distorted Chevron”, “Octagon” and “Ribbon”, respectively are shown in **Figure V-21, 22 and 23**.

Table V-2: Closest nearest-neighbor (NN) site-to-site distance, s , for specified geometry (on a square lattice) as a function of ρ . Including the number of nearest-neighbor. Note that there are two possible NN distances for the Reversed Chevron and Distorted Chevron geometry.

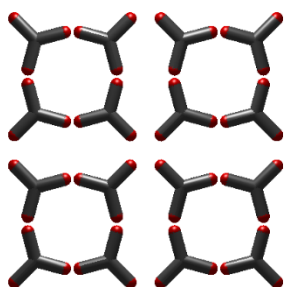
Geometry	site-to-site distances	Number of nearest-neighbor NN (N_i)
Reversed Chevron (RCH)	$s(\rho) = \min \left(\sqrt{1 - 2\sqrt{3}\rho + 4\rho^2}, \sqrt{1 - 3\rho + 3\rho^2} \right)$	2,4
Chevron (CH)	$s(\rho) = \sqrt{1 - \rho \left(\sqrt{2} + 2 \cos \left(\frac{\pi}{12} \right) \right) + 3\rho^2}$	4
Distorted Chevron (DCH)	$s(\rho) = \min \left(\sqrt{1 - \rho \left(\sqrt{2} + 2 \cos \left(\frac{\pi}{12} \right) \right) + \rho^2 (2 + \sqrt{3})}, \sqrt{2} - 2\rho \right)$	4,1
Octagon (OCT)	$s(\rho) = 1 - 2\rho \cos \left(\frac{\pi}{12} \right)$	2
Ribbon (RB)	$s(\rho) = 1 - 2\rho$	1

Table V-3: Geometry name, abbreviation and symmetry plane group of the adlayers on a square lattice (see **Figure V-21, 22 and 23**, and **Appendix C**).

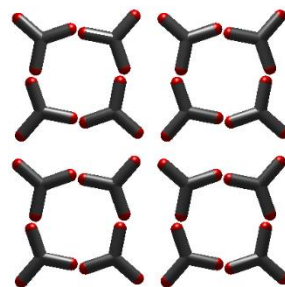
Geometry name	Abbreviation	Symmetry plane group
Ribbon	RB	p2mm
Octagon	OCT	p4mm
Distorted Octagon	DOCT	p4
Chevron	CH	pm
Distorted Reversed Chevron	DRCH1	p2
Distorted Chevron	DCH	p4gm
Reversed Chevron	RCH	p2mg
Distorted Ribbon	DRB	cm
Distorted Reversed Chevron 2	DRCH2	pg
Distorted Reversed Chevron 3	DRCH3	p4



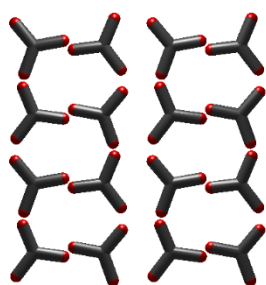
RB $\rho=0.39$ (p2mm)



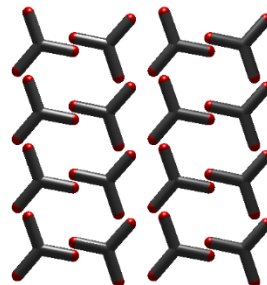
OCT $\rho=0.41$ (p4mm)



DOCT $\rho=0.42$ (p4)



DRB $\rho=0.43$ (cm)



DRCH1 $\rho=0.50$ (p2)

Figure V-21: The geometries of the unbiased search (on a square lattice) for different values of ρ (at constant $r_e=0.2$ of Lennard-Jones potential $V(\rho)$). In the parentheses is the symbol for the wallpaper symmetry (for details see Appendix C). The labels below each geometry are the abbreviations described in **Table V-3**. DOCT and DRCH1 structures are chiral, because they have no symmetry mirror plane.

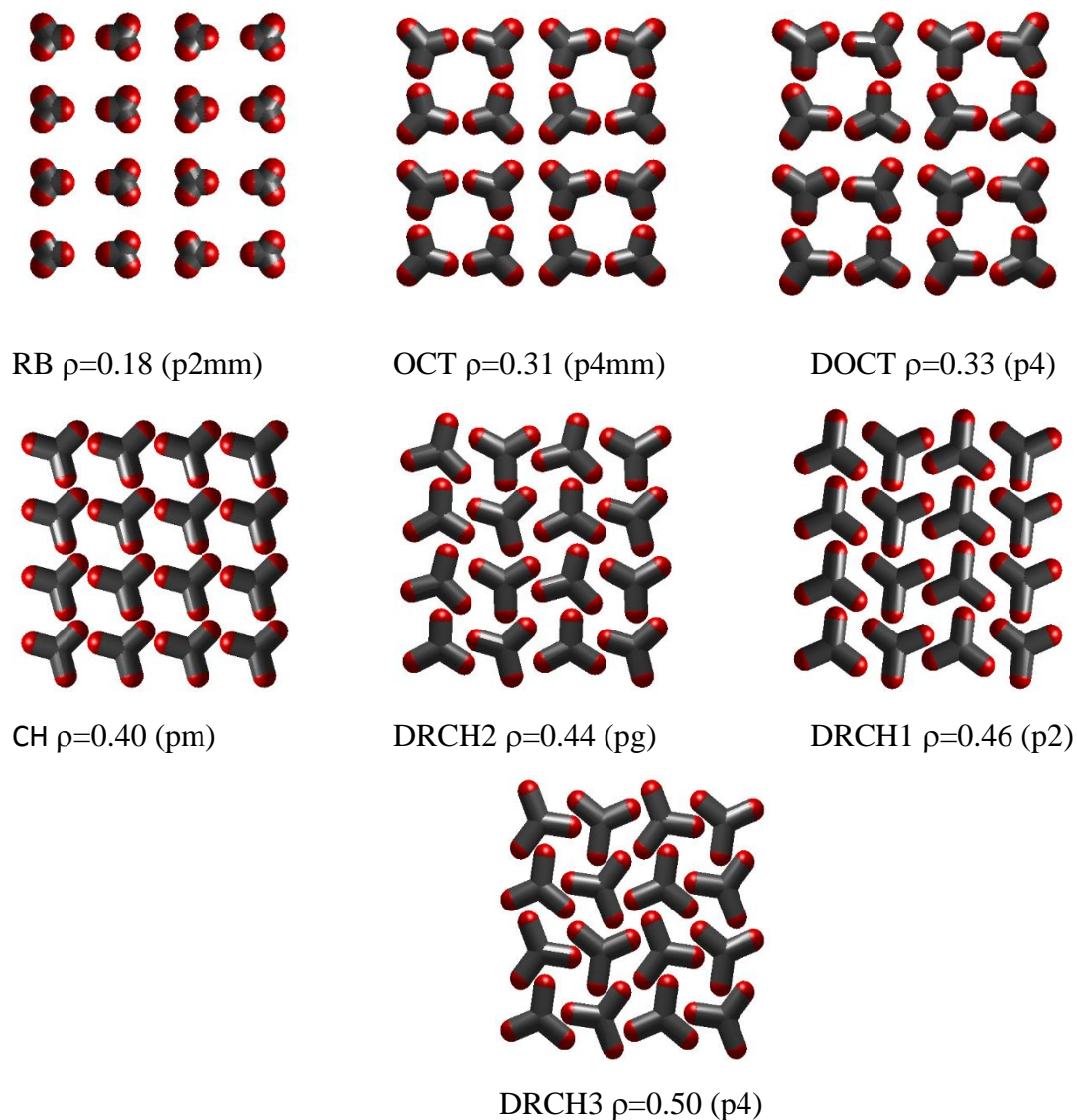


Figure V-22: The geometries of the unbiased search (on a square lattice) for different values of ρ (at constant $r_e=0.4$ of Lennard-Jones potential $V(\rho)$). In the parentheses is the symbol for the wallpaper symmetry (for details see Appendix C). The labels below each geometry are abbreviations described in **Table V-3**. DOCT and DRCH structures are chiral, because they have no symmetry mirror plane.

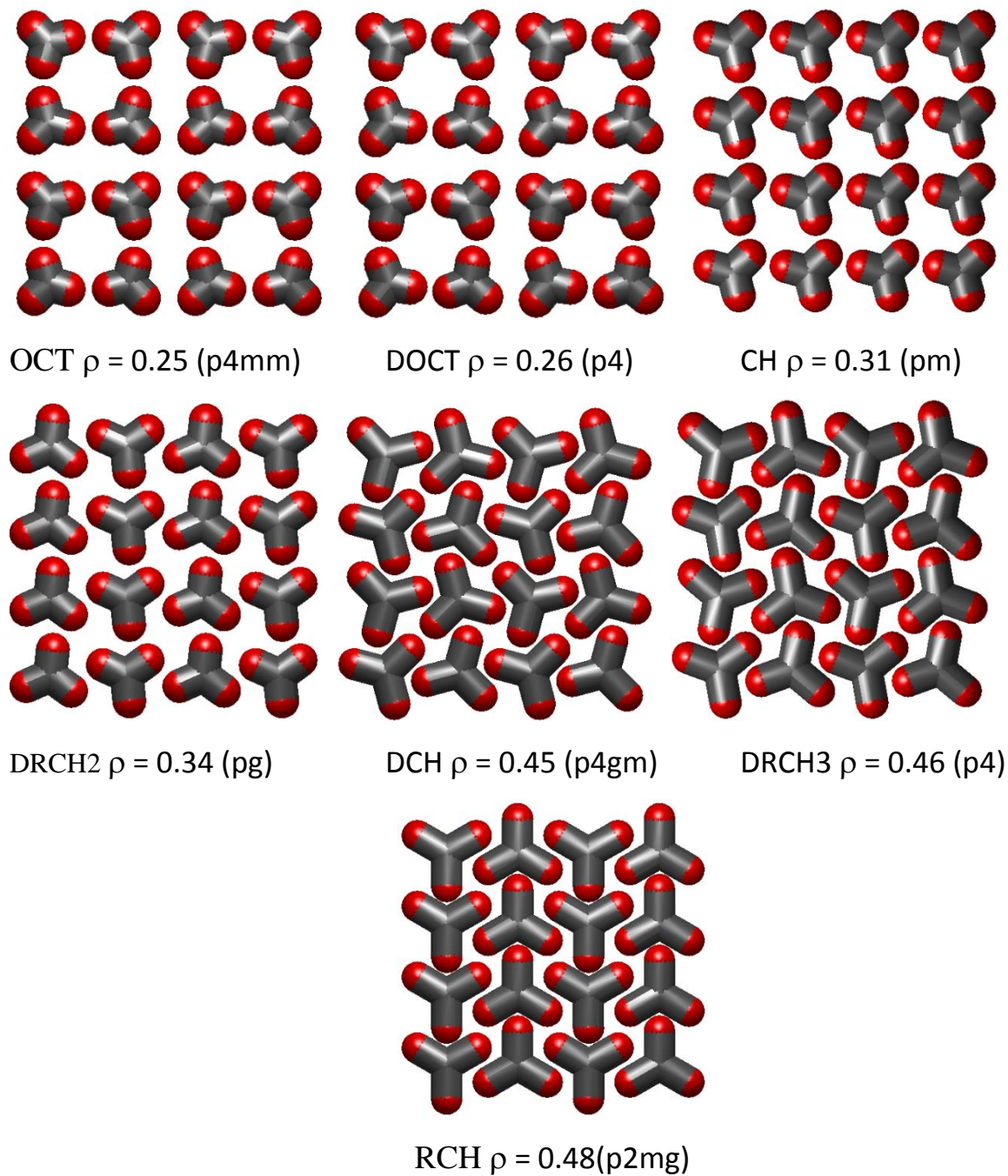


Figure V-23: The geometries of the unbiased search (on a square lattice) for different values of ρ (at constant $r_e=0.5$ of Lennard-Jones potential $V(\rho)$). In the parentheses is the symbol for the wallpaper symmetry (for details see Appendix C). The labels below each geometry are abbreviations described in **Table V-3**. DOCT and DRCH structures are chiral, because they have no symmetry mirror plane.

Results at constant values of r_e of tritopic molecule on a square lattice

To show and explain the geometries, we selected three horizontal lines of energy contour (**Figure V-19**) at constant r_e 's, one at low $r_e=0.2$, one at medium $r_e=0.4$, and one at high $r_e=0.5$.

Case 1: $r_e=0.2$ of a tritopic molecule on a square lattice

In **Figure V-24** we plot the potential energy as a function of ρ $V(\rho, r_e=0.2)$ of some ground state geometries with the potential energy, $V(\rho, r_e=0.2)$, of the unbiased calculation. For a certain ρ if the potential of the biased calculation of a certain structure matches the unbiased potential curve the ground state pattern corresponds to that structure.

The geometries found in this horizontal cut ($r_e=0.2$) are shown in **Figure V-21**. For $\rho < 0.4$ there is a competition between two structures, the ribbon "RB" and octagon "OCT". Using the radial distribution function, **Figure V-25**, we cannot distinguish which one is the global minimum, because the site-to-site distances are very close for both (See **Figure V-20**). However there is a very tiny energy difference, in the range 10^{-7} between the two, being the RB the global minimum. After this region the two become distinguishable to the benefit of OCT as the global minimum. The radial distribution function for $\rho=0.41$, **Figure V-6**, shows that the RB structure becomes repulsive (see also **Figure V-20**, $s(0.4) \approx 0.2$). At $\rho=0.42$ the global minimum is the chiral distorted octagon "DOCT" structure with $p4$ symmetry. In the region the $\rho \in [0.43-0.47]$ the distorted ribbon structure with cm symmetry is the global minimum. Finally in the region of $\rho > 0.47$ the distorted reverse chevron "DRCH" with $p2$ symmetry is the global minimum. This structure is also chiral because it has no mirror plane.

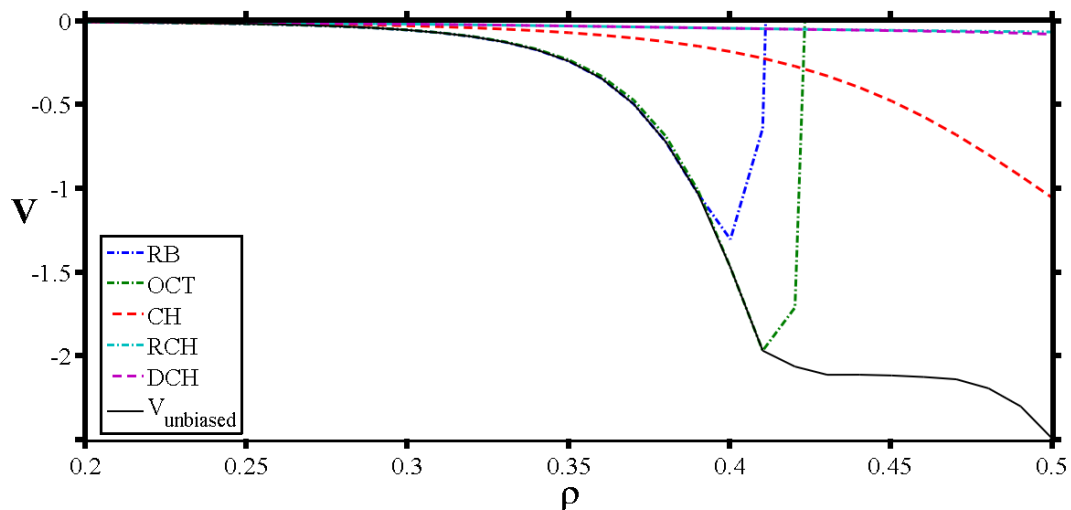


Figure V-24: The potential energy function $V(\rho)$ for the geometries described in **Figures V-21, 22, 23** (**Table V-3**) at $r_e = 0.2$. The solid black line is the potential of the GM obtained through the unbiased search.

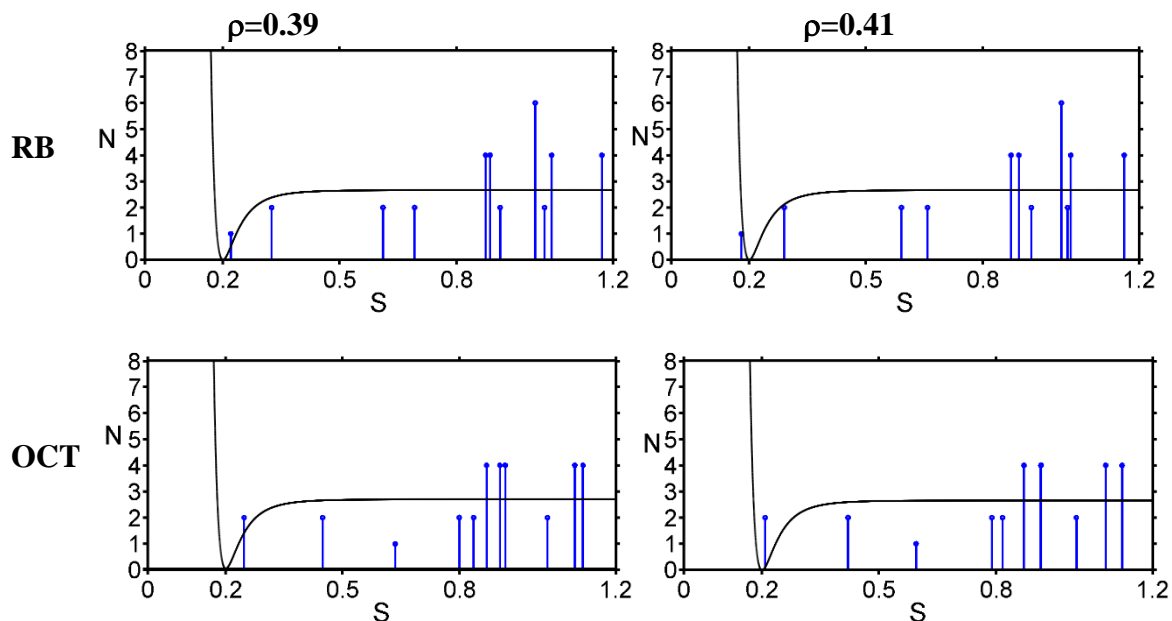


Figure V-25: Radial distribution function, showing the number of neighbor counts, $N1$ as a function of site-to-site distance $s(\rho)$, for RB and OCT geometries for the case $r_e = 0.2$. The labels RB, and OCT are described in **Table V-3** and **Figure V-21**. The black line is the Lennard-Jones potential at $r_e = 0.2$.

Local minima, $r_e=0.2$, of a tritopic molecule on a square lattice:

In **Figure V-26** we show the probability histogram for all minima of several representative examples at $r_e=0.2$. At $\rho=0.39$ there are two minima, the ribbon GM structure and another local minimum which has a low probability density $d(V) < 20\%$, with orientational angles $\{\frac{\pi}{3}, 0\}$. By $\rho=0.41$ most of the starting points descend to the octagon structure GM plus a very rare LM $d(V) < 5\%$, with orientational angles $\{107, 73\}^\circ$. At $\rho=0.42$ there are three minima. The lowest minimum is the chiral distorted octagon structure. The second LM is the distorted ribbon pattern with significantly high probability density. The last one has low probability and irregular shape. By $\rho=0.43$ the distorted octagon and distorted ribbon switch their positions so the distorted ribbon structure is the global minimum, with high probability. The last example at $\rho=0.5$ has several minima being the chiral distorted reverse chevron GM. The second LM, with the highest probability, is the irregular pattern.

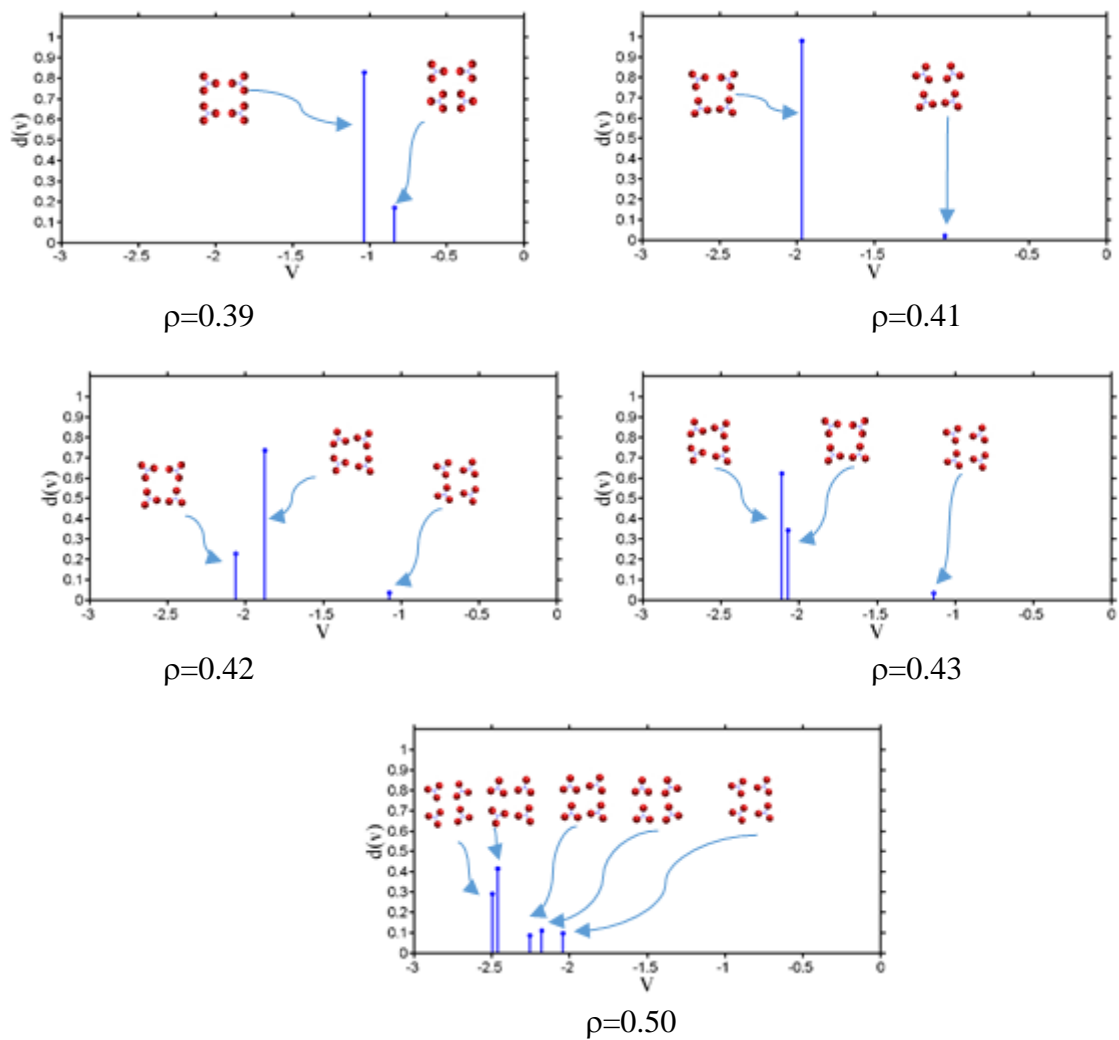


Figure V-26: Probability histograms of the minima of Lennard-Jones at constant $r_e=0.2$ for several rotor lengths ρ . In each plot are shown the cartoons of the minima found by the unbiased search of many starting points.

Case 2: $r_e=0.4$ of a tritopic molecule on a square lattice

The potential energy functions of the main ground state geometries as a function of ρ , $V(\rho, r_e=0.4)$, and unbiased potential energy curve are shown in **Figure V-27**. The patterns of the global minima are shown in **Figure V-22**. Again for short rotors ($\rho < 0.18$) using the radial distribution function, **Figure V-28**, we cannot distinguish which one, the RB structure or the OCT geometry, is the global minimum, because the site-to-site distances are very close for both (look back to $s(\rho)$ **Figure V-20**). After this region the two become distinguishable to the benefit of OCT pattern as the global minimum (see the radial distribution function for $\rho=0.31$, **Figure V-28**). In the region of $\rho=0.32$ and 0.33 , the chiral DOCT pattern is the global minimum **Figure V-28**.

As expected, from **Figure V-20** and also noticed in **Figure V-27**, the chevron “CH” structure is the ground state in the range $\rho \in [0.34-0.40]$. The radial distribution function, for a case of $\rho=0.38$ is shown in **Figure V-28**, which shows the N1 site-to-site distance at the optimum equilibrium distance of the potential. In the region of $\rho > 0.4$ the chiral distorted reverse chevron pattern “DRCH” is the global minima.

Local Minima, $r_e=0.4$, of tritopic molecule on a square lattice

In **Figure V-29** we show the histogram of the probability density of the minima of several rotor lengths at constant $r_e=0.4$. For the first one, $\rho=0.18$, all the starting points descend to the ribbon GM structure. By $\rho=0.31$, the global minimum is the octagon, the distorted ribbon is the second local minimum and an irregular pattern is the last local minimum. By $\rho=0.33$, the chevron structure appears as the last local minimum with low probability. At $\rho=0.4$ the chevron becomes the global minimum and a distorted high probable structure is a second local minimum.

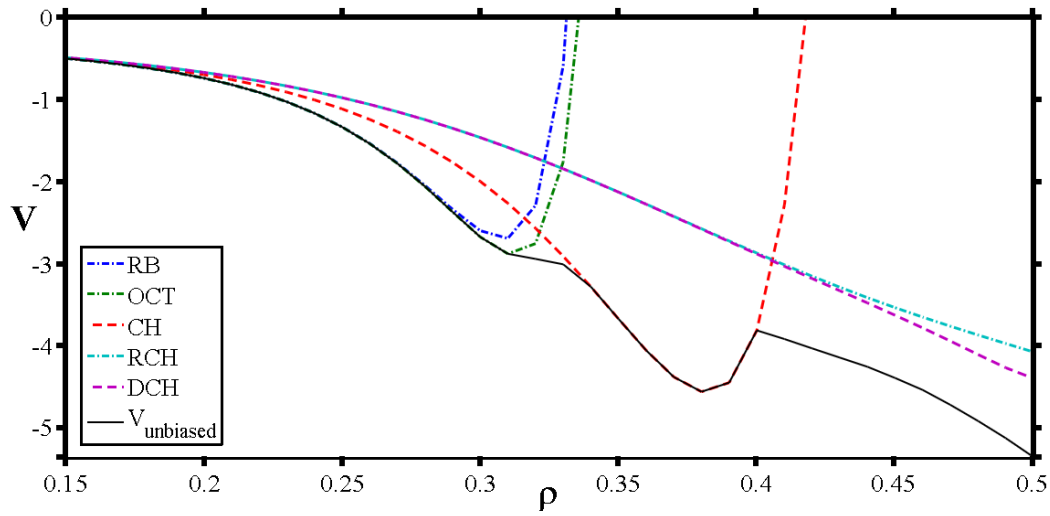


Figure V-27: The potential energy function $V(\rho)$ for the geometries (on a square lattice) described in **Figure V-22** for $r_e = 0.4$. The solid black line is the potential of the GM obtained through the unbiased search.

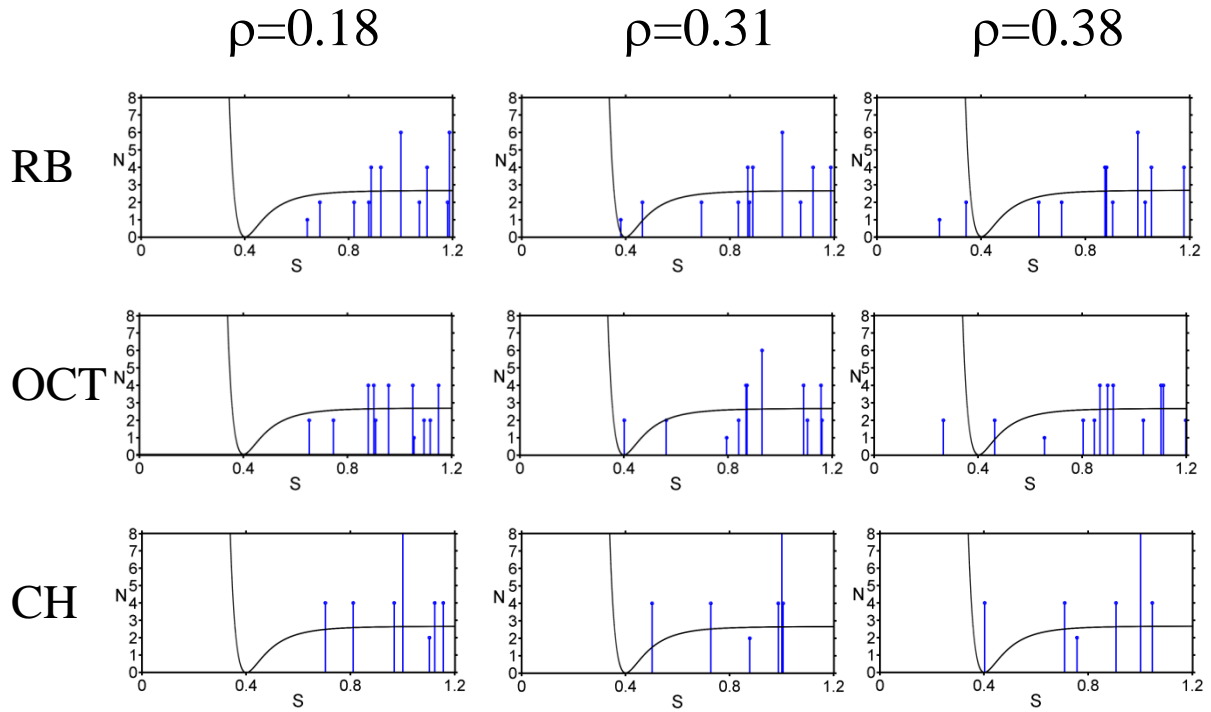


Figure V-28: Radial distribution function, showing the number of neighbor counts, $N1$ as a function of site-to-site distance $s(\rho)$, for RB, OCT and CH geometries (on a square lattice) for the case $r_e=0.4$. The labels RB, OCT and CH are described in **Table V-3** and **Figure V-22**.

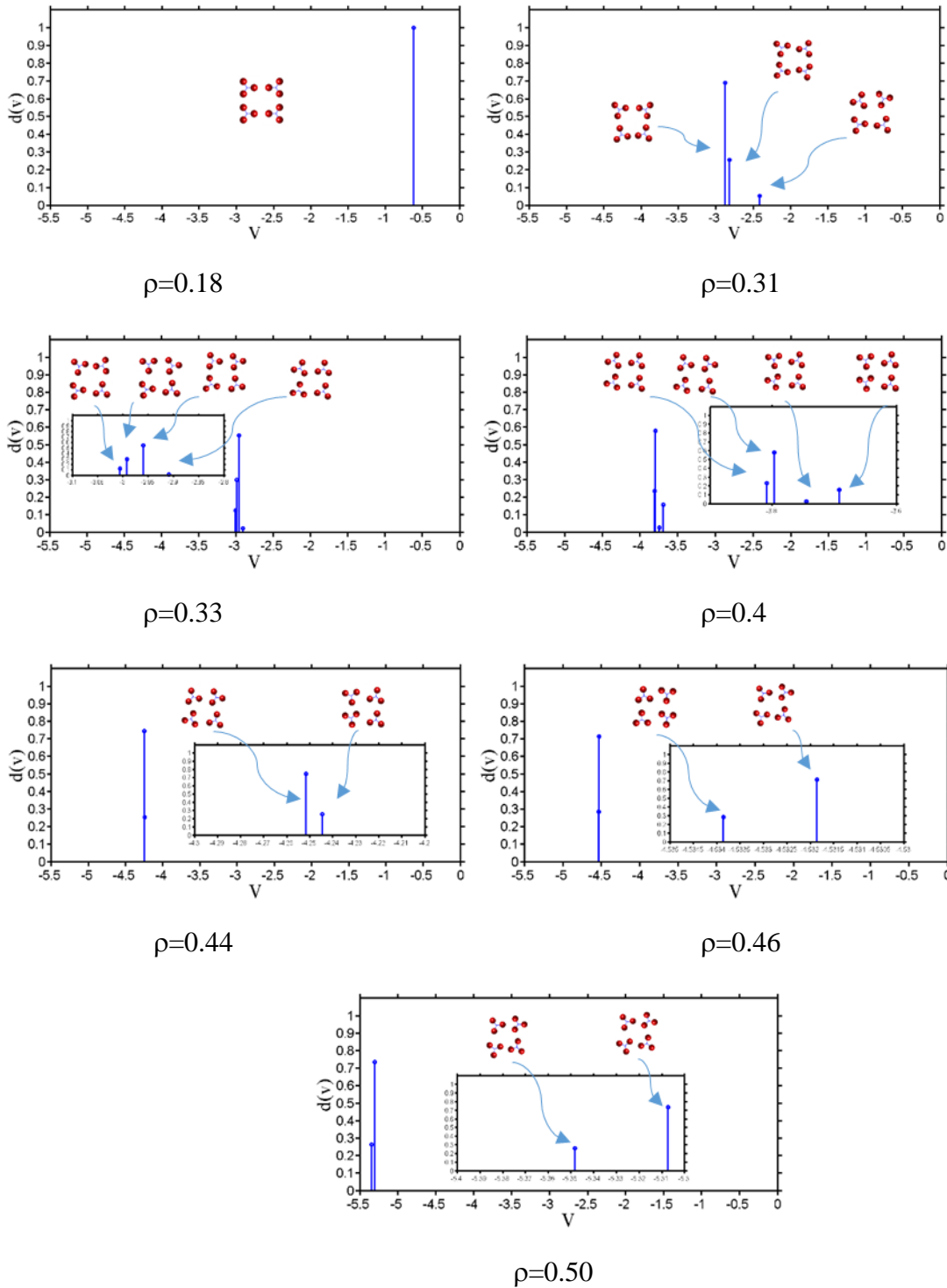


Figure V-29: Probability histograms of minima (on a square lattice) of Lennard-Jones at constant $r_e=0.4$ for several rotor lengths ρ . In each plot shown the cartoons of the minima found by the unbiased search of many starting points.

Case 3: $r_e=0.5$ of a tritopic molecule on a square lattice

The structures along $r_e=0.5$ are shown in **Figure V-23**. The potential energy curve is shown in **Figure V-30**. By examining **Figure V-30**, the region of $0 < \rho < 0.25$, it is seen that the competition between RB and OCT occurs as expected because their energies are very closed, with OCT being the global minimum of $\rho > 0.06$. As the ρ get closer to 0.25, the CH structure appears as a third minimum, until it becomes the ground state in the region of $\rho \in [0.27-0.31]$. The histogram local minima diagrams, **Figure V-31**, show some examples for $\rho = 0.25, 0.26$ and 0.31 . For $\rho > 0.31$ the local minimum chevron structure accompanies the other global minima (DRCH, DCH and RCH) although it possesses a highly positive potential energy after $\rho=0.36$ (see the histogram for LM of $\rho=0.4$ **Figure V-31** and the radial distribution functions of CH, **Figure V-32**).

A case that is worthy to focus on is the region of $0.35 < \rho < 0.46$ at which the DCH pattern is the global minimum with $p4mg$ symmetry. The same structure has been experimentally located by Kahn et al (141). They have located the most energetically stable structure for the self-assembly of a highly packed monolayer of hexaazatrinaphthylene on Au(111) surface. The radial distribution function and the histogram of the local minima diagram of $\rho=0.4$ are depicted in **Figure V-32** and **Figure V-31**, respectively.

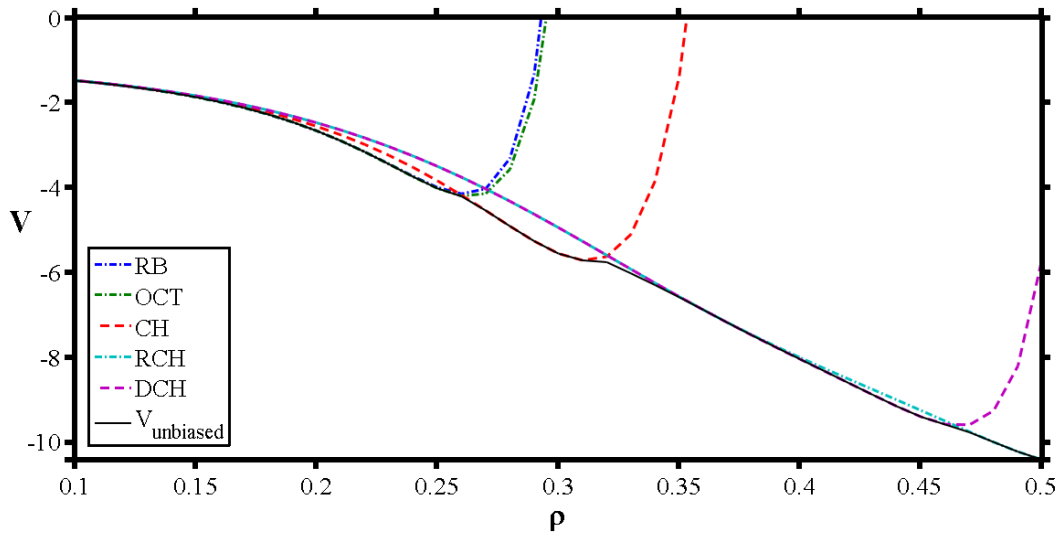


Figure V-30: The potential energy function $V(\rho)$ for the geometries (on a square lattice) described in **Figure V-25** at $r_e = 0.5$. The solid black line is the potential of the GM obtained through the unbiased search. The abbreviations are shown in **Table V-3**.

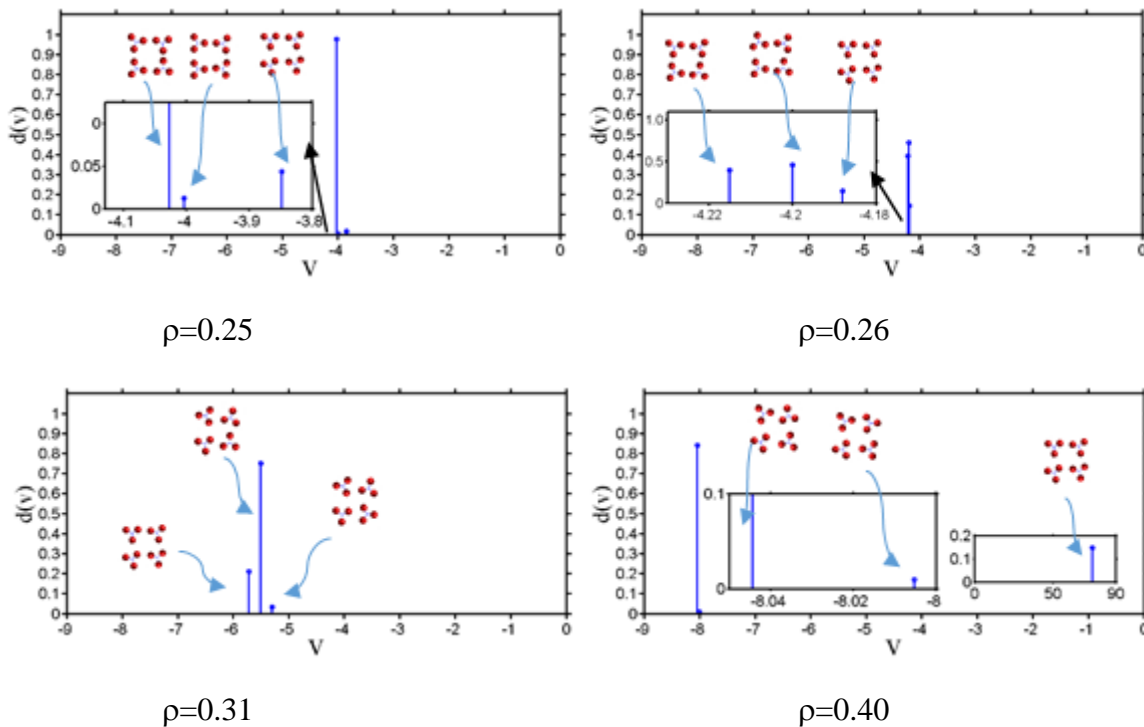


Figure V-31: Probability histograms of minima (on a square lattice) of Lennard-Jones at constant $r_e = 0.5$ for several rotor lengths ρ . In each plot the cartoons of the minima, found by the unbiased search of many starting points, are shown. Note: For $\rho = 0.40$ the chevron structure are highly positive (repulsive).

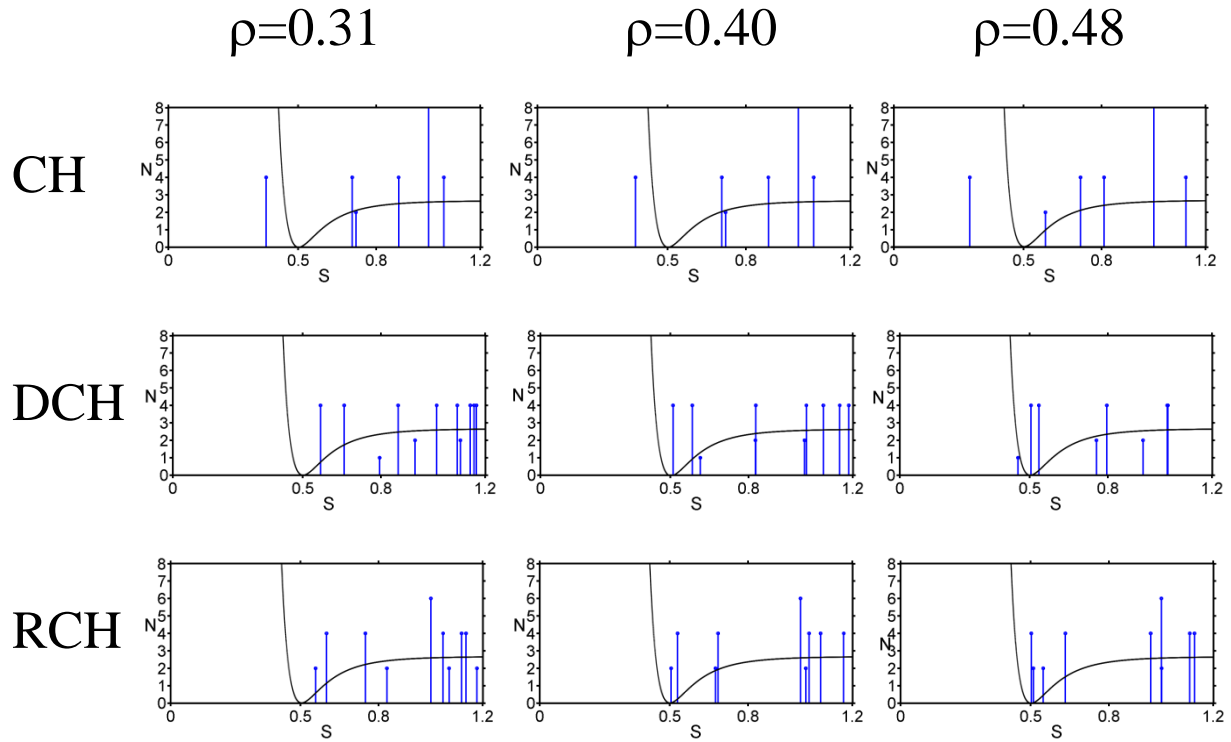


Figure V-32: Radial distribution function, showing the number of neighbor counts, N_1 as a function of site-to-site distance s , for CH, DCH and RCH geometries (on a square lattice) for the case $r_c=0.5$. The labels CH, DCH and RCH are described in **Figure V-23** and **Table V-3**.

V.5 Conclusion for a Tritopic Molecule on a Square Lattice

We have investigated the adlayer self-assembly of the tritopic model molecule on a square lattice using a simple coarse-graining Lennard-Jones potential. We have found a variety of adlayer patterns that have different porous shapes such as the octagon and the hexagon. We have located chiral patterns such as the distorted octagon “DOCT” and the distorted reverse chevron “DRCH”, although the adsorbate molecules are achiral and possess the D_{2h} symmetry point group.

At low r_e values the ribbon “RB” and the octagon “OCT” patterns, with 2-center intermolecular interaction, are energetically very close with the RB being the global minimum structure. As r_e increases, for a low ρ/r_e ratio, the octagon “OCT” structure is the dominant GM, while at higher ρ/r_e , the geometry buckles to the chiral distorted octagon “DOCT”. As the ratio increases the chevron “CH” structure dominates the other structures, with 3-center intermolecular interaction.

At high, $r_e > 0.5$, the pattern buckles to many distorted patterns as the chevron structure becomes repulsive. One of the patterns is the chiral distorted reverse chevron “DRCH”. Another structure is the distorted chevron “DCH”. This motif has been observed experimentally by Kahn et al as the lowest minima of a compact mono-layer of hexaazatrinaphthylene on gold surface (141).

Chapter VI

A Model Study of Adlayer Geometries of Rigid Tetratopic Molecules on Square and Triangular Lattices

VI.1 Introduction

Szabelski and his coworkers examined the self-assembly of a 4-fold cross-shaped model molecules on a solid surface (20, 25, 142, 143). The potential energy between two molecules is governed by the sum of the site-to-site interactions between the molecules. The authors use a constant site-to-site potential energy. The molecular size is changed by changing the number of sites on each “arm”. Small molecules have a single site; the authors go as far as three sites per arm. The molecules were placed on a large square lattice – initially sparsely—then were allowed to move on the lattice, using a Metropolis Monte Carlo algorithm. Low potential energy “clusters” were recorded. The authors’ found compact structures containing square “voids” or “pores” between the arms, which increased in size as the number of interaction sites of the molecule increased. None of the pores were chiral. This was a simple calculation, using a fixed site-to-site potential energy.

D_{4h} , D_{5h} and D_{6h} symmetry patchy models (see **Chapter I**) have been studied by Doye et al using Monte Carlo simulation (114). The interactions are based on the Lennard-Jones potential. The sites were placed on disks with 4, 5 and 6 interaction sites regularly arranged on the surface of the disks. Without considering the size of the molecule they have reported two patterns. One in which the molecules have been arranged to form square pores, the other forms rectangular pores.

In this chapter we will study the pattern of tetratopic molecule on square and triangular lattices. The method is outlined in **Section VI-2**. Our results and discussions will be shown in **Section VI-3**, including all the geometries that have been found on a square lattice. In **Section VI-4** we discuss the results for a triangular lattice. In **Section VI-5** we conclude our study and compare our results with previous studies.

VI.2 Method

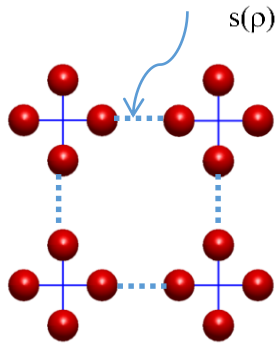
As described in **Chapter II** our model system is composed of tetratopic molecules (one molecule per lattice site). Each molecule is composed of four atom-like sites located at the tip of each arm (see **Figure II-1** in **Chapter II**). The intermolecular potential is calculated using pairwise site-to-site (coarse-graining) additive interactions using the Lennard-Jones potential. The size of the molecule is described by ρ , which is the arm length from the molecule's center of mass.

We use the same method described earlier in **Chapter II** to minimize 1000 starting points. Each starting point is a (2x2) "unit cell" space, $[\theta_1, \theta_2, \theta_3, \theta_4]$ and minimized to the zero gradient convergence criterion.

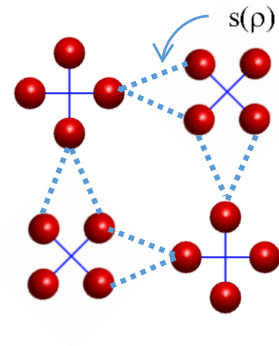
VI.3 Results and Discussion of a Tetratopic Molecule on Square Lattice:

In order to understand how the ground state (most stable) geometry changes with the parameters, it is useful to consider some key geometries. If the potential is governed by attraction, then (for a site-to-site potential) the geometry must optimize the potential energy to produce the strongest attraction. Given the nature of the site-to-site interaction, the maximum attraction is obtained when the nearest site-to-site separations are minimized. Such a geometry is shown in **Figure VI-1a**. It has p4mm symmetry, and we refer it as “square” (SQ) (p4mm), since the pores enclosed by the molecular “arms” are square. As the rotor length increases, the molecular sites must avoid each other and relax to other geometries (as will be shown later). The square geometry becomes forbidden when $s(\rho) \approx \sigma$, ($\sigma = \frac{r_e}{\sqrt{2}}$) (all of the distance parameters of the Lennard-Jones potential are defined in Chapter II). The nearest site-to-site distances $s(\rho)$ as a function of rotor length (ρ) for a square pattern are depicted in **Figure VI-2**. The relationships of $s(\rho)$ are shown in **Table VI-1**.

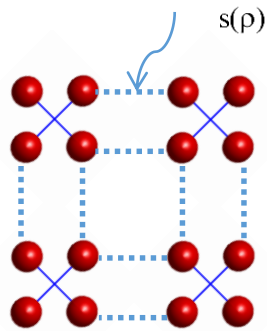
By contrast, if the rotor length is further increased, the pattern relaxes to more stable geometries, and the most stable geometry will be that in which all of the rotors twisted by $\pi/4$. This geometry is called a “cross” (CR), and also has p4mm symmetry, (**Figure VI-1c**). Another geometry, which has fixed angles, located between the square and the cross patterns is referred to as checkerboard (CB) and has p4mm symmetry, (**Figure VI-1b**). A structure which will be referred to as “compact” (CO) with p4 symmetry has shown in **Figure VI-1d**. This structure is chiral as it possesses no mirror plane of symmetry. To explain the chirality we introduce a compact structure for which all orientational angles are the same $\left\{\frac{\pi}{8}\right\}$. The last key geometry is referred as “tilt” and has orientational angles $\left\{\frac{\pi}{8}, -\frac{\pi}{8}\right\}$ with p4gm symmetry.



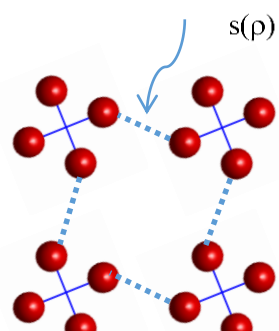
a) SQ (p4mm)



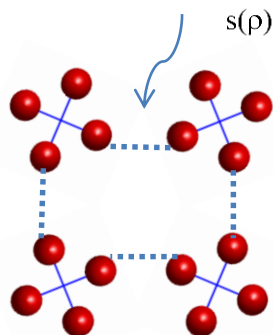
b) CB (p4mm)



c) CR (p4mm)



d) CO (p4)



e) TI (p4gm)

Figure VI-1: The main ground state pattern for the tetratopic system of rotors on a square lattice. a) Square (SQ), b) Checkerboard (CB), c) Cross (CR), d) Compact (CO), e) Tilt (TI). The symmetry plane groups are given in parenthesis (described Appendix C).

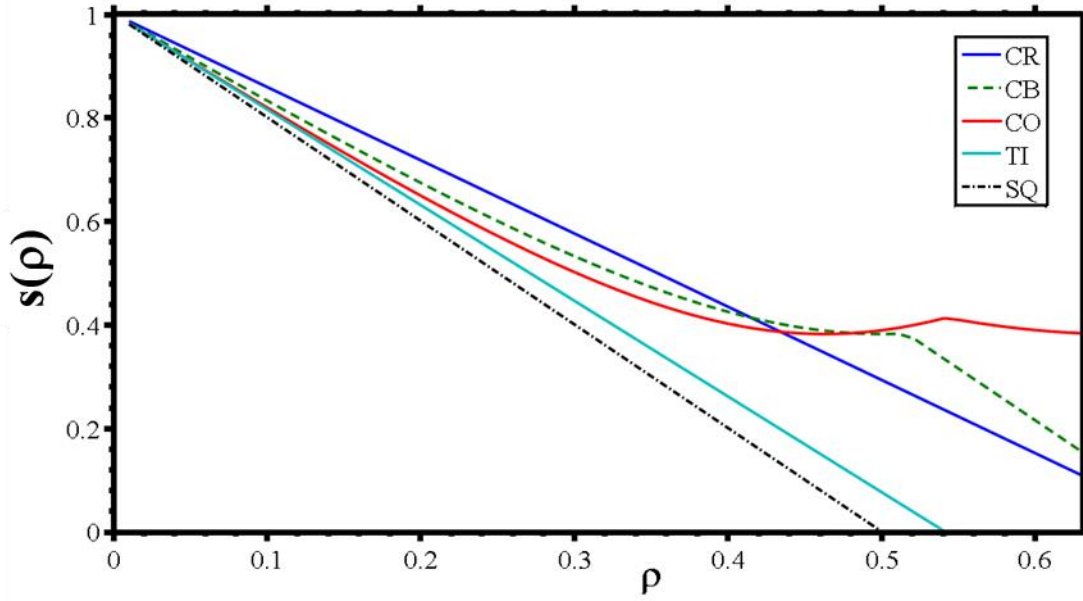


Figure VI-2: The nearest-neighbor site-to-site distance, $s(\rho)$, as a function of molecular length, ρ , for key geometries. The geometry labels square “SQ”, checkerboard “CB” cross “CR”, compact “CO” and tilt “TI” are shown in **Figure VI-1**. The number of nearest-neighbors NN (N_1) are shown in **Table VI-1**.

Table VI-1: Closest nearest-neighbor (NN) site-to-site distance, s , for specified geometries as a function of ρ . In the last column the number of the nearest-neighbors (N_1) are included.

Geometry	site-to-site distances	Number of nearest-neighbor NN (N_1)
Square “SQ”	$s(\rho) = 1 - 2\rho$	4
Checkerboard “CB”	$s(\rho) = \min(\sqrt{1 - (2 + \sqrt{2})\rho + (2 + \sqrt{2})\rho^2}, \sqrt{2} - 2\rho)$	8,2
Cross “CR”	$s(\rho) = 1 - \sqrt{2}\rho$	8
Compact “CO”	$s(\rho) = \min(\sqrt{1 - 4\rho \cos(\frac{\pi}{8}) + 4\rho^2}, \sqrt{1 - 2\sqrt{2}\rho \cos(\frac{\pi}{8}) + 2\rho^2})$	4,8
Tilt “TI”	$s(\rho) = 1 - 2\rho \cos(\frac{\pi}{8})$	4

In order to understand the changes in geometry, many of the important changes can be described by considering a single molecular rotation angle, ϕ . The square and cross patterns are both $\{\phi\}$ superlattices. The square has $\{0\}$ in the simple notation or $\theta_i=[0,0,0,0]$ in the full notation. On the other hand, the cross and checkerboard have $\left\{\frac{\pi}{4}\right\}$ and $\left\{0, \frac{\pi}{4}\right\}$ in the simple notation, respectively.

The patterns can be changed by four paths of single molecular rotations. The first path conrotatory by $\phi \in \left[0 - \frac{\pi}{4}\right]$ is notated by $\{\phi\}$, the second path disrotatory is given by $\{\phi, -\phi\}$. The third path is notated by $\{0, \phi\}$. The final path has $[0, \phi, -\phi, 0]$ full notation. The descriptions of the paths are shown in **Figure VI-3**. The first path leads to the cross pattern through a “distorted square”, which has p4 symmetry with superlattice notation $\{\phi\}$. We note that the absence of a mirror plane means that this superlattice is chiral. Path II also leads to the cross pattern “CR” through a geometry called a “distorted cross” and has p4gm symmetry group. The third and fourth paths are almost degenerate and end with the checkerboard structure “CB” through a geometry referred to as “square twisted cross” and has p4gm symmetry.

VI.3.a Order parameters

We use the $\Psi_4^c, \Psi_4^{|c|}$, and $|\Psi_4^s|$ order parameters already defined in Chapter 2. We have recorded the order parameter for each stationary point found.

The order values of parameters along the suggested single angle rotation paths are shown in **Figure VI-4** for $\phi \in \left[-\frac{\pi}{4}, \frac{\pi}{4}\right]$. By looking at the figure we note the following. The first of these order parameters, Ψ_4^c , can distinguish between the three limiting geometries shown in **Figure VI-1** and **Table VI-1**: For the SQ, the value is 1; for the CB, the value is 0; for the CR, the value is -

1; for CO, the value is 0 and for TI, the value is 0. The Ψ_4^c order parameter can therefore be used as a “binning” variable to assign geometries that are similar to these five key geometries.

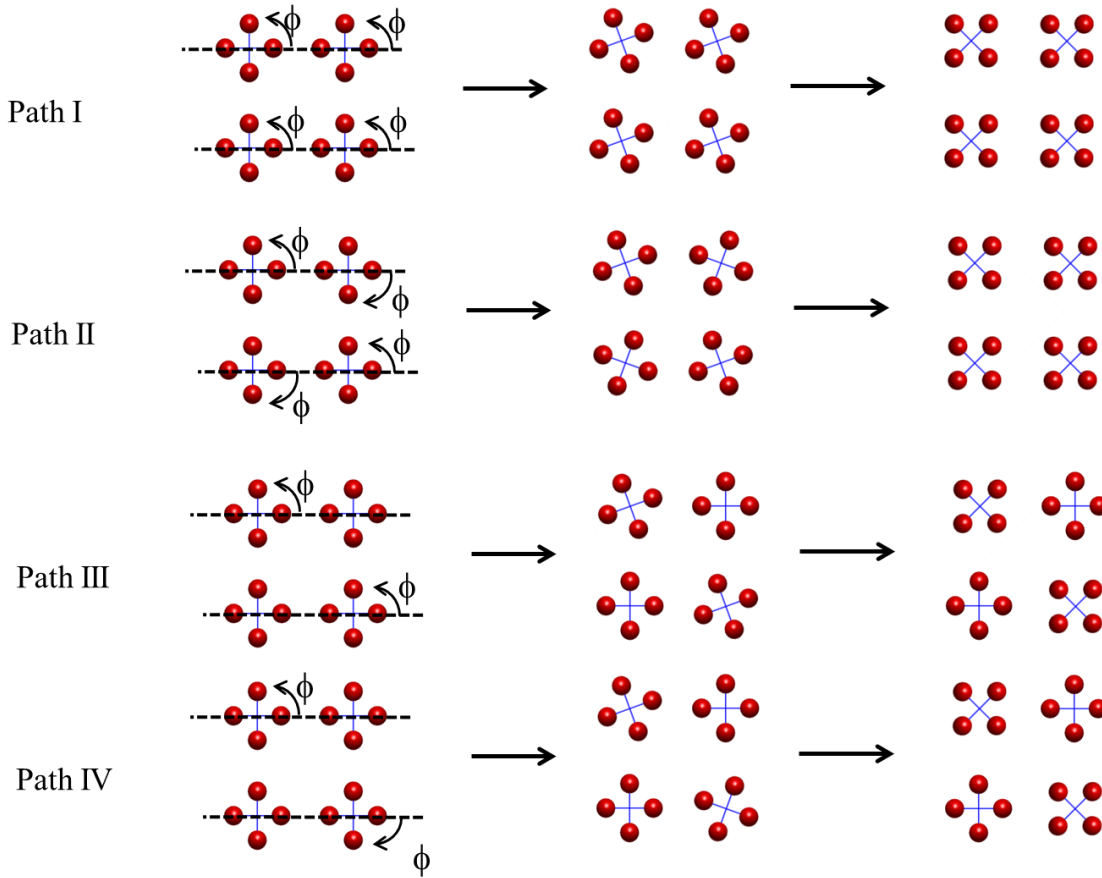


Figure VI-3: The description of rotating the square pattern. Path I conrotatory, Path II disrotatory (both lead to cross pattern), Path III and IV lead to checkerboard pattern. The patterns are described in **Figure VI-1**.

The second of these order parameters, $\Psi_4^{|c|}$, can distinguish between the geometries that have p4mm symmetry and the other geometries. For instance, SQ, CR, and CB patterns have $\Psi_4^{|c|} = 1$ while the other geometries have values < 1 .

The last of these order parameters, $|\Psi_4^s|$, can be used to identify chiral structures. Since the sense of rotation is arbitrary, enantiomers of the same geometry obey $\Psi_4^s \rightarrow -\Psi_4^s$ when all of the angles in the unit cell are reflected about either the x or the y axis. Therefore we take the absolute

value of this order parameter, since the actual sense of the rotation of the chiral structure depends on minimization (on other words the two homochiral structures are degenerate). We note the four geometries (SQ, CB, CR and TI structures shown in **Figure VI-1**) are all achiral, since they all possess a mirror plane. As will be discussed later, a path in which all angles of the unit cell are distorted equally will generate chiral structures (see **Figure VI-4** panel 2), with the “maximum chirality” being for a distortion angle of $\pi/8$. This is the case for a compact adlayer, which is shown in **Figure VI-1(d)**.

VI.3.b Results of a Full Space Minimization

The results of a full search of the input space for the GM are shown in **Figure VI-5**. The distribution of geometries is shown in **Fig VI-5(a)**, potential energies $V(\rho, r_e)$ in **Fig VI-5(b)**, order parameter $\Psi_4^c(\rho, r_e)$ in **Fig VI-5(c)**, order parameter $\Psi_4^{cl}(\rho, r_e)$ in **Fig VI-5(d)** and order parameter $\Psi_4^s(\rho, r_e)$ in **Fig VI-5(e)**. Large ρ and r_e values are unphysical, and are not color-coded. The ratio of small ρ /large r_e values are also somewhat unphysical.

We note the following from **Figure VI-5**. For small values of ρ , the square adlayer geometry (SQ) dominates. For low values of r_e , we note as the molecular size, ρ , increases, the potential energy tends to decrease. In addition, the GM geometry shifts from a pattern predominantly based on the square to those based on the cross, to eventually, at high ρ and r_e , the compact geometry.

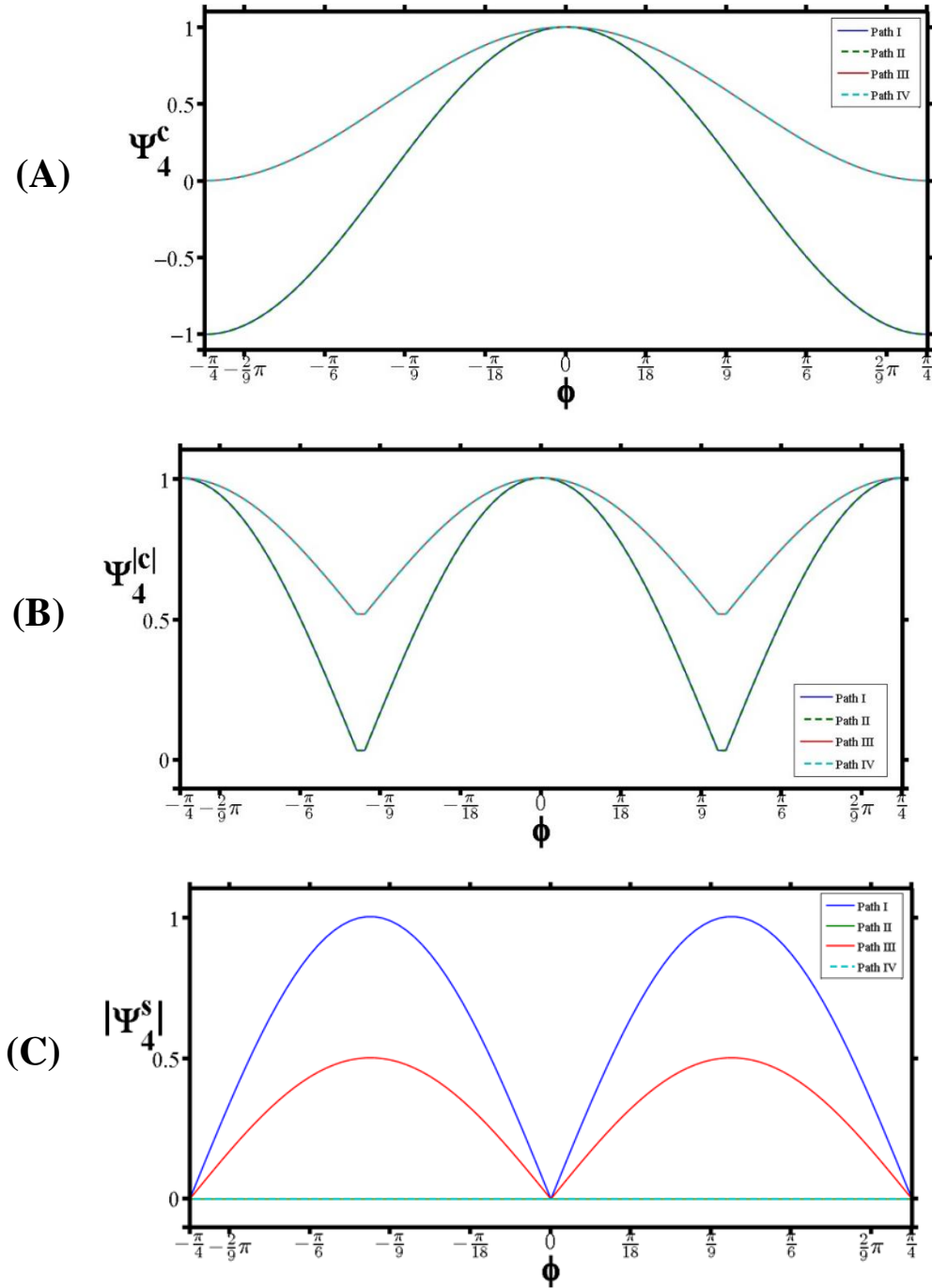


Figure VI-4: The order parameters as a function of paths that are shown in **Figure VI-1**, A) Ψ_4^c , B) $\Psi_4^{|c|}$ and C) $|\Psi_4^s|$. The legends describe each path (I, II, III and IV). Note in A path I and II coincide, path III and IV coincide. In B path II and IV are coincided. In C path I and II are coincided, path III and IV are coincided.

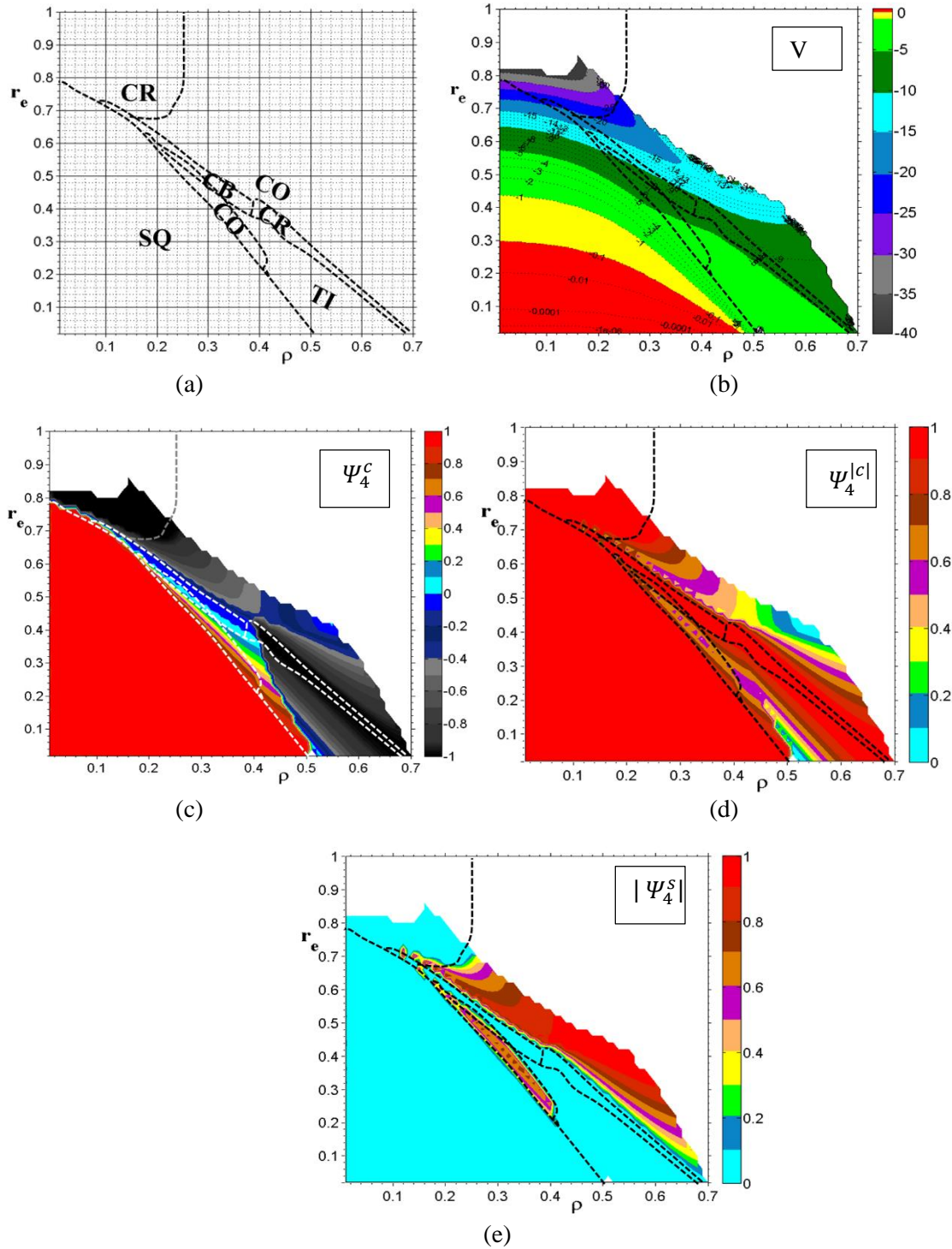


Figure VI-5: The contour plots of a full energy search. a) Geometry (ρ , r_e), b) Potential energy $V(\rho, r_e)$, c) Order parameter Ψ_4^c , d) Order parameter $\Psi_4^{|c|}$ and e) Order parameter $|\Psi_4^s|$. In each plots the color bars show the values of the contours. The labeling of the geometries SQ, CR, CB, CO and TI represent square, cross, checkerboard, compact, and tilt, respectively. The geometries are shown in **Figure VI-1**.

To explain this behavior, it is useful to take “cuts” through the parameter space. First we consider the case when r_e is a low value, $r_e=0.2$, as we expect the pore size to be large and for a larger value, $r_e=0.4$, which has less pore sizes. These two r_e values will cover all illustrative patterns we have found.

Case 1: $r_e=0.2$

The unbiased potential energy curves with the potential of the suggested key geometries are shown in **Figure VI-6**. The geometries along this constant, $r_e=0.2$, path are shown in **Figure VI-7**. We show in **Figure VI-8** the potential energy $V(\phi)$ as a function of the rotation angle ϕ for different molecule sizes (ρ).

First we consider the case when $\rho \sim 0.4$. We note from **Table VI-1** and **Figure VI-2** that $s(0.40)$ is 0.2 of the SQ pattern curve. Therefore, at $\rho=0.4$, the SQ geometry is at its optimum potential energy. Furthermore (as can be seen from **Figure VI-6**), this value of ρ is too small to allow access to the most attractive part of the potential for other geometries. Also, as can be seen from **Figure VI-8** (panel $\rho=0.4$), the SQ pattern is the GM geometry in the rotation paths suggested earlier. Thus we see at the point $(\rho, r_e) = (0.4, 0.4)$, the SQ is the preferred geometry.

However, if we increase the value of ρ , we would “hit the repulsive wall of the potential energy function” for the SQ geometry. So the adlayer distorts to avoid the repulsive wall the square geometry would impose. The distorted geometries are shown in **Figure VI-7** (see the examples $\rho=0.41, 0.45$, and 0.50). The distorted geometries are the GM of the rotational paths as shown in **Figure VI-8**. (panel $\rho \in [0.41, 0.55]$). As the ρ further increases the adlayer distorts more until it reaches the cross “CR” pattern for which all of the orientational angles are the same $\{\pi/4\}$ (see the examples $\rho=0.56$, **Figure VI-7** and **VI-8**).

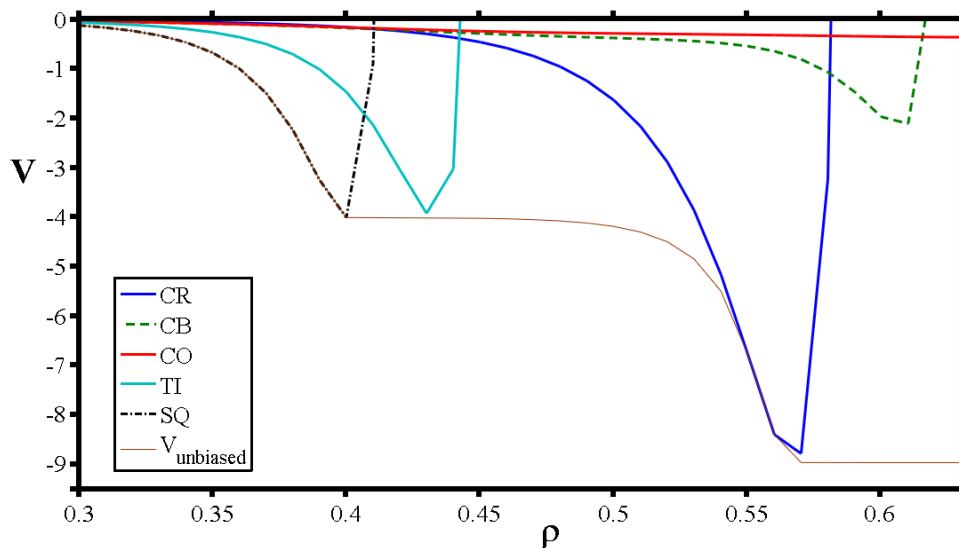


Figure VI-6: The potential energy function $V(\rho)$ for the geometries described in, **Figures VI-1**, at $r_e = 0.2$. The solid brown line is the potential of the GM obtained through the unbiased search. The abbreviations are described in **Table VI-1**.

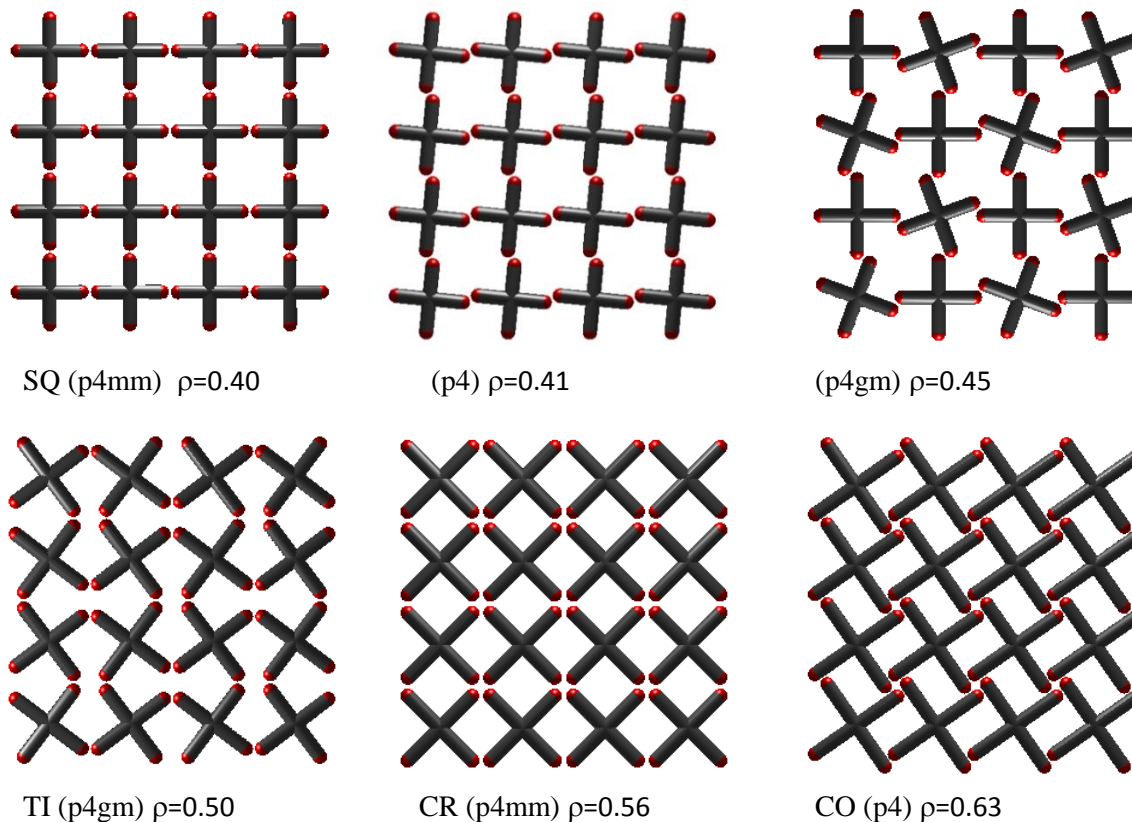


Figure VI-7: The geometries of the unbiased search for different ρ 's (at constant $r_e=0.2$). In the parenthesis are the wallpaper symmetry group symbols (for details see Appendix C).

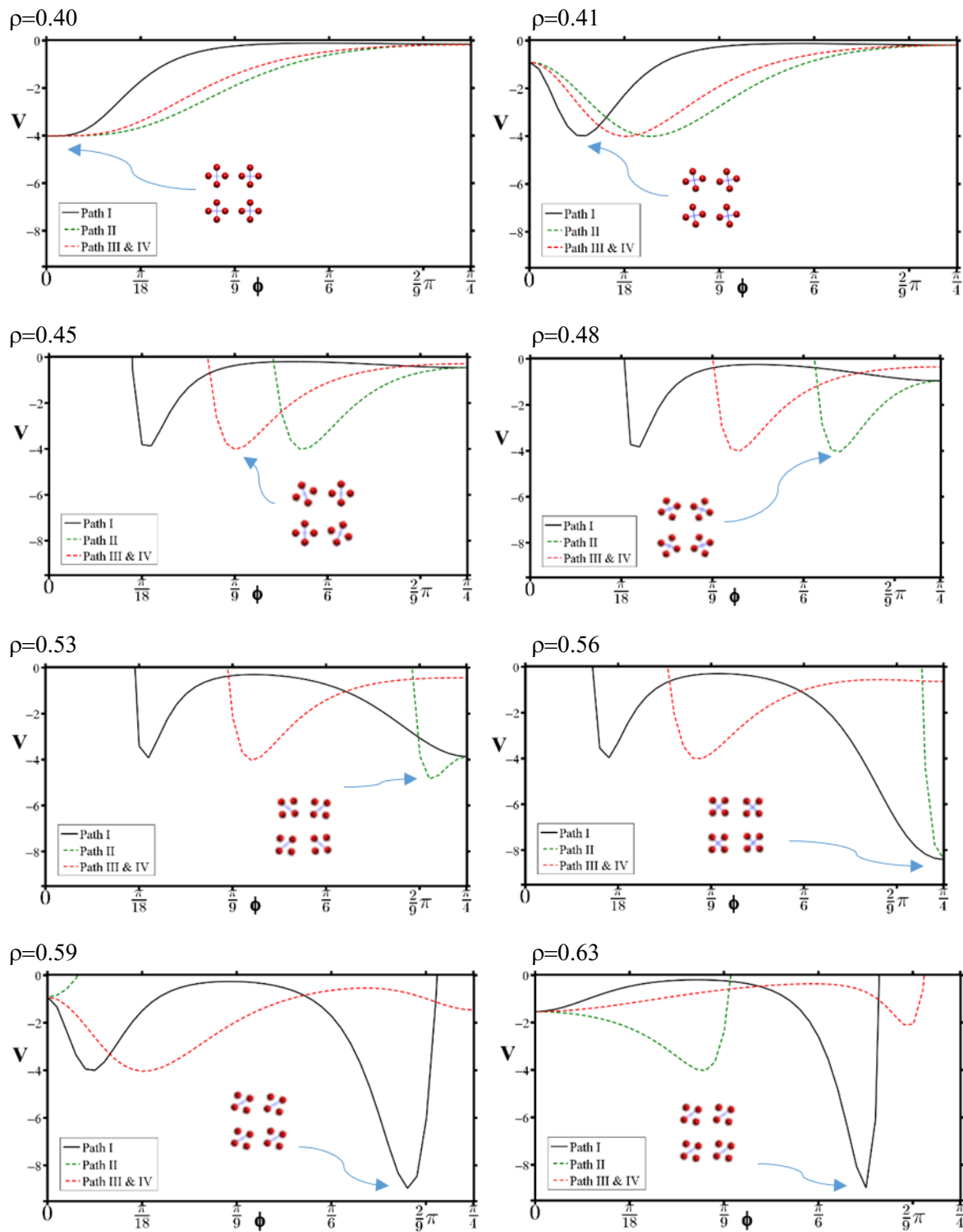


Figure VI-8: The potential energy $V(\phi)$ as a function of the rotation angle ϕ for different molecule size (ρ) at fixed $r_e=0.2$, the cartoons on the figures show the global minimum pattern among all the other geometries of paths. Note: for $\rho = 0.41, 0.59$ and 0.63 the global minimum patterns are chiral. Path IV coincide with path III because they are almost degenerate. For $\rho=0.45$ the global minimum goes through path IV.

By $\rho > 0.56$ the CR pattern hits the repulsive wall of the potential. As can be seen from **Figure VI-1** the cross pattern starts at $s(\sim 0.56) = 0.2$. At this region ($\rho > 0.56$) the chiral compact “CO” geometry is the GM, with the orientational angles less than $\pi/4$. All the CO pattern in this region has a $\Psi_4^s < 1$, (see contour diagram in **Figure VI-5e**), which means the CO example that we give in the key geometries is not seen here.

Case 2: $r_e = 0.4$

The curve of the unbiased potential energy minimization with the potential energy of the key geometries is shown in **Figure VI-9**. The geometries are shown in **Figure VI-10**. The potential energy along the distortion paths, described above, for some illustrative results (rotor size ρ) are shown in **Figure VI-11**.

Again looking back to **Figure VI-1**, we see that the $s(\rho \sim 0.3)$ is 0.4 for the SQ curve, so we expect that at this region the SQ geometry starts to hit the repulsive wall. It can be seen in **Figure VI-9** that $\rho < 0.3$ the SQ pattern is at its optimum potential energy. This also can be seen from the distortion paths in **Figure VI-11**, panel $\rho = 0.29$.

For $\rho > 0.3$, to prevent the repulsive wall the adlayer distorts to a distorted structure as shown in **Figure VI-10**, panels $\rho = 0.32$, $\rho = 0.33$ and $\rho = 0.37$. The first two have $p4$ symmetry and therefore they are homochiral because they possess no mirror plane. By increasing the rotor size the pattern reaches the checkerboard GM geometry (see the example at $\rho = 0.4$ **Figure VI-10** for geometry and **Figure VI-11** for distortion path). By $\rho = 0.41$ the next candidate GM is the CR structure. The CR structure has a little bit lower energy than the CB structure as can be seen in **Figure VI-11**. This can be explained because the CR geometry has a 4-fold attraction geometry, and the next nearest neighbor (N_2) plays a role in determining the GM.

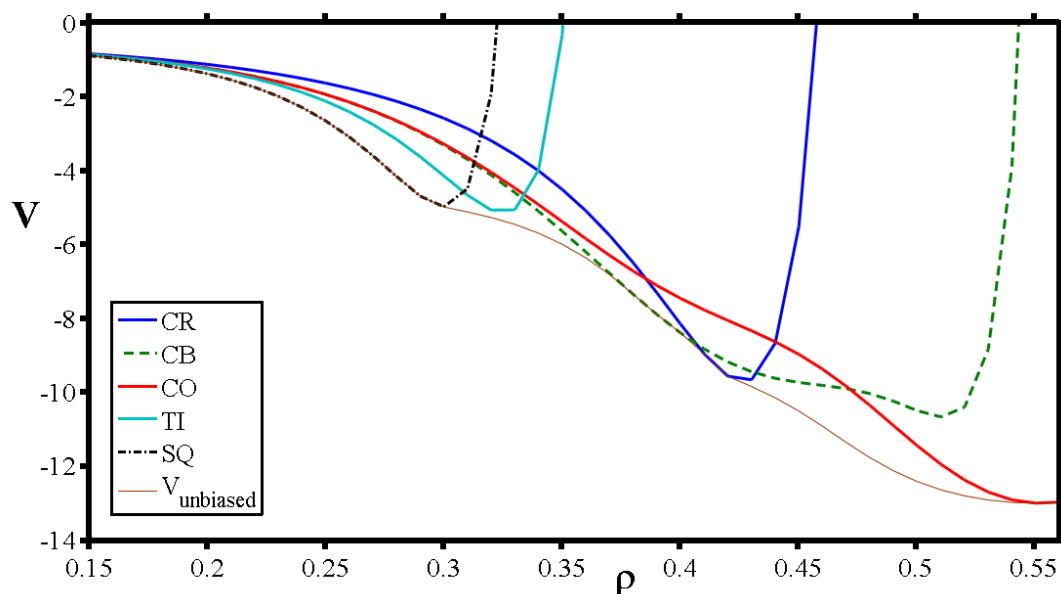


Figure VI-9: The potential energy function $V(\rho)$ for the key geometries at $r_e = 0.4$. The solid brown line is the potential of the GM obtained through the unbiased search. The abbreviations are described in **Table V-1**.

By $\rho > 0.41$ the CR pattern becomes repulsive and distorts to the CO chiral pattern, which has $p4$ symmetry. The example shown in **Figure VI-10**, $\rho = 0.55$, is the optimum key geometry suggested earlier and has a maximum value of $\Psi_4^s = 1$ (see also **Figure VI-9**). This is also seen in **Figure VI-11**, $\rho = 0.55$ panel, the optimum GM minimum occurs at $\pi/8$ orientational angles on conrotatory, path I, as described earlier, **Figure VI-3**.

VI.3.c Local Minima

With the above comments in mind, we consider the results of a large number of minimizations, to determine the amount of phase space associated with each minimum. Each local minimum reached by the minimization procedure is tested for a stationary point by checking its hessian (See **Appendix A**). The histograms of the potential energy of the several illustrative examples at $r_e = 0.4$ are shown in **Figure VI-12**. At $\rho = 0.29$, all of the initial points descend to the square GM. By $\rho = 0.32$, we note the appearance of a LM with energy only slightly greater than

that of the “distorted” square GM. Interestingly, this LM has a larger probability than the GM. This can be explained by examination of **Figure VI-11(e)** path III, where we can see a large range of the angle space associated with the CB geometry. By $\rho=0.37$, the CB is the energetic global minimum. Interestingly, the other significant minimum populated by the “quench” is an irregular structure in which one of the molecules is “trapped” at a different angle from the other three in the unit cell. The last LM has TI structure with very low probability. By $\rho=0.41$ the GM is the CR pattern. The CB structure as expected is the second minimum (see **Figure VI-11(f)**) with probability larger than GM. The third minimum with the highest probability is the one which has one angle defect from the other three angles in the unit cell. By $\rho=0.55$, the highest probable minimum is the CO pattern GM. The next LM is the structure which has irregular structure.

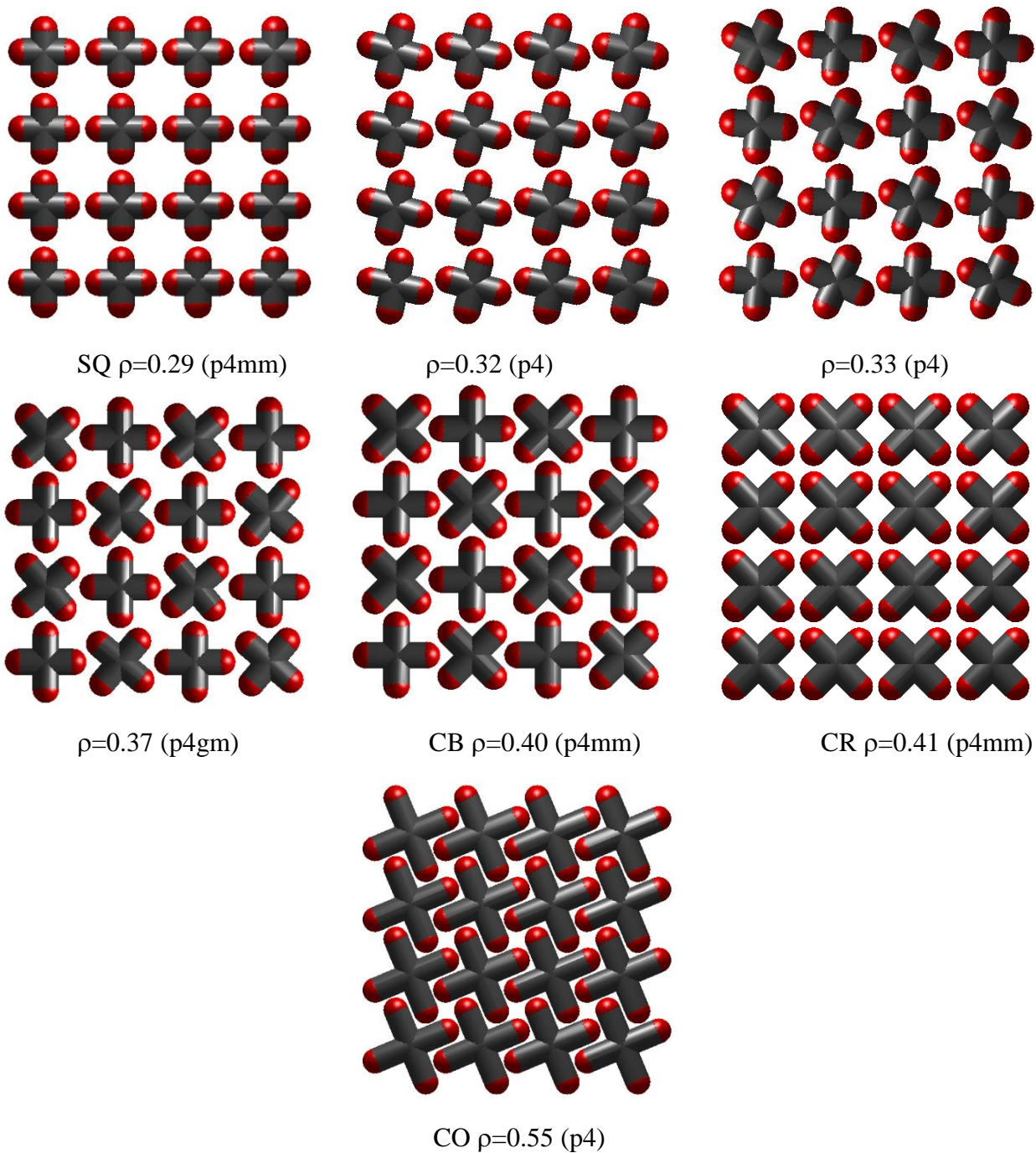


Figure VI-10: The geometries found from the unbiased search for different values of ρ (at constant $r_c=0.4$). In the parentheses are the wallpaper symmetry group symbols (for details see Appendix C).

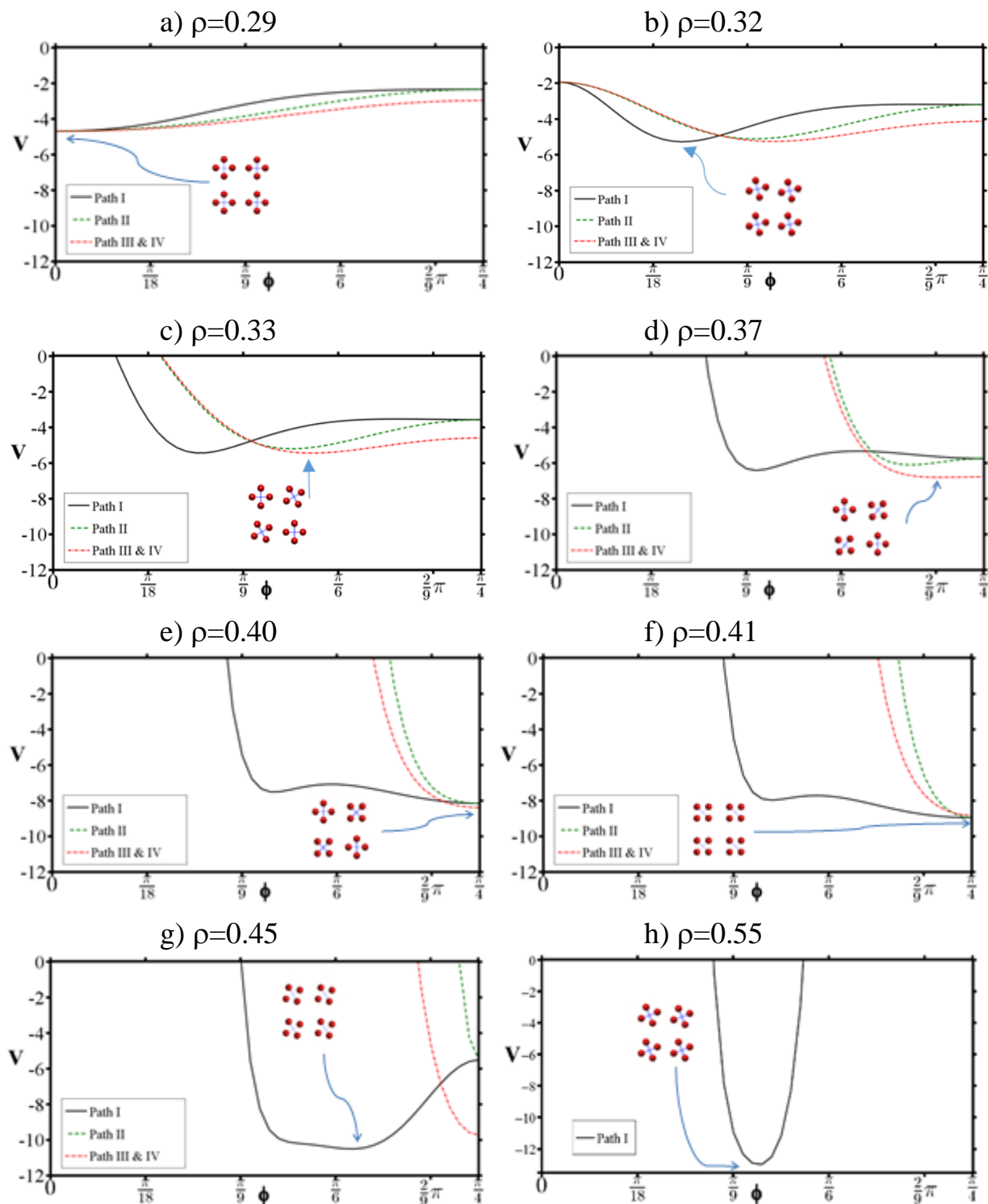


Figure VI-11: The potential energy $V(\phi)$ as a function of the rotation angle ϕ for different molecule size (ρ) at fixed $r_e=0.4$. The cartoons on the figures show the global minimum pattern among all the other geometries of paths. Note: for $\rho=0.32, 0.33,$ and 0.45 the global minimum patterns are chiral. Path IV is align with path III because they are almost degenerate. For $\rho=0.55$ path II, III, IV are repulsive and for clarity has a different scale.

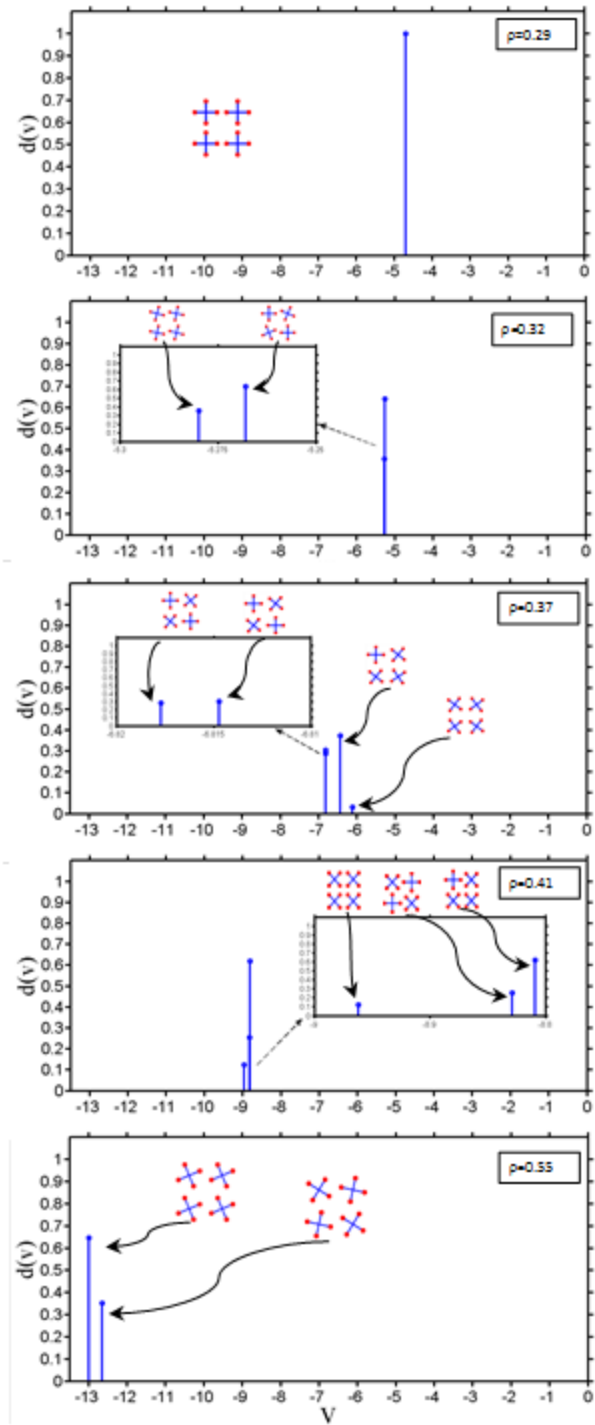


Figure VI-12: Probability histograms of minima of Lennard-Jones at constant $r_e=0.4$ for several rotor lengths, $\rho=0.29, 0.32, 0.37, 0.41$ and 0.55 . In each plot are shown the cartoons of the minima found by an unbiased search of many starting points.

VI.4 Results and Discussion of a Tetratopic Molecule on a Triangular Lattice:

The energy contour diagram of the full space search as well as the order parameters contour are shown in **Figure VI-13**. The geometries are shown in **Figures VI-14, VI-15, and VI-16**, at constant values of $r_c=0.20, 0.28, \text{ and } 0.40$, respectively. The main geometries are classified as follows

- (a) The checkerboard “CB” has p2mm wallpaper symmetry, and has orientational angles $\{0, \pi/4\}$ AABB form (see the herringbone classification in **Chapter II**).
- (b) The rectangle “RC” pattern as it has a rectangle porous shape with c2mm symmetry and angles $\{0\}$. (Note that this is equivalent to $\{\pi/3\}$).
- (c) The cross “CR” with c2mm symmetry and angles $\{\pi/4\}$.
- (d) The pinwheel 1 “PW1” with c2mm symmetry and angles $\{\phi, \pi/2-\phi, 0, \pi/4\}$.
- (e) Two herringbone structures, one with p2 symmetry and the other with p2gg symmetry.
- (f) The pinwheel 2 “PW2” with p2 symmetry.
- (g) The twisted checkerboard “TCB” with c2mm symmetry.

The nearest neighbor NN site-to-site distances $s1(\rho)$ and the next nearest neighbor NNN $s2(\rho)$ as a function of rotor length are presented in **Figure VI-17** and **Tables VI-2 and VI-3**.

VI.4.a Orientational order parameters

We employed the several order parameters to classify the adlayer geometries. Here we use the following four order parameters.

$$\Psi_4^c(\Delta\theta) = \frac{1}{4} \sum_{i=1}^4 \frac{1}{8} \sum_{j=1}^n \cos(4\Delta\theta) \quad \text{VI-4}$$

$$P_2(\Delta\theta) = \frac{1}{4} \sum_{i=1}^4 \frac{1}{8} \sum_{j=1}^n \frac{3\cos^2(\Delta\theta) - 1}{2} \quad \text{VI-5}$$

where $\Delta\theta = |\theta_i - \theta_j|$

$$\Psi_6^{|c|} = \frac{1}{4} \sum_{i=1}^4 |\cos(6\theta_i)| \quad \text{VI-6}$$

$$|\Psi_6^s| = \frac{1}{4} \left| \sum_{i=1}^4 \sin(6\theta_i) \right| \quad \text{VI-7}$$

For the checkerboard geometry the order parameters values =0.5 while for the rectangle geometry

$\Psi_4^c(\Delta\theta) = \Psi_6^{|c|} = P_2(\Delta\theta) = 1$ and $|\Psi_6^s| = 0$. The cross structure has $\Psi_4^c(\Delta\theta) = |\Psi_6^s| = P_2(\emptyset) = 1$, $\Psi_6^{|c|} = 0$.

VI.4.b Result of full search at constant values of r_e

To interpret our results we will consider cuts of **Figure IV-13** at constant values of r_e . These values cover all the geometries reported in this study, classified as low $r_e=0.2$, medium $r_e=0.28$ and high $r_e=0.4$.

Case1: $r_e=0.20$

The potential energy curve of the unbiased search with the potential energy curves for biased geometries are shown in **Figure VI-18**. Looking to the s1 curve, **Figure VI-17** we see that both the checkerboard “CB” and the rectangle “RC” structures have the same s1 value. However the s2 value of the CB is much lower than that of the RC. We expect at low ρ the global minimum geometry is checkerboard. However the number of s2 (N_2) of the RC is higher than that for the CB (see **Table VI-3**). So for some values of $\rho \in [0.34, 0.39]$ the RC is the global minimum.

The RC and CB geometries become repulsive for $\rho > 0.4$, so the adlayer relaxes to twisted geometries. By $\rho = 0.41$ the twisted checkerboard “TCB” is the global minimum. For $\rho > 0.41$ the geometries consecutively are the herringbone “HB” p2gg symmetry, pinwheel 1 “PW1” and pinwheel 2 “PW2”.

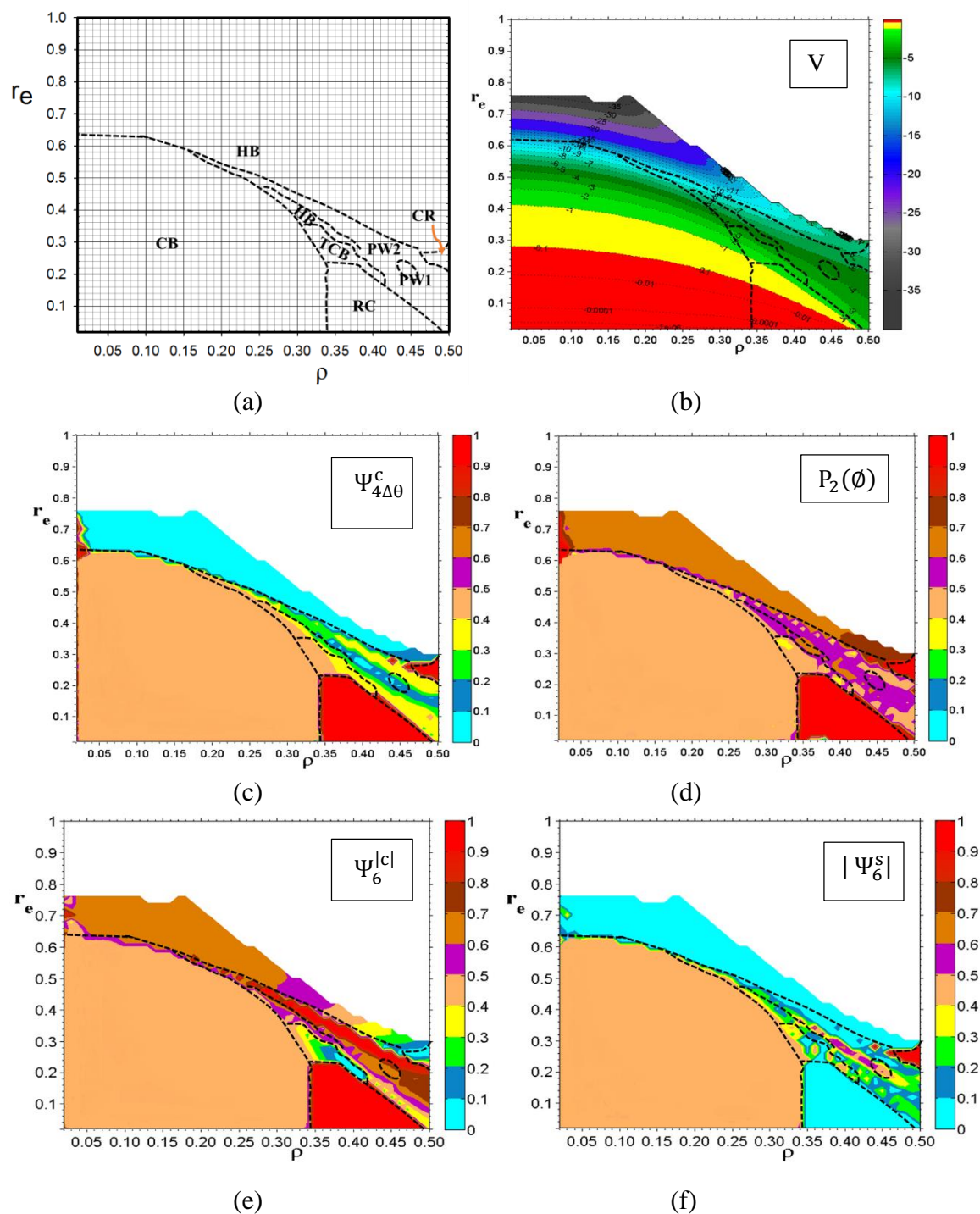
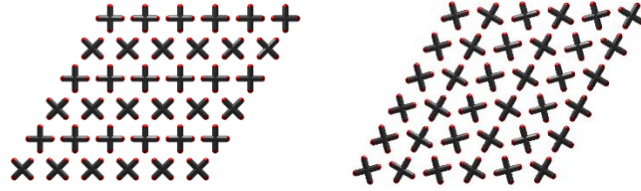
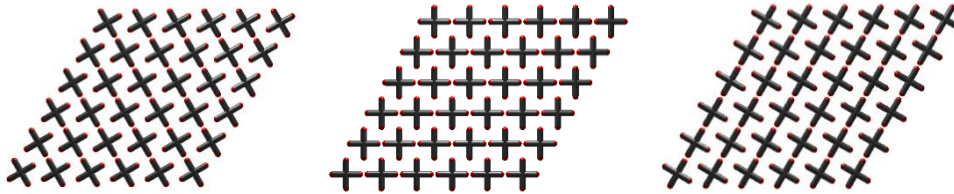


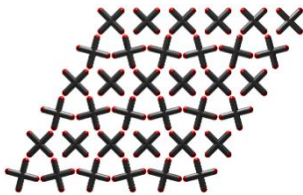
Figure VI-13: Contour plots of various properties of the most stable geometry of tetratopic molecule on a triangular lattice as a function of Lennard-Jones parameters (ρ , r_e). Panels (b) potential energy, V ; (c)-(f) orientation order parameters $\Psi_{4\Delta\theta}^c$, $P_2(\Delta\theta)$, $\Psi_6^{|c|}$, and $|\Psi_6^s|$, respectively. Panel (a) summarizes this in the “phase diagram”, in which geometries are assigned using the criteria given in the text. The “phase boundaries” established in panel (a) are reproduced in the other panels. (Abbreviations used: CB = checkerboard; rectangle = RC; HB= herringbone; PW = pinwheel; CR = cross; TCB = Twisted checkerboard.)



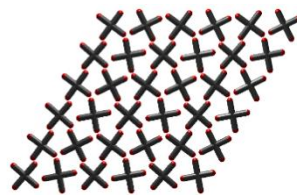
CB $\rho=0.33$ (p2mm)



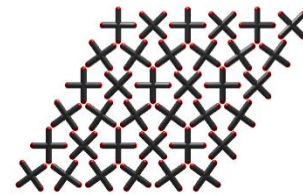
RC $\rho=0.39$ (c2mm)



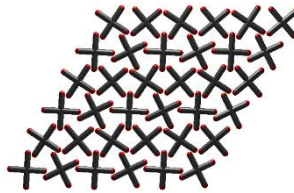
TCB $\rho=0.41$ (c2mm)



HB $\rho=0.43$ (p2gg)

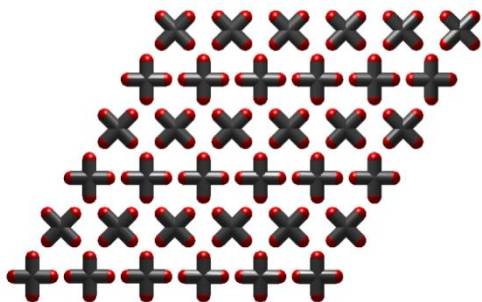


PW1 $\rho=0.45$ (c2mm)

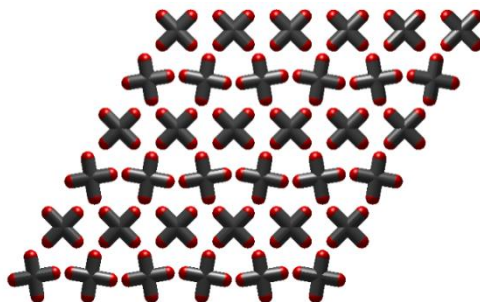


PW2 $\rho=0.5$ (p2)

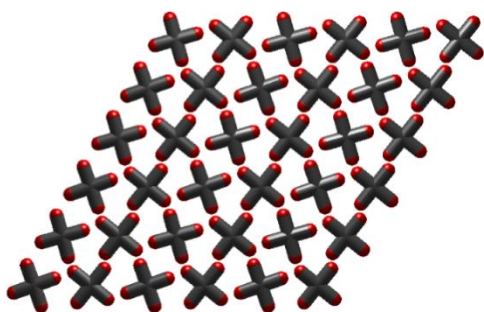
Figure VI-14: The geometries of the unbiased search for different values of ρ (at constant $r_e=0.2$). The abbreviations are described in **Figure VI-13**. In the parenthesis are the wallpaper symmetry group symbols (for details see Appendix C). Note: Two equivalent patterns of CB and three equivalent patterns of the RC pattern are shown.



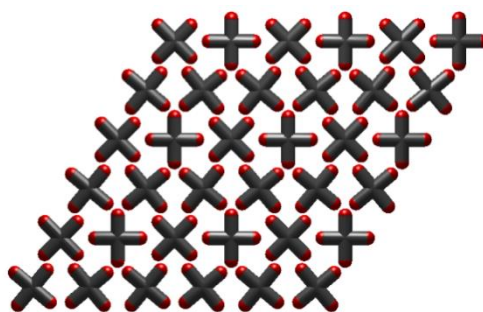
CB $\rho=0.33$ (p2mm)



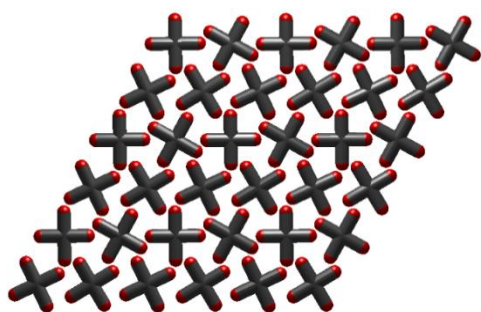
TCB $\rho=0.35$ (c2mm)



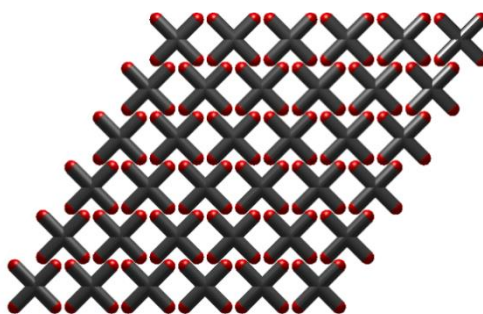
HB $\rho=0.38$ (p2gg)



PW1 $\rho=0.40$ (c2mm)

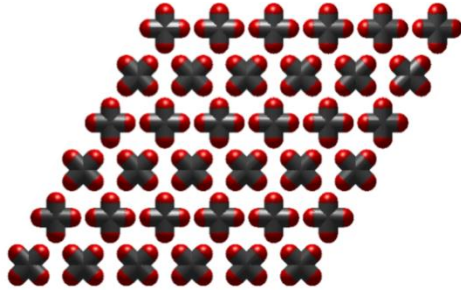


PW2 $\rho=0.43$ (p2)

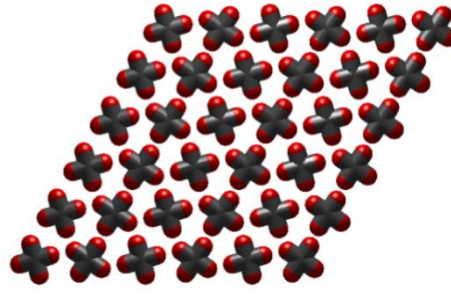


CR $\rho=0.50$ (c2mm)

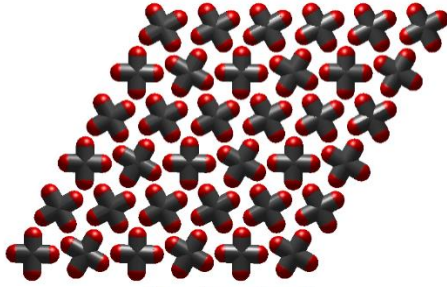
Figure VI-15: The geometries of the unbiased search for different values of ρ (at constant $r_c=0.28$). The abbreviations are described in **Figure VI-13**. In the parenthesis are the wallpaper symmetry group symbols (for details see Appendix C).



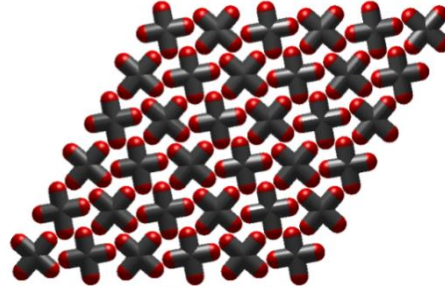
CB $\rho=0.29$ (p2mm)



CB $\rho=0.30$ (p2mm)



PW2 $\rho=0.34$ (p2)



HB $\rho=0.39$ (p2)

Figure VI-16: The geometries of the unbiased search for different values of ρ (at constant $r_e=0.40$). The abbreviations are described in **Figure VI-13**. In the parenthesis are the wallpaper symmetry group symbols (for details see Appendix C).

Table VI-2: Closest nearest-neighbor (NN) site-to-site distance, $s1$, for specified geometry as a function of ρ . Including the number of nearest-neighbor. Note: There are two possible NN distances for the PW1 and HB geometry. Note: $\vartheta=3\pi/10$, $\theta_1=5\pi/18$, $\theta_2=\pi/18$.

Geometry	site-to-site distances	Number of nearest-neighbors NN (N_1)
CB	$s1(\rho) = 1 - 2\rho$	1
RC	$s1(\rho) = 1 - 2\rho$	2
CR	$s1(\rho) = \sqrt{1 - (\sqrt{2} + \sqrt{6})\rho + 4\rho^2}$	4
PW1	$s1(\rho) = \left(\begin{array}{l} \sqrt{1 - \rho\left(\frac{\sqrt{3} + 1}{\sqrt{2}} + \cos \vartheta + \sqrt{3} \sin \vartheta + \rho^2(2 + \sqrt{2} \cos \vartheta + \sqrt{2} \sin \vartheta)\right)}, \\ \sqrt{1 - \rho(\sqrt{3} + \sqrt{3} \cos \vartheta + \sin \vartheta) + \rho^2(2 + 2 \cos \vartheta)} \end{array} \right)$	2,2
HB	$s1(\rho) = \min \left(\begin{array}{l} \sqrt{1 - 2\rho(\sin \theta_1 + \sqrt{3} \cos \theta_1) + 4\rho^2}, \\ \sqrt{1 - 2\rho(\cos \theta_2 + \sin \theta_1) + 2\rho^2(1 + \sin(\theta_1 - \theta_2))} \end{array} \right)$	2,4

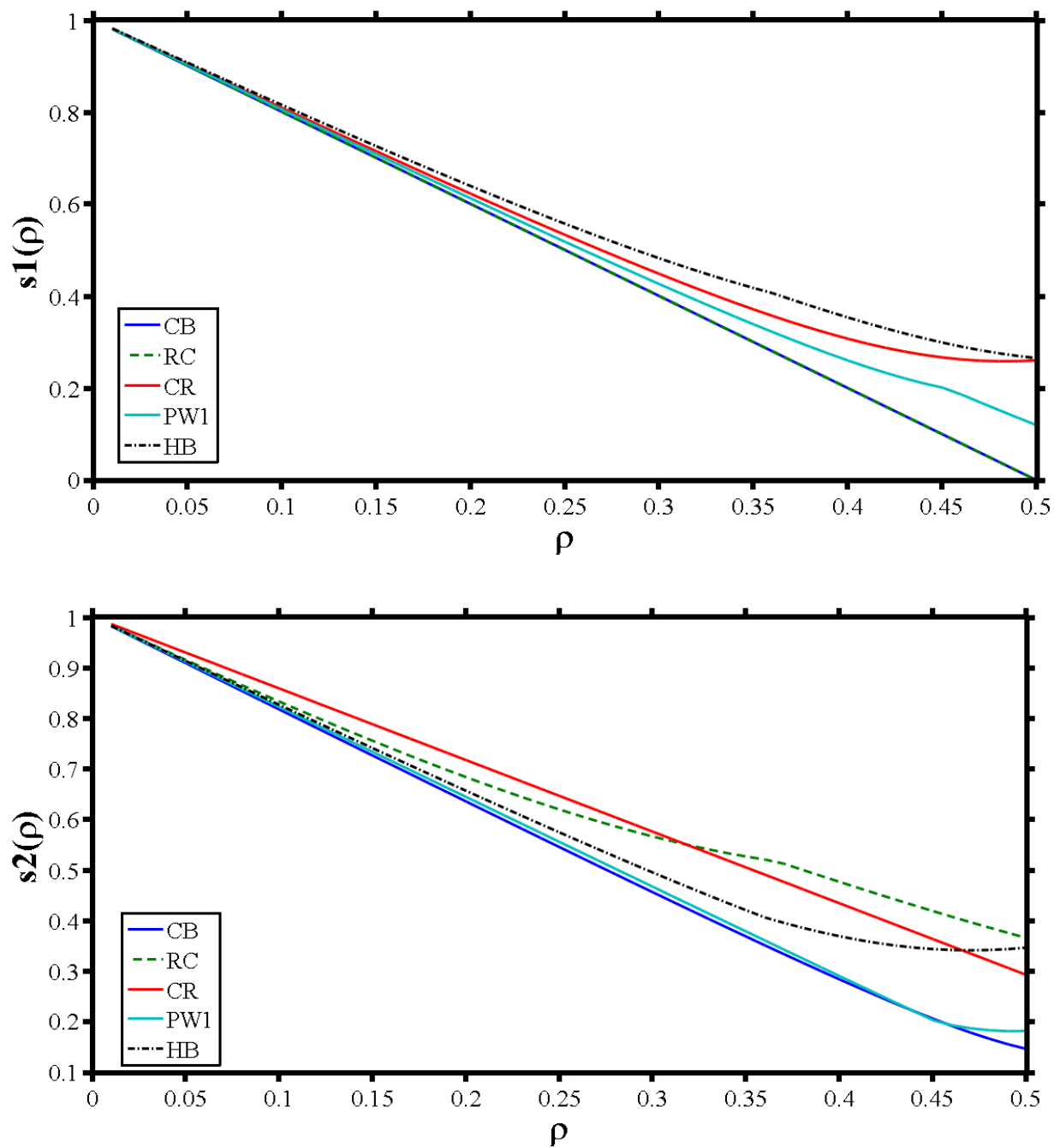


Figure VI-17: (Upper panel) the nearest neighbor NN $s1$; (Lower panel) the next nearest neighbor NNN $s2$ of the tetratopic model on a triangular lattice system. The legend inside each plot is the abbreviation of the adlayer described in **Figure VI-13**.

Table VI-3: Closest nearest-neighbor (NN) site-to-site distance, s_2 , for specified geometry as a function of ρ . We include the number of nearest-neighbor. Note: There are two possible NN distances for the SQ, PW1 and HB geometry. Note: $\vartheta=3\pi/10$, $\theta_1=5\pi/18$, $\theta_2=\pi/18$.

Geometry	site-to-site distances	Number of nearest-neighbors NN (N_2)
CB	$s_2(\rho) = \sqrt{1 - \left(\frac{1 + \sqrt{3} + \sqrt{6}}{\sqrt{2}}\right)\rho + (2 + \sqrt{2})\rho^2}$	4
RC	$s_2(\rho) = \min\left(\sqrt{1 - 2\sqrt{3}\rho + 4\rho^2}, \sqrt{1 - (1 + \sqrt{3})\rho + 2\rho^2}\right)$	4,8
CR	$s_2(\rho) = 1 - \sqrt{2}\rho$	4
PW1	$s_2(\rho) = \min\left(\sqrt{1 - \rho(\sqrt{3} + \sqrt{3}\cos\vartheta + \sin\vartheta) + \rho^2(2 + 2\cos\vartheta)}, \sqrt{1 - \rho\left(\frac{\sqrt{3} + 1}{\sqrt{2}} + \cos\vartheta + \sqrt{3}\sin\vartheta\right) + \rho^2(2 + \sqrt{2}\cos\vartheta + \sqrt{2}\sin\vartheta)}\right)$	2,2
HB	$s_2(\rho) = \min\left(\sqrt{1 - 2\rho(\cos\theta_2 + \sin\theta_1) + 2\rho^2(1 + \sin(\theta_1 - \theta_2))}, \sqrt{1 - 2\rho(\sin\theta_1 + \sqrt{3}\cos\theta_1) + 4\rho^2}\right)$	4,2

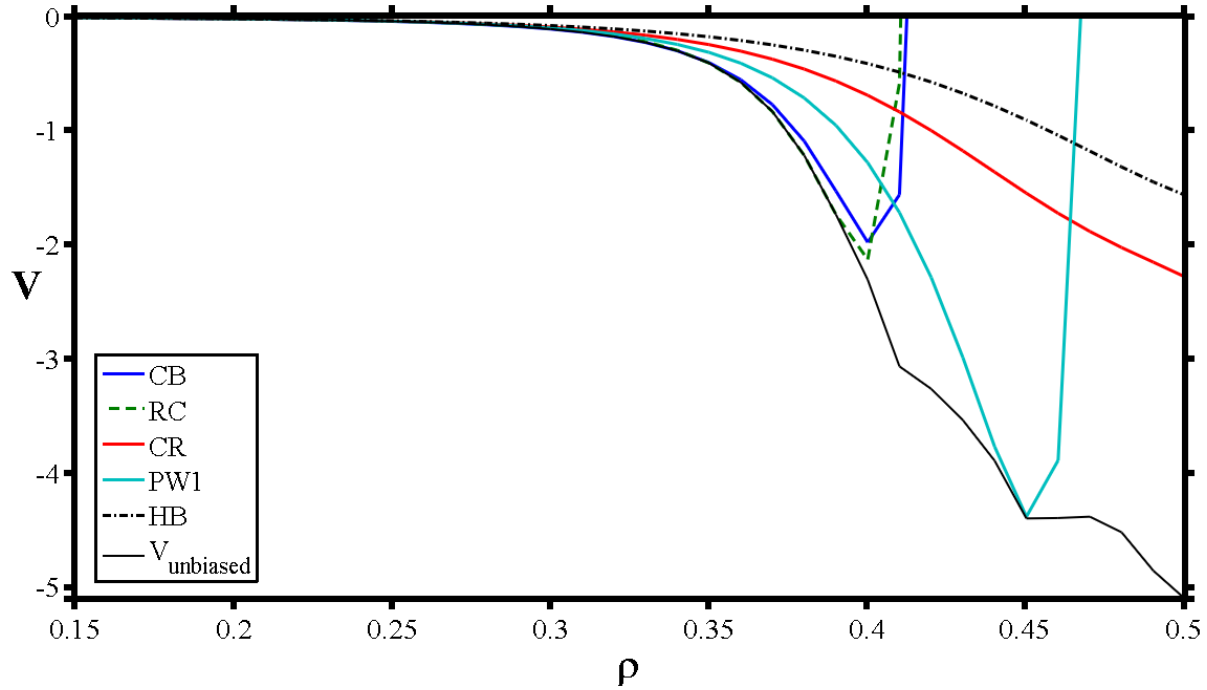


Figure VI-18: The potential energy function $V(\rho)$ for the geometries described in, **Figures VI-14**, at $r_c = 0.2$. The solid black line is the potential of the GM obtained through the unbiased search. The abbreviations in the legend are described in **Figure VI-13**.

Case2: $r_e=0.28$

The potential energy curve of the biased geometries and the potential energy curve of the unbiased minimization are shown in **Figure IV-19**. As expected the CB geometry is the GM at low values of ρ . The CB geometry becomes repulsive at $\rho>0.34$. Again the adlayer buckles to TCB at $\rho=0.35$ then to herringbone with p2gg symmetry. By $\rho = 0.39$ the pinwheel “PW1” structure is the next GM. This can be explained because the PW1 pattern has the second lowest s_1 and s_2 values among the geometries (see **Figure VI-17**). The PW1 geometry becomes repulsive for $\rho>0.4$. The adlayer relaxes to the chiral PW2 geometry with p2 symmetry. At $\rho\sim 0.45$ the PW2 geometry competes with the cross “CR” structure. This is due to the fact that the CR pattern having the third lowest s_1 and s_2 values as can be seen in **Figure VI-17**.

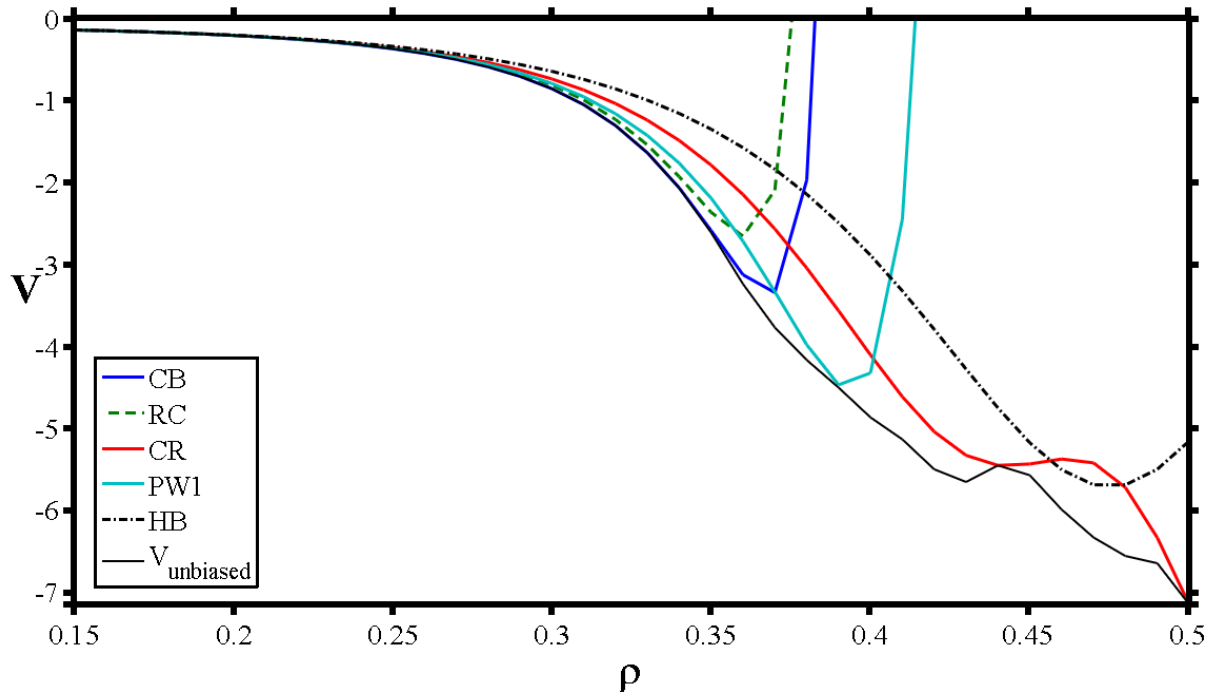


Figure VI-19: The potential energy function $V(\rho)$ for the geometries described in, **Figures VI-15**, at $r_e = 0.28$. The solid black line is the potential of the GM obtained through the unbiased search. The abbreviations in the legend are described in **Figure VI-13**.

Case3: $r_e=0.4$

The potential energy curves at $r_e=0.4$ are shown in **Figure VI-20**. At low ρ the CB structure is the global minimum. By $\rho=0.34$ the GM adlayer is the chiral PW2 structure. By $\rho>0.34$ the herringbone “HB” geometry, which has orientational angles= $\left\{\frac{5\pi}{18} \frac{\pi}{18}\right\}$ and p2 wallpaper symmetry, is the GM. The HB pattern is homochiral as it possess no mirror plane of symmetry.

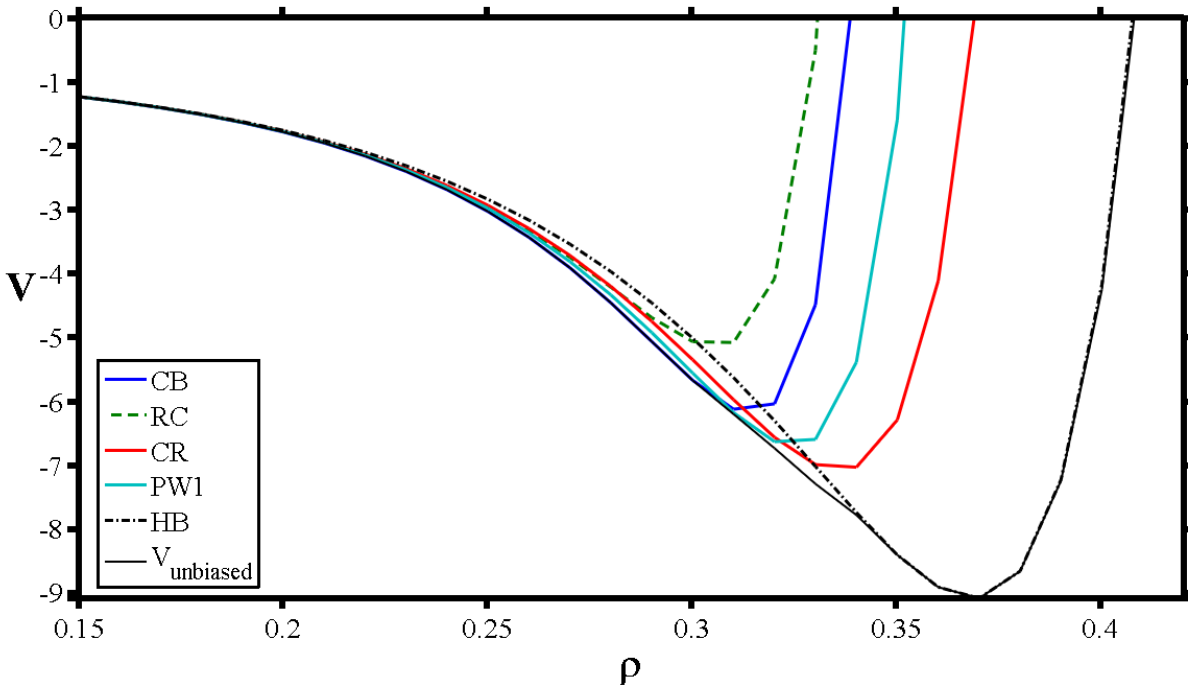


Figure VI-20: The potential energy function $V(\rho)$ for the geometries described in, **Figures VI-16**, at $r_e=0.4$. The solid black line is the potential of the GM obtained through the unbiased search. The abbreviations in the legend are described in **Figure VI-13**.

VI.5 Tetratopic Adlayer Conclusion and Comparison with Previous Studies

We have examined the geometries of the adlayer of a tetratopic model molecule on a square and a triangular lattice using Lennard-Jones coarse-graining potential. The model represents a fully occupied lattice surface. We have reported a variety of structures. On a square lattice we have found adlayers with symmetry plane group (p4mm), such as square, checkerboard and cross patterns. In addition a chiral compact geometry with p4 symmetry has been found for large ρ/r_e .

In contrast, on triangular lattices we have located several structures with c2mm symmetry such as the rectangle, cross, and pinwheel. Also we have found two chiral herringbone and pinwheel structures with p2 symmetry. In addition we have found some other distorted structures such as the twisted checkerboard and herringbone.

Experimental studies of phthalocyanine derivative adsorbates (tritopic molecules) have reported two structures resembling the cross and compact patterns. For instance, the cross structure with symmetry plane group (p4mm) has been located in a study of cobalt(II) hexadecafluorophthalocyanine ($F_{16}CoPc$) on a silver surface (14). The chiral compact and the rectangle geometries have been observed in a study of zinc(II) octachloro-phthalocyanine (Cl_8ZnPc) on a silver surface (13). The chiral herringbone has been reported for cobalt phthalocyanine on a graphite surface (81). Theoretically, the compact structure has been reported in a study by Kasperski and Szabelski (20). In addition the square and the rectangle geometries have been observed by Doye's group using Monte Carlo calculation (114).

In conclusion our coarse graining system has generated many of the reported experimental and theoretical adlayers. In addition to new geometries, such as the checkerboard, tilt and pinwheel structures, that have not been observed before.

Chapter VII

Monte Carlo Model Study of Adlayer Geometries of Rigid Ditopic Molecules on Square and Triangular lattices

VII.1 Introduction

Several research groups have reported on the self-assembly of ditopic molecules on square and triangular lattices using Monte Carlo simulation (18, 19, 37, 39, 42, 44). For instance Pastor et al (37) and Almarza (44) groups studied the rigid rod with two bonding sites on both lattices. These rods interact with the nearest-neighbors (NN) through anisotropic attractive interactions. The molecules arrange in one-dimensional linear chains with two 2-fold center of interactions.

Following the idea of the previous chapter we consider in this chapter Monte Carlo calculations for ditopic molecules on larger lattices and cluster sizes than the 2X2 unit cell used in previous chapters. The idea of this chapter is to look at several systems from earlier chapters (mainly **Chapter III** and **IV**) and examine whether the reported patterns remain when the “fixed site” geometry constraint is relaxed. Our model molecules are shown in **Section 2** including the model compound and the surface lattices. The method including the order parameters used are explained in **Section 3**. Our results and discussion is in **Section 4**. Finally the conclusions and comparison with the previous results are presented in **Section 5**.

VII.2 Model

VII.2.a. Model molecule 1

The model molecule is shown in **Figure VII-1** (91). Two interactions have been considered

between two neighboring molecules. First the tip-tip interaction is given by force field coarse-graining Lennard-Jones potential. The second interaction is between the stems of the molecules which have been described by the repulsive van der Waals radius = $\sigma/2$ of the Lennard-Jones potential. (see the interactions in **Figure VII-1 C**)

$$U^{ij}(\theta_i, \theta_j) = \omega(r_{ij}^\sigma) + \sum_{p=1}^p \sum_{q=1}^q u(r_{pq}^{ij}) \quad \text{VII-1}$$

where, where $u(r)$ is the pairwise site-to-site potential energy, typically Lennard-Jones potential, and $\omega(r)$ is the short range repulsive stem-stem interaction represent by van der Waals radius = $\sigma/2$. That is, if the stem-stem shortest distances $r_{ij}^\sigma < \sigma$, then $\omega \rightarrow \infty$.

To be consistent with the previous chapters the molecule's total length $L=2\rho$. In most cases we use 100 molecules. Each molecule is attached to the lattice site at its center of mass. For the square lattice, the lattice is a grid with 400 lattice sites, and the lattice site-to-site distance = 1 unit, which is confined in a 2 dimensional square of 20X20 dimensions. On the other hand the triangular lattice is compose of a grid of 20X20 lattice sites in a 2 dimensional rhombic lattice with angle = 60° between the main axis of the lattice (see the triangular lattice structure in **Chapter II, Figure II-3**).

The potential energy is calculated as the total tip-to-tip interaction (this is explained in **Chapter II**) potential energy for the molecules with cutoff distance = 2 L units.

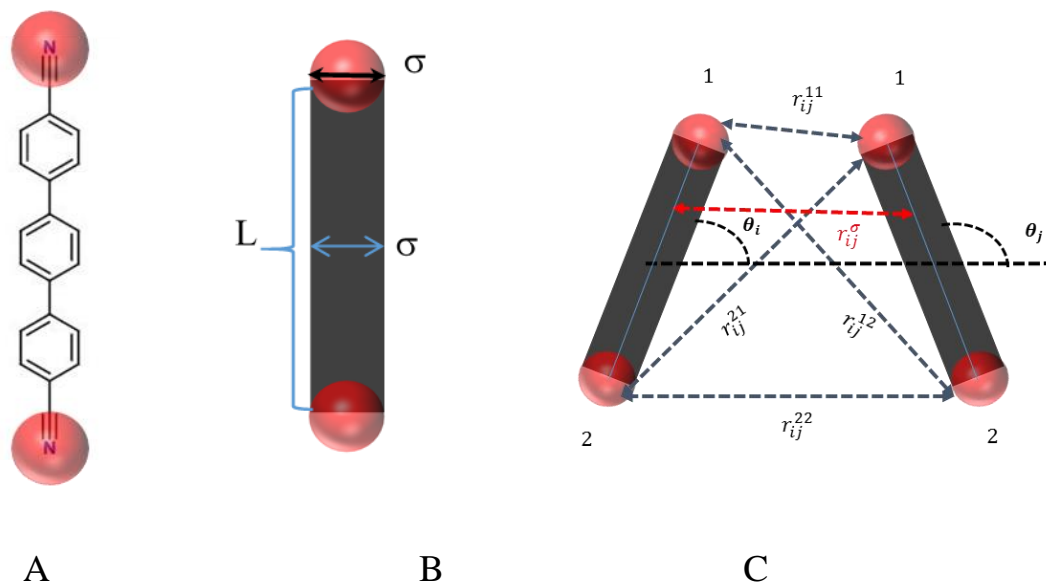


Figure VII-1: A) Dicarbonitrile-triphenyl molecule. B) Model of Molecule, L is the length of the molecule which is equal to 2ρ as described in **Chapter II, Figure II-1**. C) Scheme represents the interactions between two adjacent model molecules. σ is the van der Waals radius of the Lennard-Jones potential.

VII.2.b. Model molecule 2

This study considers a molecules with the shape described in **Figure VII-2**. This molecule was inspired by the linear class oligo-phenylene-ethynyls (ditopic molecules) (6, 7, 88-90). This molecule has two active sites one at each of the tips of the molecule (shown as red balls in **Figure V-2**). Two interactions have been considered between the two neighboring molecules. First the tip-tip interaction is given by force field coarse-graining Lennard-Jones potential. On the other hand the second interaction between the stems of the molecules which is described by the van der Waals radius = $\sigma/2$ of the Lennard-Jones potential. (See the interactions in **Figure VII-2 C**). The length of the molecule stem $L=1$ unit length, and the arm length $l=0.2$ unit length.

The potential energy between two adjacent molecules are calculated using **Equation VII-1**.

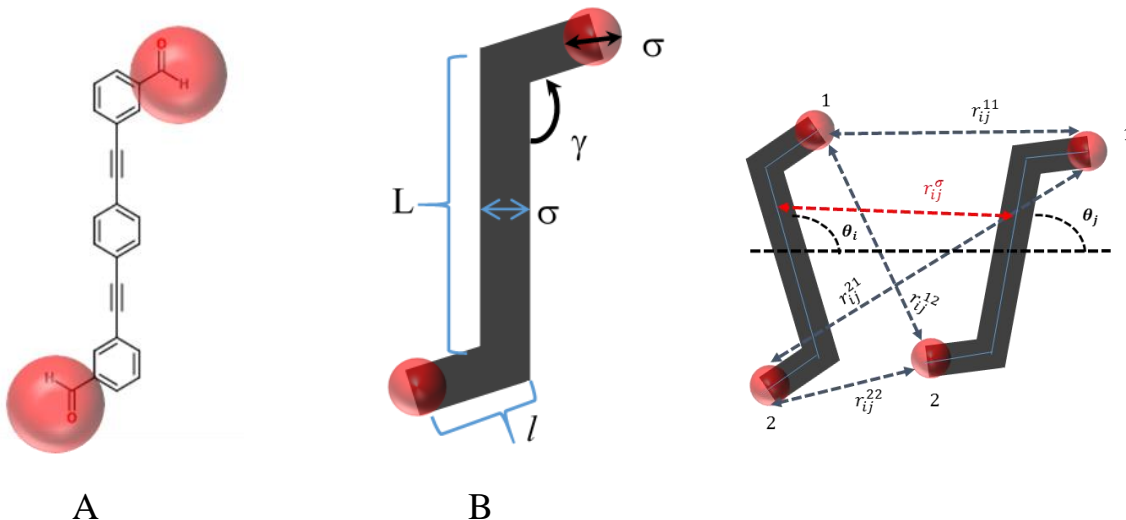


Figure VII-2: A) Oligo-phenylene-ethynylene with two main carboxylic groups. B) The force field coarse graining, the angle $\gamma=2\pi/3$, $L=1$, $l=0.2$, C) Scheme represents the interactions between two adjacent model molecules. σ is the van der Waals radius of the Lennard-Jones potential. Note: γ is selected to resemble the angle of the carboxylic group in oligo-phenylene-ethynylene with the stem of the molecule.

The surface sites have been taken as a grid of square lattice with two lattice constants one with low density of 400 sites with a distance between sites = 0.5 unit length and another with a high density of 3025 sites with a distance between sites = $\sigma = 0.18$. The molecules are attached to each site of the lattice at their center of mass.

VII.3 Method

VII.3.a NVT canonical Monte Carlo ensemble

The NVT ensemble is a Monte Carlo method in which the number of particles, the volume and the temperature are kept constant. The method of Temperature Replica Exchange Monte Carlo (T-REMC or simply REMC) is a Monte Carlo scheme that has been derived to achieve good sampling of systems that have a free-energy landscape with many local minima. In REMC the configuration swaps between the lower and higher temperature systems which allows the lower temperature system to escape from the one region of space to represent all of the energy allowed systems. The probability of the swaps can be calculated using equation VII-2:

$$\text{prop} = \min \left[1, e^{-\frac{(U_i - U_j) \left(\frac{1}{k_B T_j} - \frac{1}{k_B T_i} \right)}{k_B T_j}} \right] \quad \text{VII-2}$$

where, U and T are the potential energy and the temperature, respectively, of 2 swapped replicas; k_B is the Boltzmann constant, which is taken to be 1 for our study.

To identify the temperature where the phase transition occurs we carry out a naive calculations with 32 equally spaced temperatures selected for each system. Upon this calculation we selected our final 32 replicas used to collect the data. The system was advanced to 1000 Monte Carlo steps and the pause while attempt swap using Calvo's All-exchanges approach (144) (the method is explained in **Appendix D**).

The Monte Carlo "MC" step is composed of two movements applied to a randomly chosen molecules. First, there is the possibility of translation between randomly chosen empty lattice sites. The second movement is a single-molecule trial rotation $[-\delta\theta, \delta\theta]$ angle around the molecule's center of mass (the molecule is randomly chosen). The two movements are equally probable. Each MC step is subjected to Boltzmann acceptance criterion.

$$\text{acc} = \min \left[1, e^{\frac{-(U_{\text{new}} - U_{\text{old}})}{k_B T}} \right] \quad \text{VII-3}$$

where U are the potential of two updated configurations (new and old), k_B is the Boltzmann constant and T is the temperature of the system.

VII.3.b Grand canonical ensemble:

To determine thermodynamically stable ordered or disordered structures of model molecules using grand canonical ensemble (145, 146), the Temperature Replica Exchange Monte Carlo (T-REMC) simulation is carried out to study the structure of a monolayer self-assembly (MSA), using the grand canonical ensemble (or μ, V, T ensemble), where μ is the chemical

potential, V is the volume, T is the Temperature. In this ensemble μ , V, and T are fixed. 32 replicas have been created with an equally spaced temperature scale in the range [0.5-0.01] (D_e/k_B).

At each temperature, 5 moves are applied on each replica (displacement, rotation, flip, insertion and removal of molecules). All of the moves are equally probable. For the displacement rotation and flip moves a molecule is selected at random and given a new conformation by either moving to a new empty lattice site or rotating with a random angle or flipping around the molecule main axis. These moves are accepted within the Boltzmann acceptance criterion equation VII-2.

The creation of the particle is accepted with a probability:

$$\text{acc}(N \rightarrow N+1) = \min \left[1, \frac{N_s}{N+1} e^{(\mu - U_{N+1} + U_N) \left(\frac{1}{k_B T} \right)} \right] \quad \text{VII-4}$$

The removal of a particle is accepted with a probability:

$$\text{acc}(N \rightarrow N-1) = \min \left[1, \frac{N}{N_s} e^{-(\mu + U_{N-1} - U_N) \left(\frac{1}{k_B T} \right)} \right] \quad \text{VII-5}$$

where U is the total potential of the configuration, N_s is the number of sites on the lattice (represent the volume of the container), N is the number of molecules, μ is the chemical potential which is related to the particle density $\rho = N/N_s$.

$$\mu = k_B T \ln(\rho) \quad \text{VII-6}$$

All exchanges between replicas, Calvo's method (144) (**appendix D**), are used for swapping between replicas. The probability of swapping between replicas can be calculated using:

$$P(R_o \rightarrow R_n) = \min \left[1, e^{\left[(V_{R_n} - V_{R_o}) \left(\frac{1}{k_B T_{R_n}} - \frac{1}{k_B T_{R_o}} \right) \right] - \left[\left(\frac{\mu_{R_n}}{k_B T_{R_n}} - \frac{\mu_{R_o}}{k_B T_{R_o}} \right) (N_{R_n} - N_{R_o}) \right]} \right] \quad \text{VII-7}$$

where R_o and R_n are the old and new replicas, respectively.

For each swapping step the replicas are advanced to 1000 of the 4 moves and then paused while exchange is carried out. This is described as one Monte Carlo (MC) cycle. The only adjusted move is the angle selection, which is selected to get ~50% acceptance while the other moves depend on the vacancy of the lattice site.

We started with the same unbiased randomly chosen structure of 10 molecules for each replica. To determine the temperature where the phase transitions occur a naïve search of equally spaced temperature in the range of [1.0-0.001] was performed.

The system is subjected to 10^7 MC equilibration steps, then 10^8 MC collections steps. In each step we collect the potential energy, the square of the potential energy of each configuration and the order parameters. The heat capacity per molecule C_v/N can be calculated using:

$$\frac{C_v}{N} = \frac{\langle U^2 \rangle - \langle U \rangle^2}{k_B T^2} \quad \text{VII-8}$$

VII.3.c Order Parameters

$$\Psi_a^c(\Delta\theta) = \frac{1}{N} \sum_{i=1}^{i=N} \cos(a\Delta\theta) \quad \text{VII-9}$$

Where $\Delta\theta = |\theta_i - \theta_j|$ is the relative angle between two adjacent rotors with less than 2 units between their center of mass.

$$|\Psi_a^s(\theta)| = \left| \frac{1}{N} \sum_{i=1}^{i=N} \sin(a\theta_i) \right| \quad \text{VII-10}$$

$$|\Psi_a^c(\theta)| = \left| \frac{1}{N} \sum_{i=1}^{i=N} \cos(a\theta_i) \right| \quad \text{VII-11}$$

Where θ_i is the angle of i th rotor, N is the number of the molecules and “ a ” is a constant integer which depends on the system (this will explained for each individual system we show). Mainly $a=4$ for a square lattice and 6 for a triangular lattice.

VII.4 Result and Discussion

We have studied several molecules with different rotor lengths on both square and triangular lattice surfaces. These are selected as illustrative examples of the main structures in the parameter “phase diagram” in previous chapters.

VII.4.a Molecule 1, $\rho=0.29$ $r_e=0.4$ on square lattice, lattice constant =1:

The heat capacity, potential energy curve and order parameters curve as a function of temperature are shown in **Figure VII-3**. We notice the phase transition occurs at $T=0.15$. The snapshots at low temperature the geometry show a short stripe geometry as expected (see the geometry for this system in **Chapter III**).

We use the order parameters with $a=4$, $\Psi_4^c(\Delta\theta)$ and $\Psi_4^s(\theta)$. The first order parameter shows the four fold symmetry and is close to 1 as can be seen in **Figure VII-3**. While the second parameter, Ψ_4^s , used to check the chirality of the system. Clearly the value of Ψ_4^s is equal 0 at all temperatures, as the short stripe geometry is achiral.

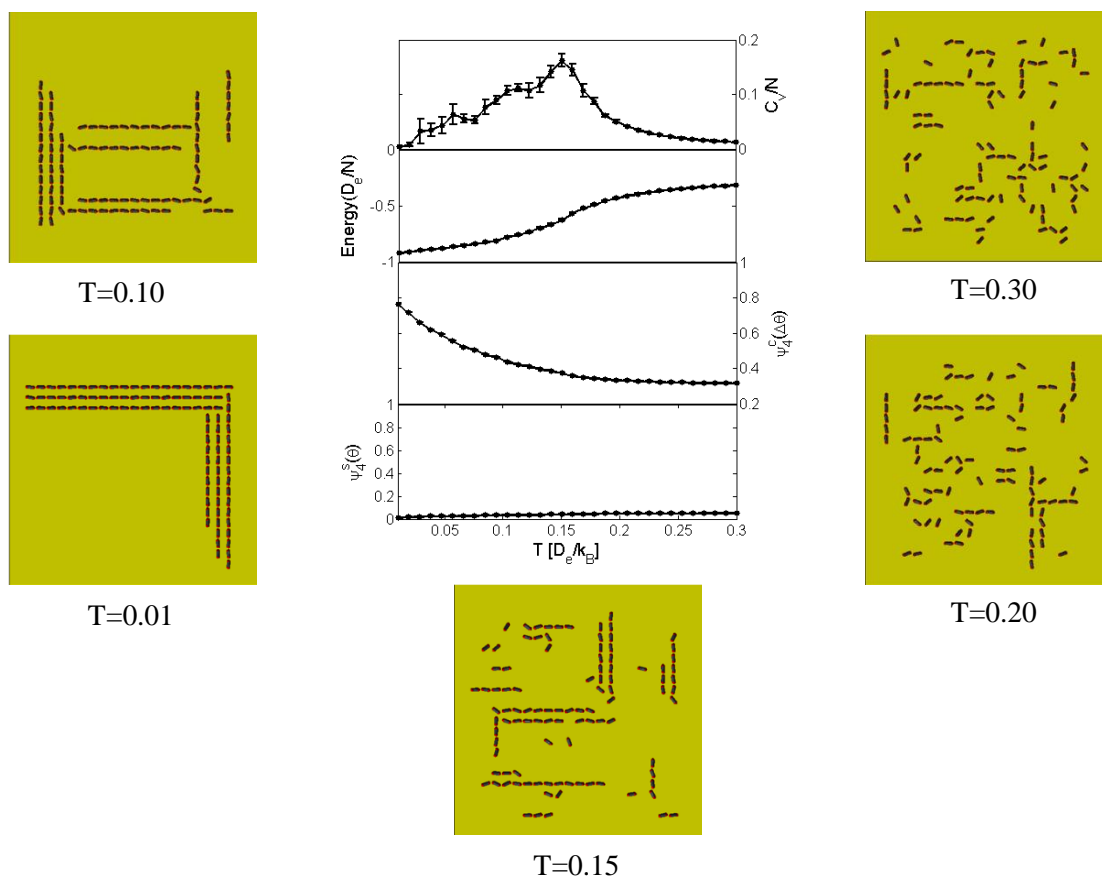


Figure VII-3: Energy, the heat capacity, and two order parameters as a function of temperature from NVT the Monte Carlo trajectories for a ditopic molecule with the Lennard-Jones potential, $r_e=0.40$, $\rho = 0.29$. (For an explanation of the parameters, see text.) Shown on the left of the figure are snapshots of typical structures at low temperature ($T=0.01, 0.10$); shown in the middle is a snapshot of a typical structure at the phase transition temperature ($T=0.15$); shown on the right are snapshots of typical structures at high temperature ($T=0.2, 0.3$).

VII.4.b Molecule 1, $\rho=0.42$, $r_e=0.4$ on square lattice, lattice constant =1:

In **Figure VII.4** we show the heat capacity, the potential energy average and order parameters curves as a function of temperature. We notice that the phase transition occurs at $T=0.30$. We also show snapshots at high temperature with random distribution of the molecules except for some spots with symmetric windmill structure. The snapshots at low temperature which has perfectly symmetric windmill structures. The snapshot at the phase transition ($T=0.3$) shows spots with windmill structure and spots with random distribution.

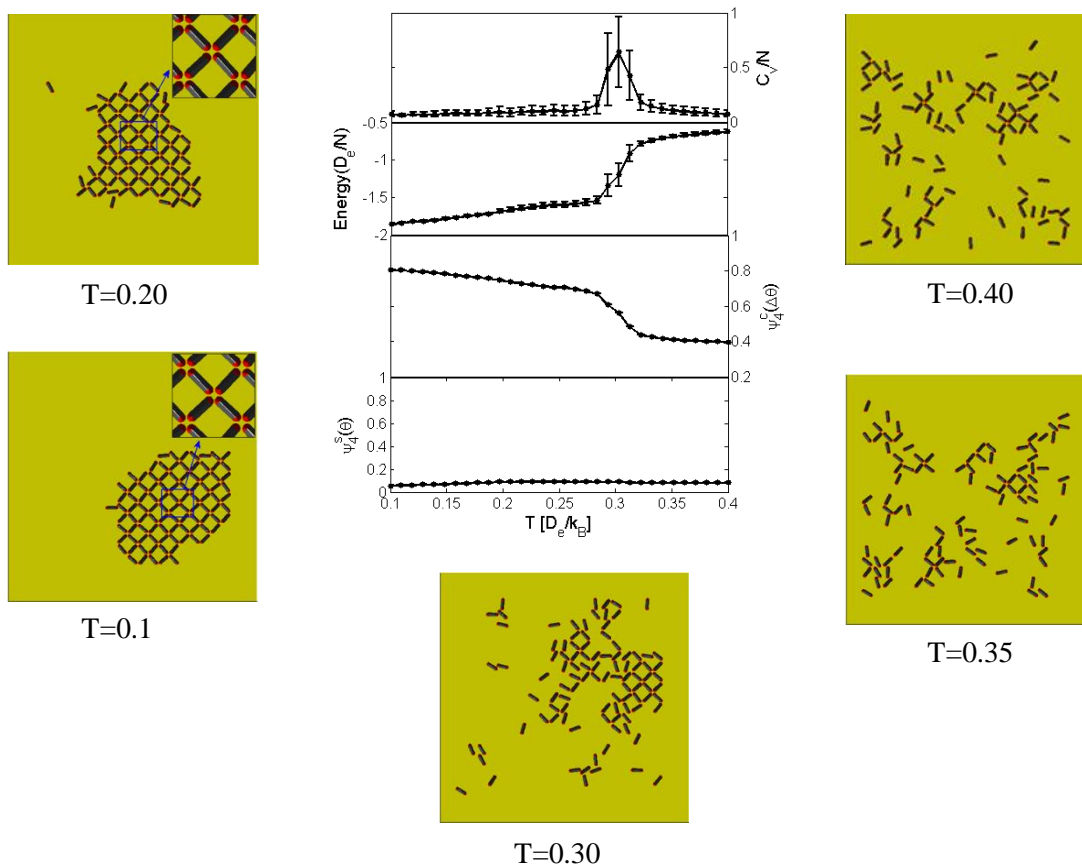


Figure VII-4: Energy, heat capacity, and two order parameters as a function of temperature from NVT Monte Carlo trajectories for a ditopic molecule with the Lennard-Jones potential, $r_e=0.40$ $\rho = 0.42$. (For an explanation of the parameters, see text.) Shown on the left of the figure are snapshots of typical structures at low temperature ($T=0.10, 0.20$); shown in the middle is a snapshot of a typical structure at the phase transition temperature ($T=0.30$); shown on the right are snapshots of typical structures at high temperature ($T=0.35, 0.4$).

We use the order parameters with $a=4$, $\Psi_4^c(\Delta\theta)$ and $\Psi_4^s(\theta)$. For this system the first order parameter = 1 with a 4 fold symmetric unit cell such as the windmill structure. The second parameter is used to show the chirality of the adlayer. As we notice the $\Psi_4^s \approx 0$ at all temperatures, which means the adlayer is achiral.

VII.4.c Molecule 1, $\rho=0.5$, $r_e=0.4$ on a square lattice, lattice constant =1:

The heat capacity, the potential energy average and order parameters curves as a function of temperature are shown in **Figure VII-5**. The phase change occurs at $T= 0.27$ (see the snapshot at phase transition in **Figure VII-5**). We use the same order parameters as in the previous molecule

with $a=4$. As can be seen from the snapshot the pattern is the chiral windmill. This is also confirmed by the high value of Ψ_4^S which is close to 1 at low temperature. And the 4 fold symmetry adlayer can be seen by $\Psi_4^C(\Delta\theta) \approx 1$.

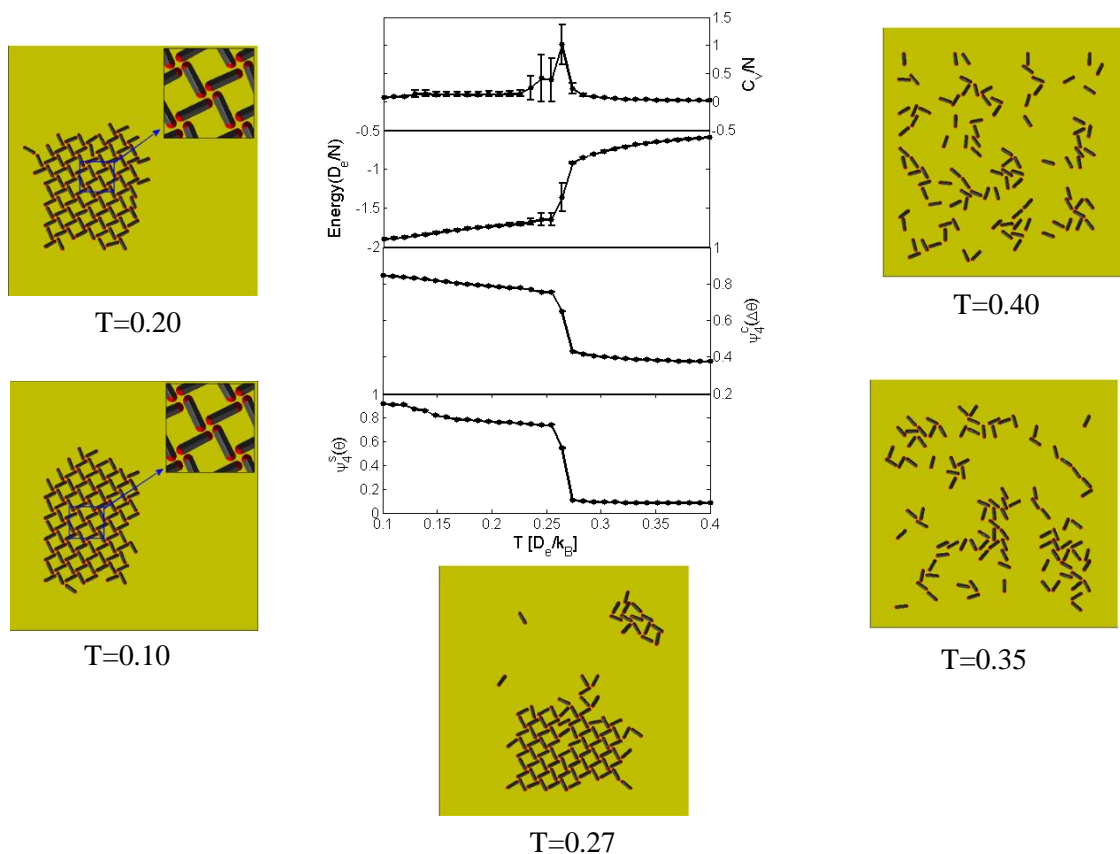


Figure VII-5: Energy, the heat capacity, and two order parameters as a function of temperature from NVT Monte Carlo trajectories for a ditopic molecule with the Lennard-Jones potential, $r_e=0.40$ $\rho = 0.5$. (For an explanation of the parameters, see text.) Shown on the left of the figure are snapshots of typical structures at low temperature ($T=0.10, 0.20$); shown in the middle is a snapshot of a typical structure at the phase transition temperature ($T=0.27$); shown on the right are snapshot of typical structures at high temperature ($T=0.35, 0.4$).

VII.4.d Molecule 1, $\rho=0.34$, $r_e=0.4$ on a triangular lattice, lattice constant =1:

The phase transition occurs at $T=0.3$ as can be noticed from the **Figure VII-6**, from the heat capacity and potential energy curves.

We have used the order parameters with $a=6$, $\Psi_6^c(\theta)$ and $\Psi_6^s(\theta)$. The first order parameter $= 1$ for hexagonal geometry. This can be noted by its value at low temperature which is consistent with the snapshot for the honeycomb geometry. The second order parameter confirms the chirality of the geometry. Geometrically, the honeycomb geometry is achiral which is confirmed by the 0 value of Ψ_6^s at all temperatures (see the last panel of **Figure VII-6**).

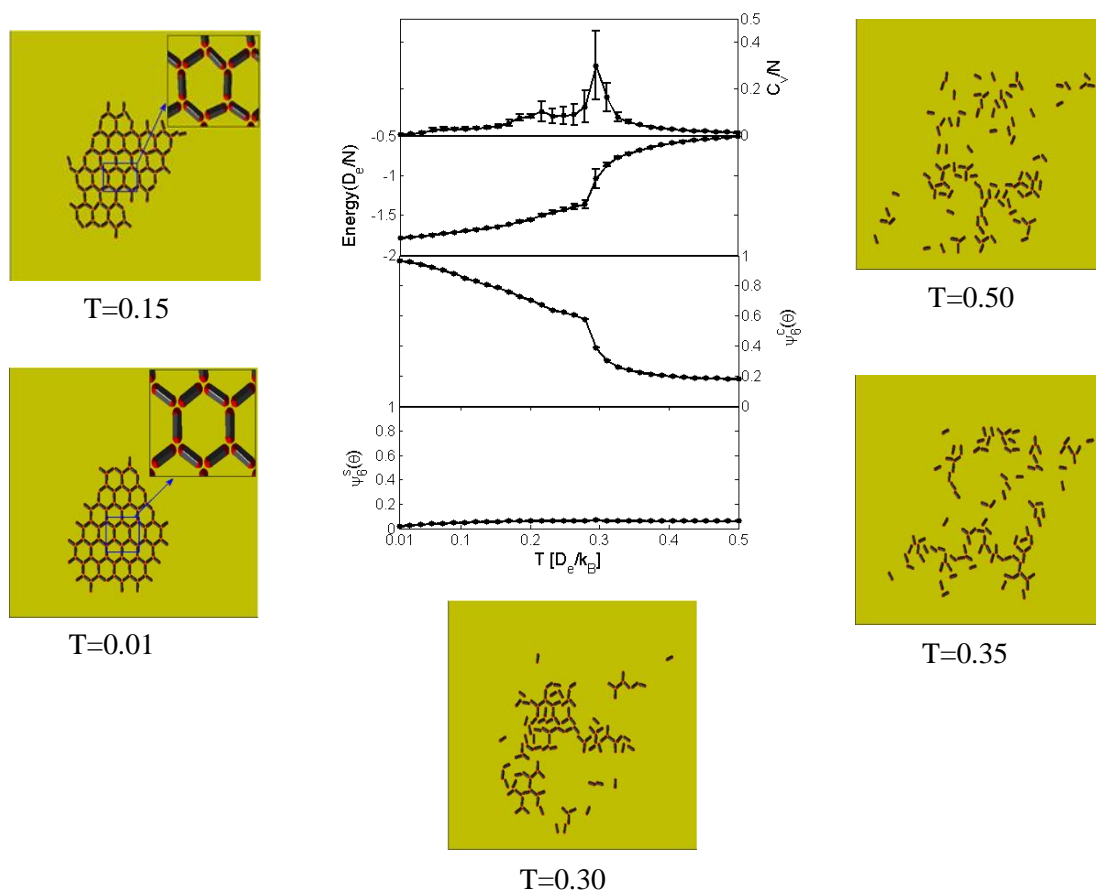


Figure VII-6: Energy, the heat capacity, and two order parameters as a function of temperature from NVT Monte Carlo trajectories for a ditopic molecule with the Lennard-Jones potential, $r_e=0.40$ $\rho = 0.34$. (For an explanation of the parameters, see text.) Shown on the left of the figure are snapshots of typical structures at low temperature ($T=0.01, 0.15$); shown in the middle is a snapshot of a typical structure at the phase transition temperature ($T=0.30$); shown on the right are snapshots of typical structures at high temperature ($T=0.35, 0.5$).

VII.4.e Molecule 1, $\rho=0.45$, $r_e=0.4$ on a triangular lattice, lattice constant =1:

The snapshots shown in **Figure VII-7** with random distribution of the molecules at high temperature and chiral pinwheel structures at low temperature. The phase change occurs at $T=0.26$ as shown in the heat capacity curve as function of temperature, the first panel of **Figure VII-7**.

We use the same order parameters as explained for the previous systems with $\Psi_6^c(\theta)$ and $\Psi_6^s(\theta)$. The structure is semi-hexagonal as can be noticed from the Ψ_6^c value. The chirality can be confirmed by the high value of $\Psi_6^s(\theta)$ at low temperature in the last panel of **Figure VII-7**.

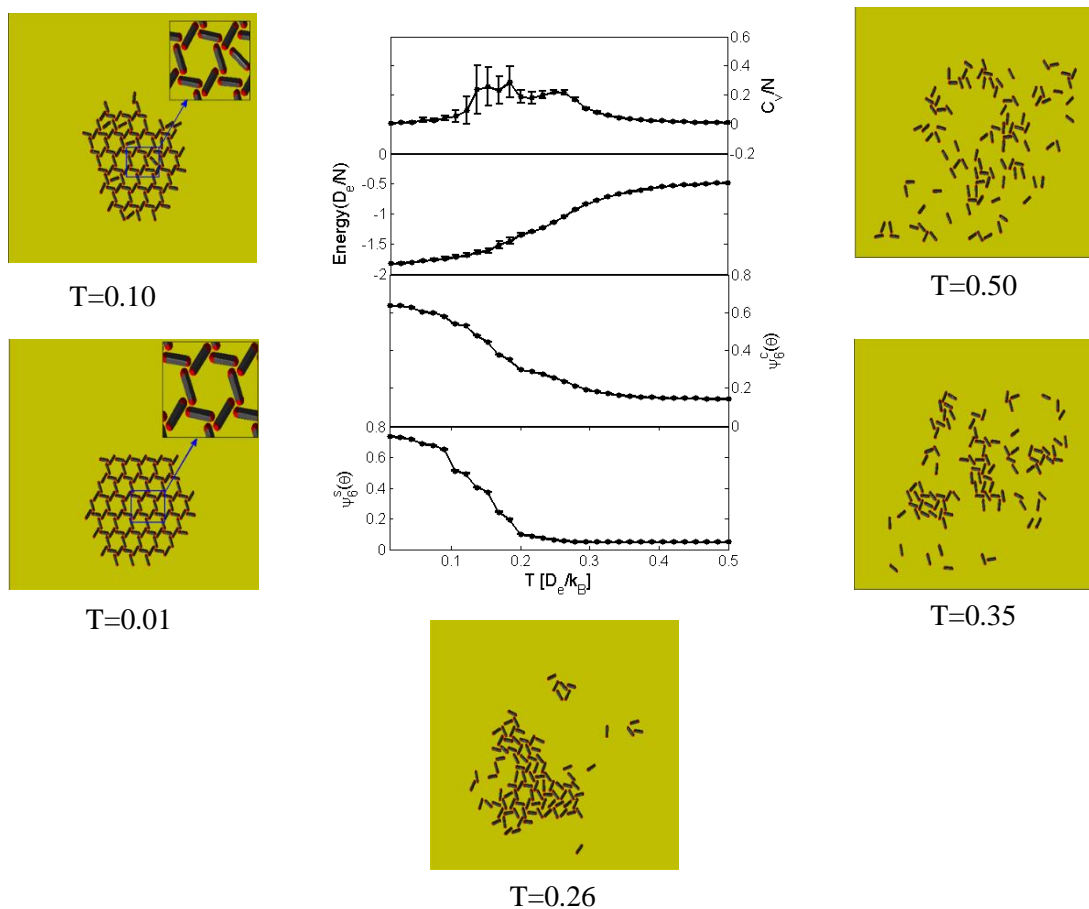


Figure VII-7: Energy, the heat capacity, and two order parameters as a function of temperature from NVT Monte Carlo trajectories for a ditopic molecule with the Lennard-Jones potential, $r_e=0.40$ $\rho = 0.45$. (For an explanation of the parameters, see text.) Shown on the left of the figure are snapshots of typical structures at low temperature ($T=0.01, 0.10$); shown in the middle is a snapshot of a typical structure at the phase transition temperature ($T=0.26$); shown on the right are snapshots of typical structures at high temperature ($T=0.35, 0.5$).

VII.4.f Molecule 1, $\rho=0.50$, $r_e=0.4$ on a triangular lattice, lattice constant =1:

As shown in **Figure VII-8** the phase change occurs at $T=0.15$. The snapshot at low temperature shows a chiral pinwheel structure with rotors in the center of a semi-hexagonal structure.

We have used $\Psi_6^c(\theta)$ and $\Psi_6^s(\theta)$ order parameters. The central molecules break the hexagonal pattern. This can be seen from the value of Ψ_6^c at low temperature compared with the high temperature values. The chirality of the pinwheel is also emphasized by the relatively high value of Ψ_6^s .

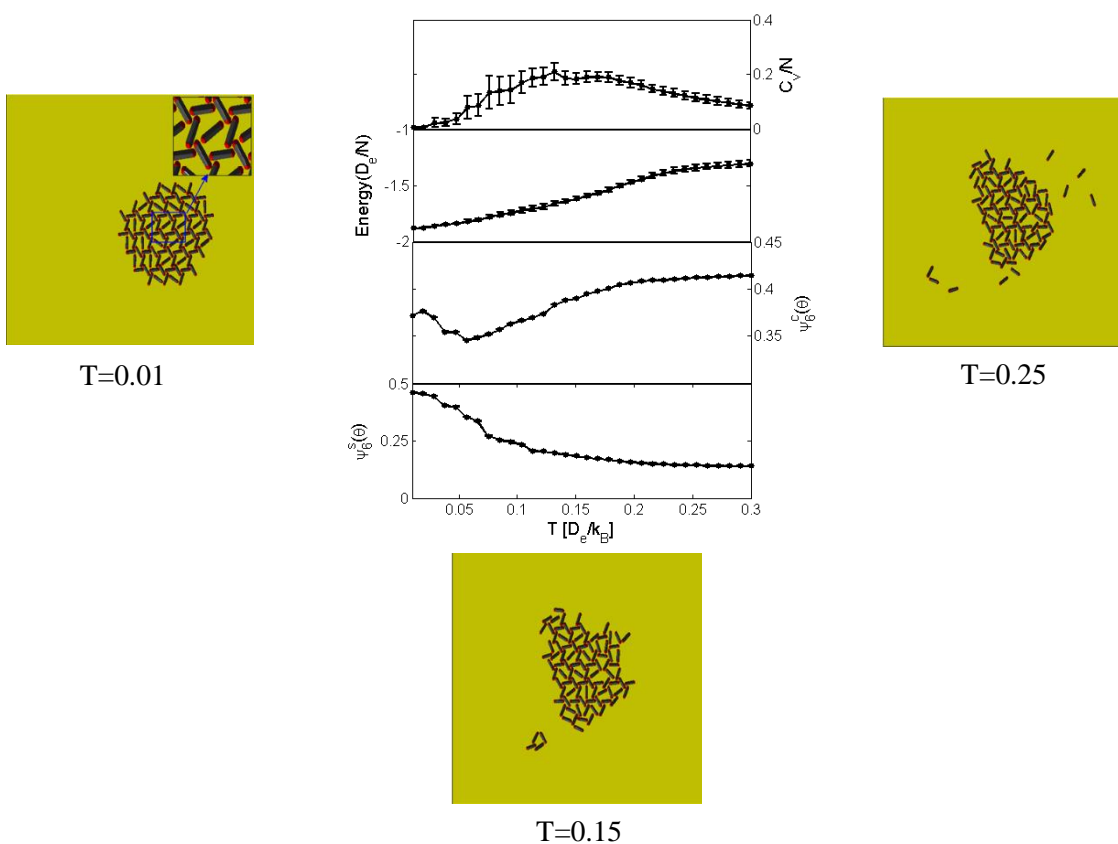


Figure VII-8: Energy, the heat capacity, and two order parameters as a function of temperature from NVT Monte Carlo trajectories for a ditopic molecule with the Lennard-Jones potential, $r_e=0.40$ $\rho = 0.5$. (For an explanation of the parameters, see text.) Shown on the left of the figure is a snapshot of a typical structure at low temperature ($T=0.01$); shown in the middle is a snapshot of a typical structure at the phase transition temperature ($T=0.15$); shown on the right is a snapshot of a typical structure at high temperature ($T=0.25$).

VII.4.g Molecule 2, $\rho=0.50$, $r_e=0.2$ on a square lattice, lattice constant =0.5:

The results shown here are for Molecule 2 with stem length = $2\rho=1.0$ and lattice grids with site-to-site distances = 0.5. We use the grand canonical ensemble described earlier. The heat capacity, the potential energy, the molecular density N/N_s and order parameters curves as a function of temperature are shown in **Figure VII-9**. The three snapshots are at three different temperatures, high $T=0.5$, medium $T=0.20$ and low $T=0.01$ are shown in **Figure VII-10**. We notice from **Figure VII-9** the phase change occurs at $T\approx 0.25$.

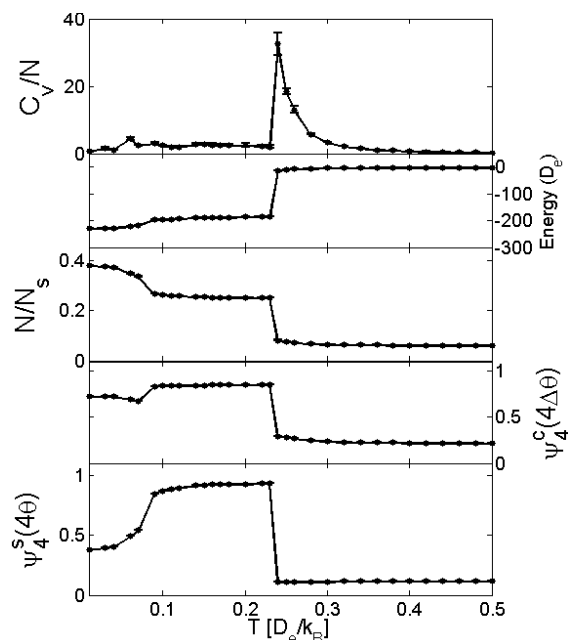


Figure VII-9: Energy, the heat capacity, the molecular density per lattice sites N/N_s , and two order parameters as a function of temperature from the grand canonical Monte Carlo trajectories for molecule 2 with the Lennard-Jones potential, $r_e=0.20$ $\rho = 0.5$. Note: low density square lattice is used. (For an explanation of the parameters, see text.)

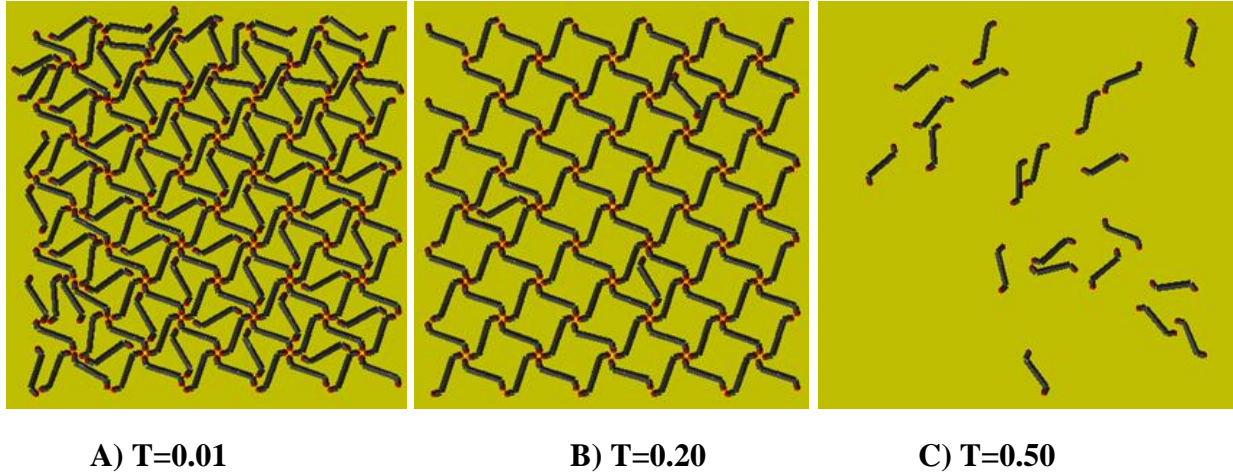


Figure VII-10: Snapshots of Monte Carlo simulation of molecule 2, $r_c=0.20$ $\rho = 0.5$; A) high $T=0.5$, B) medium $T=0.20$ and C) low $T=0.01$.

We used order parameters with $a=4$, $\Psi_4^c(\Delta\theta)$ and $\Psi_4^s(\theta)$. The first parameter describes the four fold symmetry, which clearly is very high at low temperature. The $\Psi_4^c(\Delta\theta)$ slightly decreases at $T<0.1$ due to the adsorbed molecules in the center of the pores (see the snapshots in **Figure VII-10**). The second order parameter explains the chirality of the adlayer, which is ≈ 1 for the $T \in [0.1-0.22]$ and decreases to less than 0.5 at lower temperatures due to the molecules inside of the pores.

VII.4.h Molecule 2, $\rho=0.50$, $r_c=0.2$ on a square lattice, lattice constant =0.18

This results are for molecule 2 on a high density square lattice, with site-to-site distances $= \sigma =0.18$. We have used the grand canonical ensemble for a maximum number of molecules =100 to decrease the cost of the calculation. The results of the heat capacity, energy, molecular density N/N_s , and order parameters curves with three snapshots at high, low and the phase transition temperatures are shown in **Figure VII-11**. The phase change occurs at $T=0.35$.

As noticed from the Ψ_4^s order parameter and the snapshots the adlayer is clearly achiral. The adlayer at low temperature has a herringbone property with four fold symmetry (this can be noticed from $\Psi_4^c(\Delta\theta)=1$). All the angles are arbitrarily equal.

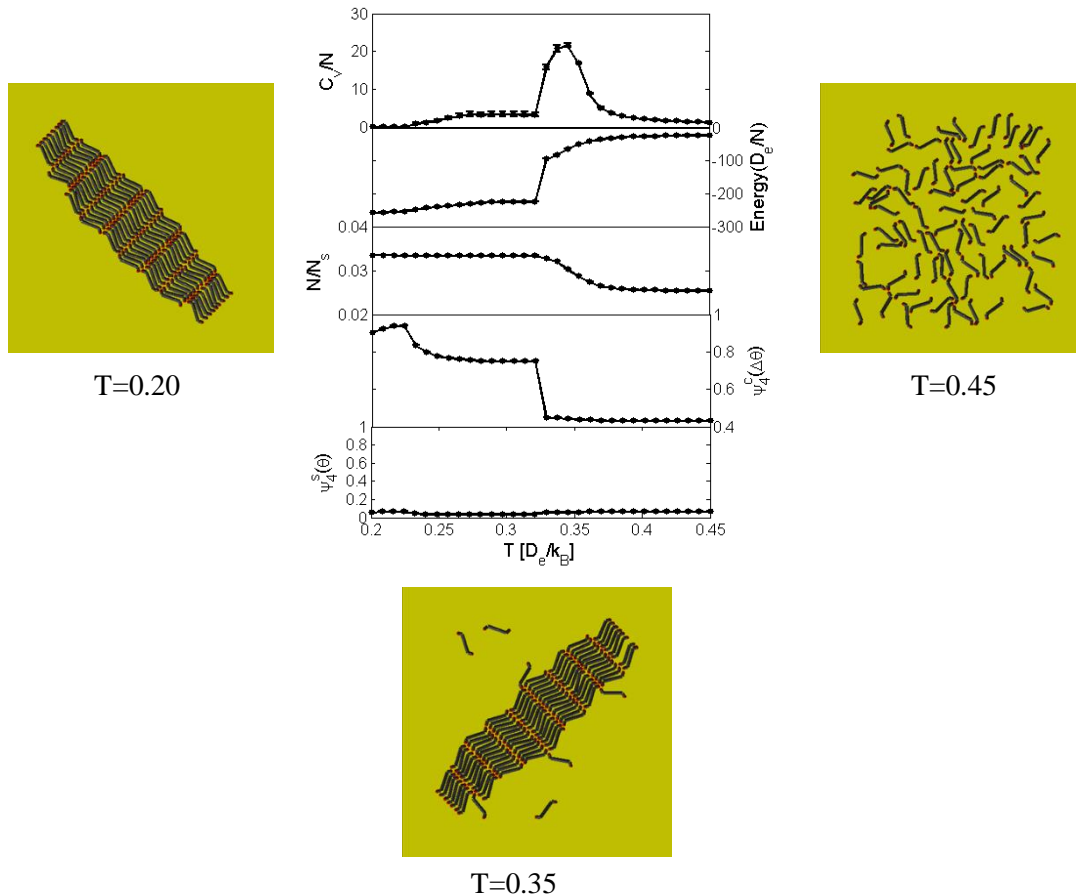


Figure VII-11: Energy, the heat capacity, the molecular density and two order parameters as a function of temperature from grand canonical Monte Carlo trajectories for a ditopic molecule with Lennard-Jones potential, $r_e=0.40$ $\rho = 0.5$. (For an explanation of the parameters, see text.). Shown on the left of the figure is a snapshot of a typical structure at low temperature ($T=0.20$); shown on the middle is a snapshot of a typical structure at the phase transition temperature ($T=0.35$); shown on the right is a snapshot of a typical structure at high temperature ($T=0.45$).

VII.5 Conclusion

We have investigated the adlayer of ditopic molecule on a square and a triangular lattice using Replica Exchange Monte Carlo (REMC) simulation. We considered rotors with different lengths, having two coarse grained sites at the tips of each molecule. The site-to-site interactions are expressed by the Lennard-Jones potential. A repulsive van der Waals radius was also applied between the stems of the molecules with a radius = $\sigma/2$ of the Lennard-Jones potential.

We have found several ground state adlayers which are in general consistent with the results in previous chapters using the minimization method of the “fixed site” constraint molecules. For instance, the short stripe structure on a square lattice for a small molecule $\rho=0.29$ are the same for both Monte Carlo simulation and the ground state minimization method. Also achiral and chiral windmill structures on a square lattice are found for both $\rho=0.42$, $\rho=0.5$, respectively. The same results are found using the minimization method.

On the other hand, the honeycomb and pinwheel adlayers on a triangular lattice are also consistent with the results in chapter IV. With the exception of the central molecule, inside the hexagonal structure, which disappears in the case of Monte Carlo simulation.

The Monte Carlo results for the system with $\rho=0.5$ on a triangular lattice produces the pinwheel adlayer with semi-hexagonal porous sites. However the global minimum of this system is the butterfly structure as found in **Chapter IV** using the minimization method of the “fixed site” molecules constraint. This could be due to the system needing to be cooled to lower temperatures which makes the cost of the system prohibitively high.

Our results for the oligo-phenylene-ethynylenes model molecule 2 are very consistent with the experimental results. For instance, Linderoth’s group has reported both the chiral windmill structure (6, 7, 88-90) and the herringbone pattern (6, 90) exist on the surface of Au(111).

In conclusion, our simple model can be used to investigate the self-assembly of an infinite system.

APPENDIX

Appendix A : Method

A.I Method for Finding Stationary Points

A.I.a Method for finding global minima:

The method we have used for global minimizing is a quasi-Newton method using an analytical gradient (147, 148). The quasi-Newton method and the step size are explained in section A.II. A random selection of $[\theta_1, \theta_2, \theta_3, \theta_4]$ unit cell angles is chosen using a random number for each of the angles. The potential energy is minimized for 1000 steps until we reach an angle threshold of 10^{-6} and/or 10^{-6} potential energy and $\text{RMS} = 10^{-6}$ of the gradient convergence. This procedure is repeated for 1000 starting points in the set of primary cell angles. The lowest energy is obtained and reported as a global minimum and the angles are also reported. This procedure is presented in **Figure A-1**.

A.I.b Method for finding local minima:

A random point in the angle space $\theta = [\theta_1, \theta_2, \theta_3, \theta_4]$ is selected as a starting point. The Quasi-Newton method, using an analytical gradient, is then used to find the local minimum. 1000 minimizing steps are further applied until we reach a 10^{-6} angle threshold and/or 10^{-6} potential energy and $\text{RMS} = 10^{-6}$ of the gradient convergence. This is repeated for 1000 starting points. All of the minimized structures were collected and sorted according to recognition techniques derived and will be shown next.

The stationary points are verified by calculating the analytical gradient ∇V vector, which is the set of first derivatives of the potential function $V(\theta_1, \theta_2, \theta_3, \theta_4)$, and the hessian matrix (H) which contains the second partial derivative of the function (Appendix B).

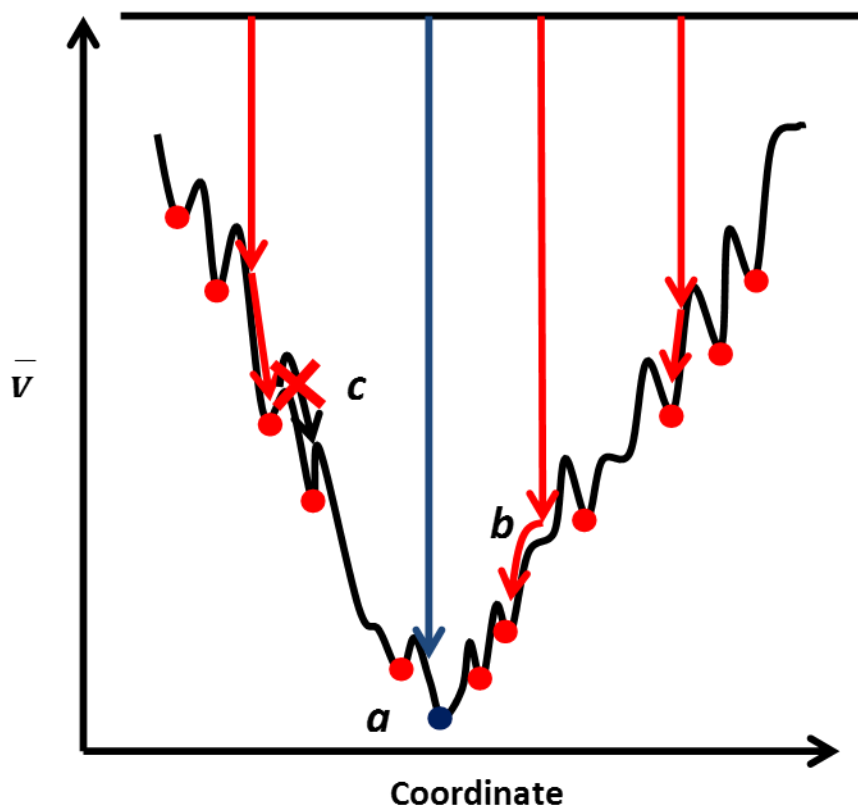


Figure A-1: A schematic representation of an energy funnel and the global minimizing method. (a) Global minimum. (b) Allowed local minimizing. (c) Minimizing path to global minimum not allowed. \bar{V} is the potential energy calculated by using the equations method shown in **Chapter II** (see the text).

For all stationary points the gradient must reach a 10^{-6} tolerance level. Then the stationary points are tested according to the eigen values of the Hessian matrix (148):

1. If all eigen values > 0 then the stationary point is a minimum.
2. If all eigen values < 0 then the stationary point is a maximum.
3. If there are positive and negative eigen values then the stationary point is a saddle point. The order of the saddle point depends of how many negative eigen values are available. For example if one eigen value is available then it is a first order saddle point and so on.

A.II Quasi-Newton Broyden–Fletcher–Goldfarb–Shanno (BFGS) minimization method

The BFGS algorithm is a quasi-Newton method that accumulates information about the Hessian matrix H , and the inverse of the Hessian matrix H^{-1} , and uses this information to determine the search direction on the potential energy surface.

The potential function $V(\theta^i)$ is a function of the rotor angles.

The update step is:

$$\theta^{i+1} = \theta^i + \lambda \Delta \theta^i \quad (\text{A1})$$

The step direction:

$$\Delta \theta^i = -H_i^{-1} \nabla V(\theta^i) \quad (\text{A2})$$

Where H is the Hessian matrix (see **Appendix B**), and ∇V is the gradient of the potential function.

The step size $\lambda \in [0,1]$ can be calculated by a line search such that:

$$V(\theta^i + \lambda_i \Delta \theta^{i+1}) = \min_{\lambda} V(\theta^i + \lambda \Delta \theta^i) \quad (\text{A3})$$

Hessian is updated using (BFGS) update:

$$H_{i+1} = H_i + \frac{yy^T}{y^T s} - \frac{H_i s s^T H_i}{s^T H_i s} \quad (\text{A4})$$

$$\text{Where: } s = \theta^{i+1} - \theta^i, \quad y = \nabla V(\theta^{i+1}) - \nabla V(\theta^i)$$

Algorithm: The BFGS algorithm

- 1: Initialize the Hessian Matrix H_i
- 2: Evaluate the forces $\nabla V(\theta^i)$ of the initial positions.
- 3: Update the positions using equation (A3) and line minimization procedure.
- 4: Evaluate the forces on the new positions $\nabla V(\theta^{i+1})$.
- 5: Update the Hessian matrix H_{i+1} using equation (A4).
- 6: Continue until a convergence criterion is reached. If not, go to step 3.

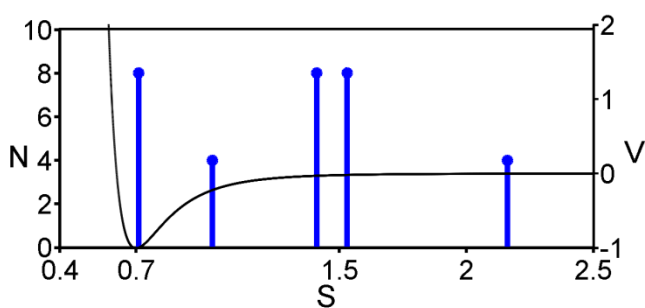
A.III Method for Finding Radial Distribution Function of a ditopic molecule a square lattice:

The radial distribution function RDF is defined as the site-to-site distance between the unit cell rotors and its nearest neighbors. This gives a total of [4 (unit cell) x 32 (distances around each rotor) = 128] per 4 rotors in the unit cell. **Figure A-2**, explains the RDF function for rotor θ_i in the unit cell. This information has been used to build the RDF by counting the site-to-site distances within 0.01 thresholds. These numbers are normalized to the number of rotors in a unit cell [4 rotors per unit cell], which gives peaks represent, the first one is the nearest-neighbor N_1 , and the second one is next-nearest-neighbor N_2 and so on.

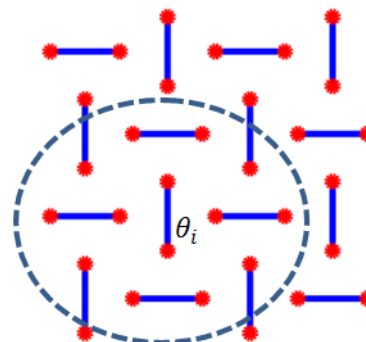
This can be expressed by the radial distribution formula $I(r)$

$$N = I(r) = \frac{1}{4} \sum_{i=1}^4 \sum_{j=1}^8 \delta(r_{pq}^{ij}) \quad (A5)$$

Where i and j are neighbors rotors and p and q are the Cartesian coordinates for i and j , respectively.



(A)



(B)

Figure A-2: (A) The radial distribution function RDF, the frequency peaks are the number of nearest neighbors within 0.01 threshold distance unit. (B) A schematic representation of the herringbone structure (LJ , $\rho = 0.84$ and $r_e = 0.7$) showing θ_i , the center rotor and the counted nearest neighbor rotors, located inside the oval structure.

Appendix B : The potential function and its gradient and hessian

The Morse and Lennard-Jones potentials are written in the form:

$$V_{morse}(r) = D_e e^{-\beta(r-r_e)} [e^{-\beta(r-r_e)} - 2] \quad (B1)$$

$$V_{LJ}(r) = D_e \left[\left(\frac{r_e}{r} \right)^{12} - 2 \left(\frac{r_e}{r} \right)^6 \right] \quad (B2)$$

Where r , the atomic-atomic distances, is a function of θ 's, the angle of rotors, as shown in **Chapter II, Figure II-6**.

The gradient ∇V is calculated by using the chain rule:

All the parameters described in the context (see **Chapter II, Figure II-6** and **Figure II-7**).

$$\frac{dV}{d\theta} = \frac{dV}{dr} \times \frac{dr}{d\theta} \quad (B3)$$

Morse Potential: $\frac{dV}{dr} = 2 \times \beta \times D_e \times e^{-\beta(r-r_e)} [1 - e^{-\beta(r-r_e)}]$ (B4)

Lennard-Jones $\frac{dV}{dr} = 12 \times \frac{D_e}{r_e} \left[\left(\frac{r_e}{r} \right)^7 - \left(\frac{r_e}{r} \right)^{13} \right]$ (B5)

$$\nabla V = \left[\frac{dV}{d\theta_1}, \frac{dV}{d\theta_2}, \frac{dV}{d\theta_3}, \dots, \frac{dV}{d\theta_n} \right] \quad (B6)$$

Where n is the number of molecules on the surface.





The Hessian is an $(n \times n)$ matrix which contains the second partial derivatives of the potential:

$$H = \begin{bmatrix} \frac{\partial^2 V}{\partial \theta_1^2} & \frac{\partial^2 V}{\partial \theta_1 \theta_2} & \dots & \frac{\partial^2 V}{\partial \theta_1 \theta_n} \\ \frac{\partial^2 V}{\partial \theta_2 \theta_1} & \frac{\partial^2 V}{\partial \theta_2^2} & \dots & \frac{\partial^2 V}{\partial \theta_2 \theta_n} \\ \vdots & \vdots & \ddots & \vdots \\ \frac{\partial^2 V}{\partial \theta_n \theta_1} & \frac{\partial^2 V}{\partial \theta_n \theta_2} & \dots & \frac{\partial^2 V}{\partial \theta_n^2} \end{bmatrix} \quad (B7)$$



Appendix C : Wallpaper Symmetry Groups

Periodic arrangements on the surface resulting from monolayer formation can be represented by one of the 17 wallpaper group symmetries, Chart C.1. This approach is based on the determination of the surface symmetry elements in Table C.1.

Table C-1: Schematic representation of the symmetry elements of the wallpaper plane groups.

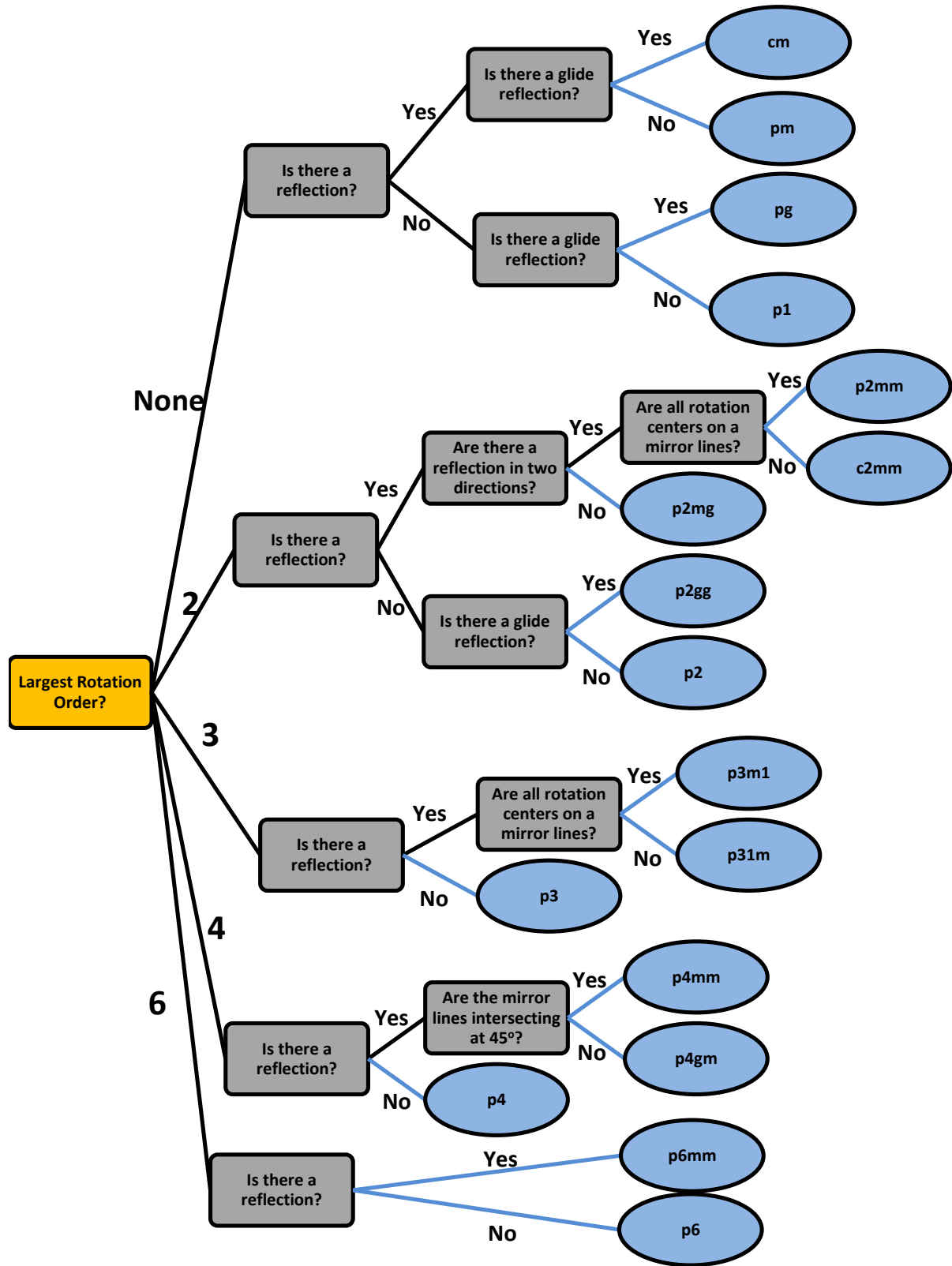
<u>Center of rotation</u>	<u>Order</u>	<u>Angle</u>
	6	$\frac{2\pi}{6}$
	4	$\frac{2\pi}{4}$
	3	$\frac{2\pi}{3}$
	2	$\frac{2\pi}{2}$

Reflection of plane

-  Mirror plane
-  Glide Reflection

Patterns are created by repeating a shape to fill the plane by either translation, reflection, glide reflection, or rotation (the plane symmetry elements). Translation shifts the pattern some distance from the original and leaves the pattern appearing unchanged. The rotations are clockwise by half-turns (180° turn), 120° turn, 90° turn and 60° turn. A reflection through a plane looks like a flip along an axis. The axes can be horizontal, vertical or at some angle. A glide reflection is composed of a reflection across an axis and a translation along the axis.

Chart C.1: Flow chart describes the 17 plane groups used to describe monolayer symmetry:



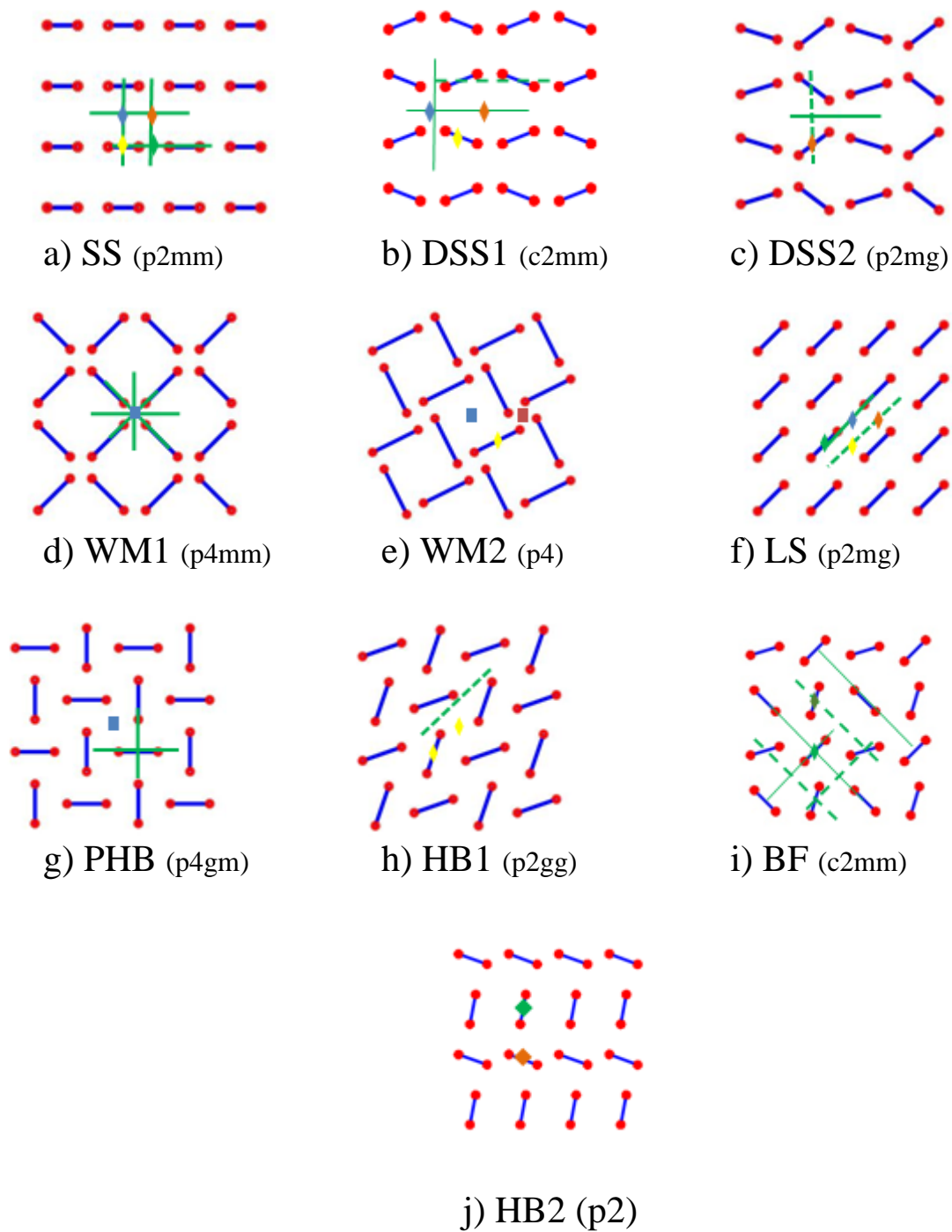


Figure C-1: The main symmetry elements and the wallpaper symmetry groups of the main patterns of a ditopic molecule on the square lattice surface. The abbreviations are described in the text (**Chapter III**) except for DSS which stand for distorted short stripe.

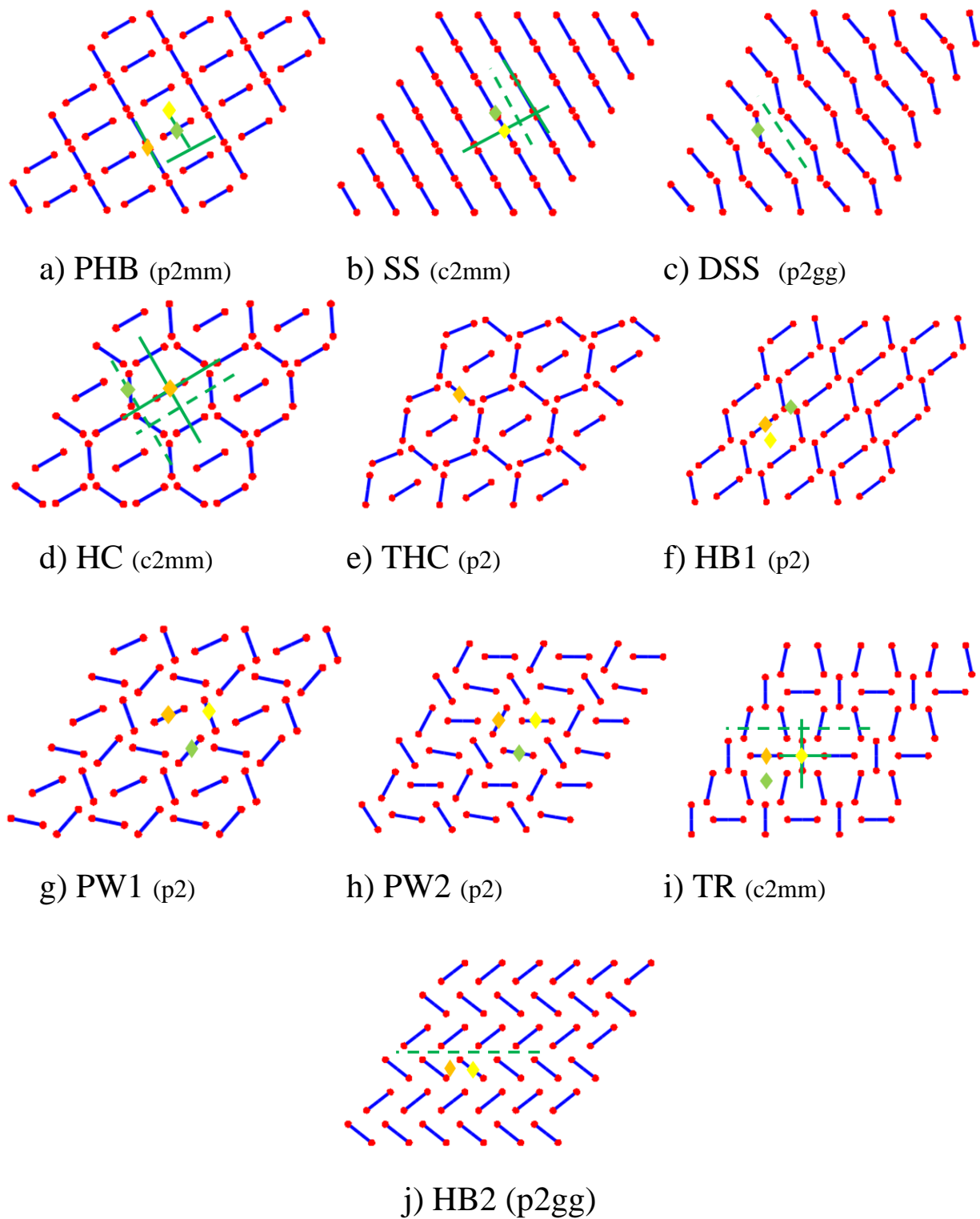


Figure C-2: The main symmetry elements and the wallpaper symmetry groups of the main patterns of a ditopic molecule on the triangular lattice surface. The abbreviations are described in the text (**Chapter III**).

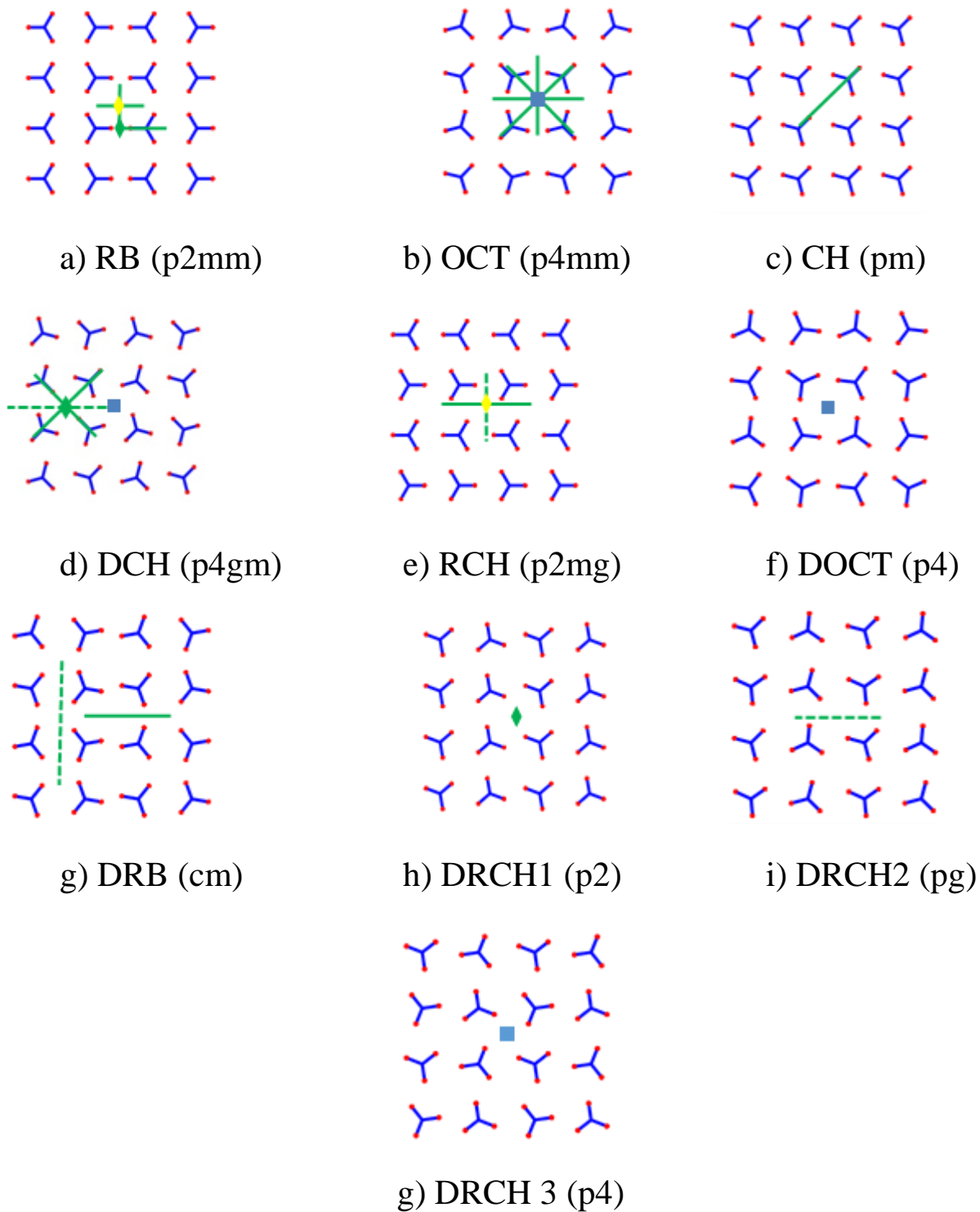
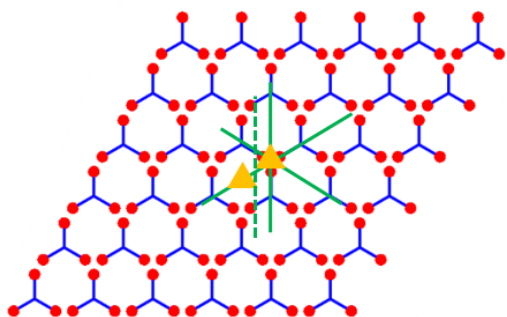
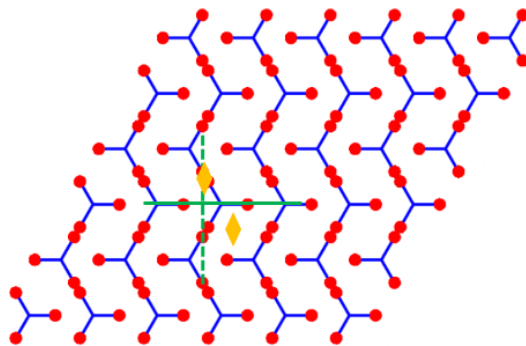


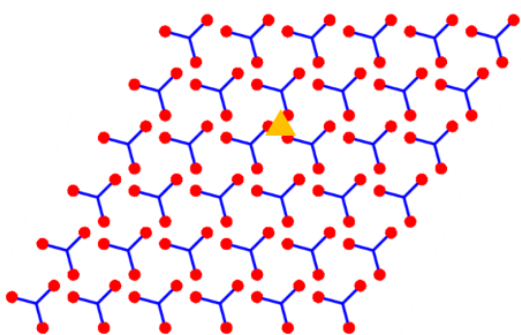
Figure C-3: The main symmetry elements and the wallpaper symmetry groups of the main patterns of a tritopic molecule on the square lattice surface. The abbreviations are described in the text (**Chapter IV**).



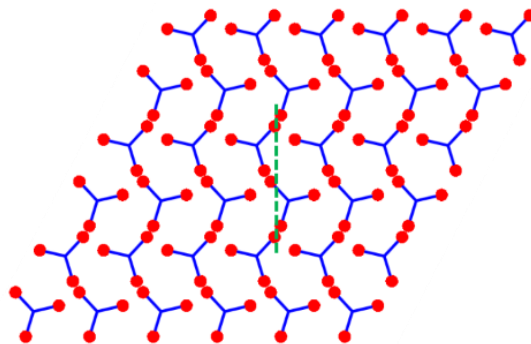
a) HC(p3m1)



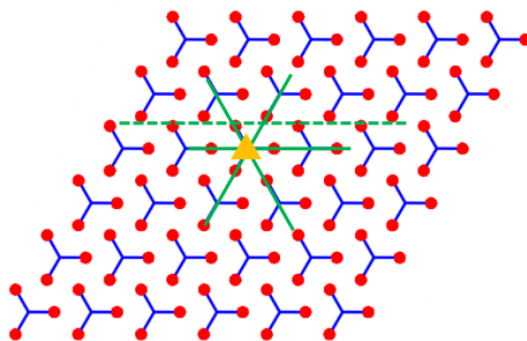
b) RCh (p2mg)



c) Ch(p3)

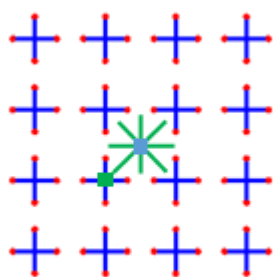


d) HB (pg)

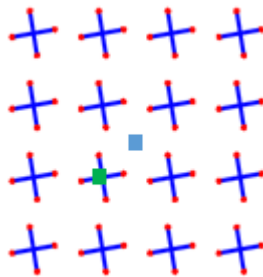


d) PCh (p3m1)

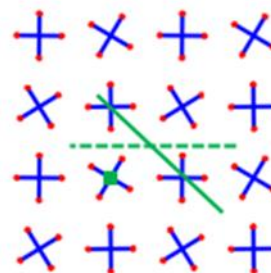
Figure C-4: The main symmetry elements and the wallpaper symmetry groups of the main patterns of a tritopic molecule on the triangular lattice surface. The abbreviations are described in the text (**Chapter IV**).



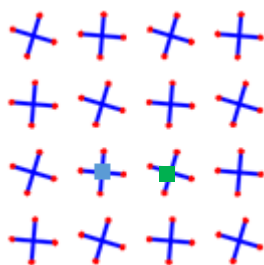
a) SQ (p4mm)



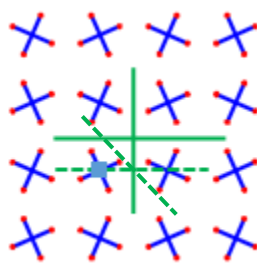
b) CO1 (p4)



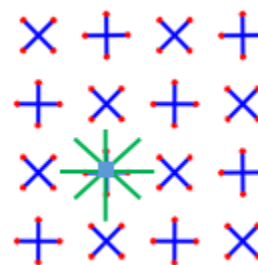
c) DCB (p4gm)



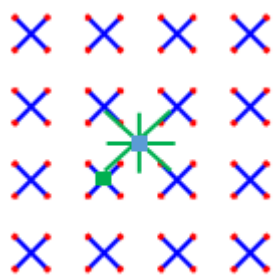
d) HB1 (p4)



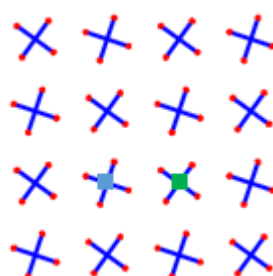
e) TI (p4gm)



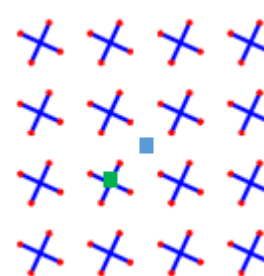
f) CB (p4mm)



g) CR (p4mm)



h) HB2 (p4)



i) CO2 (p4)

Figure C-5: The main symmetry elements and the wallpaper symmetry groups of the main patterns of a tetratopic molecule on the square lattice surface. The abbreviations are described in the text (**Chapter V**).

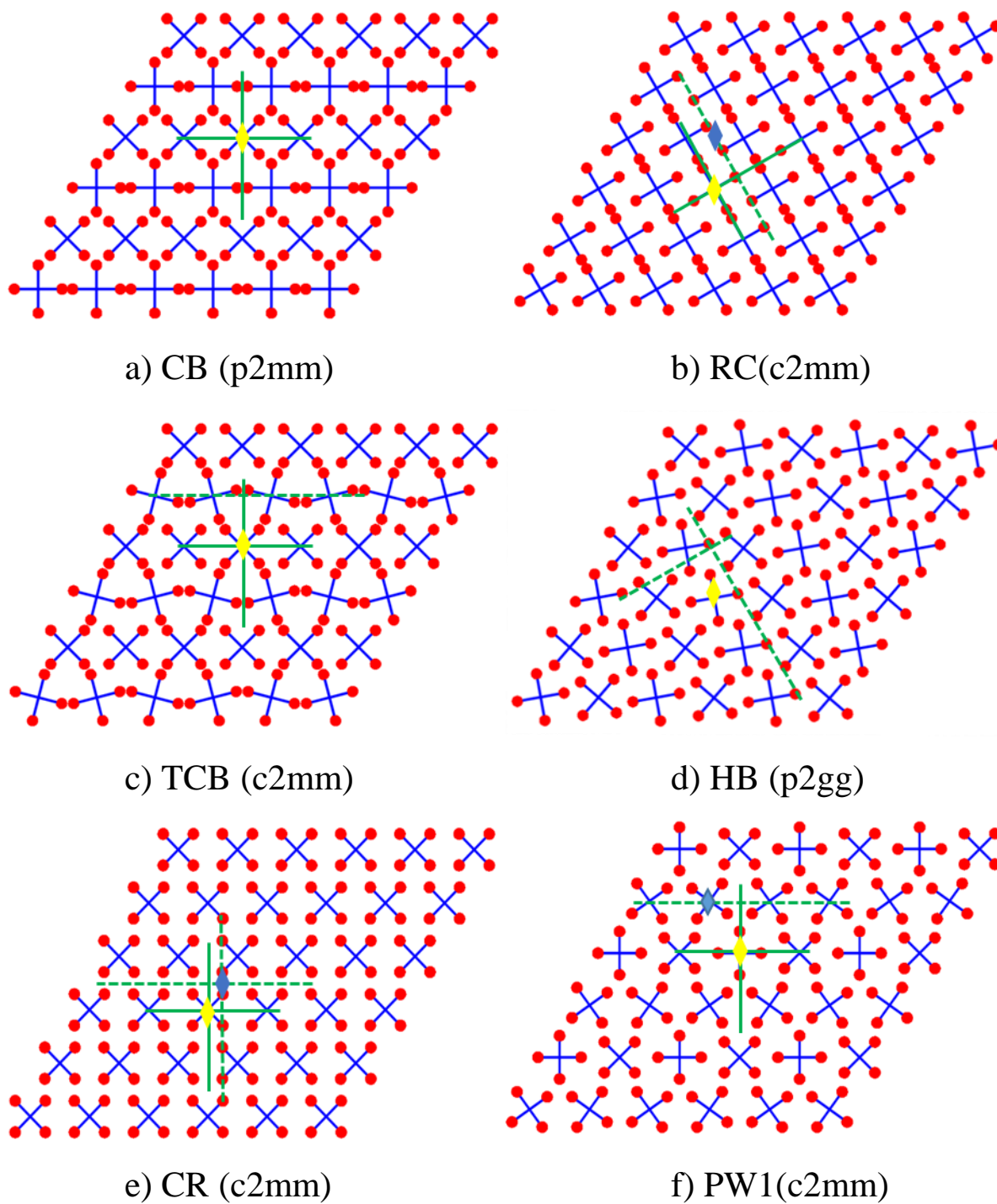
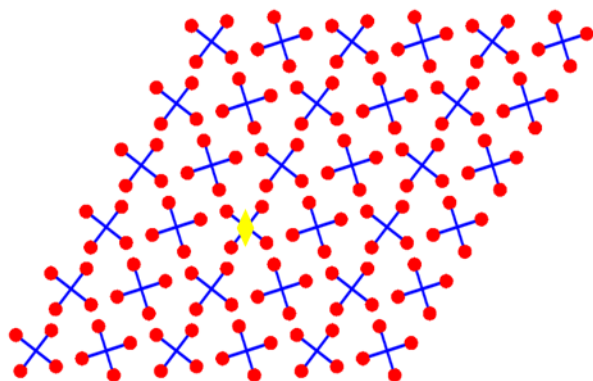
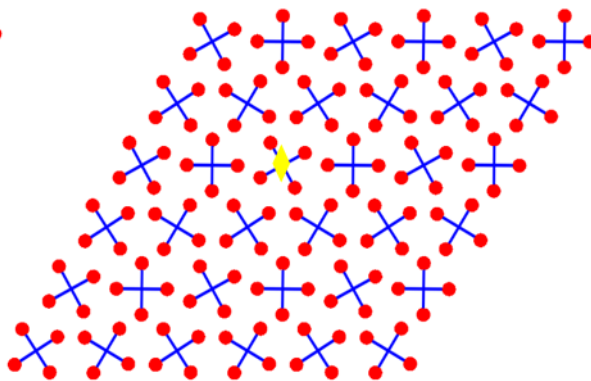


Figure C-6: The main symmetry elements and the wallpaper symmetry groups of the main patterns of a tetratopic molecule on the triangular lattice surface. The abbreviations are described in the text (**Chapter V**). Cont'd see next page for g and h.



g) HB (p2)



h) PW2 (p2)

Figure C.6: continued.

Appendix D : Calvo's approach of Temperature Replica Exchange Monte Carlo (T-REMC)

The exchange probability between two replicas $i < j$:

$$P_{ij} = \min \left[1, e^{-\frac{(U_i - U_j)}{k_B T_j} - \frac{1}{k_B T_i}} \right] \quad (D1)$$

where, U is the potential energy for each replica, k_B is the Boltzmann constant, and T is the temperature

Each pair (i, j) is denoted by a single number r , including the rejection move for $r=0$ and given $P_0=1$. One specific ℓ is the randomly selected according to its normalized probability \tilde{P}_ℓ :

$$\tilde{P}_\ell = \frac{\sum_{0 \dots \ell} P_\ell}{\sum_r P_r} \quad (D2)$$

The move ℓ succeeded if:

$$\tilde{P}_{\ell-1} < \xi < \tilde{P}_\ell \quad (D3)$$

Where, ξ is random number selected in the interval $[0, 1]$.

Example: If three replica (T_1 , T_2 , and T_3) have to be applied:

We calculate the probability between each two replica using equation D1 as follows:

$P_0=1$, $P_1=P_{12}$, $P_2=P_{13}$, and $P_3=P_{23}$. After that we calculate the sum of the probabilities $sum = \sum_i^3 P_i$.

Then a random number (ξ) has been generated. Finally, the swapping algorithm are:

If $\xi < 1/sum$ don't switch

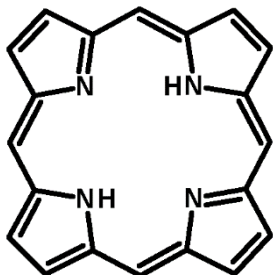
If $1/sum \leq \xi < (1 + P_1)/sum$ switch 1→2

If $(1 + P_1)/sum \leq \xi < (1 + P_1 + P_2)/sum$ switch 1→3

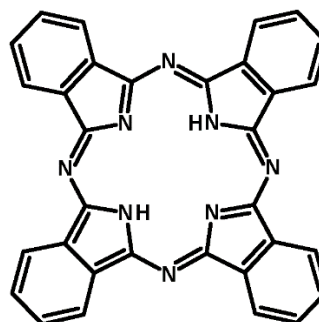
If $(1 + P_1 + P_2)/sum \leq \xi < 1$ switch 2→3

Supporting Material:

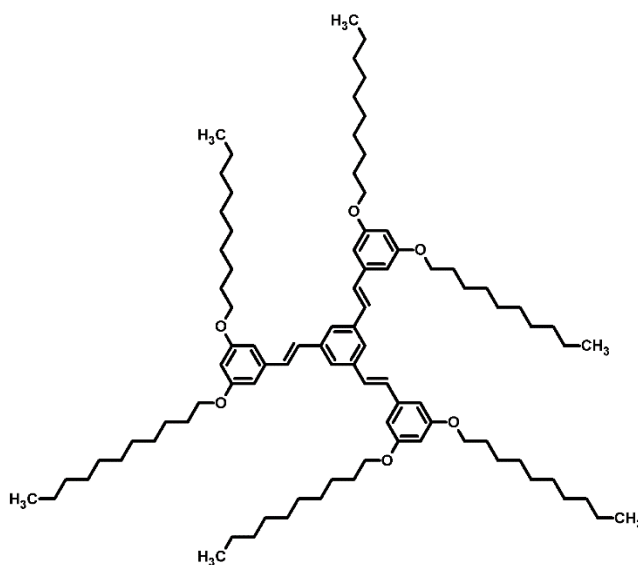
Chemical structures mentioned in the dissertation



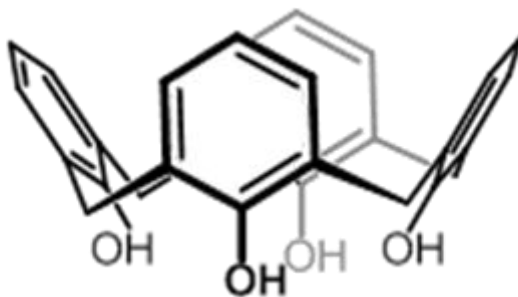
porphyrin



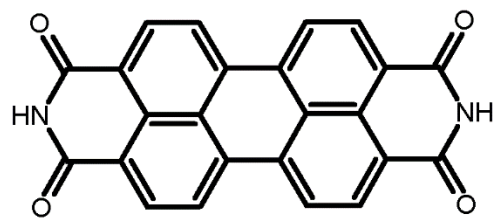
phthalocyanine



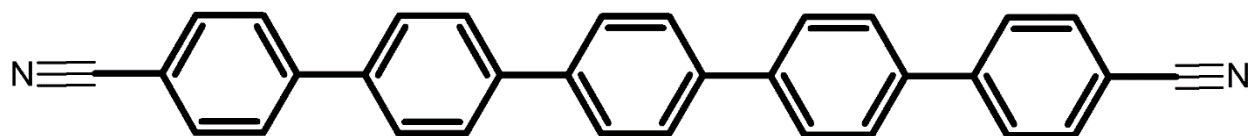
1,3,5-tris[(E)-2-(3,5-didecyloxyphenyl)-ethenyl]- benzene TSB35



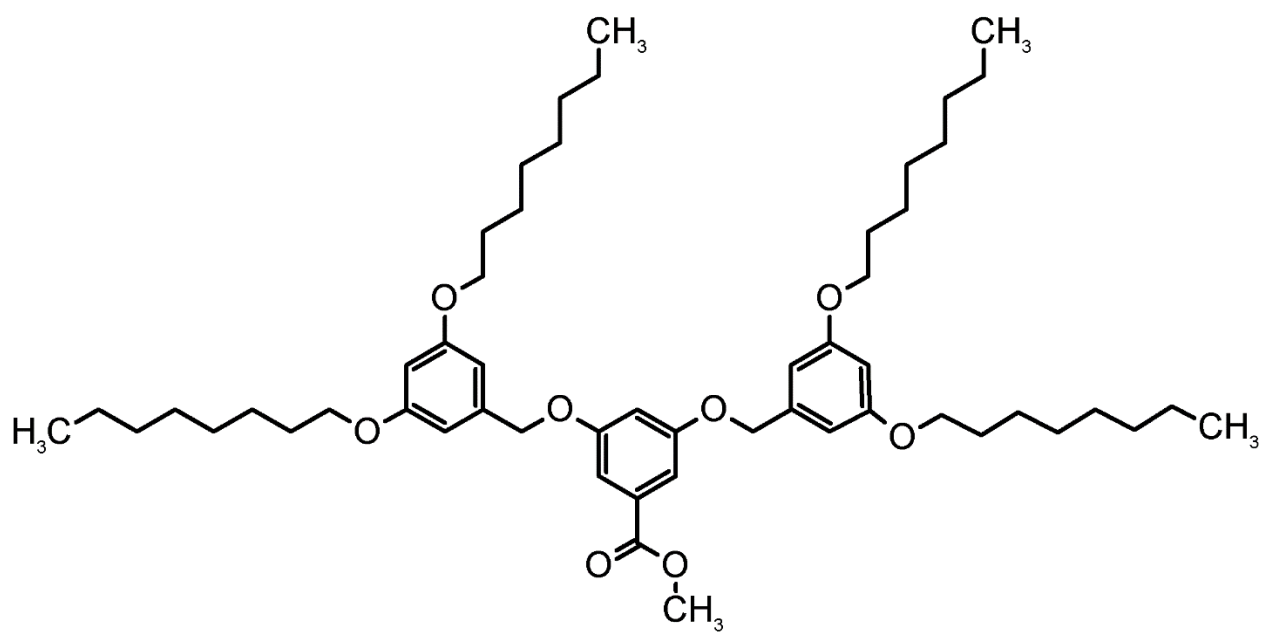
calix[4]arene



perylene tetra-carboxylic di-imide (PTCIDI)



dicyanoquinquiphenyl



Fréchet dendron

List of References

1. Chen C. Julian. Introduction to Scanning Tunneling Microscopy. Second ed. New York: Oxford Univ. Press; 2008.
2. Binnig G, Quate C.F., Gerber C. Atomic force microscope. *Phys. Rev. Lett.* 1986; **56**:930.
3. K. W. Kolasinski. *Surface Science, foundations of catalysis and nanoscience*. Second ed. Wiley, editor. USA; 2009.
4. Binnig G, Rohrer H, Gerber Ch, Weibel E. Surface Studies by Scanning Tunneling Microscopy. *Phys. Rev. Lett.* 1982; **49**:57.
5. Barth J.V. Molecular architectonic on metal surfaces. *Annu. Rev. Phys. Chem.* 2007; **58**:375.
6. Busse C, Weigelt S, Petersen L, Lægsgaard E, Besenbacher F, Linderoth T.R., et al. Chiral Ordering and Conformational Dynamics for a Class of Oligo-phenylene-ethynylenes on Au (111). *J. Phys. Chem. B.* 2007; **111**:5850.
7. Knudsen M. M., Kalashnyk N, Masini F, Cramer J.R., Lægsgaard E, Besenbacher F, et al. Controlling chiral organization of molecular rods on Au (111) by molecular design. *J. Am. Chem. Soc.* 2011; **133**:4896.
8. Kudernac T, Lei S, Elemans J. A., De Feyter S. Two-dimensional supramolecular self-assembly: nanoporous networks on surfaces. *Chem. Soc. Rev.* 2009; **38**:402.
9. H. Zhou, J. D. Wuest. Crankshafts: Using Simple, Flat C_{2h} -Symmetric Molecules to Direct the Assembly of Chiral 2D Nanopatterns. *Langmuir.* 2013; **29**:7229.
10. Bubnis G, Cleary S, Mayne H. Self-assembly and structural behavior of a model rigid C_{60} -terminated thiolate on Au (111). *Chem. Phys. Lett.* 2009; **470**:289.
11. Bubnis G, Mayne H. A Modeling Study of the Self-Assembly of Various Hydrogen-Bonding Fullerene Derivatives on Au (111). *J. Phys. Chem. C.* 2010; **114**:13071.
12. Smerdon J. A, Rankin R. B, Greeley J. P, Guisinger N. P, Guest J. R. Chiral “Pinwheel” Heterojunctions Self-Assembled from C_{60} and Pentacene. *ACS nano.* 2013; **7**:3086.
13. Calmettes B, Nagarajan S, Gourdon A, Abel M, Porte L, Coratger R. Bicomponent supramolecular packing in flexible phthalocyanine networks. *Ang. Chemie. Intern. Ed.* 2008; **47**:6994.
14. Toader M, Gopakumar T. G, Abdel-Hafiez M, Hietschold M. Exploring the $F_{16}CoPc/Ag$ (110) Interface Using Scanning Tunneling Microscopy and Spectroscopy. Part 1: Template-Guided Adlayer Structure Formation. *J. Phys. Chem. C.* 2010; **114**:3537.
15. Lu X, Hipps K, Wang X, Mazur U. Scanning tunneling microscopy of metal phthalocyanines: d7 and d9 cases. *J. Am. Chem. Soc.* 1996; **118**:7197.
16. Lu X, Hipps K. Scanning tunneling microscopy of metal phthalocyanines: d6 and d8 cases. *J. Phys. Chem. B.* 1997; **101**:5391.
17. Pint C. L, Roth M, Wexler C. Behavior of hexane on graphite at near-monolayer densities: Molecular dynamics study. *Phys. Rev. B.* 2006; **73**:085422.

18. Kuchta B, Eters R. Calculated properties of monolayer and multilayer N₂ on graphite. *Phys. Rev. B.* 1987; **36**:3400.
19. Nieckarz D, Szabelski P. Understanding Pattern Formation in 2D Metal–Organic Coordination Systems on Solid Surfaces. *J. Phys. Chem. C.* 2013; **117**:11229.
20. Szabelski P, Kasperski A. Two-dimensional chiral molecular networks from achiral building blocks: a computational study. *Top. in Catal.* 2011; **54**:1368.
21. Tahara K, Ghijsens E, Matsushita M, Szabelski P, De Feyter S, Tobe Y. Formation of a non-crystalline bimolecular porous network at a liquid/solid interface. *Chem. Comm.* 2011; **47**:11459.
22. Szabelski P, Rżysko W, Pańczyk T, Ghijsens E, Tahara K, Tobe Y, et al. Self-assembly of molecular tripods in two dimensions: structure and thermodynamics from computer simulations. *RSC Adv.* 2013; **3**:25159.
23. Szabelski P, De Feyter S, Drach M, Lei S. Computer simulation of chiral nanoporous networks on solid surfaces. *Langmuir.* 2010; **26**:9506.
24. Nieckarz D, Szabelski P. Simulation of the self-assembly of simple molecular bricks into Sierpiński triangles. *Chem. Comm.* 2014; **50**:6843.
25. Kasperski A, Szabelski P. Theoretical modeling of the formation of chiral molecular patterns in self-assembled overlayers. *Surf Sci.* 2014; **629**:57.
26. Balbás Gamba M, Rohr C, Gruber K, Hermann B. A., Franosch T. Simulating self-organized molecular patterns using interaction-site models. *Euro. Phys. J. E.* 2012; **35**(25).
27. Furukawa S, Uji-i H, Tahara K, Ichikawa T, Sonoda M, De Schryver F. C, et al. Molecular geometry directed Kagome and honeycomb networks: toward two-dimensional crystal engineering. *J. Am. Chem. Soc.* 2006; **128**:3502.
28. Kalia R, Vashishta P, Mahanti S. Orientational Order-Disorder Transition on a Surface. *Phys Rev. Lett.* 1982; **49**:676.
29. Chacón E, Tarazona P. Orientational phase transitions in systems of adsorbed molecules. *Phys. Rev. B.* 1989; **39**:7111.
30. Cai Z. Orientational phase transitions in systems of adsorbed molecules. *Phys. Rev. B.* 1991; **43**:6163.
31. Massidda V, Hernando J. Order-disorder transitions for a two-dimensional lattice of reorientable quadrupoles in the mean-field approximation. *Physica A: Stat. Mech. and App.* 1984; **128**:318.
32. Massidda V, Hernando J. Order-disorder transitions for a two-dimensional lattice of reorientable molecules: II. The case of dipoles and quadrupoles. *Physica A: Stat. Mech. and App.* 1984 1990; **167**:887.
33. Tang S, Mahanti S, Kalia R. Lennard-Jones molecules on a two-dimensional lattice: A model anisotropic XY system. *Phys. Rev. B.* 1985; **32**:3148.
34. Mouritsen O, Berlinsky A. Fluctuation-Induced First-Order Phase Transition in an Anisotropic Planar Model of N₂ on Graphite. *Phys. Rev. Lett.* 1982; **48**:181.

35. Ramseyer C, Pouthier V, Humbert J, Girardet C. Orientational ordering in physisorbed molecular layers induced by surface geometry and confinement. *Intern. J. Quan. Chem.* 2004; **99**:735.
36. O'Shea S. F, Klein M. L. Orientational phases of classical quadrupoles on a triangular net. *Chem. Phys. Lett.* 1979; **66**:381.
37. López L, Ramirez-Pastor A. Adsorption of Self-Assembled Rigid Rods on Two-Dimensional Lattices. *Langmuir.* 2012; **28**:14917.
38. López L, Linares D, Ramirez-Pastor A. Comment on "Effect of polydispersity on the ordering transition of adsorbed self-assembled rigid rods". *Phys. Rev. E.* 2012; **85**:053101.
39. López L, Linares D, Ramirez-Pastor A. Critical behavior of self-assembled rigid rods on triangular and honeycomb lattices. *J. Chem. Phys.* 2010; **133**:134702.
40. López L, Linares D, Ramirez-Pastor A, Stariolo D, Cannas S. Critical behavior of self-assembled rigid rods on two-dimensional lattices: Bethe-Peierls approximation and Monte Carlo simulations. *J. Chem. Phys.* 2013; **138**:234706.
41. López L, Linares D, Ramirez-Pastor A. Critical exponents and universality for the isotropic-nematic phase transition in a system of self-assembled rigid rods on a lattice. *Phys. Rev. E.* 2009; **80**:040105.
42. López L, Linares D, Ramirez-Pastor A, Cannas S. Phase diagram of self-assembled rigid rods on two-dimensional lattices: Theory and Monte Carlo simulations. *J. Chem. Phys.* 2010; **133**:134706.
43. Almarza N. G, Tavares J, da Gama M. T. Effect of polydispersity on the ordering transition of adsorbed self-assembled rigid rods. *Phys. Rev. E.* 2010; **82**:061117.
44. Almarza N. G, Tavares J, da Gama M. T. Communication: The criticality of self-assembled rigid rods on triangular lattices. *J. Chem. Phys.* 2011; **134**:071101.
45. Almarza N. G, Tavares J, da Gama M. T. Reply to "Comment on 'Effect of polydispersity on the ordering transition of adsorbed self-assembled rigid rods'". *Phys. Rev. E.* 2012; **85**:053102.
46. Ciesielski A, Szabelski P. J, Rżysko W, Cadeddu A, Cook T. R, Stang P. J, et al. Concentration-dependent supramolecular engineering of hydrogen-bonded nanostructures at surfaces: predicting self-assembly in 2D. *J. Am. Chem. Soc.* 2013; **135**:6942.
47. Hosseini M, Lehn J. Anion receptor molecules. Chain length dependent selective binding of organic and biological dicarboxylate anions by ditopic polyammonium macrocycles. *J. Am. Chem. Soc.* 1982; **104**:3525.
48. Barth J. V, Costantini G, Kern K. Engineering atomic and molecular nanostructures at surfaces. *Nature.* 2005; **437**:671.
49. Vilan A, Cahen D. How organic molecules can control electronic devices. *Trends. Biotechnol.* 2002; **20**:22.
50. Uemura S, Sakata M, Hirayama C, Kunitake M. Fullerene adlayers on various single-crystal metal surfaces prepared by transfer from L films. *Langmuir.* 2004; **20**:9198.

51. Maruccio G, Cingolani R, Rinaldi R. Projecting the nanoworld: concepts, results and perspectives of molecular electronics. *J. Mat. Chem.* 2004; **14**:542.
52. Bonifazi D, Enger O, Diederich F. Supramolecular [60] fullerene chemistry on surfaces. *Chem. Soc. Rev.* 2007; **36**:390.
53. Benjamin S. C, Ardavan A, Briggs GAD, Britz D. A, Gunlycke D, Jefferson J, et al. Towards a fullerene-based quantum computer. *J. Phys.: Cond. Matter.* 2006; **18**:S867.
54. Baiker A. Progress in asymmetric heterogeneous catalysis: Design of novel chirally modified platinum metal catalysts. *J. Mol. Cata. A: Chemical.* 1997; **115**:473.
55. Borszeczy K, Mallat T, Baiker A. Enantioselective hydrogenation of α , β -unsaturated acids. Substrate-modifier interaction over cinchonidine modified PdAl₂O₃. *Tetrahedron: Asymmetry.* 1997; **8**:3745.
56. Baddeley C. Fundamental investigations of enantioselective heterogeneous catalysis. *Top. in Cata.* 2003; **25**:17.
57. Lorenzo M. O, Baddeley C, Muryn C, Raval R. Extended surface chirality from supramolecular assemblies of adsorbed chiral molecules. *Nature.* 2000; **404**:376.
58. Hazen R. M, Filley T. R, Goodfriend G. A. Selective adsorption of L- and D-amino acids on calcite: Implications for biochemical homochirality. *Proc. Natl. Acad. Sci. U S A.* 2001 May 8; **98**:5487.
59. Hazen R. M, Sholl D. S. Chiral selection on inorganic crystalline surfaces. *Nat. Mater.* 2003; **2**:367.
60. Bu Y, Wang S, Chen Q, Jin H, Lin J, Wang J. Self-assembly of osmium complexes on reduced graphene oxide: A case study toward electrochemical chiral sensing. *Electrochem. Comm.* 2012; **16**:80.
61. Walter M. G, Rudine A. B, Wamser C. C. Porphyrins and phthalocyanines in solar photovoltaic cells. *J. Porph. Phthal.* 2010; **14**:759.
62. Yella A, Lee H. W, Tsao H. N, Yi C, Chandiran A. K, Nazeeruddin M. K, et al. Porphyrin-sensitized solar cells with cobalt (II/III)-based redox electrolyte exceed 12 percent efficiency. *Science.* 2011 Nov 4; **334**:629.
63. Kroto H, Heath J, O'Brien S, Curl R, Smalley R. C₆₀ buckminsterfullerene. *Nature.* 1985; **318**:162.
64. Kroto H. W, Allaf A, Balm S. C₆₀: Buckminsterfullerene. *Chem. Rev.* 1991; **91**:1213.
65. Smeets S, Xie D, McCusker L. B, Baerlocher C, Zones SI, Thompson JA, et al. SSZ-45: A High-Silica Zeolite with Small Pore Openings, Large Cavities, and Unusual Adsorption Properties. *Chem. Mater.* 2014; **26**:3909.
66. Schull G, Douillard L, Fiorini-Debuisschert C, Charra F, Mathevet F, Kreher D, et al. Single-molecule dynamics in a self-assembled 2D molecular sieve. *Nano. letters.* 2006; **6**:1360.
67. Shen Y, Zeng L, Lei D, Zhang X, Deng K, Feng Y, et al. Competitive adsorption and dynamics of guest molecules in 2D molecular sieves. *J. Mater. Chem.* 2011; **21**:8787.

68. Kühnle A, Linderoth T. R, Hammer B, Besenbacher F. Chiral recognition in dimerization of adsorbed cysteine observed by scanning tunnelling microscopy. *Nature*. 2002; **415**:891.
69. Pan G, Luo J, Zheng Q, Wan L. Chiral molecular cavities of calix [4] crown on Au (111). *J. Nanosc. Nanotech.* 2008; **8**:5702.
70. Lopinski G, Moffatt D, Wayner D, Wolkow R. Determination of the absolute chirality of individual adsorbed molecules using the scanning tunnelling microscope. *Nature*. 1998; **392**:909.
71. Desiraju G. R. Supramolecular synthons in crystal engineering—a new organic synthesis. *Angew. Chemie Intern. Ed.* 1995; **34**:2311.
72. Yokoyama T, Kamikado T, Yokoyama S, Mashiko S. Conformation selective assembly of carboxyphenyl substituted porphyrins on Au (111). *J. Chem. Phys.* 2004; **121**:11993.
73. Dmitriev A, Lin N, Weckesser J, Barth J, Kern K. Supramolecular assemblies of trimesic acid on a Cu (100) surface. *J. Phys. Chem. B.* 2002; **106**:6907.
74. Lin N, Payer D, Dmitriev A, Strunskus T, Wöll C, Barth J. V, et al. Two-Dimensional Adatom Gas Bestowing Dynamic Heterogeneity on Surfaces. *Angew. Chemie Intern Ed.* 2005; **44**:1488.
75. Griessl S, Lackinger M, Edelwirth M, Hietschold M, Heckl W. M. Self-assembled two-dimensional molecular host-guest architectures from trimesic acid. *Single Molecules.* 2002; **3**:25.
76. Nilsson L, Šljivančanin Ž, Balog R, Xu W, Linderoth T. R, Lægsgaard E, et al. Linear hydrogen adsorbate structures on graphite induced by self-assembled molecular monolayers. *Carbon.* 2012; **50**:2052.
77. Bartels L. Tailoring molecular layers at metal surfaces. *Nature chemistry.* 2010; **2**:87.
78. Kühnle A. Self-assembly of organic molecules at metal surfaces. *Current Opinion in Colloid & Interface Science.* 2009; **14**:157.
79. Toader M, Shukryna P, Knupfer M, Zahn D. R, Hietschold M. Site-Dependent Donation/Backdonation Charge Transfer at the CoPc/Ag (111) Interface. *Langmuir.* 2012; **28**:13325.
80. Toader M, Knupfer M, Zahn D. R, Hietschold M. Initial growth at the F₁₆CoPc/Ag (111) interface. *Surf. Sci.* 2011; **605**:1510.
81. Scheffler M, Smykalla L, Baumann D, Schlegel R, Hänke T, Toader M, et al. Structural study of monolayer cobalt phthalocyanine adsorbed on graphite. *Surf. Sci.* 2013; **608**:55.
82. Toader M, Hietschold M. SnPc on Ag (111): A Scanning Tunneling Microscopy Study at the Submolecular Level. *J. Phys. Chem. C.* 2011; **115**:12494.
83. Toader M, Hietschold M. Tuning the energy level alignment at the SnPc/Ag (111) interface using an STM tip. *J. Phys. Chem.C.* 2011; **115**:3099.
84. Toader M, Knupfer M, Zahn D. R, Hietschold M. Initial growth of Lutetium (III) Bis-phthalocyanine on Ag (111) surface. *J. Am. Chem. Soc.* 2011; **133**:5538.

85. Rohr C, Balbás Gamba M, Gruber K, Constable E, Frey E, Franosch T, et al. Molecular Jigsaw: Pattern Diversity Encoded by Elementary Geometrical Features. *Nano letters*. 2010; **10**:833.
86. Hermann B, Rohr C, Gamba M. B, Malecki A, Malarek M, Frey E, et al. Molecular self-organization: Predicting the pattern diversity and lowest energy state of competing ordering motifs. *Phys. Rev. B*. 2010; **82**:165451.
87. Weigelt S, Schnadt J, Tuxen A. K, Masini F, Bombis C, Busse C, et al. Formation of trioctylamine from octylamine on Au (111). *J. Am. Chem. Soc.* 2008; **130**:5388.
88. Masini F, Kalashnyk N, Knudsen M. M, Cramer J. R, Lægsgaard E, Besenbacher F, et al. Chiral induction by seeding surface assemblies of chiral switches. *J. Am. Chem. Soc.* 2011; **133**:13910.
89. Nuermairaiti A, Bombis C, Knudsen M. M, Cramer J. R, Lægsgaard E, Besenbacher F, et al. Chiral Induction with Chiral Conformational Switches in the Limit of Low “Sergeants to Soldiers” Ratio. *ACS nano*. 2014; **8**:8074.
90. Bombis C, Weigelt S, Knudsen M. M, Nørgaard M, Busse C, Lægsgaard E, et al. Steering organizational and conformational surface chirality by controlling molecular chemical functionality. *ACS nano*. 2009; **4**:297.
91. Schlickum U, Decker R, Klappenberger F, Zoppellaro G, Klyatskaya S, Auwärter W, et al. Chiral kagomé lattice from simple ditopic molecular bricks. *J. Am. Chem. Soc.* 2008; **13**:11778.
92. Berlinsky A, Harris A. Orientational phases of hydrogen molecules on a triangular lattice. *Phys. Rev. Lett.* 1978; **40**:1579.
93. Marx D, Wiechert H. Ordering and phase transitions in adsorbed monolayers of diatomic molecules. *Adv. Chem. Phys.* 1997; **95**:213.
94. Dawoud J, Sallabi A, Jack D. A perturbation theory study of H₂ on LiF (001). *Surf. Sci.* 2007; **601**:3731.
95. Dawoud J, Sallabi A, Jack D. A Monte Carlo simulation study of H₂ layers on NaCl (001). *Appl. Surf. Sci.* 2008; **254**:7807.
96. Dawoud J, Jack D. D₂ layers on MgO (001): Simulation study. *Appl. Surf. Sci.* 2009; **256**:1443.
97. Dawoud J, Sallabi A, Fafous I, Jack D. Structures of D₂ Layers on MgO (001). *e-J. Surf. Sc. Nanotech.* 2009; **7**:207.
98. Dawoud J, Fafous I, Hamzeh S, Jack D. Structures of D₂ layers on LiF (001). *J. Colloid. Interface Sci.* 2010; **343**(1):217.
99. Sallabi A, Dawoud J, Jack D. A Monte Carlo simulation study of Nitrogen on LiF (001). *Appl. Surf. Sci.* 2010; **256**:2974.
100. The Cambridge Cluster Database. Wales D. J., Doye J. P. K., Dullweber A., Hodges M. P., Naumkin F. Y. , Calvo F., Hernández-Rojas J., and Middleton T. F., Available from: <http://www-wales.ch.cam.ac.uk/CCD.html>.

101. Miller M. A, Doye J. P, Wales DJ. Structural relaxation in Morse clusters: energy landscapes. *J. Chem. Phys.* 1999; **110**:328.
102. Wales D. J, Doye J. P, Miller M. A, Mortenson P. N, Walsh T. R. Energy landscapes: from clusters to biomolecules. *Adv. Chem. Phys.* 2000; **115**:1.
103. Feng Y, Cheng L, Liu H. Putative global minimum structures of Morse clusters as a function of the range of the potential: $161 \leq n \leq 240$. *J. Phys. Chem. A.* 2009; **113** :13651.
104. Mehta D, Hughes C, Schröck M, Wales D. J. Potential energy landscapes for the 2D XY model: Minima, transition states, and pathways. *J. Chem. Phys.* 2013; **139**:194503.
105. Otero R, Schöck M, Molina L. M, Lægsgaard E, Stensgaard I, Hammer B, et al. Guanine quartet networks stabilized by cooperative hydrogen bonds. *Ang. Chemie Intern. Ed.* 2005; **44**:2270.
106. Smit B, Hilbers P, Esselink K. Computer simulations of surfactant self assembly. *Intern. J. Mod. Phys. C.* 1993; **4**:393.
107. Izvekov S, Voth G. A. Multiscale coarse graining of liquid-state systems. *J. Chem. Phys.* 2005; **123**:134105.
108. Bubnis G. J, Mayne H. R. Adlayer Morphologies and Free Energy Landscapes of Clusters of Bis-Fullerenes on Model Gold Surfaces. *J. Phys. Chem. A.* 2011; **115**:7044.
109. Cross C, Fung B. A simplified approach to molecular dynamics simulations of liquid crystals with atom–atom potentials. *J. Chem. Phys.* 1994; **101**:6839.
110. Girifalco L. Molecular properties of fullerene in the gas and solid phases. *J. Phys. Chem.* 1992; **96**:858.
111. Marrink S. J, Risselada H. J, Yefimov S, Tieleman D. P, De Vries A. H. The MARTINI force field: coarse grained model for biomolecular simulations. *J. Phys. Chem. B.* 2007; **111**:7812.
112. Zhang Z, Glotzer S. C. Self-assembly of patchy particles. *Nano Letters.* 2004; **4**:1407.
113. Loget G, Kuhn A. Bulk synthesis of Janus objects and asymmetric patchy particles. *J. Mat. Chem.* 2012; **22**:15457.
114. Doye J. P, Louis A. A, Lin I, Allen LR, Noya EG, Wilber AW, et al. Controlling crystallization and its absence: proteins, colloids and patchy models. *Phys. Chem. Chemical Phys.* 2007; **9**:2197.
115. Berezutskiy G. N. A model study of adlayer pattern formation of a linear molecule on square and triangular lattices; 2011, Master Thesis, Chem. Dept. /University of New Hampshire.
116. Zhao J, Li Y, Lin Z, Xie L, Shi N, Wu X, et al. Molecule length directed self-assembly behavior of tetratopic oligomeric phenylene– ethynylenes end-capped with carboxylic groups by scanning tunneling microscopy. *J. Phys. Chem. C.* 2010; **114**:9931.
117. Xu L, Miao X, Zha B, Miao K, Deng W. Dipole-controlled self-assembly of 2, 7-bis (n-alkoxy)-9-fluorenone: Odd–even and chain-length effects. *J. Phys. Chem. C.* 2013; **117**:12707.
118. Allen M. P, Tildesley D. J. Computer simulation of liquids. Oxford university press; 1989.

119. Nelson D. R, Halperin B. Dislocation-mediated melting in two dimensions. *Phys. Rev. B.* 1979; **19**:2457.
120. Steinhardt P. J, Nelson D. R, Ronchetti M. Bond-orientational order in liquids and glasses. *Phys. Rev. B.* 1983; **28**:784.
121. Kapfer S. C, Mickel W, Mecke K, Schröder-Turk GE. Jammed spheres: Minkowski tensors reveal onset of local crystallinity. *Phys. Rev. E.* 2012; **85**:030301.
122. Talbot J, Tildesley D, Steele W. Molecular-dynamics simulation of fluid N₂ adsorbed on a graphite surface. *Faraday Discuss Chem. Soc.* 1985; **80**:91.
123. Geng J, Selinger J. V. Theory and simulation of two-dimensional nematic and tetratic phases. *Phys. Rev. E.* 2009; **80**:011707.
124. Connolly M, Roth M, Gray P. A, Wexler C. Explicit hydrogen molecular dynamics simulations of hexane deposited onto graphite at various coverages. *Langmuir.* 2008; **24**:3228.
125. Connolly M, Roth M, Wexler C, Gray P. A. Molecular Dynamics Simulations of Hexane Deposited onto Graphite: An Explicit-Hydrogen Model at $\rho =$. *Am. J. Undergrad. Res.* 2007; **6**:27.
126. Raval R. Chiral expression from molecular assemblies at metal surfaces: insights from surface science techniques. *Chem. Soc. Rev.* 2009; **38**:707.
127. Foroughi L. M, Matzger A. J. Two-dimensional chirality: Intelligent design. *Nature chemistry.* 2011; **3**(9):663.
128. Chen T, Wang D, Wan L. Two-dimensional chiral molecular assembly on solid surfaces: formation and regulation. *Nat. Sci. Rev.* 2015: doi: 10.1093/nsr/nwv012.
129. Linares M, Minoia A, Brocorens P, Beljonne D, Lazzaroni R. Expression of chirality in molecular layers at surfaces: insights from modelling. *Chem. Soc. Rev.* 2009; **38**(3):806.
130. Oura K, Zotov A, Lifshits V, Saranin A, Katayama M. *Surface science.* Springer; 2003.
131. Doucet J. Relation between the herringbone packing and the chain behaviour in the ordered smectic phases. *J. de Physique Lettres.* 1979; **40**:185.
132. Clair S, Pons S, Seitsonen A. P, Brune H, Kern K, Barth J. V. STM Study of Terephthalic Acid Self-Assembly on Au(111): Hydrogen-Bonded Sheets on an Inhomogeneous Substrate. *J. Phys. Chem. B.* 2004; **108**:14585.
133. Chen Q, Chen T, Wang D, Liu HB, Li Y. L, Wan L. J. Structure and structural transition of chiral domains in oligo(p-phenylenevinylene) assembly investigated by scanning tunneling microscopy. *Proc, Natl, Acad, Sci, U S A.* 2010 Feb 16; **107**:2769.
134. Chen Z, Klyatskaya S, Urgel J. I, Écija D, Fuhr O, Auwärter W, et al. Synthesis, characterization, monolayer assembly and 2D lanthanide coordination of a linear terphenyl-di (propiolonitrile) linker on Ag (111). *Beilstein Journal of Nanotech.* 2015; **6**:327.
135. Stepanow S, Lin N, Vidal F, Landa A, Ruben M, Barth J. V, et al. Programming supramolecular assembly and chirality in two-dimensional dicarboxylate networks on a Cu (100) surface. *Nano letters.* 2005; **5**:901.

136. Hammonds K. D, McDonald I. R, Tildesley D. J. Computational studies of the structure of carbon dioxide monolayers physisorbed on the basal plane of graphite. *Mol. Phys.* 1990; **70**:175.
137. Mederos L, Chacón E, Tarazona P. Pinwheel and herringbone phases in systems of adsorbed molecules. *Phys. Rev. B.* 1990; **42**:8571.
138. Lawrence-Hurt L, Global energy minimization of linear molecules in a hexagonal adlayer; 2011, Master Thesis, Math. Dept. /University of New Hampshire.
139. Fortuna S, Cheung D. L, Troisi A. Hexagonal lattice model of the patterns formed by hydrogen-bonded molecules on the surface. *J. Phys. Chem. B.* 2010; **114**:1849.
140. Lackinger M, Griessl S, Markert T, Jamitzky F, Heckl W. M. Self-assembly of benzenedicarboxylic acid isomers at the liquid solid interface: Steric aspects of hydrogen bonding. *J. Phys. Chem. B.* 2004; **108**:13652.
141. Ha S. D, Kaafarani B. R, Barlow S, Marder S. R, Kahn A. Multiphase growth and electronic structure of ultrathin hexaazatrinaphthylene on Au (111). *J. Phys. Chem. C.* 2007; **111**:10493.
142. Kasperski A, Nieckarz D, Szabelski P. Structure formation in adsorbed overlayers comprising functional cross-shaped molecules: A Monte Carlo study. *Surf. Sci.* 2015. DOI: 10.1016/j.susc.2015.02.005
143. Kasperski A, Szabelski P. Two-dimensional molecular sieves: structure design by computer simulations. *Adsorption.* 2013; **19**:283.
144. Calvo F. All-exchanges parallel tempering. *J. Chem. Phys.* 2005; **123**:124106.
145. Frenkel D, Smit B. Understanding molecular simulation: from algorithms to applications. Academic press; 2001.
146. Yan Q, de Pablo J. J. Hyper-parallel tempering Monte Carlo: Application to the Lennard-Jones fluid and the restricted primitive model. *J. Chem. Phys.* 1999; **111** (21):9509.
147. Pfrommer B. G, Côté M, Louie S. G, Cohen M. L. Relaxation of crystals with the quasi-Newton method. *J. Comp. Phys.* 1997; **131**:233.
148. Snyman J. Practical mathematical optimization: an introduction to basic optimization theory and classical and new gradient-based algorithms. Springer Science & Business Media; 2005.